



N°d'ordre NNT : 2017LYSEI085

THESE de DOCTORAT DE L'UNIVERSITE DE LYON
Préparée au sein de
L'Institut National des Sciences Appliquées de Lyon

Ecole Doctorale 162
Mécanique, Énergétique, Génie civil, Acoustique

Spécialité de doctorat :
MÉCANIQUE – GÉNIE MÉCANIQUE – GÉNIE CIVIL

Soutenue publiquement le 28/09/2017, par :
Hu XIONG

**Simulation of forming, compaction and consolidation of
thermoplastic composites based on solid shell elements**

**Simulations de la mise en forme, la compaction et la
consolidation de composites thermoplastiques basées sur des
éléments finis solides-coques**

Devant le jury composé de :

F. JACQUEMIN	Professeur (Université de Nantes)	Rapporteur
R. AYAD	Professeur (Université de Reims)	Rapporteur
J. BIKARD	Docteur ingénieur (Solvay, Saint-Fons)	Examineur
D. BAILLIS	Professeur (INSA de Lyon)	Examinatrice
P. BOISSE	Professeur (INSA de Lyon)	Directeur de thèse
N. HAMILA	Maitre de conférences HDR (INSA de Lyon)	Co-directeur de thèse

Département FEDORA – INSA Lyon - Ecoles Doctorales – Quinquennal 2016-2020

SIGLE	ECOLE DOCTORALE	NOM ET COORDONNEES DU RESPONSABLE
CHIMIE	CHIMIE DE LYON http://www.edchimie-lyon.fr Sec : Renée EL MELHEM Bat Blaise Pascal 3 ^e étage secretariat@edchimie-lyon.fr Insa : R. GOURDON	M. Stéphane DANIELE Institut de Recherches sur la Catalyse et l'Environnement de Lyon IRCELYON-UMR 5256 Équipe CDFA 2 avenue Albert Einstein 69626 Villeurbanne cedex directeur@edchimie-lyon.fr
E.E.A.	ELECTRONIQUE, ELECTROTECHNIQUE, AUTOMATIQUE http://edeea.ec-lyon.fr Sec : M.C. HAVGOUDOUKIAN Ecole-Doctorale.eea@ec-lyon.fr	M. Gérard SCORLETTI Ecole Centrale de Lyon 36 avenue Guy de Collongue 69134 ECULLY Tél : 04.72.18 60.97 Fax : 04 78 43 37 17 Gerard.scorletti@ec-lyon.fr
E2M2	EVOLUTION, ECOSYSTEME, MICROBIOLOGIE, MODELISATION http://e2m2.universite-lyon.fr Sec : Sylvie ROBERJOT Bât Atrium - UCB Lyon 1 04.72.44.83.62 Insa : H. CHARLES secretariat.e2m2@univ-lyon1.fr	M. Fabrice CORDEY CNRS UMR 5276 Lab. de géologie de Lyon Université Claude Bernard Lyon 1 Bât Géode 2 rue Raphaël Dubois 69622 VILLEURBANNE Cédex Tél : 06.07.53.89.13 cordey@univ-lyon1.fr
EDISS	INTERDISCIPLINAIRE SCIENCESSANTE http://www.edisslyon.fr Sec : Sylvie ROBERJOT Bât Atrium - UCB Lyon 1 04.72.44.83.62 Insa : M. LAGARDE secretariat.ediss@univ-lyon1.fr	Mme Emmanuelle CANET-SOULAS INSERM U1060, CarMeN lab, Univ. Lyon 1 Bâtiment IMBL 11 avenue Jean Capelle INSA de Lyon 696621 Villeurbanne Tél : 04.72.68.49.09 Fax :04 72 68 49 16 Emmanuelle.canet@univ-lyon1.fr
INFOMATHS	INFORMATIQUE ET MATHEMATIQUES http://infomaths.univ-lyon1.fr Sec :Renée EL MELHEM Bat Blaise Pascal, 3 ^e étage Tél : 04.72. 43. 80. 46 Fax : 04.72.43.16.87 infomaths@univ-lyon1.fr	M. Luca ZAMBONI Bâtiment Braconnier 43 Boulevard du 11 novembre 1918 69622 VILLEURBANNE Cedex Tél :04 26 23 45 52 zamboni@maths.univ-lyon1.fr
Matériaux	MATERIAUX DE LYON http://ed34.universite-lyon.fr Sec : Marion COMBE Tél:04-72-43-71-70 -Fax : 87.12 Bat. Direction ed.materiaux@insa-lyon.fr	M. Jean-Yves BUFFIERE INSA de Lyon MATEIS Bâtiment Saint Exupéry 7 avenue Jean Capelle 69621 VILLEURBANNE Cedex Tél : 04.72.43 71.70 Fax 04 72 43 85 28 Ed.materiaux@insa-lyon.fr
MEGA	MECANIQUE, ENERGETIQUE, GENIE CIVIL, ACOUSTIQUE http://mega.universite-lyon.fr Sec : Marion COMBE Tél:04-72-43-71-70 -Fax : 87.12 Bat. Direction mega@insa-lyon.fr	M. Philippe BOISSE INSA de Lyon Laboratoire LAMCOS Bâtiment Jacquard 25 bis avenue Jean Capelle 69621 VILLEURBANNE Cedex Tél : 04.72 .43.71.70 Fax : 04 72 43 72 37 Philippe.boisse@insa-lyon.fr
ScSo	ScSo* http://recherche.univ-lyon2.fr/scso/ Sec : Viviane POLSINELLI Brigitte DUBOIS Insa : J.Y. TOUSSAINT Tél : 04 78 69 72 76 viviane.polsinelli@univ-lyon2.fr	M. Christian MONTES Université Lyon 2 86 rue Pasteur 69365 LYON Cedex 07 Christian.montes@univ-lyon2.fr

*ScSo : Histoire, Géographie, Aménagement, Urbanisme, Archéologie, Science politique, Sociologie, Anthropologie

Abstract

As the pre-impregnated thermoplastic composites have recently attached increasing interest in the automotive industry for their excellent mechanical properties and their rapid cycle manufacturing process, modelling and numerical simulations of forming processes for composites parts with complex geometry is necessary to predict and optimize manufacturing practices. This thesis is devoted to modelling and simulation of the consolidation behavior during thermoplastic prepreg composites forming process. A new seven-node prismatic solid-shell element is proposed: six located at the apexes and the seventh sited at the center. A shear stain field is assumed to subdue transverse shear locking, the enhanced assumed strain method by addition of an extra displacement DOF from the central node and a reduced integration scheme are combined offering a linear varying strain field along the thickness direction to circumvent thickness locking, and an hourglass stabilization procedure is employed in order to correct the element's rank deficiency for pinching. This element permits the modelling of three-dimensional constitutive behavior of thermoplastic prepreg with the consolidation effect, which is modelled by a viscoelastic relaxation model. An intimate contact model is employed to predict the evolution of the consolidation which permits the microstructure prediction of void presented through the prepreg. Within a hyperelastic framework, several simulation tests are launched by combining the new developed finite element and the consolidation models. The comparison with conventional shell element and experimental results shows the efficiency of the proposed solid-shell element not only dealing with the in-plan deformation and bending deformation problems, but also in analyzation of the consolidation behavior, and the degree of intimate contact provides the level of consolidation by applied process conditions, which is essential for the appearance of defects in final composite part.

KEYWORDS: Thermoplastic prepregs, Solid-shell element, Consolidation model, Viscoelasticity, Intimate contact, Forming.

Résumé

Les composites thermoplastiques préimprégnés suscitent un intérêt croissant pour l'industrie automobile grâce à leurs excellentes propriétés mécaniques et leur procédé de fabrication rapide. Dans ce contexte, la modélisation et la simulation numérique des procédés de mise en forme de pièces composites à géométries complexes sont nécessaires pour prédire et optimiser les pratiques de fabrication. Cette thèse est consacrée à la modélisation et à la simulation du comportement de consolidation des composites thermoplastiques préimprégnés lors du processus de mise en forme. Un nouvel élément solide-coque prismatique à sept nœuds est proposé: six situés aux sommets et le septième situé au centre. Le champ de cisaillement transverse est supposé afin de réprimer le verrouillage de cisaillement transversal. La méthode de déformation renforcée supposée par addition d'un DOF de déplacement supplémentaire depuis le nœud central et un schéma d'intégration réduit sont combinées offrant un champ de déformation linéaire le long de la direction d'épaisseur pour contourner le verrouillage. De plus, une procédure de stabilisation de sablier est employée afin de corriger le défaut de rang de l'élément pour le pincement. Cet élément utilise un modèle de relaxation viscoélastique pour modéliser le comportement tridimensionnel de composites thermoplastiques préimprégnés avec effet de consolidation. Un modèle de contact intime est également utilisé pour prédire l'évolution de la consolidation et la microstructure du vide présente au sein du préimprégné. A l'aide d'une loi hyperélastique, plusieurs simulations ont été conduites en combinant le nouvel élément fini et les modèles de consolidation. La comparaison des résultats de simulation avec les essais expérimentaux montre l'efficacité de l'élément solide-coque face aux problèmes de déformations dans le plan et en flexion, mais également pour l'analyse du comportement de consolidation. De plus, le degré de contact intime fournit le degré de consolidation par conditions de procédé appliqué, ce qui est essentiel pour l'apparition de défauts dans la pièce finale de composite.

MOTS CLES: Thermoplastique, Élément solide-coque, Modèle de consolidation, Viscoélasticité, Contact intime, Mise en forme.

Contents

Abstract	I
Résumé	III
Contents.....	1
List of Figures	5
List of Tables.....	9
Introduction	11
Chapter 1	13
Introduction to composite materials: definition, processing techniques	13
1.1 General introduction to composites materials	13
1.2 Composites with continuous fibers and organic matrix	14
1.2.1 Fibers.....	14
1.2.2 Yarns	16
1.2.3 Reinforcements.....	16
1.2.4 Organic matrix.....	17
1.2.5 Prepregs (Pre-impregnated composites).....	18
1.3 Manufacturing processes	19
1.3.1 Liquid composite molding (LCM)	19
1.3.2 Thermoforming process.....	20
1.4 Simulation models for the forming of reinforcements	21
1.4.1 Simulation models at microscopic scale.....	22
1.4.2 Simulation models at the mesoscopic scale.....	22
1.4.3 Simulations at macroscopic scale	24
Chapter 2	31
Mechanical characterizations of thermoplastic prepregs at high temperature.....	31
2.1 Different deformation modes of woven reinforcements.....	31
2.1.1 Biaxial tensile deformation.....	31
2.1.2 In-plan shear deformation.....	34
2.1.3 Bending deformation	37
2.1.4 Transverse shearing deformation	39
2.1.5 Transverse compaction/consolidation	40
2.2 Thermomechanical analysis for thermoplastic pre-impregnated composite	41
2.2.1 Presentation of thermoforming process	41
2.2.2 Presentation of material	43
2.2.3 Bending behavior	44
2.2.4 In-plan shearing behavior	45

2.2.5	Transverse compaction behavior	46
Chapter 3	49
Development of a prismatic solid-shell element for thermo-forming process of thermoplastic prepregs		49
3.1	Introduction	49
3.2	Formulation of solid-shell element SB6Y18	52
3.2.1	In plan strain	53
3.2.2	Pinching	59
3.2.3	Transverse shear	59
3.2.4	Final assessment	64
3.3	Solid-shell element SB7Y19: Supplementary degree of freedom	65
3.3.1	Full 3D behavior law	65
3.3.2	Computing external nodal forces due to a normal pressure	66
3.4	Validation and numerical examples	67
3.4.1	Linear tests	67
3.4.2	Non-linear tests	76
3.5	Non-linear analysis of element SB7Y19 in large deformation	81
3.5.1	Continuum mechanics in large deformation	81
3.5.2	Tensor of deformation gradient	83
3.5.3	Validation tests	85
3.6	Conclusion of chapter 3	87
Chapter 4	89
Viscoelastic characterization for consolidation behavior and a model for the prediction of the consolidation		89
4.1	Introduction	89
4.2	Hyper-elasticity law	90
4.2.1	Definition of hyper-elasticity	90
4.2.2	Hyper-elasticity for woven reinforcement	92
4.2.3	Visco-hyper-elasticity for thermoplastic prepregs	93
4.3	Viscoelastic characterization for consolidation behavior	95
4.3.1	Review of the relatives works	95
4.3.2	Viscoelastic model for consolidation behavior	99
4.3.3	Identification of parameters	101
4.4	Intimate contact model for the prediction of consolidation	104
4.4.1	Intimate contact model	104
4.4.2	Verification test	107
4.4.3	Identification of parameters	108
4.5	Conclusion of chapter 4	110

Chapter 5	111
Numerical simulations.....	111
5.1 Introduction	111
5.2 Central difference method of explicit schema.....	111
5.2.1 Principle of virtual work.....	111
5.2.2 Finite element discretization.....	112
5.2.3 Temporal integration schema	113
5.3 Elementary validation tests	113
5.3.1 Bias-extension test.....	113
5.3.2 Bending test.....	115
5.3.3 Compaction test.....	115
5.4 Simulation of thermoforming	119
5.5 Conclusion of chapter 5.....	126
Conclusions and perspectives.....	127
Bibliography.....	134

List of Figures

Figure 1. 1 : Different type of 2D woven fabrics	16
Figure 1. 2 : Different weaving structure patterns of 3D woven fabric.....	17
Figure 1. 3 : Fabrication methods for composite prepreg sheet stock [CAM 10]	19
Figure 1. 4 : RTM and VARTM.....	20
Figure 1. 5 : Analysis of composite at different scale	21
Figure 1. 6 : Simulation of the reinforcement at microscopic scale [DUR 10].....	22
Figure 1. 7 : Model of Kawabatta for simulation at mesoscopic scale [KAW 73].....	23
Figure 1. 8 : Generation of the geometry of reinforcement composites	24
Figure 1. 9 : Generation of the 3D interlock structure by micro-tomography [NAO 14]	24
Figure 1. 10 : Fishnet algorithm	25
Figure 1. 11 : Modelling of a partial O connected to its four adjacent partials [SZE 05]	26
Figure 1. 12 : Forming simulation by discrete approach [SKO 07]	26
Figure 1. 13 : Experimental and numerical results of double dome benchmark tests with $\pm 45^\circ$ by hypoelastic approach [KHA 10]	27
Figure 1. 14 : Forming simulation of an interlock reinforcement by hyperelastic approach [CHA 12]	27
Figure 1. 15 : Semi-discrete approach for interlock forming simulation [DEL 09]	28
Figure 1. 16 : A representative cell of the meso-mechanical model for NCF with semi-discrete approach [CRE 06]	28
Figure 1. 17 : Semi-discrete triangular element and the forming simulation [HAM 09]	29
Figure 2. 1 : Yarn's tensile behavior [DUM 03]	31
Figure 2. 2 : The schematic of biaxial phenomenon [BOI 04]	32
Figure 2. 3 : Biaxial tension test device and measuring results [BUE 01]	32
Figure 2. 4 : Tensile test of a pre-impregnated thermoplastic yarn at high temperature [WAN 15].....	33
Figure 2. 5 : Shear load versus the displacement [DUM 03]	34
Figure 2. 6 : Displacement field in a yarn during the three phases of shear [ZOU 06].....	35
Figure 2. 7 : Picture frame test device in isothermal oven [LUS 02]	35
Figure 2. 8 : Schematic of an idealized sample for Bias extension test before and after deformation [WAN 08].....	36
Figure 2. 9 : Bias extension test set-up for thermoplastics [GUZ 15]	37
Figure 2. 10 : Forming of an unbalanced textile reinforcement [BOI 11].....	38
Figure 2. 11 : The standard cantilever bending experiment [PEI 30].....	38
Figure 2. 12 : The configuration of flexometer proposed by De Bilbao [DEB 10].....	39
Figure 2. 13 : Bending test set-up configuration [LIA 14]	39
Figure 2. 14 : Transverse shearing test device for interlock reinforcement [CHA 12]	40
Figure 2. 15 : Transverse compaction test device and measuring results [NGU 13]	40
Figure 2. 16 : Five principal steps during thermoforming process.....	42
Figure 2. 17 : Typical thermoforming setup [CAM 10]	42
Figure 2. 18 : Multilayer of the CFRTP before and after consolidation at macro and mesoscopic levels	43
Figure 2. 19 : Image of bending deflexion shape	45
Figure 2. 20 : Bending test results for 2x2 twill in glass/PA66 prepreg.....	45
Figure 2. 21 : Results of bias extension test at different temperature for 2x2 twill in glass/PA66 prepreg	46
Figure 2. 22 : Compaction test device at high temperature.....	47
Figure 2. 23 : Compaction test results at different temperature for 2x2 twill in glass/PA66 prepreg... ..	48

Figure 3. 1: Description of prismatic solid-shell element.....	52
Figure 3. 2: Six-node prismatic element.....	52
Figure 3. 3: Normal vectors and tangential vectors for each triangular side	55
Figure 3. 4: Linking the triangle to the prism.....	57
Figure 3. 5: Geometry of C^0 triangular element	60
Figure 3. 6: Nodal kinematics	60
Figure 3. 7: Square plate simply supported at three corners.....	68
Figure 3. 8: Clamped circular plate (an only quarter due to symmetries)	69
Figure 3. 9: Twisted beam.....	70
Figure 3. 10: Pinched hemispherical shell.....	71
Figure 3. 11: Convergence of the displacement for the pinched hemisphere	72
Figure 3. 12: Pinched cylinder with free ends.....	73
Figure 3. 13: Scordelis-Lo roof.	74
Figure 3. 14: Convergence of normalized deflection at free edge's mid-point w	74
Figure 3. 15: The hyperbolic paraboloid problem.....	75
Figure 3. 16: Convergence of the displacement and in strain energy for the hyperbolic paraboloid problem	75
Figure 3. 17: Cantilever subjected to end shear force	76
Figure 3. 18: Hemispherical shell subjected to alternating radial forces.....	77
Figure 3. 19: Pinched semi-cylindrical isotropic shells subjected to an end pinching force	78
Figure 3. 20: Open-end cylindrical shell subjected to radial pulling forces	80
Figure 3. 21: Undeformed (initial) and deformed (current) configurations of a body	81
Figure 3. 22: Definition of the stress vector	82
Figure 3. 23: Geometry of elementary test.....	85
Figure 4. 1: Consolidation model by the piston and spring analogy [DAV 87].....	97
Figure 4. 2: Consolidation model containing squeezing and percolation flows [BEL 16].....	97
Figure 4. 3: Consolidation and in-plane flow processes for the consolidation of commingled thermoplastic fabrics [VAN 91a].....	98
Figure 4. 4: Generalized relaxation model	100
Figure 4. 5: Load vs. time curves of experimental data and optimal results	104
Figure 4. 6: Discretization by regular rectangular elements with intimate contact model	105
Figure 4. 7: Calculation of mass flows by volume control for one element at time t	105
Figure 4. 8: Degree of intimate contact versus contact time as a function of applied pressure (three top) and temperature (two bottom)	108
Figure 4. 9: Displacement vs. time curves of experimental data and the optimized results of intimate contact model.....	109
Figure 5. 1: Simulation of the Bias-extension test vs experimental data and simulation with shell element at $T = 270^\circ\text{C}$	114
Figure 5. 2: Bending test of a clamped rectangular plate of fabric.....	115
Figure 5. 3: Compaction test of a square thermoplastic composite plate with 4 element	116
Figure 5. 4: Distribution of stress σ_{33} in the bottom face (top) and its stress distribution in bottom face along the radius comparing to analytical results	117
Figure 5. 5: Compaction test of thermoplastic composite plate at 300°C	119
Figure 5. 6: Geometry of circular cylinder test	119
Figure 5. 7: Simulation results after forming process: distribution of transverse stress σ_{33} (MPa/top) and degree of intimate contact D_n (bottom)	120
Figure 5. 8: Distribution of transverse stress σ_{33} (MPa) during consolidation process	120

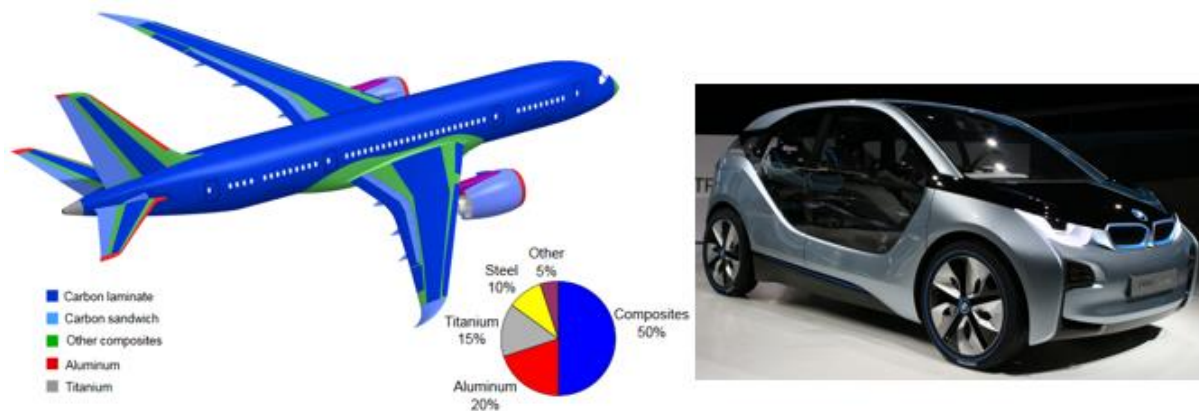
Figure 5. 9: Distribution of thickness E_n (mm) during consolidation process.....	121
Figure 5. 10: Degree of contact intimate during the evolution of consolidation after a consolidated displacement $\Delta u=0.1\text{mm}$	121
Figure 5. 11: <i>Meshed geometry of double dome test</i>	122
Figure 5. 12: Simulation results during foming step of Double dome test.....	123
Figure 5. 13: Distribution of transverse stress σ_{33} (middle face) during consolidation process.....	123
Figure 5. 14: Degree of contact intimate in the middle face during the evolution of consolidation after the consolidated displacement $\Delta u=0.2\text{mm}$ (left row) and $\Delta u=0.5\text{mm}$ (right row)	125

List of Tables

Table 1. 1 : Typical Compositions of Glass Fibers (in wt%) [FRE 01].....	15
Table 1. 2 : Property or characteristic of different types of glass fibers [FRE 01]	15
Table 2. 1 : Principal properties of studied material.....	44
Table 2. 2 : Bending parameters for 2x2 twill in glass/PA66 prepreg	44
Table 3. 1 : Definition of the two covariant basis.....	62
Table 3. 2 : Patch test: Displacements of the considering points.....	68
Table 3. 3 : Center displacement and stress component normal to the mid-plane.....	69
Table 3. 4 : Center displacement and stress component in case 1	70
Table 3. 5 : Center displacement and stress component in case 2	70
Table 3. 6 : Twisted beam: Loading point displacement	71
Table 3. 7 : Pinched hemispherical: Loading point displacement for different type of elements.....	72
Table 3. 8 : Pinched cylinder: Loading point displacement for different type of elements	73
Table 3. 9 : Results of the elementary tests for validation of deformation gradient tensor	86
Table 3. 10 : Loading point displacement of cantilever test.....	86
Table 3. 11 : Loading point displacement of hemispherical shell test.....	87
Table 4. 1 : Deformation modes and their respective invariants for a hyperelastic woven reinforcement	92
Table 4. 2 : In-plan shear parameters with viscoelastic behavior.....	95
Table 4. 3 : Optimized parameters related to consolidation deformation mode at different temperature	103
Table 5. 1 : Results of bending test with three different finite element solutions	115

Introduction

In recent years, composite materials have become one of the most widely used materials because of their high specific stiffness and strength to weight ratio, corrosion resistance, high-impact strength and low thermal conductivity etc. Many industries have been attracted to explore and increase their usage by these advantages, such as, in the areas of energy [AHM 70][AHM 70][AHM 70][AHM 70][AHM 70][AIM 08][ALV 07][AUS 88][BAL 89] [BRØ 05][BRØ 05][BRØ 05][BRØ 05], medicine [RAM 01], sport [EAS 12], and the most particularly in the aeronautic or automotive areas. Two biggest plane makers Airbus and Boeing have launched their new aircrafts with an increased trend of using composite materials. For example, the two competitors A350 and B787 [BOE 13] (**Figure I. 1-a**), composite materials take up more than 50% of the weight for both of them that covers both of their wing and fuselage. In view of the general trend to reduce the impacts on the environment of the vehicle, and obtaining a better performance, the automotive industry has shown increasing interest in the manufacturing processes of thermoplastic–matrix composites materials [FUC 08], the first volume production vehicle on market BMW i3 [BIR 13] (**Figure I. 1-b**) features a passenger cabin made of continuous fiber reinforced composites.



(a): Composite structure content of the B787 (b): Composite body BMW i3 [BIR 13]

Figure I. 1: Application of composites in aeronautic and automotive industry

As one of the biggest part of composite's family, continuous fiber-reinforced thermoplastics composites (CFRTP) already play key role in the automotive community for its manufacturing processes, especially, in thermoforming and thermoforming-stamping techniques for their rapid cycle times and the possible use of pre-existing equipment. Both techniques can be easily automated and are based on the same technology as metal sheet shaping.

This Ph. D thesis is supported by a French project STIICPA, whose objective is to reduce the pollutant emissions by reducing the weight of the vehicle. Hence, composite materials used in this project, even for better environmental impacts than the materials used currently, in terms of impact of the manufacturing process as recyclability. This project brings together 7 partners of industrialists and universities: SOLVAY, Plastic Omnium, Pole Européen de Plasturgie,

Centre Technique Des Industries Mécaniques, LAMCOS (Laboratoire de Mécanique des Contacts et des Structures - INSA de Lyon), LTN (Laboratoire de Thermocinétique de Nantes-Polytech Nantes), GEM (Institut de Recherche en Génie Civil et Mécanique - Ecole Centrale de Nantes).

Chapter 1

Introduction to composite materials: definition, processing techniques

1.1 General introduction to composites materials

Definition

The definition of composite materials (or shortened to composites) in the literature differ widely, and the most universal used definition is, as the name implies, composite materials are a combination of at least two materials in such a way that certain improved or desired properties are achieved better than the used of individual component, they are very common in our daily lives like wood, concrete, tire, and bone etc. Composite materials generally consist of two phases: a reinforcement which gives the material its main mechanical characteristics, and a matrix which ensures cohesion. The variety of materials available to form the reinforcement and the matrix allows to imagine new composite materials suitable for many industrial situations.

Matrix

Actually, the developed matrices of composite materials are generally classified into two categories.

-Organic matrices (thermoplastic, thermosetting and elastomers). They represent the vast majority of matrices used industrially due to their low cost and ease of implementation of the manufacturing process;

- Mineral matrices (ceramic and metallic). Ceramic matrices (oxides and hydrocarbons), carbon matrices and metal (aluminum, magnesium, iron, cobalt, copper) are for advanced applications where hostile environmental conditions (high temperatures, unfavorable humidity) do not allow the use of an organic matrix. Their complex manufacturing processes make them expensive and difficult to produce.

Reinforcement

The reinforcements also may be classified according to their geometry.

- Particulate reinforcements: the matrix is reinforced with a disperse phase of particles with or without preferential orientation. This is usually granular inclusions (chalk), lamellar (talca, mica) or acicular (wallastonite, short fibers). The particulate reinforced composites are rarely used for structural purposes, but rather for specific or consumer product applications;

- Short fiber reinforcements: the matrix is reinforced with a disperse phase of short fibers (lengths less than 100 times of their diameter) with or without preferential orientation. Composites reinforced with short fibers are generally isotropic for their mechanical properties.

- Continuous fiber reinforcements: the matrix is reinforced with a disperse phase continuous fibers whose length is close to that of the final part. Preferred directions of the fibers give the finished piece its main mechanical properties. In this type of reinforcement, the matrix is present only to ensure cohesion of the assembly and provide resistance to forces applied in directions different from those of the fibers.

This work concerns specifically continuous fiber-reinforced thermoplastic composites (CFRTP). Various kinds of fibers: glass, carbon or aramid (Kevlar) could be used for the reinforcements. However, glass fibers are chosen in the context of the project due to the popularity and their low cost face to their thermomechanical properties.

1.2 Composites with continuous fibers and organic matrix

Composites with continuous fibers and organic matrix are widely used in industry, especially in the military sector [LUC 00] [BHA 06], aeronautics [MAZ 05] and in naval application [SMI 90] [MOU 01]. In recent years, the automotive sector also shows an increasing interest in these materials to reduce vehicle weight [VER 06] [FUC 08]. However, large production rates of this sector require short production cycles. Before presenting this transformation stage, a more detailed description of the various constituents of the material is needed to understand the different involved phenomena.

The final behavior of the composite is determined by its multiscale structure and multi material. The fibers are firstly produced and then assembled into yarns (a bundle of fibers), after different patterns of weaves, the variety of reinforcements is thus obtained. Following the manufacturing process, the addition of the matrix takes place before the forming. This is the case of thermoforming process of prepregs (pre-impregnated) reinforcements concerned for the subject of this work. More details would be presented thereafter.

1.2.1 Fibers

Fibers are the principal constituents in a fiber-reinforced composite material. They occupy the largest volume fraction in a composite laminate and share the major portion of the load acting on a composite structure.

Glass fibers are the most common of all reinforced fibers for polymeric matrix composites (PMC). The principal advantages of glass fibers are low cost, high tensile strength, high chemical resistance, and excellent insulating properties [MAL 07]. According to the usage, the fibers are made of several types of compositions as raw material. The principal ingredient in all glass fibers is silica (SiO_2). Other oxides, such as sodium oxide (CaO) which allows to lower the melt temperature and the aluminum oxide (Al_2O_3), which improves the mechanical properties of the material.

Among the various conventional glass compositions, the most commonly used to form such fibers are described in **Table 1. 1**. The two types of glass fibers commonly used in the fiber-reinforced plastics (FRP) industry are E-glass and S-glass. E-glass has the lowest cost of all commercially available reinforcing fibers, it represents more than 95% of the global market for glass fibers for applications of conventional reinforcements with thermoplastic or thermosetting resins. S-glass, originally developed for aircraft components and missile casings, has the highest tensile strength among all fibers in use. The other types of glass fibers and their property is shown in **Table 1. 2** [FRE 01].

TYPE	SiO ₂	Al ₂ O ₃	CaO	MgO	B ₂ O ₃	Na ₂ O	Fe ₂ O ₃	TiO ₂	K ₂ O	F ₂
E-glass	52-56	12-15	21-23	0.4-4	4-6	0-1	0.2-0.4	0-1.5	-	0-1
S-glass	60-65.5	23-25	0-9	6-11	-	0-0.1	0-0.1	-	-	-

Table 1. 1 : Typical Compositions of Glass Fibers (in wt%) [FRE 01]

Letter designation	Property or characteristic
E, electrical	Low electrical conductivity
S, strength	High strength
C, chemical	High chemical durability
M, modulus	High stiffness
A, alkali	High alkali or soda lime glass
D, dielectric	Low dielectric constant

Table 1. 2 : Property or characteristic of different types of glass fibers [FRE 01]

Carbon fibers are mainly used for high performance structures in aeronautics or the sports industry because of their exceptionally high tensile strength–weight ratios as well as tensile modulus–weight ratios, very low coefficient of linear thermal expansion (which provides dimensional stability in such applications as space antennas), high fatigue strengths, and high thermal conductivity (which is even higher than that of copper) [MAL 07], that is the reason that this kind of fibers is chosen for the project STIICPA. The disadvantages are their low strain-to-failure, low impact resistance, and high electrical conductivity, which may cause “shorting” in unprotected electrical machinery. Their high cost has so far excluded them from widespread commercial applications. They are used mostly in the aerospace industry, where weight saving is considered more critical than cost.

The aramid or Kevlar fibers are known for their use in the field of ballistic protection. Having good tensile strength, good vibration damping factor and low density allows their application in the aeronautics industry. Because of their disadvantage of low compressive strength, high moisture recovery, they are often criticized for the difficulty in cutting of dry reinforcements.

Besides the mentioned synthetic fibers, other possibilities like the flax and the hemp, based on natural fibers have attracted more attention and have developed significantly because of their biodegradability, low cost, low relative density, high specific mechanical properties, and renewable nature [OKS 03] [SUD 05] [CEL 13].

1.2.2 Yarns

The yarns are obtained by assembly of the fibers whose nominal diameter is generally between 5 and 24 microns, each yarn comprises between 1000 (1K) and 12000 (12K) fibers. Different assembly types may be carried: the fibers in the yarn can be twisted, interlaced or simply juxtaposed (stratify or roving), giving the yarn more or less coherence. The variables for generally characteristics used to describe a yarn are:

- Material (glass, carbon) and type of assemblage (twisted, stratified)
- Amount of fibers
- Tensile stiffness
- Tensile breaking load
- Mass per unit length (tex, 1 tex=1g/km)

1.2.3 Reinforcements

The reinforcements are obtained by a weaving process of yarns. Different types of weaving generate different internal geometries like, woven, braided, weft knit and non-crimp. The most common reinforcements are woven fabrics due to their good drape ability and availability. They are available as 2D, 3D, and 2.5D (interlocks) forms. Two orthogonal series of yarns, one is parallel to the length of roll called warp yarn, the other is perpendicular to the warp yarn called weft yarn, constitute 2D woven fabrics.

In the family of 2D woven fabrics, there are three principal weaving patterns shown in **Figure 1. 1**:

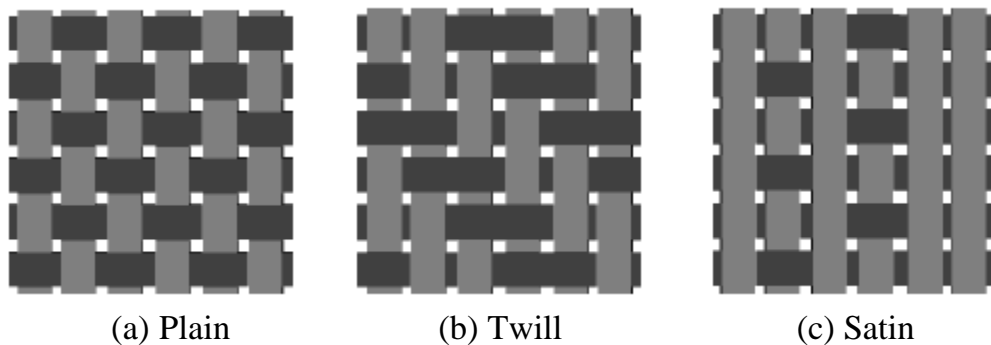


Figure 1. 1 : Different type of 2D woven fabrics

Plain woven fabric: Plain is the simplest kind of woven style. The warp yarn and weft yarn pass over and under each other alternatively to form the whole fabric.

Twill woven fabric: In a twill fabric $N \times M$, N warp yarns pass over and under M weft yarn regularly, twill is another common woven fabric.

Satin woven fabric: Satin has more complex weaving style. N warp yarns pass over and under just one weft yarn, so the warp and the weft yarns are not balanced any more.

For 3D and 2.5D woven fabrics, the warp yarns pass over several plans of the weft yarns through the thickness of material for obtaining a high thickness strength and stiffness of final composites. Different weaving structure patterns of 3D woven fabric presented in **Figure 1. 2** have a great influence on its behavior [GU 02]:

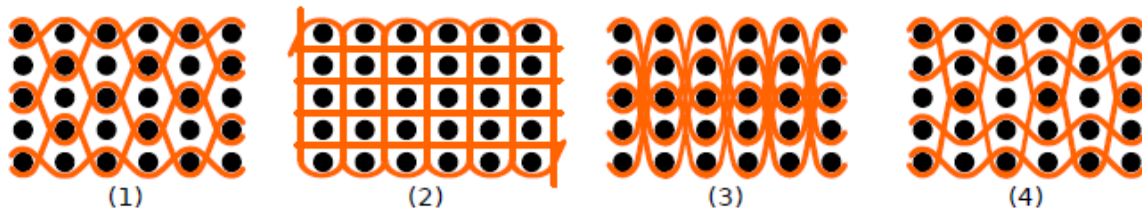


Figure 1. 2 : Different weaving structure patterns of 3D woven fabric

-Fig1: Orthogonal structure with layer to layer binding. The warp yarns link two layers through each other.

-Fig2: Orthogonal structure. The warp yarns cross from the external faces through all the thickness the fabric to bind all the layers together.

-Fig3: Angle interlock structure. The warp yarns blind several layers with the same path curve.

-Fig4: Modified angle interlock structure. The warp yarns blind several layers with different path curves.

1.2.4 Organic matrix

The role of the matrix is binding the fibers together in an orderly array and protecting them from the environment, they also provides the composites with toughness, damage tolerance, and impact and abrasion resistance. The organic matrices are polymeric matrices that are classified as thermosets and thermoplastics.

Thermosets

Thermoset composite matrices are composed of reticulated or three dimensional macromolecular chains, which include polyesters, vinyl esters, epoxies, bismaleimides, cyanate esters, polyimides, and phenolics. Before heating treatment, the resin is in a liquid or pasty soluble at room temperature, which favors its handling and impregnation of the fibers.

After undergoing a heating cycle known as polymerization cycle or curing cycle, the resin becomes irreversibly solid. Thus, thermoset composite parts can be shaped only once since the matrix becomes infusible and insoluble after curing. Thermosetting resins are most commonly used in industry and exhibit good mechanical properties and good resistance.

Thermoplastics

Thermoplastic matrices are composed of linear or one-dimensional chains and ramified or two-dimensional chains. Unlike the thermosetting resins, the material is generally in the solid state at room temperature. Under the action of heat, the polymer can be softened then melted and deformed and can regain its original solid state by cooling without any chemical modification (under certain conditions, e.g. oxidation). The transformation process is reversible, therefore, material and fabricated parts can potentially be recycled.

Faced with thermoset matrix, thermoplastic matrix composites present many benefits:

- Equal or superior mechanical properties.
- A shorter forming cycle
- Greater ease of storage.
- Reversible and recycling.

Industrial development of composite structures with thermoplastic matrix is now booming. The five most important materials are: Polyetheretherketone (PEEK), polyetherketoneketone (PEKK), polyphenylene sulfide (PPS), polypropylene (PP), and polyetherimide (PEI). PEEK, PEKK, PPS, and PEI are high-performance thermoplastics with good mechanical properties, but are also costly. While PP is a lower temperature resin that is used extensively in the automotive industry.

Polyamide 66

Polyamide 6.6 or PA 6.6 is a semi-crystalline thermoplastic polymer material that is used in the project STIICPA. The internal structure of the polyamide is constituted by a partial arrangement of polymer chains embedded in an amorphous phase (without a preferred orientation). The proportion of the crystalline phase in the material is defined as the degree of crystallinity. The thermomechanical properties of the material depend heavily on this value.

PA 6.6 has unique physicochemical and thermomechanical properties such as [GUE 94]:

- Intrinsic resistance to oils and greases.
- Resistance to solvents and bases.
- Withstands high fatigue.
- High melting point (260 ° C).
- Conservation of mechanical properties over a wide temperature range.
- Good resistance to creep.
- High resistance to rupture.
- Fire resistance.

Its disadvantages include mainly the absorption of humidity which affects their properties and their oxidizability at high temperatures, for example: PA 6.6 becomes brittle after 2 hours of exposure in air at 250 ° C.

Given these excellent properties, this type of polymer matrix is a promising candidate in automotive applications especially as its melting temperature is higher than the temperature of cataphoresis. This manuscript is one of many works that are being developed to industrialize the manufacture of such products.

1.2.5 Prepregs (Pre-impregnated composites)

Prepregs or pre-impregnated composites are the results of fiber reinforcement pre-impregnated with a thermoplastic or thermoset resin before forming process.

Unlike thermosetting which can be easily impregnated through the fibers due to its low viscosity at room temperature, the thermoplastic has to be heated beyond the melting temperature and requires a long time compaction phase in order to properly impregnate the fibers. This step affects the forming cycle by increasing consolidation time, necessary for the removal of pores by compaction. That is called the pre-consolidation step, where a stack of different prepregs is consolidated under high pressure in the form of semi-finished plates.

Two examples of methods for the pre-consolidation of thermoplastic prepregs are shown in **Figure 1. 3** [CAM 10] In **Figure 1. 3** (a), a stack of prepregs is heated and then consolidated

using a plate press. The **Figure 1.3 (b)** shows a process known as "Rolling Forming" in which all plies are passed between two rollers during the entire heating and cooling phase. There exists also other prepresses that are not pre-consolidated but powdered or commingled.

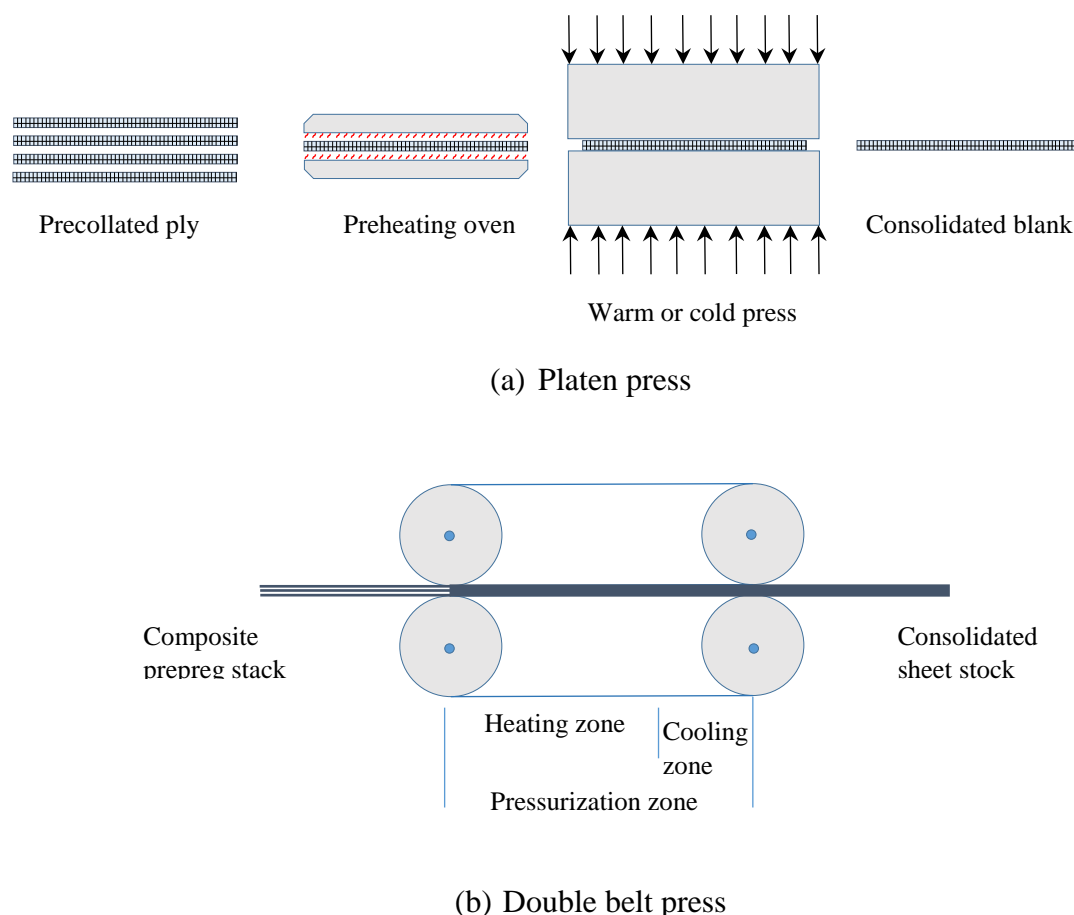


Figure 1.3 : Fabrication methods for composite prepreg sheet stock [CAM 10]

1.3 Manufacturing processes

There are variety of processing methods available to the composites manufacturing. Depending on the quality, property, quantity, and cost of the product, a suitable processing method can be selected. Here, two different processing methods are briefly introduced: Liquid Composite Molding (LCM), and thermo-forming where more detailed explanation will be given concerning in the present work.

1.3.1 Liquid composite molding (LCM)

LCM process concentrates on the forming of woven reinforcement composites with polymer matrix. Among the technologies to produce the composite parts, the most commonly used is Resin Transfer Molding (RTM) (**Figure 1.4**). This process can be broken down into five steps.

1. Cutting the fabric in required dimension
2. Dye reinforcement forming which aims to press the reinforcement into shape of final part by external force

3. Injection of resin into the closed mold under a pressure of 0.1 to 0.4 MPa, at a high temperature
4. Polymerization of resin
5. Cooling and demolding, and the final composite part can be obtained

Thanks to this process, the reinforcement with high air void contents can be compressed and resulted with high volume fraction (vf), moreover, it is capable of fabricate parts with high complex shapes. Hence RTM is more preferable comparing to those more traditional fabrication technology such as Compacting Prepreg or Autoclave.

However, in order to obtain a better resin impregnation on the reinforcement and to facilitate the removal of entrapped air to reduce the possible voids in the final composite part, several technics have been developed over those years. Two of the improved versions of RTM process are Vacuum-assisted resin transfer molding (VARTM) (**Figure 1. 4.(d)**) and Seemann composite resin infusion molding (SCRIMP).

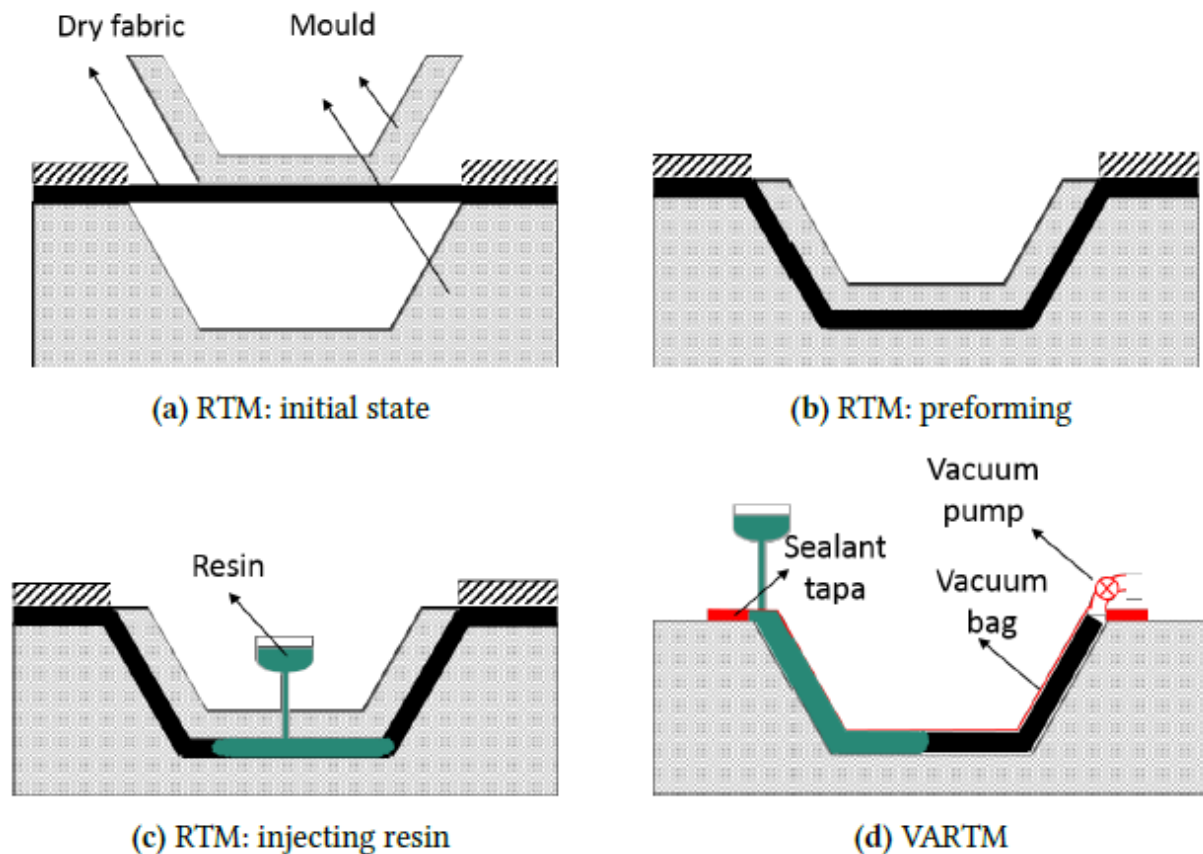


Figure 1. 4 : RTM and VARTM

1.3.2 Thermoforming process

As an alternative to the LCM processes, prepreg composite forming or thermoforming process has become one of the main manufacturing processes for high performance composites material. Comparing to the LCM processes, it is a fast manufacturing process whose duration can be in the range of 1 min. It attracts more and more industry interests for its rapid cycle times

and the possible use of pre-existing equipment. This technique can be easily automated and are based on the same technology as metal sheet shaping [CAM 10] This process is the focus of our work and more details will be presented in 2.2.1.

1.4 Simulation models for the forming of reinforcements

Considering that the optimal research of reinforcement preforming could be costly and sometimes time consuming, the simulation of the reinforcement forming permit numerically optimize the mold and the reinforcements, it also helps determine the ideal conditions (temperature, shaping speed, initial size and geometry of the reinforcement, etc.), to optimize both the process and the quality of the structure. A major research effort is devoted to the behavior of dry reinforcement and the simulation of deformation. The objective is to predict the geometrical and mechanical characteristics likely to appear during the forming:

- the position of the yarns and fibers after deformation
- the mechanical characteristics of deformed reinforcement
- the possible appearance of wrinkles, twist of yarns, failure of fibers

These characteristics and defects are not all defined at the same scale: the failure of fibers is a microscopic phenomenon which is difficult to detect when observed at macroscopic scale, and the wrinkle of reinforcement (macroscopic phenomenon) cannot be detected at the microscopic scale. Therefore, different types of simulations were developed at a precise scale (**Figure 1. 5**):

- At the microscopic scale: study of the fibers and their interactions. Only a maximum of few fibers per yarn can be simulated.
- At the mesoscopic scale: study of the yarns, their behaviors and local characteristics in reinforcement. The simulated volumes are generally representative unit cell (RUC) of reinforcement
- At the macroscopic scale: study of the deformation of the reinforcement in its entirety, to characterize the appearance of wrinkles, slips of yarns and more generally the formability of a complex geometry part.

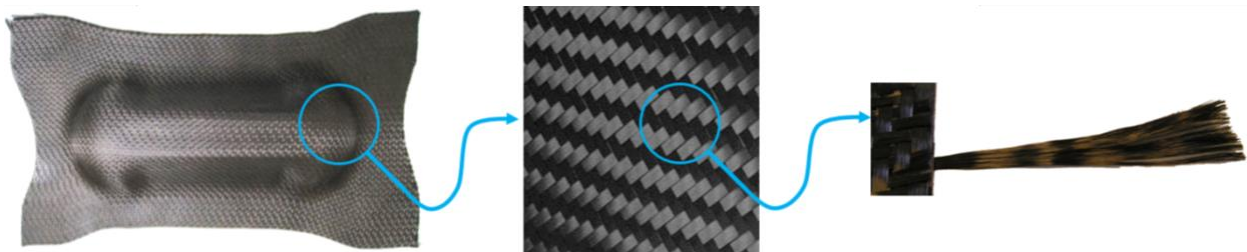


Figure 1. 5: Analysis of composite at different scale

1.4.1 Simulation models at microscopic scale

The microscopic scale is the smallest scale for the simulation of textile composites. At this scale, fibers are the most basic constituents. The behavior of fiber is linear orthotropic, and their characteristic values are given. However, if several fibers crowd together, it causes the difficulty to manager the interaction and contact between them.

Some studies, including that of Durville [DUR 10], allow to obtain promising results for the simulation of reinforcement at microscopic scale. In this work (**Figure 1. 6**), the representation of all fibers constituting woven structures is considered as 3D beam models, and contact-friction interaction between fibers is taken into account. Knowing the initial geometry of the fabric, the path of the fibers and the yarns, the section of the yarns, the detection of the numerous contacts occurring within collections of fibers is an essential point of the approach. Based on the determination of proximity zones between fibers, and on the construction of intermediate geometries to approximate the actual contact zones, it generates automatically contact elements made of pairs of material particles which are candidates to contact.

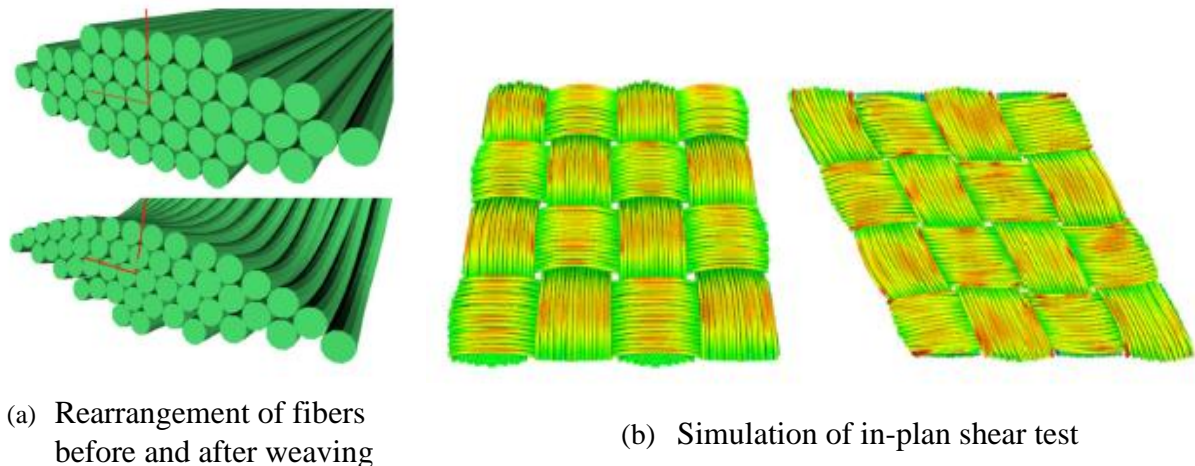


Figure 1. 6: Simulation of the reinforcement at microscopic scale [DUR 10]

1.4.2 Simulation models at the mesoscopic scale

For the simulation models at the mesoscopic scale, a representative unit cell (RUC) made of yarns that are considered as 3D continuum is concerned. The objective of these models are to determine several behaviors and proprieties of the reinforcement which are difficult obtained by experiments.

For the mesoscopic scale simulation models, three principal works are needed to be done:

- (1) Construction and meshing of geometrical structure of RUC
- (2) Calculation of the local properties of yarns, with the given local fiber volume fraction and fiber orientation.
- (3) Definition of periodic boundary conditions on RUC [LOM 08].

In the study of construction of the geometrical structure for yarns, several models have been proposed. The **Figure 1. 7** shows a well know model proposed by Kawabatta [KAW 73] [KAW

80] Yarns were seen as a composition of hinged elastic bars, the interactions between the yarns at the crossover point are modeled by different types of springs. This model is simple and efficient especially for the determination of the mechanical behavior of yarns in tensile. However, facing the more complex application like considering the shearing deformation, it occurs the problem with the simplification of the geometry, in particularly, for the lateral contacts (interpenetration between yarns).

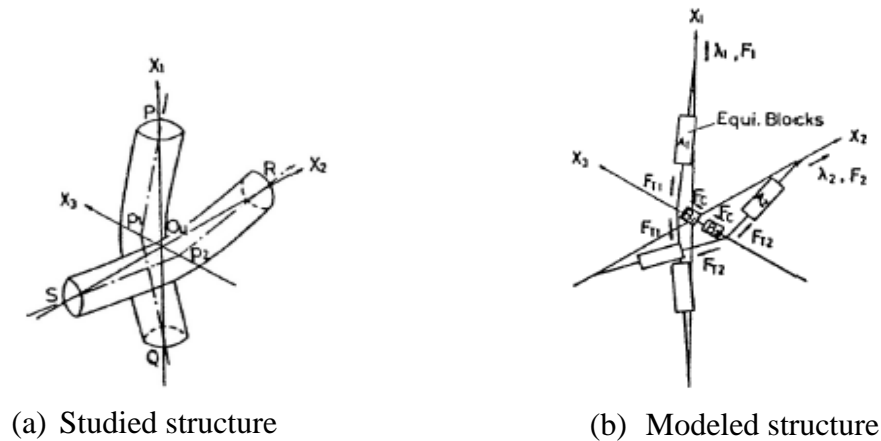


Figure 1. 7 : Model of Kawabatta for simulation at mesoscopic scale [KAW 73]

Currently, there exist various models used to obtain the final geometry of textile fabric, such as WiseTex [LOM 11] and TexGen [SHE 07]. In the model of WiseTex **Figure 1. 8** (a), the cross-section of yarn is considered as a simplified shape (circular lenticular and elliptical) and keeps constant along the trajectory. While in the model of TexGen WiseTex **Figure 1. 8** (b), the cross-section of yarn is no longer symmetric and it varies along the mean line. In these two approaches, some techniques are applied to avoid the interpenetration, but they are a little far from the reality with certain assumptions. Hence, others models based on experimental observation are proposed. Hivet et al [HIV 05] developed a 3D geometrical model for yarns whose cross section shape come from the experiment observation. This model is able to accurately describe yarn's cross-section variation along the trajectory without interpenetration. Based on the x-ray tomography technology, Naouar et al [NAO 14] proposed a more precise method to construct the yarn geometry for 2D and 3D fabrics (**Figure 1. 9**). The fabric is scanned by x-ray devices, and image processing algorithms are used to gain the 3D structure from tomography data and some simulations were done based on this model.

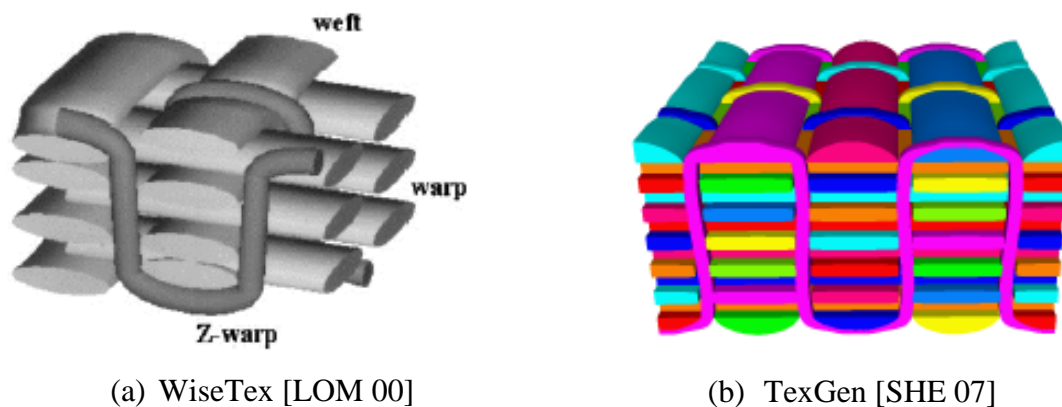


Figure 1. 8: Generation of the geometry of reinforcement composites

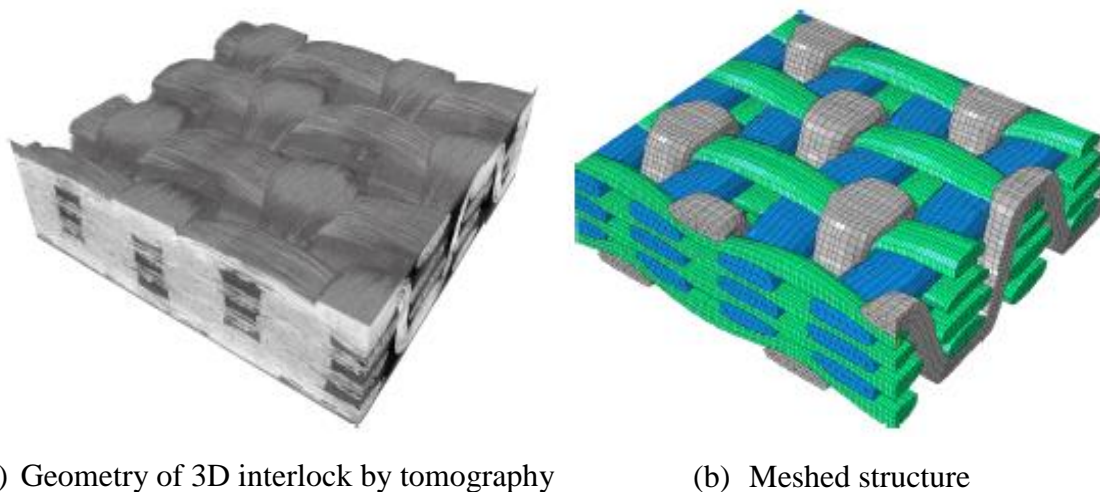


Figure 1. 9: Generation of the 3D interlock structure by micro-tomography [NAO 14]

After construction of the geometrical structure, a model concerning the constitutive relation of yarn has to be build. The behavior of yarn is very special because of its fibrous nature. Two extensively used models on mesoscopic simulations are hypo elasticity [GAS 00] and hyper elasticity [CHA 11]. They relate stress and strain and allow taking into account material non-linearity. The related parameters can be measured from tension test, shear test, compaction test etc.

1.4.3 Simulations at macroscopic scale

At the macroscopic scale, the objective is the simulation of reinforcement preforming. It relates to: the characterization of the global deformation of fabric, the study of the formability of the woven composite part, which aims at predict the appearance of macroscopic defaults such as wrinkles and slips of yarns. Many models permit to simulate the deformation of woven reinforcement, they are usually grouped into two categories: the geometric approaches based on the kinematic description and the mechanical approaches based on the finite element technology. All these macroscopic models require a local characterization of reinforcement's behavior, which can be obtained by the mesoscopic or even microscopic models.

Geometric approaches

The geometric approaches based on fishnet algorithms are favored for their simplicity and high efficiency, since they are capable of provide the first draping appearance (which is sufficient in some industrial occasions) in a short computer time [MAR 56] [VAN 91b] [BOR 02]. Several assumptions are supposed in these models: the yarns are inextensible, no slip exists between the warp and weft yarns, no slip exists between the woven fabric and the preforming tools, and the crossover points in the net are free of rotation. As is shown in **Figure 1. 10** (a), the reinforcement is considered as assemble of bars articulated at the crossover points. The algorithm determine the position of a moving point C from the intersection of two geodetic traced on the surface draped by the issues of two related points A and B. The position of the starting point is thus paramount and affects the final result [WAN 99].

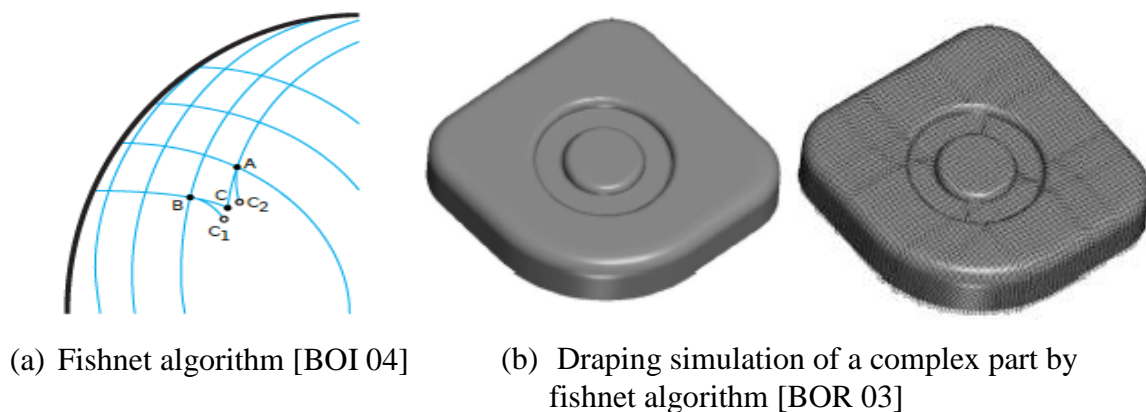


Figure 1. 10: Fishnet algorithm

In these approaches, the mechanical characterizations and the weaving pattern are not considered. The shearing locking and variation of thickness in compression are absent from this basic modelling. What's more, the lack of contact analysis prevents the use of external tools such as blank holders which are needed in some forming cases. Therefore, the fishnet algorithm is useful as preliminary approach to determine the degree of complexity of forming a composite part. An example of application in a complex part is given in **Figure 1. 10** (b).

Mechanical approaches

Among the mechanical modeling, three types of approaches can be distinguished: discrete, continuous and semi-discrete.

Discrete approaches

By extension of the theory of fishnet algorithm, the principle of the discrete approaches is that the textile reinforcements are considered as a discontinuous assemblage of deformable elements [CHE 01] [SHA 04] [SZE 05] [BOU 07]. The reinforcement is modeled by interconnected nodes with bars and springs aiming to model the response in elongation, shear, torsion and bending. The work of Sze and Liu [SZE 05] are particularly interesting on the variety modeling of solicitations for dry 2D reinforcements, as shown in **Figure 1. 11**.

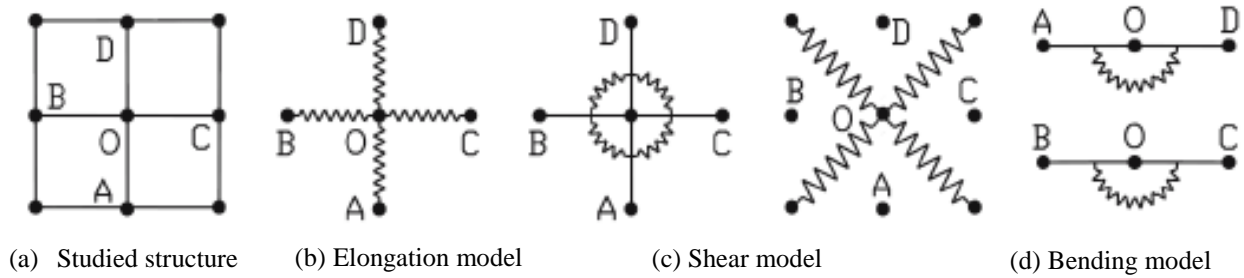


Figure 1. 11: Modelling of a partial O connected to its four adjacent partials [SZE 05]

Moreover, the discrete approach can be applied for the thermoplastic prepregs in adding the contribution of the matrix. Such as the model of Skordos et al. [SKO 07] which based on the work of Sharma [SHA 04], in this model, the nonlinear elasto-visco-plastic elements are introduced to get a proper behavior of thermoplastic pre-impregnated woven composites in considering the deformation rate dependence.

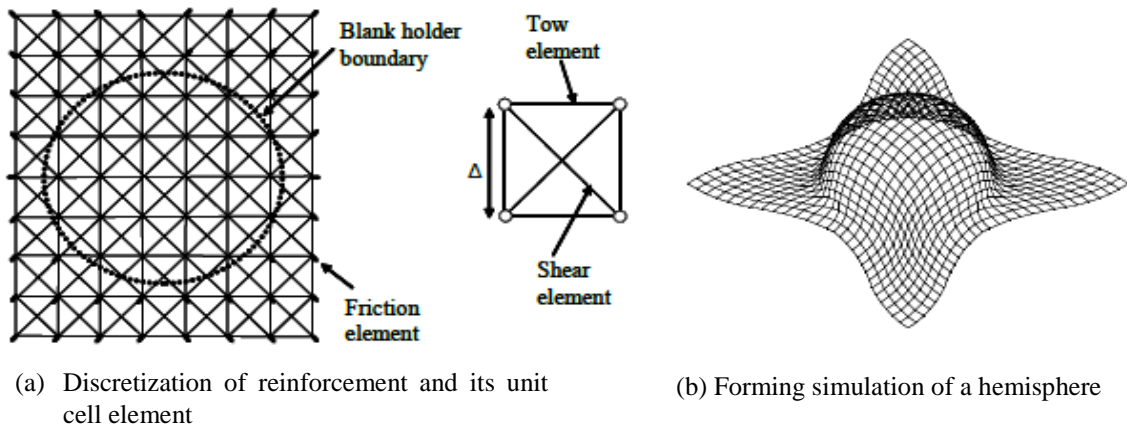


Figure 1. 12: Forming simulation by discrete approach [SKO 07]

Continuous approaches

As seen in the preceding section, the reinforcement is not continuous at lower scales, after the homogenization method, the fibrous reinforcement or prepreg is assumed continuum with the assumption of no significant sliding between fibers and yarns in the deformation [BOI 95], that is the continuous approach.

The advantage of this approach is that it can be implemented in commercial FE codes, specific mechanical behavior of the fibrous reinforcement, especially for which depends on the fiber directions, could be considered in the constitutive model of the continuum. Most of the proposed continuous approaches for FE forming simulations are based on hypoelastic and hyperelastic approaches. They are principally realized in plates and shell elements for the thin fabric, and solid elements for thick elements. This manuscript focus on this approach to develop elements and models of behavior.

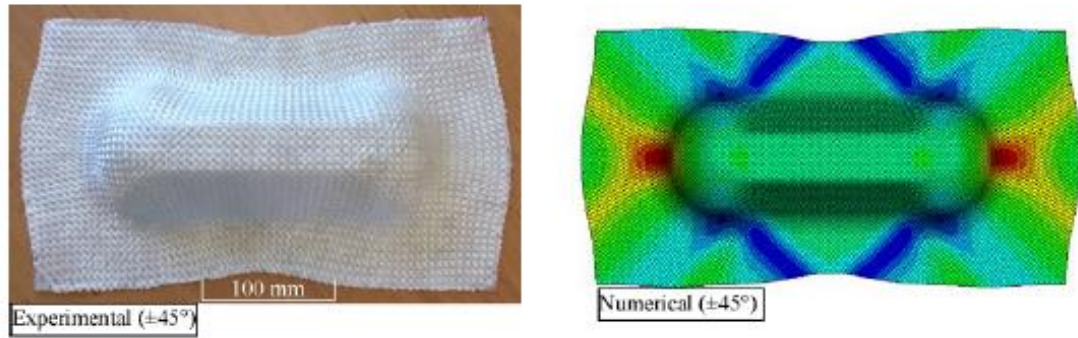


Figure 1. 13: Experimental and numerical results of double dome benchmark tests with $\pm 45^\circ$ by hypoelastic approach [KHA 10]

In hypoelastic approach, a deformation rate is related to a stress rate, and an objective derivative must be used. This objective derivative can be defined by a rotation (the most material possible) for the hypoelastic constitutive law and to update the orthotropic frame. The rotations used in Green-Naghdi and Jaumann derivatives are the average rotations of the material. Consequently, these approaches can't be used for fibrous materials under large strains because the update of material direction must follow the fiber direction accurately. To overcome this problem, the non-orthogonal constitutive models were proposed by Yu at al [YU 02] and Peng et al [PEN 05]. In the non-orthogonal constitutive models, the stress and strain were related using the constitutive relation in a non-orthogonal frame defined by the fiber directions. The fiber direction was updated from the deformation gradient tensor which makes sure to follow the correct material directions. The non-orthogonal constitutive models can be used to simulate large strains for fibrous materials.

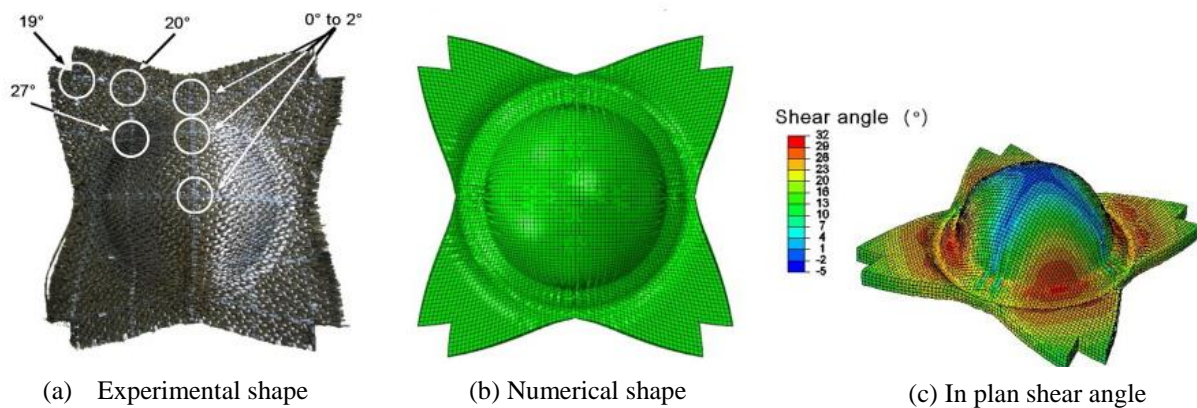


Figure 1. 14: Forming simulation of an interlock reinforcement by hyperelastic approach [CHA 12]

Another type of continuous approach is called hyperelastic approach. The starting point is an elastic potential (internal energy) given as a function of right Cauchy-Green deformation tensor. For 2D fabrics, the hyper-elastic potential is constructed by three terms (supposedly decoupled): two tension energies in two yarn directions and one in plane shear energy [HOL 00] [AIM 08] [PEN 13]. The tension and in-plane shear tests on woven reinforcements are used to identify the various terms of proposed potential function. For 3D interlock fabrics, the hyper-

elastic potential energy is assumed to be composed of six parts: two tension energies in two yarn directions, one transverse compression energy in thickness direction, and two transverse shearing energies in two yarn's directions [CHA 12].

Semi-discrete approaches

The semi-discrete approaches use the stress resultants especially for the textile reinforcements, they can be considered as a compromise of the two discussed approaches. One part of its behavior is modeled as a continuous solid while the other part is modeled by the discrete elements. De Luycker [DEL 09] proposed a new element shown in **Figure 1. 15** to simulate a 3D interlock. The semi-discrete element is combined by a solid element for the phenomenon of shear and transversal compaction, and several bar elements for the tensile of yarns. Another meso-mechanical modelling method used for the biaxial NCF is proposed by Creech and Pickett [CRE 06]. The yarns of the layers are discretized by 3D solid elements, and the stitching part is approximated by bar elements (**Figure 1. 16**). Additional stitch-to-yarn connection elements are used with an appropriate contact algorithm in order to treat the contact and frictional sliding between yarns and stitches. These two approaches are based on dissociation of the global behavior. While Hamila and Boisse [HAM 09] proposed a semi-discrete triangular shell finite element which was composed of unit cells (**Figure 1. 17**). These unit cells are subjected to tension, in plane shearing and bending. The displacement of any point in the representative unit cell comes from element interpolation. The advantage of such element is that the local directions of yarns could be represented more faithfully and simply during preforming in taking account of the complex anisotropy of the material.

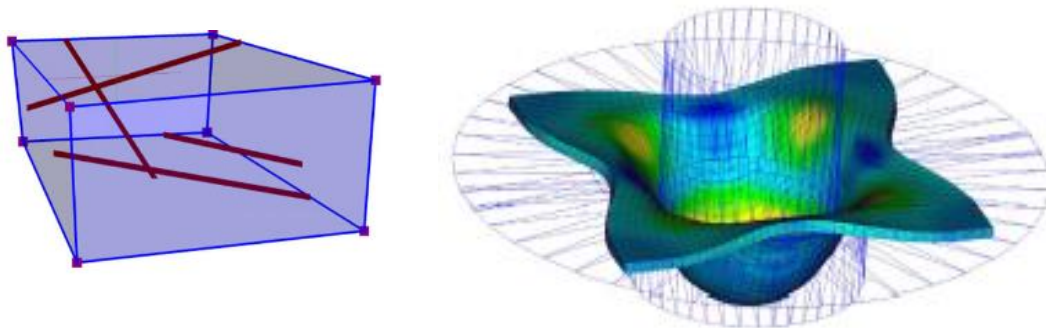


Figure 1. 15: Semi-discrete approach for interlock forming simulation [DEL 09]

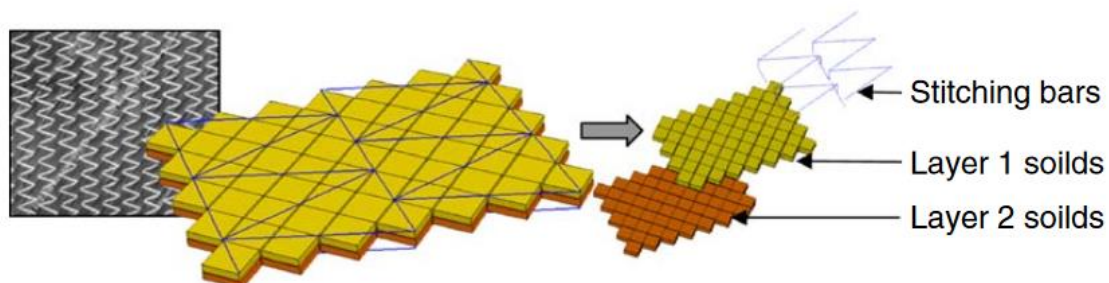


Figure 1. 16: A representative cell of the meso-mechanical model for NCF with semi-discrete approach [CRE 06]

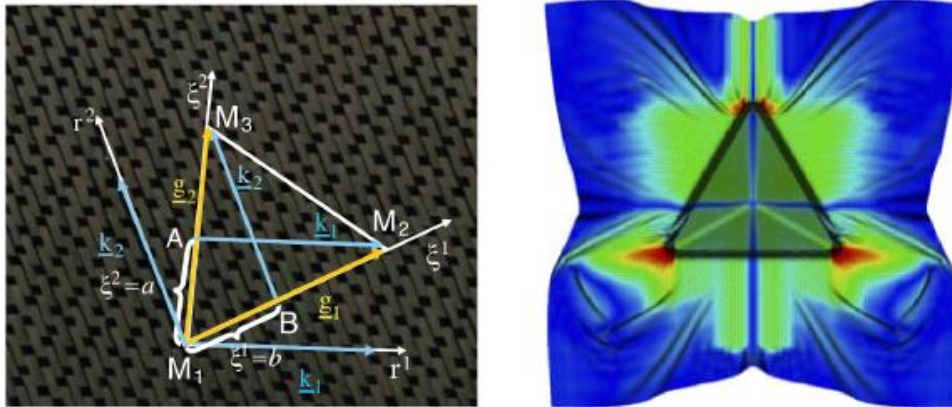


Figure 1.17: Semi-discrete triangular element and the forming simulation [HAM 09]

Chapter 2

Mechanical characterizations of thermoplastic prepregs at high temperature

2.1 Different deformation modes of woven reinforcements

As mentioned in Chapter 1, three different scales: microscopic, mesoscopic, and macroscopic, have been proposed to investigate on the deformation behaviors of composite material during forming process. At macroscopic scales, the mechanical behaviors of the actual dimensions of the composite structure are described, that is what this manuscript focus on. This mechanical behaviors are modeled by different deformation modes: the tensile deformation, in-plane shear deformation, and bending deformation for 2D woven fabrics, while for 3D interlock composites, out of plane deformations like longitudinal and transverse shearing deformation and transverse compaction deformation have been taken into account. In this chapter, different deformation modes of woven reinforcements at macroscopic scales are presented.

2.1.1 Biaxial tensile deformation

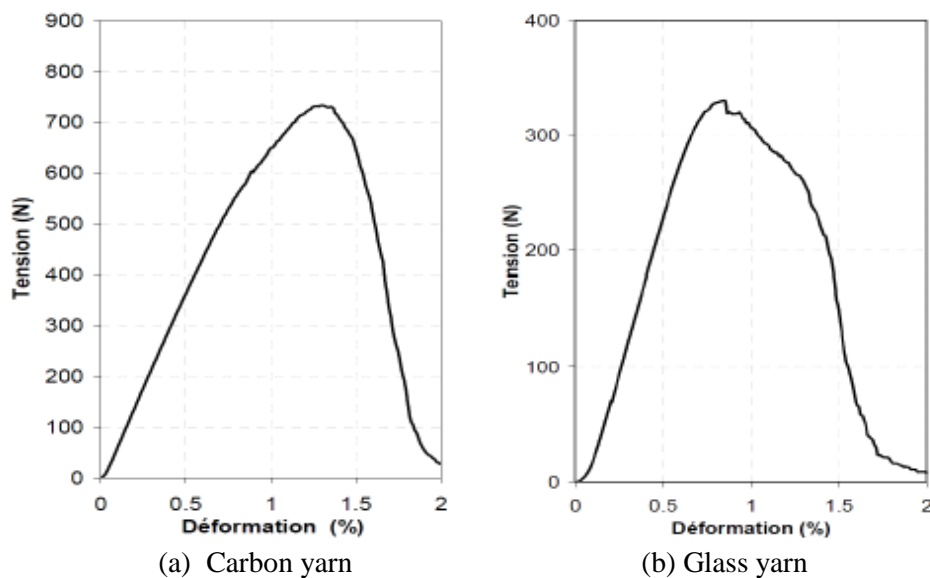


Figure 2. 1: Yarn's tensile behavior [DUM 03]

The elongation of the reinforcement following the principal direction of the yarns is always ignored in most models because of the high stiffness of fibers. As shown in **Figure 2. 1:** Yarn's tensile behavior **Figure 2. 1**, typical tensile tests result for a single yarn that made of glass fibers and carbon fibers present the linear tensile behavior with a nonlinear part at the beginning of loading, and the level of 1-3% deformation indicates the essential inextensibility of the fibers.

However, for textile materials, when a woven fabric is subjected to a tension, because of the yarn undulations, the undulated yarns tend to become straight to remove the undulation. In consequence, a non-linear tensile behavior appears at the beginning of loading. Because of the architecture of woven fabric, the yarns are woven and undulated in both warp and weft directions. In the extreme case (**Figure 2. 2** $T_{22}=0$), subjected load applied in one direction makes the parallel yarns completely straight, while yarns in the perpendicular direction are heavily undulated. In intermediate case corresponds to biaxial phenomenon. This is very analogous to the conception Poisson ratio in the continuum mechanics, when one direction is deformed, it would have influence on other directions. The coefficient of biaxial tension k is the ratio of the deformations along two yarn direction of woven reinforcement. It allows to quantify the degree of interaction between the warp and weft yarns. This coefficient can be imposed in a biaxial tensile device [KAW 73] [BUE 01] . The device of biaxial tensile test for plain fabric and the influence of the coefficient k are shown in the **Figure 2. 3**.

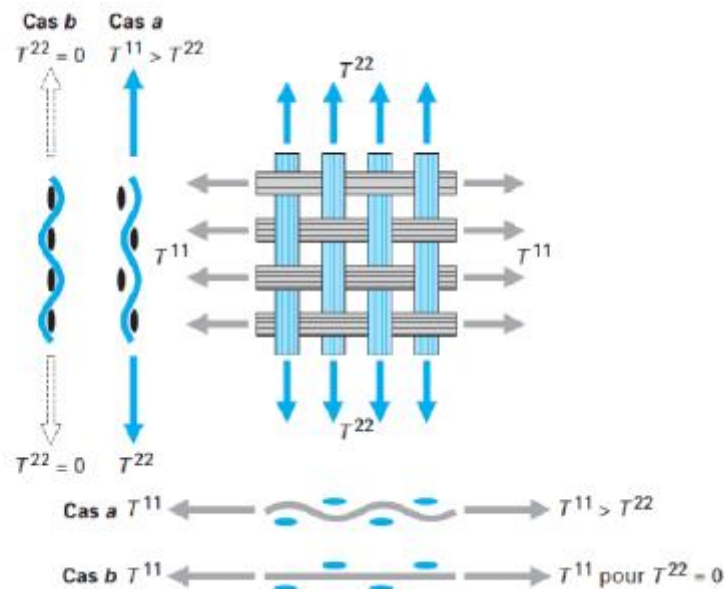


Figure 2. 2: The schematic of biaxial phenomenon [BOI 04]

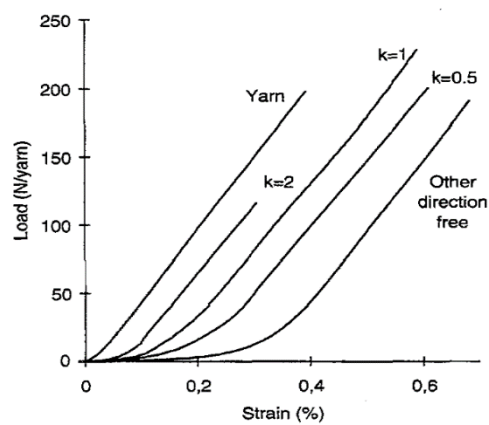
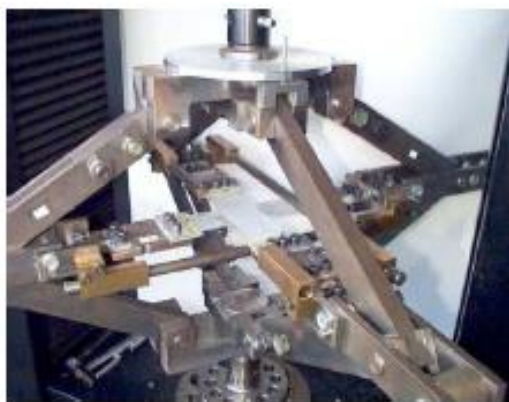


Figure 2. 3: Biaxial tension test device and measuring results [BUE 01]

Most of the studies for biaxial tensile test are for the dry fabrics. While little studies taking account the influence of resin are carried out for the thermoplastic prepreps, the principle reasons are the control of heating for a homogeneous temperature on the specimen during the test, and the setting up to fix and insure the warp and weft yarns in perfect direction. A recent study on the thermomechanical behavior of pre-impregnated composites has indicated that the influence of resin can be neglected in the uniaxial case [WAN 15]. In this study, series of tensile tests with different temperatures and velocities of solicitation are applied for Carbon/PPS thermoplastic prepreps. The experimental device is shown in **Figure 2. 4** (a), and the influences of temperature and velocity could be concluded from the **Figure 2. 4** (b) and **Figure 2. 4** (c). In addition, the relaxation tests in order to characterize the viscous effect are performed at the matrix melting condition, the results indicate that the viscous effect can be neglected in tension.

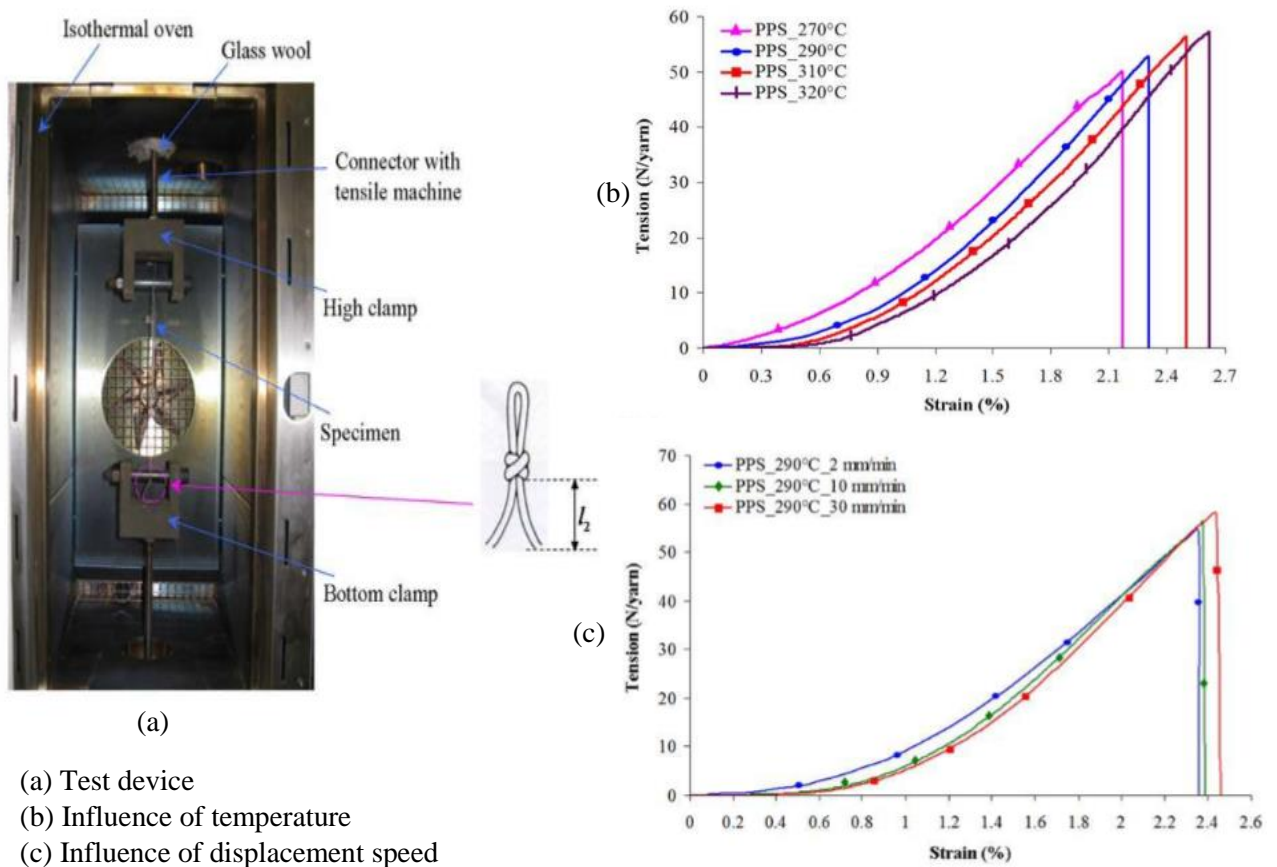


Figure 2. 4: Tensile test of a pre-impregnated thermoplastic yarn at high temperature [WAN 15]

2.1.2 In-plan shear deformation

In plan-shear deformation is the rotation between the two yarns around the crossover point. This point of contact remains constant during the deformation according to the no sliding assumption.

Comparing to the large stiffness in tensile, the in-plan shear stiffness is so low that this type of deformation is the most dominant deformation mode for reinforcement and prepreg in the forming. The study and the characterization of this mode of deformation is therefore crucial to develop a model of behavior for dry or pre-impregnated reinforcements.

The shear behavior is non-linear which can be obtained by experience as shown in **Figure 2. 5**. It can be divided into three parts. At the beginning with low shear angles, the yarns freely rotate against each other in a rigid body motion, the shear rigidity coming mainly from the friction between the yarns is very weak. Then gradually, in the second part, the locking angle corresponds to the angle from which the geometry of the weaving does not allow the rotation any more, the yarns become in contact with their neighbors and are laterally compressed, so the shear rigidity increases. Finally, the effect of the transverse compression becomes more and more remarkable up to the compaction limit of yarns, the shear rigidity increases very rapidly and it can cause the appearance of wrinkles caused by the shear locking. These shear deformation mechanisms can be observed by optical measurements at macro- and micro-level (**Figure 2. 6**).

The in-plane shear characterization for woven reinforcements and prepregs reinforced with woven reinforcements can be carried out by two standard tests: picture frame and bias extension tests.

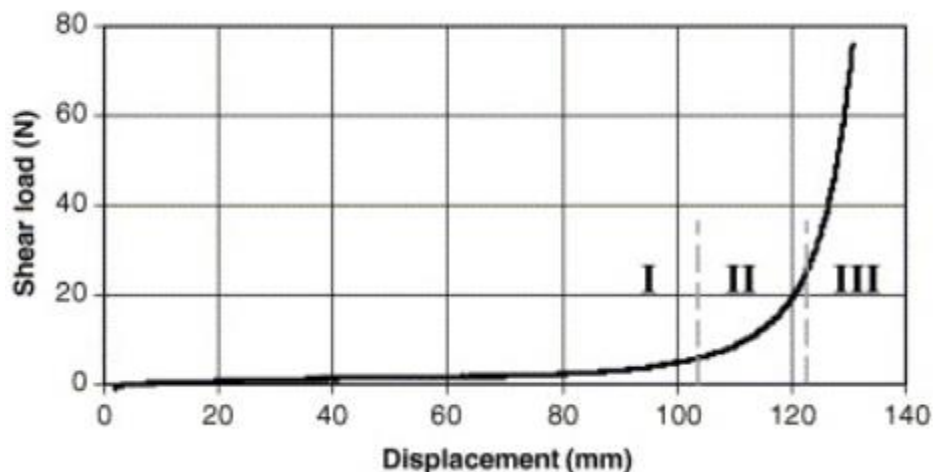


Figure 2. 5: Shear load versus the displacement [DUM 03]

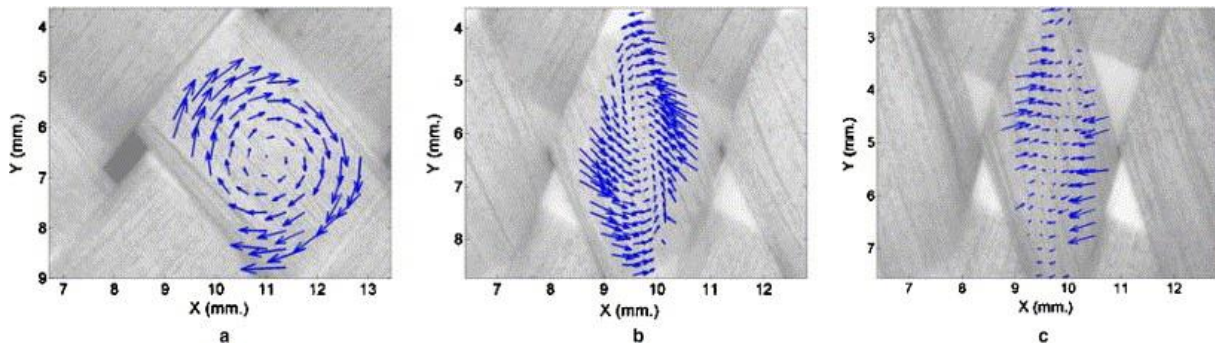


Figure 2. 6: Displacement field in a yarn during the three phases of shear [ZOU 06]

Picture frame test

Picture frame test is a classical test and widely used to characterize the in-plan shear behavior of woven textile reinforcements [CAO 08] and thermoplastic pre-impregnated composites [MCG 97] [MCG 98] [HAR 02] [LUS 02] [LEB 03] with an extra woven (**Figure 2. 7**). As it is shown in the figure, the sample is cut into square and fixed in a pin joint frame which is stretched diagonally to realize a pure shear deformation. Two assumptions concerning the deformation of the fabric sample are made: the shear deformation in the sample is homogenous, and the shear angle of the fabric is the same with the frame. In this test, careful fabric handling and alignment are required in the clamping. Misalignment of the yarns introduces parasitic tensile, this will significantly perturb the measurement due to the huge tensile rigidity comparing to shear rigidity. And this is the disadvantage of this test. Geometrically, the shear angle (radians γ depends directly on the imposed displacement d and the length of the frame L_f :

$$\gamma = \frac{\pi}{2} - 2\cos^{-1}\left(\frac{\sqrt{2}}{2} + \frac{d}{2L_f}\right) \quad (2.1)$$

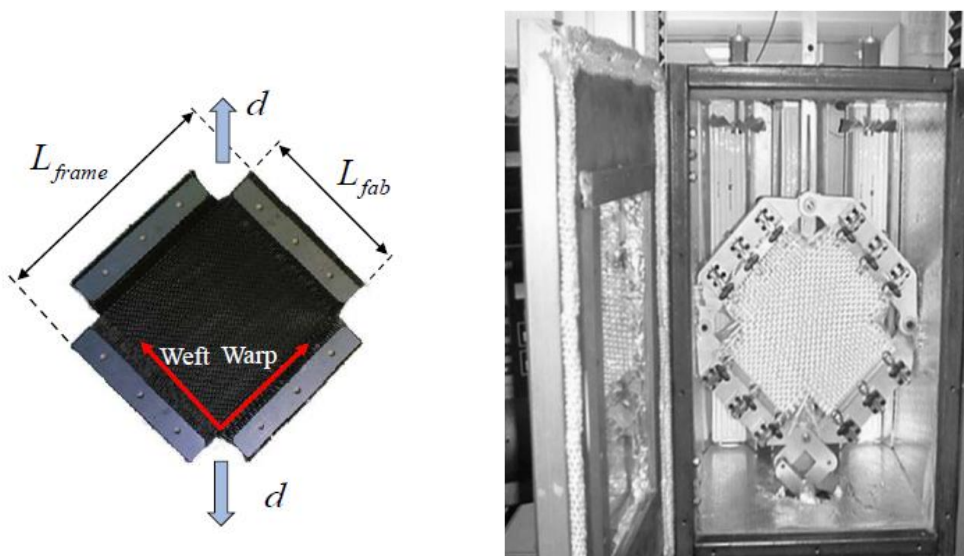


Figure 2. 7: Picture frame test device in isothermal oven [LUS 02]

Bias extension test

Due to simplicity of test procedure and minimal equipment requirement, bias extension test [CAO 08] is an alternative to the picture frame test. It involves clamping a rectangular sample of woven material, the directions of warp and weft yarns are orientated initially at $\pm 45^\circ$ to the direction of applied tensile force. Specimens are cut into the shape shown in **Figure 2. 8**: Schematic of an idealized sample for Bias extension test before and after deformation, the deformed fabric has four kinds of distinct zones: the zones C are the triangles next to the clamp area, and there is no shearing deformation; zone A is located at the center of the sample, and it undergoes a pure shear deformation due to the free ends of yarns; the transition regions between A and C are marked as B, where one yarn direction is clamped at its end and the other direction is free. The shear strain of B is half of the one of A. In an ideal bias extension test, the in-plane shear (A and B) and bending deformation (on common borders of A and B, B and C) dominate the deformation of the fabric. In order to obtain all three regions, the initial length of the sample (L) must be more than twice the width of the sample (W). The shear angle (radian) in the pure shear region A can be calculated from the geometric values:

$$\gamma = \frac{\pi}{2} - 2\cos^{-1}\left(\frac{\sqrt{2}}{2}\left(1 + \frac{U}{L-W}\right)\right) \quad (2.2)$$

where U is the imposed displacement of tensile machine. And this expression is available with the no sliding assumption between the yarns.

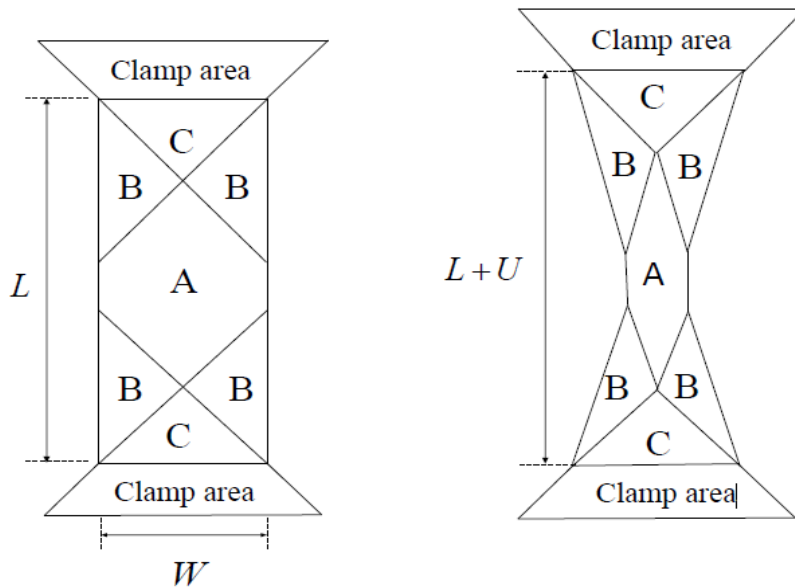


Figure 2. 8: Schematic of an idealized sample for Bias extension test before and after deformation [WAN 08]

Supposing that the external power imposed by tensile machine are completely transmitted to the internal power of shear deformation in all the regions:

$$P_{int} = P_{ext} \Rightarrow F\dot{d} = C_s^\gamma S^\gamma \dot{\gamma} + C_s^{\frac{\gamma}{2}} S^{\frac{\gamma}{2}} \frac{\dot{\gamma}}{2} \quad (2.3)$$

where S^γ and S_s^γ , C_s^γ and $C_s^{\frac{\gamma}{2}}$ are the areas and normalized torques of zone A and zones B, respectively. Substitute equation ((2.1) and equation ((2.2), we obtain:

$$C_s^\gamma = \frac{1}{2L-3W} \left(\left(\frac{L}{W} - 1 \right) \cdot F \cdot \left(\cos \frac{\gamma}{2} - \sin \frac{\gamma}{2} \right) - W \cdot C_s^{\frac{\gamma}{2}} \right) \quad (2.4)$$

For thermoplastic pre-impregnated composites, many researchers have used this method with an isothermal oven to obtain an elevated temperature. Wang [WAN 14] and Guzman [GUZ 15] have respectively done the bias extension test for thermoplastics at various temperatures. The setup is shown in **Figure 2. 9**, a specific spring system is employed to assist the clamps, and in consequence, the slippage of the sample can be prevented during the melting of the resin.

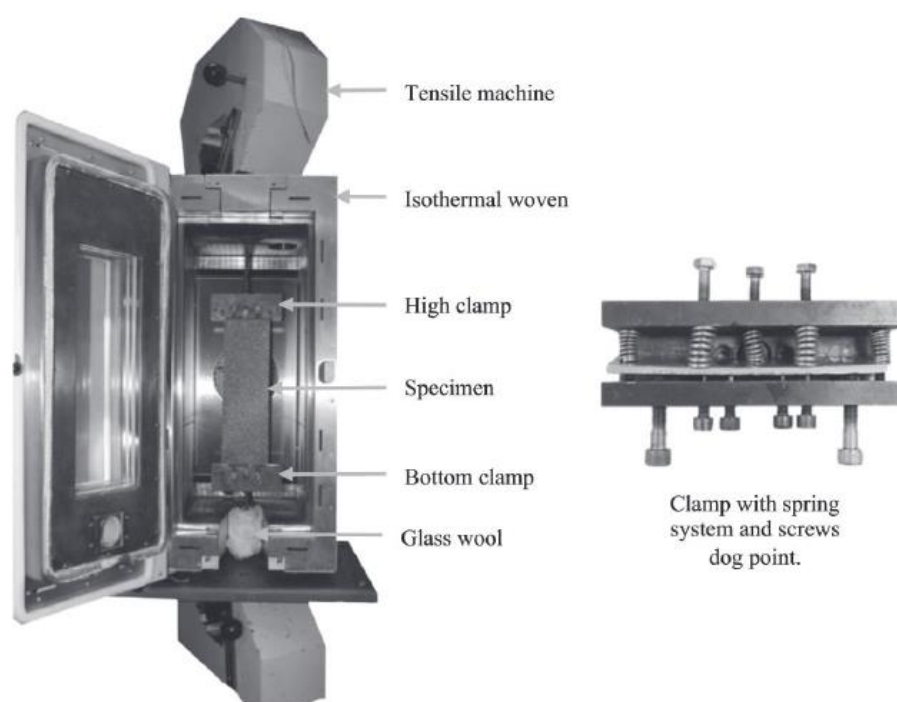


Figure 2. 9: Bias extension test set-up for thermoplastics [GUZ 15]

2.1.3 Bending deformation

The bending stiffness for dry reinforcements and prepreps is generally very small and had been neglected for a long time. However, recent studies have shown that bending stiffness plays a very important role in the forming simulation, especially for the development of wrinkles [HAM 07] [BOI 11] (**Figure 2. 10: Forming of an unbalanced textile reinforcement**). Unlike the conventional continuum materials, the bending stiffness is not directly related to the in-plan modulus. It needs to be measured through the experiment by finding the relationship between the bending moment and the curvature. There exists various experimental devices to characterize this mode of deformation.

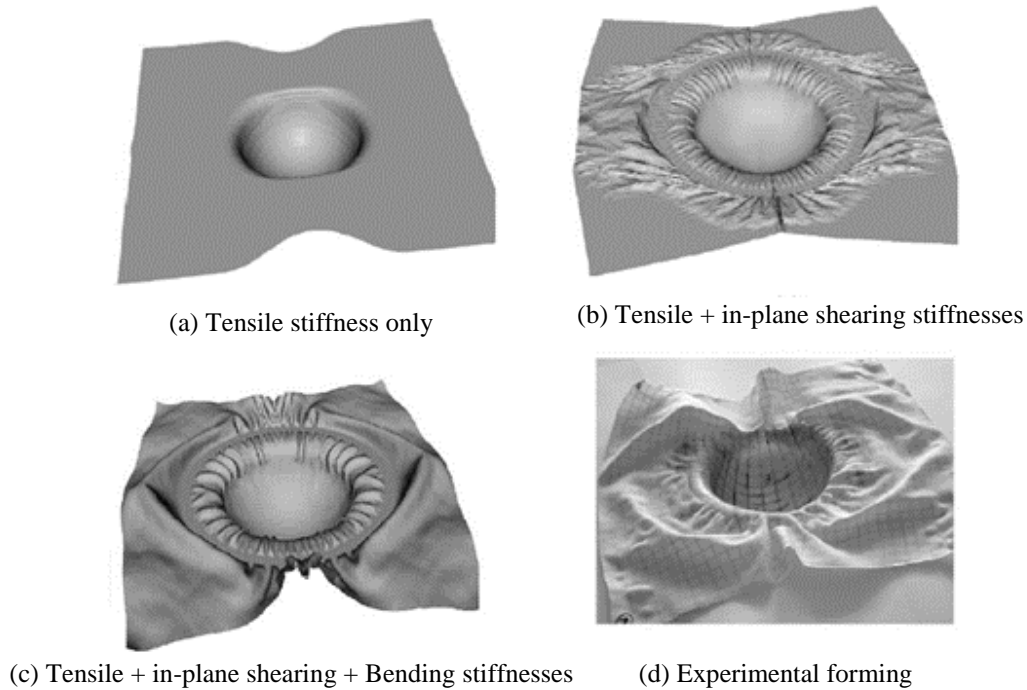


Figure 2. 10: Forming of an unbalanced textile reinforcement [BOI 11]

The first test to measure the bending stiffness at a macroscopic scale is the standard cantilever test (**Figure 2. 11**) proposed by Peirce [PEI 30]. He used an elastic linear behavior for the bending. In this test, the strip of fabric is set on the horizontal board and moved slowly until the tip of the fabric strip touches the tilted board with a 41.5° deflection angle. The bending stiffness can be calculated by the measurement of bending length l .

$$M = B \cdot b \cdot \chi$$

$$B = \frac{l^3 \cos(\theta/2)}{8 \tan \theta} w, \quad \theta = 41.5^\circ \quad (2.5)$$

Where b is the width of strip.

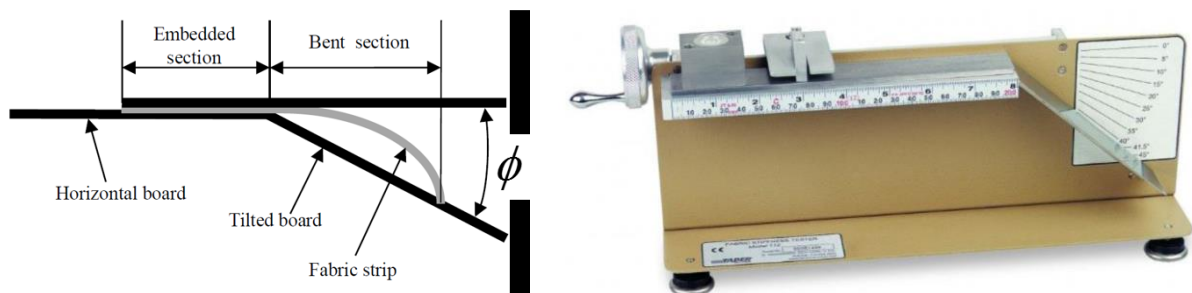


Figure 2. 11: The standard cantilever bending experiment [PEI 30]

De Bilbao et al. used the cantilever principle, to analyze fibrous reinforcement bending [DEB 10]. The bending test device called flexometer is shown in **Figure 2. 12**, An optical module is employed to take the picture of the bent shape of sample. And the moment-curvature curve is obtained by computation of the midline of the bent shape.

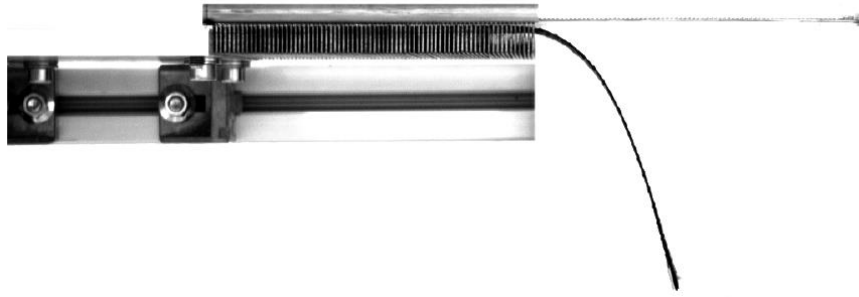


Figure 2.12 : The configuration of flexometer proposed by De Bilbao [DEB 10]

Many experimental methods have been proposed to characterize bending behavior for dry woven textile reinforcements. While in thermoplastic composites cases, there are few studies and go on developing [MAR 95] [LIA 14] [MAR 15]. The difficulty is that for the purpose of determining the influence of temperature in the mechanical behavior, the thermal conditions have to be ensured during the test.

Liang [LIA 14] developed another setup based on the method of De Bilbao. The setup is placed in a thermal oven (**Figure 2.13**), and a metallic support for clamping the specimen is equipped with an independent heating system. Several thermocouples are distributed near the strip in order to obtain a homogeneous temperature field. Similar to the method of De Bilbao, the curve of bending moment vs. curvature is analyzed from the bent shape by camera. In his study, series of different temperature tests are carried out, and a temperature dependent bending behavior model is constructed. This model will be concerned in this manuscript.

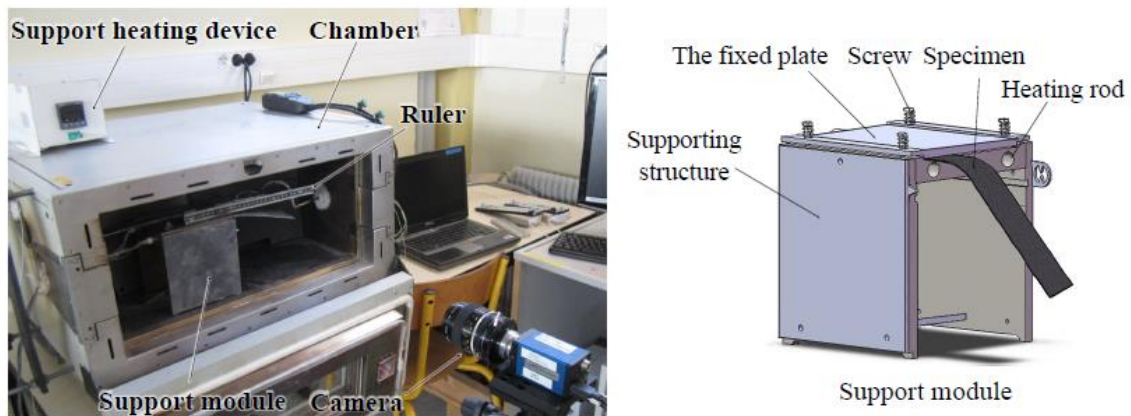


Figure 2.13: Bending test set-up configuration [LIA 14]

2.1.4 Transverse shearing deformation

Transverse shearing reflects the angle variation of cross-section in the longitudinal and transverse direction of composites structure, such as laminated composites or interlock reinforcement. Some authors have proposed experimental methods to characterize their model [HAR 05] [CHA 12] [HAA 14a]. One set-up presented in **Figure 2.14** is used by Charmetant for the characterization of transverse shearing for interlock reinforcement. Experimental results proves that the viscous contributions can be neglect and only elastic part is considered in transverse shear model.

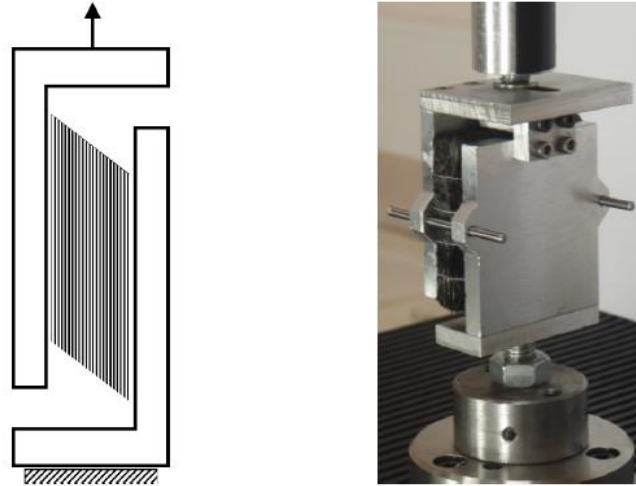


Figure 2. 14: Transverse shearing test device for interlock reinforcement [CHA 12]

2.1.5 Transverse compaction/consolidation

It is important to know the behavior of transverse compaction. For dry fabric reinforcement, the compressibility indicates the fiber content and the permeability for the distribution of resin during the forming process especially for the injection stage of RTM process. Many authors have developed both experimental methods and modeling approaches for this deformation mode. Among them, Q.T.Nguyen et al. [NGU 13] investigated the compaction behavior for multi-layer textile reinforcements at mesoscopic scale. The setup is shown in figure. The reinforcement is positioned on the bottom plate, a displacement sensor measures the distance between the bottom and top plates. Experimental results in **Figure 2. 15** express a non-linear behavior for the transverse compaction deformation.

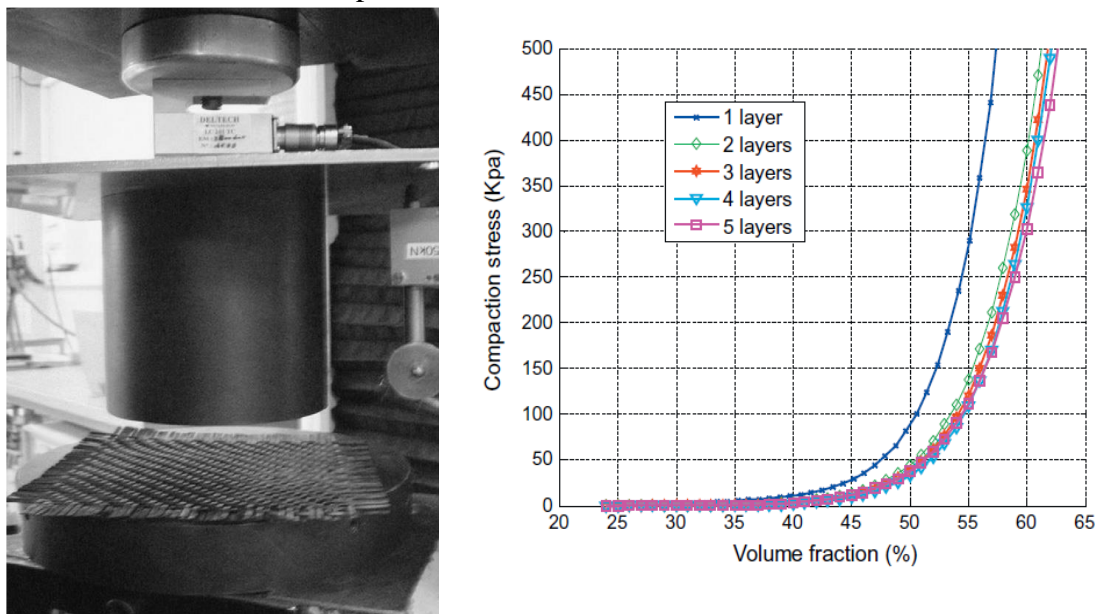


Figure 2. 15: Transverse compaction test device and measuring results [NGU 13]

For thermoplastic pre-impregnated composites, transverse compaction plays an important role on the consolidation stage. As mentioned in section 1.3.2, after forming, the material must be compacted to eliminate the residual porosities. Investigation of this deformation mode for

thermoplastic prepreps seems more complex than for dry textile reinforcements, due to the unknown content of void in the material, lack of a suitable approach to simulate transverse compaction, and the temperature variation during the consolidation. This is what this manuscript concerns and will be discussed in the following sections.

2.2 Thermomechanical analysis for thermoplastic pre-impregnated composite

2.2.1 Presentation of thermoforming process

As mentioned in previous chapter, thermoforming process has attracted more and more industry interests for the manufacturing of high performance composites material.

The first step of thermoforming aims at heating the material above its melting temperature. The main methods used for preheating are infrared lamps (IR), convection ovens and heating plate presses. IR heating is the most popular. The heating time is very short (1-2 minutes). However, temperature gradients in the thickness can appear that are managed by the imposition of a gradual heating (pre-heating cycle). A second constraint associated to this method is the poor distribution of the temperature in the case of complex geometries. For the problems during the practical application, like the thin structures, the IR heating is well suited. However, the convection heating is slow (5-10 min) but result in a homogeneous temperature distribution in the thickness at the end of heating. Finally, conduction heating is rarely used because the material tends to remain glued to the heating plates.

After heating, the material is transported to the press. The transfer time is a critical parameter. This transportation must be as soon as possible to prevent the material cools above its crystallization temperature. The existing automation systems such as conveyors and robots can reduce this time. The temperature in this step is dropped by about 10%. This is usually compensated during the heating step. The next step is the forming.

During the forming step, the reinforcement is deformed by applying a pressure between two complementary tools: punch and die. These tools are usually equipped with a system to maintain a constant temperature below melting point. The forming takes a few seconds.

After forming, the part is then kept under pressure to remove porosities and to ensure cohesion between the different layers and cooled to a temperature allowing the dimensional stability of the part. That is the consolidation phase. There are four primary resin flow phenomena that must be dealt with during the forming and consolidation steps: resin percolation, transverse squeeze flow, interply slip, and intraply slip. Resin percolation is the flow of the viscous polymer through or along the fiber bed that allows the plies to bond together, while transverse squeeze flow eliminates slight variations in prepreg thickness by allowing the prepreg layers to spread laterally due to applied pressure. These two resin flow phenomena play an important role during consolidation.

The structure is finally removed from the mold and continues its cooling to the ambient air. All phases are shown schematically in **Figure 2. 16** and **Figure 2. 17**.

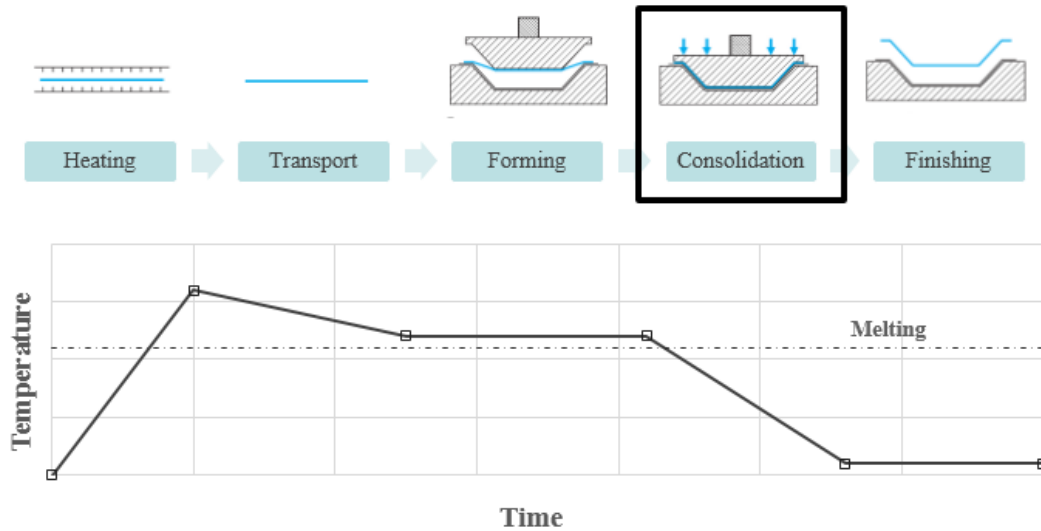


Figure 2. 16: Principal steps during thermoforming process

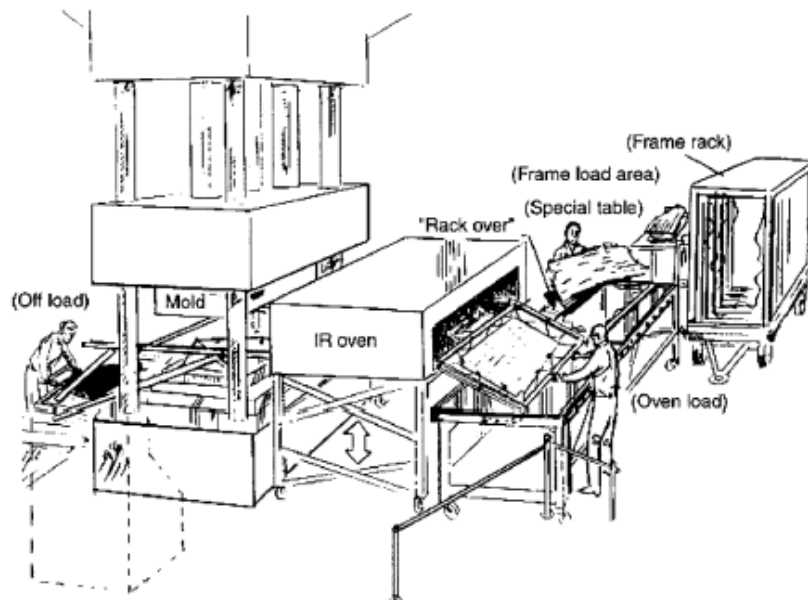


Figure 2. 17: Typical thermoforming setup [CAM 10]

All the steps are performed in a few minutes which can be further reduced if the production line enables the manufacture of the two parts at the same time, one in the heating module and the other in the forming module. All these features make the thermoforming a privileged candidate for largely production of composite parts, particularly in the automotive sector.

However, the optimum process automation means that involved physical phenomena are controlled. Such as the temperature, the applied pressure as well as the stacking sequence are supplementary parameters that have a main importance in the process result quality. The double-curved structures exhibit different types of defects (wrinkling, porosities, fiber fracture, etc.) that are difficult to predict. The consolidation step is absolutely necessary in order to remove certain defects resulting from the previous steps. According to the temperature path during the consolidation step, it is clear that the temperature and also the pressure during the

consolidation step especially appear as an essential factor since it modifies the behavior of the resin and its flow.

According to the experimental analysis at Common Research Center of EADS Suresnes [CHE 02], the stages of the process are represented for the state of the laminated part by micrographies (**Figure 2. 18**), from which the porosities are remained between the layers of plate and entre the fibers of layers before reconsolidation stage, all the porosities are removed at the end of the stage. This micrographic analysis clearly shows the importance of the reconsolidation phrase since its application of pressure proves to be necessary to remove the numerous porosities. Moreover, during the forming stage, the reconsolidation or the porosity closing also appears according to the geometry and the resulting stress states.

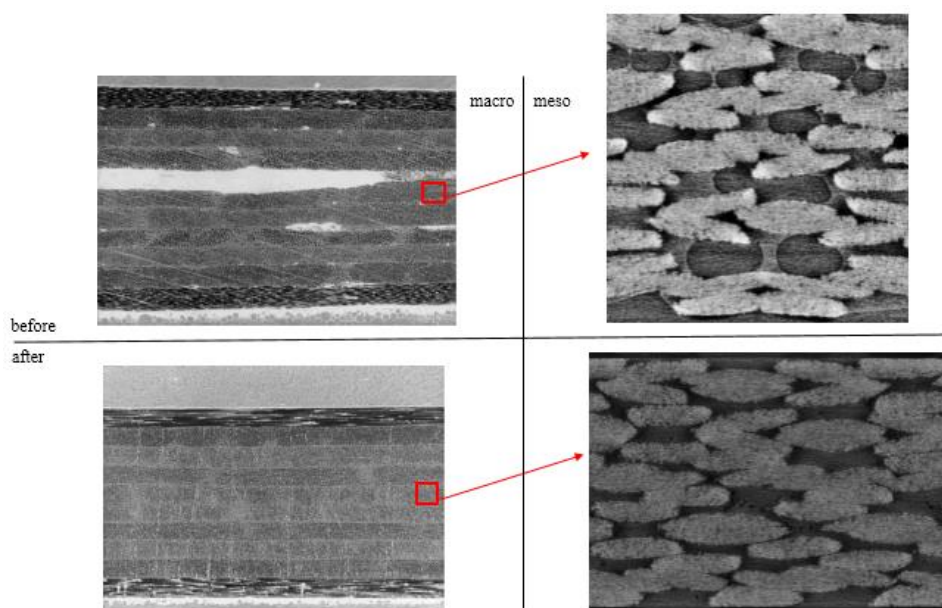


Figure 2. 18: Multilayer of the CFRTP before and after consolidation at macro and mesoscopic levels

The numerical simulation software appears to be an effective framework for the numerical modelling of thermoforming process in order to avoid the trial error. There exists a certain number of finite elements software. Most of them are based on shell element with zero normal stress assumption which is nor more valid when the through thickness stress plays a main role, especially during the consolidation stage and more generally in all the forming stage. Hence, the main subject of study in this work is to model the thermoforming process with the presence of through thickness stress. For this purpose, a new finite element will be proposed using complete three-dimension constitutive laws and the description of consolidation behavior will be characterized. The mechanical properties and deformation or particular material mechanisms, due to the fibrous nature of the reinforcement, are constantly evolving. The identification, modeling and the evolution of properties and deformation mechanisms during forming step and particularly consolidation step, will be firstly studied.

2.2.2 Presentation of material

In this work, the material used is thermoplastic pre-impregnated plate produced by Solvay. It is composed by 4 layers of 2x2 twill in carbon fiber and pre-impregnated by thermoplastic

resin Polyamide 6.6 (PA66). Their principal properties of material are shown in **Table 2. 1**. And the mechanical characterizations are presented in the following sections by correspondent experimental tests.

Matrix	PA66
Fibers	Carbon
Weaving pattern	2x2 twill
Number of layer	4
Thickness (mm)	2.05
Surface density (g.mm ⁻²)	2600
Fiber volume content	0.6

Table 2. 1: Principal properties of studied material

2.2.3 Bending behavior

The experimental method used to characterize the bending behavior of our material is the method developed in [LIA 14], more details concerning the set-up are presented in section 2.1.3. The length and width of sample are 200mm x 30mm. A series of test are launched within a set of temperature from 250° to 300°. And supplementary tests with two different directions (warp and weft) are carried out for the study of the influent of direction, the results reveal the equilibration of the material that their bending stiffness are nearly equal in the two directions.

The bending deflection shape is acquired by a CCD camera (**Figure 2. 19:** Image of bending deflexion shape) and image processing is used to extract its midline. The midline is fitted by uniform quartic B-spline curves that gives the curvature, and the curves of bending moment versus curvature are shown in **Figure 2. 20**.

The results shows that the bending deflection increases with temperature. A thermos-dependence for the bending stiffness is noticeable. A linear relation between the bending stiffness and the temperature in this set of temperature is assumed in the form of equation (2.6), the bending stiffness in the two yarn directions are supposed the same because of the regularity and balance of this material.

$$\begin{aligned} M_{warp} &= (\alpha_{ben} T + \beta_{ben}) \chi_{warp} \\ M_{weft} &= (\alpha_{ben} T + \beta_{ben}) \chi_{weft} \end{aligned} \quad (2.6)$$

With the two coefficients identified from the experimental results given in

Table 2. 2.

α_{ben}	Unit	β_{ben}	Unit
-3.876	N mm K ⁻¹	2143.3	N mm

Table 2. 2: Bending parameters for 2x2 twill in carbon/PA66 prepeg

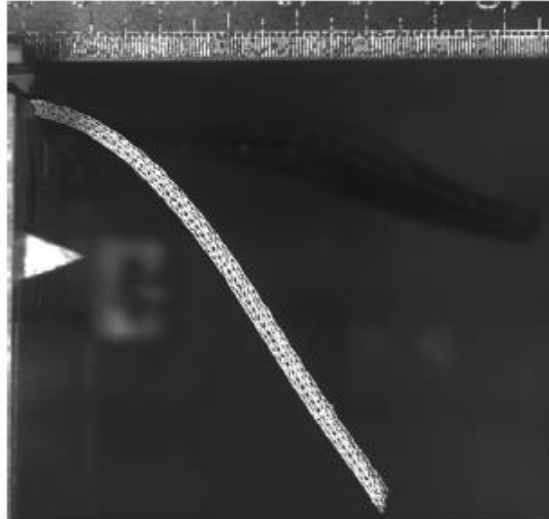


Figure 2.19: Image of bending deflexion shape

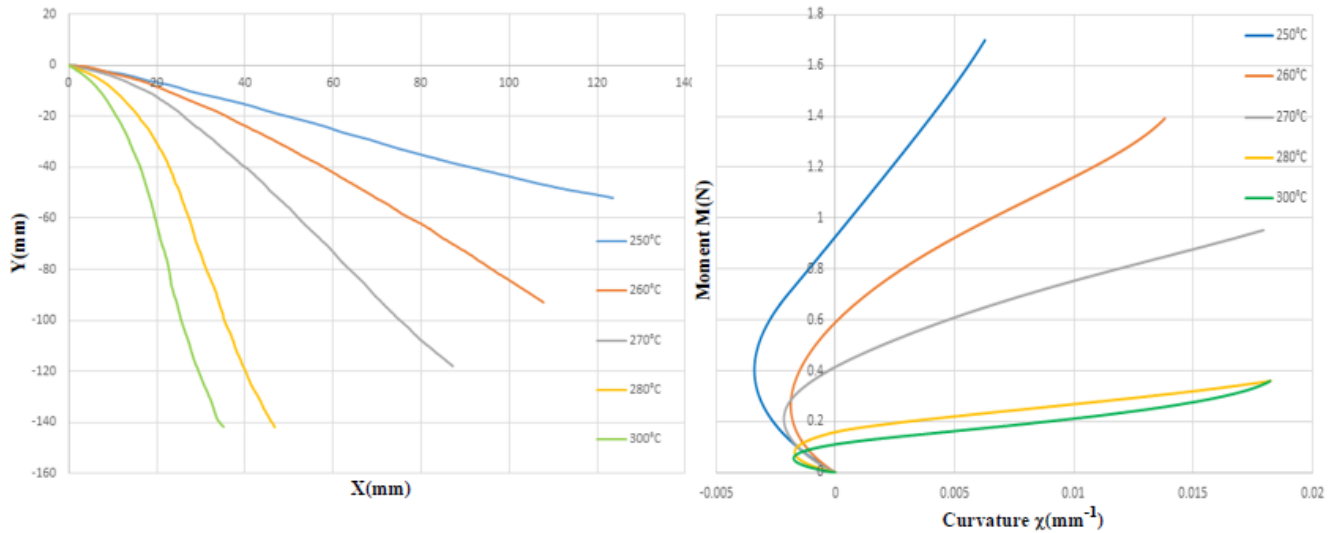
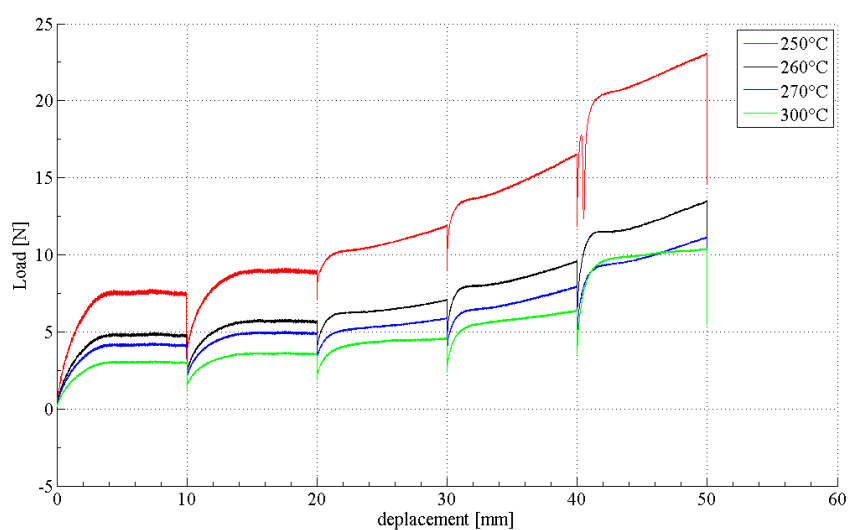


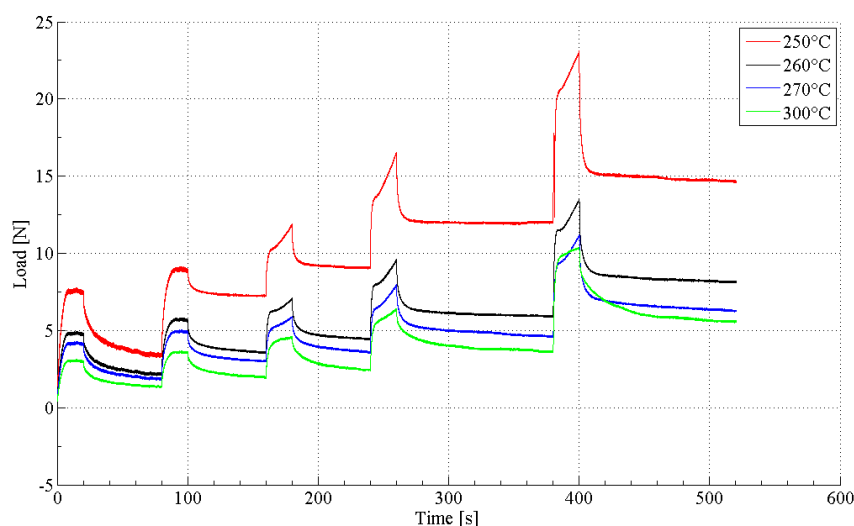
Figure 2.20: Bending test results for 2x2 twill in carbon/PA66 prepreg

2.2.4 In-plan shearing behavior

Characterization of the in-plan shearing behavior by bias extension test for the studied material is detailed in [WAN 14] [GUZ 15]. Like bending test, a series of tests are launched within a range of temperatures from 250° to 300° to study their behavior during forming process. The velocity of the imposed displacement is 30mm/min. To highlight the viscoelastic behavior of the material, a displacement by increments of 10mm is applied. Figure presents the load vs time and displacement curves. These results indicate that in-plan shear stiffness increases as the temperature decreases. The relaxation of efforts proves a remarkable viscoelastic behavior. A non-linear visco-hyperelastic model based on the generalization of Maxwell rheological model established Guzman is employed with the parameters are identified. More details concerning the behavior and the material parameters will be presented in section 4.2.3.



(a) Load versus displacement curves at different temperature



(b) Load versus time curves at different temperature

Figure 2. 21: Results of bias extension test at different temperature for 2x2 twill in carbon/PA66 prepreg

2.2.5 Transverse compaction behavior

For the purpose of the modelling of consolidation effects, characterization of the transverse compaction behavior seems indispensable. In the previous section, the transverse compaction test is presented for dry reinforcement. While for our pre-impregnated prepreps, the temperature must be controlled to analysis its thermo-dependence behavior.

– *Set-up description*

The **Figure 2. 22:** Compaction test device at high temperature shows the compaction test device for thermoplastic prepreps. The specimen with a dimension of 60mm x 60mm, is placed between two metallic plates linking to a universal tensile test machine, both of them are placed in an isothermal oven. Three thermocouples are disposed for this test, one is inserted in the

cross-section of material, and the other two are fixed in the two plates. A CCD camera associated with acquisition software, takes the picture of the distance between two plates through the transparent door of chamber. By the correction of images, the compression displacement of sample is more precise than the transverse displacement of universal tensile machine who includes the amortization part of its mechanical system.

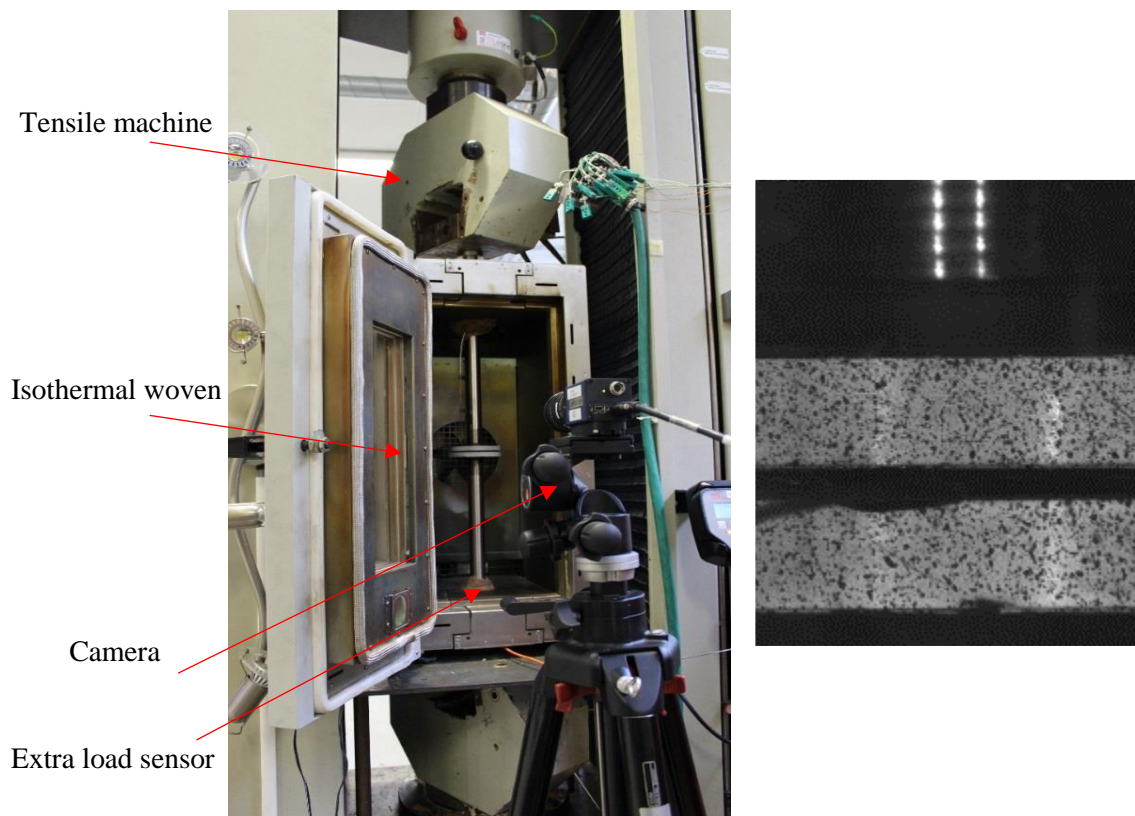


Figure 2. 22: Compaction test device at high temperature

– *Experimental conditions*

In order to reduce the exposition time of the material, the system is firstly heated up to about 300°C before putting the specimen. After placing the sample, it needs about 5min of heating time to reach a homogenous temperature field for the sample and the two plates. Then, cooling slightly to the needed test temperature, the loading program and camera are launched. A series of tests are performed over the range of processing temperatures (250-300°C), with a constant compaction speed of 0.2mm/min. The imposed displacement is limited by the maximum load value 8000N, when this value arrives, the test finishes and the state of displacement remains. Finally, the woven is opened for cooling and the top plate is reset to the initial position.

– *Experimental results*

The average curves of the load versus time and load versus displacement at different temperature are figured in the **Figure 2. 24:** Compaction test results at different temperature for 2x2 twill in carbon/PA66 prepreg and **Figure 2. 24**. According to the results, the compaction stiffness decreases when the temperature increases. And each time after the limit load achieved, the position of two plates remains fixed, a relaxation of load could be observed due to the viscosity. The viscosity of the material is not only that of the resin, but also it is linked to the

flow of resin percolation through or along the fiber bed and transverse squeeze flow through the thickness. These two flows are significant for the viscosity behavior during compaction effects. Hence, a viscoelastic model with thermo-dependence will be used for characterization of compaction behavior.

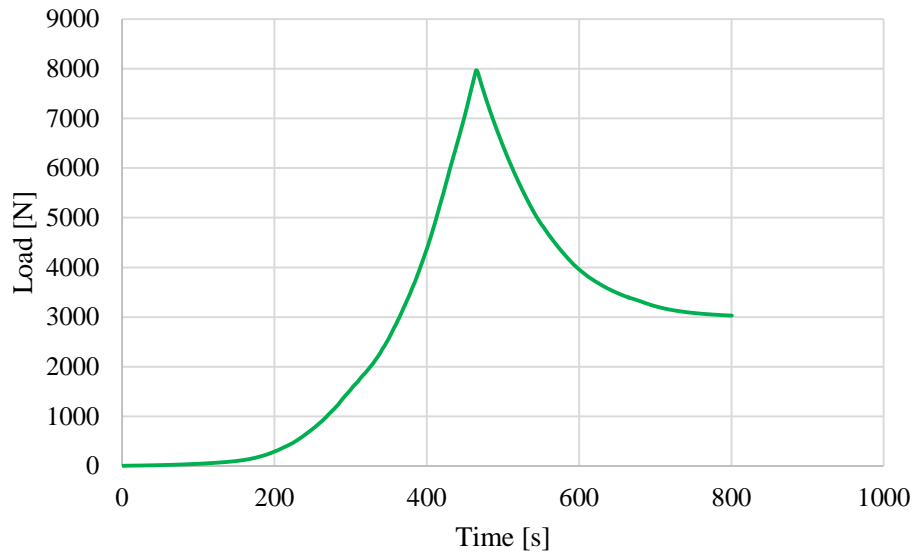


Figure 2. 23: Load versus time curve during compaction test at $T=300^{\circ}\text{C}$

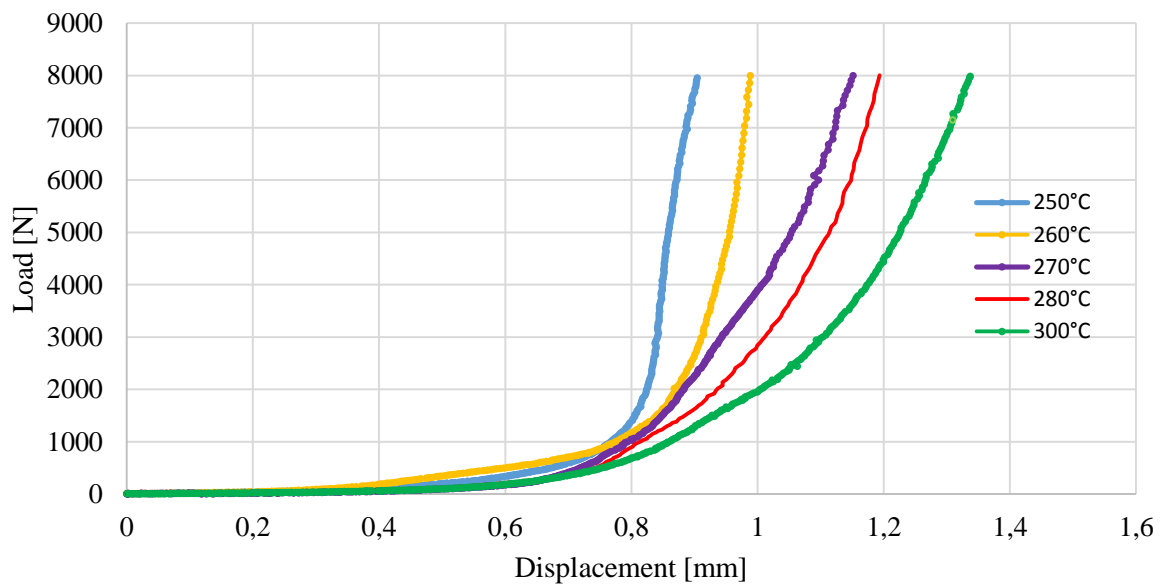


Figure 2. 24: Compaction test results at different temperature for 2x2 twill in carbon/PA66 prepreg

Chapter 3

Development of a prismatic solid-shell element for thermo-forming process of thermoplastic prepregs

As mentioned in chapter 1, there exists different approaches for the forming simulation. Shell finite elements are widely used and have shown their efficiency and accuracy in the modelling of prepreg ply. In this work, a new seven-node prismatic solid-shell element is developed: six are located at the apexes and are fitted with three translational DOFs whereas the seventh is sited at the center and is endowed with only one DOF (a displacement along the ‘thickness’ direction). To subdue transverse shear locking, an intermediate material frame related to the element sides is introduced in order to fix nodal transverse shear strain components. Indeed, the enhanced assumed strain method and a reduced integration scheme are combined offering the a linear varying strain field along the thickness direction to circumvent thickness locking, and a hourglass stabilization procedure is employed in order to correct the element’s rank deficiency for pinching. An additional node is added at the center providing a quadratic interpolation of the displacement in the thickness direction. Getting a linear normal strain component, along with a full 3D constitutive strain-stress behavior, allows to achieve similar results in bending cases as those obtained with the usual plane stress state hypothesis. The predominance of this element is the ability of three dimensional analysis, especially for the transverse stress existence through the thickness of material, which is essential for the consolidation modelling.

3.1 Introduction

Shell structure analysis using shell finite elements is an important task of finite element research because of its large industrial application and have been developed for several decades [BAT 96] [CHA 03]. However, for the simulation of sheet metal forming in case of hemming, bottoming, ironing and hydroforming, classical shell elements based on the degenerated shell concept or classical shell theories generally include the hypothesis of a plane stress state may cause the problems because of the omittance of the normal stress in the thickness direction. Solid-shell elements which possess no rotational degrees of freedom (d.o.f.s) are one of the approaches used to overcome the problem of plane stress state by general tridimensional constitutive relations. Furthermore, because of its simplicity of geometric and kinematic descriptions, the contact forces realistically applied on the outer surfaces, the correct modeling of boundaries non-parallel to the shell normal or director, the avoidance of the complication on handling finite rotational increments, and the consideration of large transverse shear deformations. Solid-shell elements show more advantageous than the degenerated shell elements. Nevertheless, formulating robust solid-shell elements is indeed more demanding

cause of the sensibility of locking phenomena. Besides shear and membrane lockings that occur in shell element, three main cases of locking can be expected: the thickness locking as well as the transverse shear locking occurring in bending situations and the volumetric locking due to the plastic incompressibility.

In the work of Sze [SZE 02a], all kinds of locking phenomena for plate/shell analysis with three-dimensional continuum finite element models are presented, advanced finite element techniques in order to alleviate or resolve the locking phenomena have been summarized.

A straightforward modification to overcome the thickness locking due to the coupling with Poisson's ratio –between the normal and in plane bending strains– is to apply the plane stress condition to the degenerated shell concept but this leads to difficulties in case of non-linear material behavior such as plasticity [AHM 70] [AUS 88] [KIM 88]. Another possibility is to impose a linear distribution of the normal strain by assuming a quadratic interpolation of the displacement in thickness direction. Details of these modifications can be found in references [HAU 98] [HAU 00] [SZE 00] [SZE 02b] [SZE 02c] [VU 03] [LEG 03] [FON 04] [KIM 05]. The most popular strategy to alleviate locking pathologies is the concept of reduced integration with hourglass stabilization (RI). Finite elements of this kind are especially attractive due to their computational efficiency with the ability to accommodate several integration points along the thickness direction. To this end, the recent developments of Reese [REE 07], Alves de Sousa et al [ALV 07], Cardoso et al [CAR 08] and Schwarze et al [SCH 09a] [SCH 09b] [SCH 11] seem to achieve efficient and accurate solid-shell elements where the capabilities of the ANS (Assumed Natural Strain), the EAS (Enhanced Assumed Strain) and RI techniques are combined together and where a reformulation for plane stress condition is not necessary. The EAS concept was initially introduced by Simo et al. [SIM 90] where, under certain conditions, the strain field can be enriched in order to improve the element's performance. The mathematical basis for such element formulations is given by the well-known Veubeke-Hu-Washizu [FRA 51] three-field variational principle. For the purpose of improving the efficiency of the elements, a lot of works has been done to reduce the number of additional (EAS) parameters as it can be seen in references [HAU 98] [VU 03] [FON 04] [REE 07] [ALV 07] [CAR 08] [AYA 09] [SCH 09a] [SCH 09b] [SCH 11]. The works of Alves de Sousa et al [ALV 07] and Cardoso et al [CAR 08] proved that only a single enhancing parameter was enough to considerably reduce the volumetric locking and Poisson's locking. This, thanks to a combination between EAS and reduced integration (RI) with the use of an enhancing strain variable along the thickness direction offering the possibility of a linear varying strain field. Recalling that the cause of thickness locking is the lack of linear thickness strain modes, another possibility to remove the Poisson thickness locking is to enrich the strain field of the element by an additional linear component of the thickness strain. According to the EAS methodology, the extra strain parameter is independently interpolated for each element and can be condensed out on the element level (easily in the linear elastic case); see for example references [BIS 00] [BRA 02] [BRA 05]. Moreover, the EAS method is also the most important strategy to cure volumetric locking that has been implanted into many shell formulations and in the solid-shell formulations of Sze and Yao [SZE 00], and Fontes Valente et al. [FON 04], to name only a few. In addition, the transverse shear strain field is modeled by the use of the ANS method by Dvorkin and Bathe [BAT 85] which is based on the evaluation of the shear terms at assumed

shear locking-free collocation points, the values of which being interpolated within the reference element, and also by Boisse [BOI 94] and Sabourin [BAS 12] [SAN 11a]. In the work of Cardoso et al [CAR 08], Abed-Meraim et al [ABE 09] and Bassa [BAS 12], a physical stabilization procedure is employed in order to correct the element's rank deficiency eliminating 3D hourglass modes without resorting to empirical parameters.

Abaqus library includes the solid shell element 'SC6R'. Geometrically speaking it is a triangular prism with three degrees of freedom per node (three translations) but the bending behavior is greatly improved. As well, is included a hexahedral element called 'SC8R'. These two elements are suitable for thin or thick shells and are used like shell elements: no deliberate thickness reduction due to forces normal to the mid-plane! The kinematic is based on Mindlin's theory (thick plates) and the letter 'R' indicates a reduced integration: only several quadrature points along thickness direction. In Abaqus data file, a "thickness" is requested even if the effective thickness –for stiffness matrix or other calculations on real physics– is computed from the nodal coordinates. This requested value is used to stabilize "hourglass" modes; among them a kind of "twisting" mode along the thickness direction (z). In addition, since a "thickness" is evoked, a precaution has to be taken in the elemental node numbering because it provides the desired normal. The major disadvantage of these solid-shells fitted with a reduced integration is the risk of zero energy modes and transverse shear locking emergence.

Most research efforts with these technologies for solid-shell elements were mainly applied to hexahedral finite elements [HAU 98] [HAU 00] [SZE 00] [SZE 02b] [VU 03] [LEG 03] [FON 04] [KIM 05] [REE 07] [ALV 07] [CAR 08] [SCH 09a] [SCH 09b] [ABE 09] [BAS 12] [SAN 11a]. There are not many developments for triangular prism solid-shell elements. The behavior of the standard (displacement base) 6-node "prism" and 8-node "brick" is quite different, that's why the strategies to cure the different locking problems may be different. The transverse shear locking of the former is quite lower while the latter has a better in-plane behavior. One obvious and important advantage of a triangular prism element is that the triangular mesh generators are quite more efficient, and provide elements with a better aspect ratio.

In the author's knowledge, the first approach on prismatic solid-shell element was proposed by Sze et al. [SZE 01]. The ANS method is employed to alleviate shear and trapezoidal lockings, a modified generalized laminate stiffness matrix is circumvented thickness locking. Lately, an original approach was proposed by Flores in [FLO 13a] [FLO 13b] on prismatic finite elements. Volumetric locking is cured by averaging volumetric deformation over the element and by the use of an assumed strain for the in-plane components that uses neighboring elements. An EAS method with an additional degree of freedom avoids locking due to Poisson effects. Transverse shear locking is cured using an assumed natural strain (ANS) to modify the metric tensor components associated with shell normal direction.

In this work, a solid-shell prismatic finite element is proposed according to several elements on the basis of triangular shell elements. The EAS method combined with RI technique is introduced to avoid the thickness locking by not taking into account shear strain energy and to describe the bending behavior with a Kirchhoff-like theory (so called Discrete Kirchhoff Theory). The idea is to base the bending formulation on shell elements DKT (Triangle) and to

extrapolate the usual shell degrees of freedom from the translational nodal displacements of the prism (see **Figure 3. 1**). Regarding the transverse shear, the triangular shell element proposed by Boisse [BOI 94] has been employed. A strain interpolation avoids shear locking and an intermediate material frame related to the element sides is introduced in order to nodal transverse shear strain components. Aiming to directly formulate the problem with a three dimensional behavior law, an additional degree of freedom is added at the center of each element adopting the same strategy used in [BAS 12].

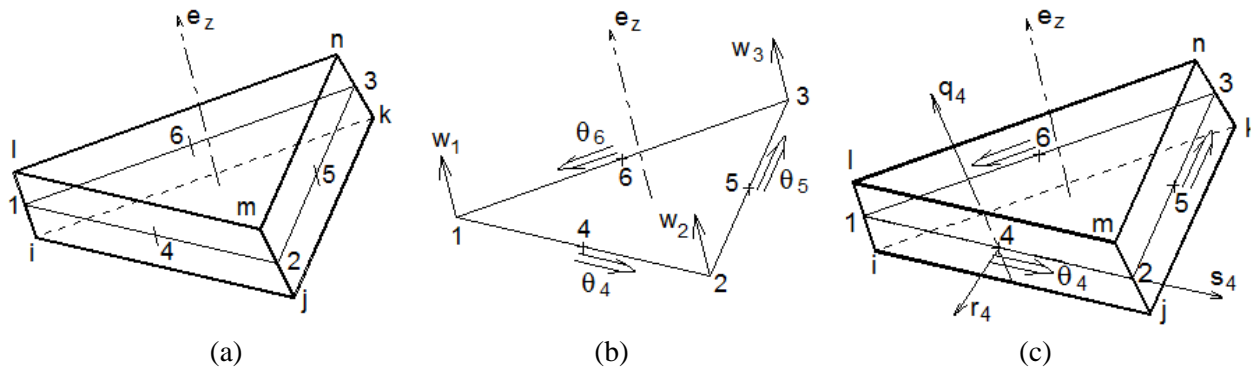


Figure 3. 1: Description of prismatic solid-shell element

3.2 Formulation of solid-shell element SB6Y18

As shown in **Figure 3. 2**, a reduced integration is used according to ‘ ξ ’ and ‘ η ’, five integration points are distributed through the thickness along the privileged direction ‘ ζ ’. In order to highlight the zero-energy modes, the usual interpolation function for the prism can be written as equation (3.1), this method from Belytschko [BEL 94] [BEL 13] [FLA 81] has been similarly applied to a 8-node detailed in [BAS 12].

$$\langle N \rangle = \frac{1}{2} \langle (1-\xi-\eta)(1-\zeta) \mid \xi(1-\zeta) \mid \eta(1-\zeta) \mid (1-\xi-\eta)(1+\zeta) \mid \xi(1+\zeta) \mid \eta(1+\zeta) \rangle \quad (3.1)$$

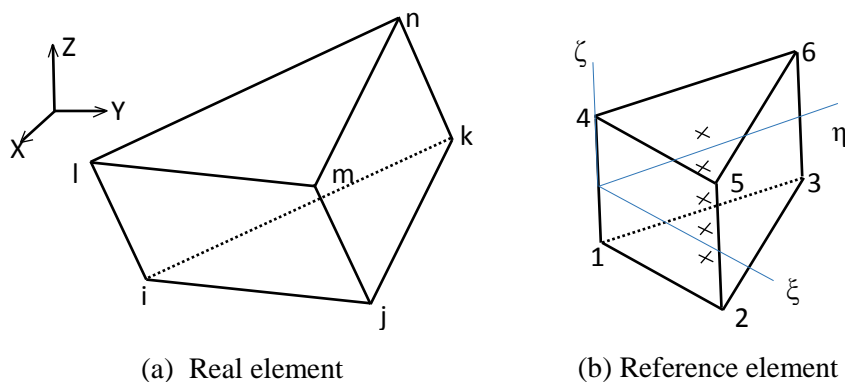


Figure 3. 2: Six-node prismatic element

The nodal coordinates is:

$$\begin{aligned}\{\mathbf{x}_e\} &= \langle x_i \quad x_j \quad x_k \quad x_l \quad x_m \quad x_n \rangle \\ \{\mathbf{y}_e\} &= \langle y_i \quad y_j \quad y_k \quad y_l \quad y_m \quad y_n \rangle \\ \{\mathbf{z}_e\} &= \langle z_i \quad z_j \quad z_k \quad z_l \quad z_m \quad z_n \rangle\end{aligned}\quad (3.2)$$

The nodal displacements is:

$$\begin{aligned}\{\mathbf{U}_{xe}\} &= \langle u_i \quad u_j \quad u_k \quad u_l \quad u_m \quad u_n \rangle \\ \{\mathbf{U}_{ye}\} &= \langle v_i \quad v_j \quad v_k \quad v_l \quad v_m \quad v_n \rangle \\ \{\mathbf{U}_{ze}\} &= \langle w_i \quad w_j \quad w_k \quad w_l \quad w_m \quad w_n \rangle\end{aligned}\quad (3.3)$$

Still in the local frame, the 3 components of the displacement are sought under the form:

$$\begin{cases} u_x = a_{0u} + a_{xu}x + a_{yu}y + a_{zu}z + c_{1u}\eta\xi + c_{2u}\xi\xi \\ u_y = a_{0v} + a_{xv}x + a_{yv}y + a_{zv}z + c_{1v}\eta\xi + c_{2v}\xi\xi \\ u_z = a_{0w} + a_{xw}x + a_{yw}y + a_{zw}z + c_{1w}\eta\xi + c_{2w}\xi\xi \end{cases}\quad (3.4)$$

with

$$\begin{cases} a_{xu} = \langle \mathbf{b}_x \rangle \cdot \{\mathbf{U}_{xe}\} & a_{yu} = \langle \mathbf{b}_y \rangle \cdot \{\mathbf{U}_{xe}\} & a_{zu} = \langle \mathbf{b}_z \rangle \cdot \{\mathbf{U}_{xe}\} & c_{au} = \langle \boldsymbol{\gamma}_\alpha \rangle \cdot \{\mathbf{U}_{xe}\} \\ a_{xv} = \langle \mathbf{b}_x \rangle \cdot \{\mathbf{U}_{ye}\} & a_{yv} = \langle \mathbf{b}_y \rangle \cdot \{\mathbf{U}_{ye}\} & a_{zv} = \langle \mathbf{b}_z \rangle \cdot \{\mathbf{U}_{ye}\} & c_{av} = \langle \boldsymbol{\gamma}_\alpha \rangle \cdot \{\mathbf{U}_{ye}\} \\ a_{xw} = \langle \mathbf{b}_x \rangle \cdot \{\mathbf{U}_{ze}\} & a_{yw} = \langle \mathbf{b}_y \rangle \cdot \{\mathbf{U}_{ze}\} & a_{zw} = \langle \mathbf{b}_z \rangle \cdot \{\mathbf{U}_{ze}\} & c_{aw} = \langle \boldsymbol{\gamma}_\alpha \rangle \cdot \{\mathbf{U}_{ze}\} \end{cases}\quad (3.5)$$

and for $\alpha = 1, 2$

$$\langle \boldsymbol{\gamma}_\alpha \rangle = \frac{1}{2} \left(\langle \mathbf{h}_\alpha \rangle - \langle \mathbf{h}_\alpha \rangle \cdot \langle \mathbf{x}_e \rangle \langle \mathbf{b}_x \rangle - \langle \mathbf{h}_\alpha \rangle \cdot \langle \mathbf{y}_e \rangle \langle \mathbf{b}_y \rangle - \langle \mathbf{h}_\alpha \rangle \cdot \langle \mathbf{z}_e \rangle \langle \mathbf{b}_z \rangle \right)\quad (3.6)$$

$\langle \mathbf{h}_1 \rangle = \langle 0 \quad 0 \quad -1 \quad 0 \quad 0 \quad 1 \rangle$: is the row-matrix gathering the product $\eta\xi$ at the 6 nodes of the prism;

$\langle \mathbf{h}_2 \rangle = \langle 0 \quad -1 \quad 0 \quad 0 \quad 1 \quad 0 \rangle$: comes from $\xi\xi$.

$$\begin{bmatrix} \langle \mathbf{b}_x \rangle \\ \langle \mathbf{b}_y \rangle \\ \langle \mathbf{b}_z \rangle \end{bmatrix} = [\mathbf{J}_0^{-1}] \begin{bmatrix} \langle \mathbf{b}_\xi \rangle \\ \langle \mathbf{b}_\eta \rangle \\ \langle \mathbf{b}_\zeta \rangle \end{bmatrix}; \begin{bmatrix} \langle \mathbf{b}_\xi \rangle \\ \langle \mathbf{b}_\eta \rangle \\ \langle \mathbf{b}_\zeta \rangle \end{bmatrix} = \begin{bmatrix} \langle \mathbf{N}_{,\xi} \rangle \\ \langle \mathbf{N}_{,\eta} \rangle \\ \langle \mathbf{N}_{,\zeta} \rangle \end{bmatrix}_{\xi=\eta=\zeta=0}; [\mathbf{J}_0] = \begin{bmatrix} \langle \mathbf{N}_{,\xi} \rangle \\ \langle \mathbf{N}_{,\eta} \rangle \\ \langle \mathbf{N}_{,\zeta} \rangle \end{bmatrix} \begin{bmatrix} \{\mathbf{x}_e\} & \{\mathbf{y}_e\} & \{\mathbf{z}_e\} \end{bmatrix}\quad (3.7)$$

3.2.1 In plan strain

Rewriting $h_1 = \eta\xi$ and $h_2 = \xi\xi$, a straightforward calculus gives:

$$\begin{Bmatrix} \varepsilon_{xx} \\ \varepsilon_{yy} \\ 2.\varepsilon_{xy} \end{Bmatrix} = \left(\begin{bmatrix} \langle \mathbf{b}_x \rangle & | & \\ \langle \mathbf{b}_y \rangle & | & \\ \langle \mathbf{b}_y \rangle & | & \langle \mathbf{b}_x \rangle \end{bmatrix} + \begin{bmatrix} h_{1,x}\langle \gamma_1 \rangle + h_{2,x}\langle \gamma_2 \rangle & | & \\ h_{1,y}\langle \gamma_1 \rangle + h_{2,y}\langle \gamma_2 \rangle & | & h_{1,x}\langle \gamma_1 \rangle + h_{2,x}\langle \gamma_2 \rangle \\ h_{1,y}\langle \gamma_1 \rangle + h_{2,y}\langle \gamma_2 \rangle & | & h_{1,x}\langle \gamma_1 \rangle + h_{2,x}\langle \gamma_2 \rangle \end{bmatrix} \right) \begin{Bmatrix} \mathbf{U}_{xe} \\ \mathbf{U}_{ye} \end{Bmatrix} \quad (3.8)$$

The first \mathbf{B} matrix corresponds to the constant part of the strain interpolation and the second one ensures the stability. It is proposed here to reformulate the stabilization term using a different methodology that ensures the stability using a new formulation that gives accurate results with coarse meshes. The non-constant part is directly derived from shell theory and is as follows:

$$\begin{Bmatrix} \varepsilon_{xx} \\ \varepsilon_{yy} \\ 2.\varepsilon_{xy} \end{Bmatrix} = \{\boldsymbol{\varepsilon}^m\} + z.\{\boldsymbol{\kappa}\}; \{\boldsymbol{\varepsilon}^m\} = \begin{Bmatrix} \varepsilon_{xx}^m \\ \varepsilon_{yy}^m \\ 2.\varepsilon_{xy}^m \end{Bmatrix} = [\mathbf{B}^m] \cdot \begin{Bmatrix} \mathbf{U}_{xe} \\ \mathbf{U}_{ye} \end{Bmatrix}; [\mathbf{B}^m] = \begin{bmatrix} \langle \mathbf{b}_x \rangle & | & \\ \langle \mathbf{b}_y \rangle & | & \langle \mathbf{b}_y \rangle \\ \langle \mathbf{b}_y \rangle & | & \langle \mathbf{b}_x \rangle \end{bmatrix} \quad (3.9)$$

$\{\boldsymbol{\kappa}\}$ might be assimilated to a curvature, and its computation is obtained using the DKT6 formulation.

For the prism described here, **Figure 3. 1(a)** shows the mean triangular area defined by points 1, 2 and 3 (midpoints of the edges i-l, j-m, k-n, respectively), the normal to this surface being \mathbf{e}_z . **Figure 3. 1(b)** shows this mid-surface as a 6-node triangular element whose degrees of freedom defining bending effects are three translations (w_1, w_2, w_3) in the \mathbf{e}_z direction and three rotations ($\theta_4, \theta_5, \theta_6$) in the direction of each side, at the nodes 4, 5 and 6 located at the midpoints of these sides. Finally **Figure 3. 1(c)** shows how to express, for example, θ_4 by using nodal displacement components (projection on the axis r_4) of nodes i, j, m, l of the prism. And it would be the same for θ_5 by using translational dof of nodes j, k, n, m and for θ_6 with translations of nodes k, l, n of the prism. Finally, rotations $\theta_4, \theta_5, \theta_6$ are connected to the nodal displacements. Otherwise, w_1 is obtained with the translations of nodes i and l, w_2 with the translations of nodes j and m, and w_3 with the translations of nodes k and n.

So, it only remains to find the matrices \mathbf{B}_w and \mathbf{B}_θ giving the curvatures from translational degrees of freedom (w_1, w_2, w_3) for \mathbf{B}_w and rotations ($\theta_4, \theta_5, \theta_6$) for \mathbf{B}_θ .

- DKT6 Shell Finite Element

The DKT6 [ROE 92] element defines the element defines the bending of a plate with a Kirchhoff kinematic. It has three translational degrees of freedom (dof) normal to the surface, located at the vertices, and three rotational dof, located at midpoints of the sides (**Figure 3. 1(b)**).

Conventionally, interpolation functions use area coordinates (A: area of the triangle):

$$\begin{aligned} w(x, y) &= N_1 \cdot w_1 + N_2 \cdot w_2 + N_3 \cdot w_3; \quad N_i(x, y) = A_i(x, y) / A \\ \theta_x(x, y) &= (1 - 2N_3) \cdot \theta_{x4} + (1 - 2N_1) \cdot \theta_{x5} + (1 - 2N_2) \cdot \theta_{x6} \\ \theta_y(x, y) &= (1 - 2N_3) \cdot \theta_{y4} + (1 - 2N_1) \cdot \theta_{y5} + (1 - 2N_2) \cdot \theta_{y6} \end{aligned} \quad (3.10)$$

Hence at node 4 (middle of the side 1-2), $\theta_x = \theta_{x4}$, $\theta_y = \theta_{y4}$, and the same goes for the node 5 (middle of the side 2-3) and the node 6 (middle of the side 3-1). After derivations:

$$\begin{aligned} N_{1,x}(x,y) &= \frac{1}{2A}(y_2 - y_3) ; N_{1,y}(x,y) = \frac{1}{2A}(x_3 - x_2) \\ N_{2,x}(x,y) &= \frac{1}{2A}(y_3 - y_1) ; N_{2,y}(x,y) = \frac{1}{2A}(x_1 - x_3) \\ N_{3,x}(x,y) &= \frac{1}{2A}(y_1 - y_2) ; N_{3,y}(x,y) = \frac{1}{2A}(x_2 - x_1) \end{aligned} \quad (3.11)$$

For simplicity, the following notation is used: $x_{mn} = x_m - x_n$; $y_{mn} = y_m - y_n$

Hence, the matrix linking the curvatures to the rotations is given by:

$$\{\kappa\} = \begin{Bmatrix} \kappa_{xx} \\ \kappa_{yy} \\ 2\kappa_{xy} \end{Bmatrix} = \begin{Bmatrix} \theta_{y,x} \\ -\theta_{x,y} \\ \theta_{y,y} - \theta_{x,x} \end{Bmatrix} = \frac{1}{A} \begin{bmatrix} y_{21} & y_{32} & y_{13} \\ x_{21} & x_{32} & x_{13} \\ y_{12} & x_{12} & y_{23} & x_{23} & y_{31} & x_{31} \end{bmatrix} \begin{Bmatrix} \theta_{x4} \\ \theta_{y4} \\ \theta_{x5} \\ \theta_{y5} \\ \theta_{x6} \\ \theta_{y6} \end{Bmatrix} \quad (3.12)$$

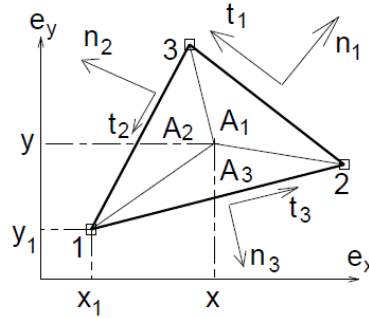


Figure 3. 3: Normal vectors and tangential vectors for each triangular side

It is useful to express the normal vectors and the tangential vectors in the local basis (see **Figure 3. 3**):

$$\begin{aligned} \vec{n}_1 &= c_1 \vec{e}_x + s_1 \vec{e}_y & \vec{t}_1 &= -s_1 \vec{e}_x + c_1 \vec{e}_y & \text{with } c_1 &= \frac{y_{32}}{L_1} \text{ and } s_1 = -\frac{x_{32}}{L_1} ; L_1 : \text{side length 2-3} \\ \vec{n}_2 &= c_2 \vec{e}_x + s_2 \vec{e}_y & \vec{t}_2 &= -s_2 \vec{e}_x + c_2 \vec{e}_y & \text{with } c_2 &= \frac{y_{13}}{L_2} \text{ and } s_2 = -\frac{x_{13}}{L_2} ; L_2 : \text{side length 3-1} \\ \vec{n}_3 &= c_3 \vec{e}_x + s_3 \vec{e}_y & \vec{t}_3 &= -s_3 \vec{e}_x + c_3 \vec{e}_y & \text{with } c_3 &= \frac{y_{21}}{L_3} \text{ and } s_3 = -\frac{x_{21}}{L_3} ; L_3 : \text{side length 2-1} \end{aligned}$$

Then, decomposing the rotations vectors in their local base ($\mathbf{e}_x, \mathbf{e}_y$), they are expressed by:

$$\begin{aligned} \vec{\theta}_4 &= \theta_{x4} \vec{e}_x + \theta_{y4} \vec{e}_y = \theta_4 \vec{t}_3 + \frac{w_2 - w_1}{L_3} \vec{n}_3 \\ \theta_{x4} &= -s_3 \theta_4 + c_3 \frac{w_2 - w_1}{L_3} ; \theta_{y4} = c_3 \theta_4 + s_3 \frac{w_2 - w_1}{L_3} \end{aligned} \quad (3.13)$$

$\bar{\theta}_5, \bar{\theta}_6, \theta_{x5}, \theta_{y5}, \theta_{x6}, \theta_{y6}$ are given by index permutation.

The curvatures will be expressed in terms of the rotational degrees of freedom and the normal nodal displacement as follows:

$$\{\kappa\} = [\mathbf{B}_\theta] \begin{Bmatrix} \theta_4 \\ \theta_5 \\ \theta_6 \end{Bmatrix} + [\mathbf{B}_w] \begin{Bmatrix} w_1 \\ w_2 \\ w_3 \end{Bmatrix} \quad (3.14)$$

After development, the matrices \mathbf{B}_θ and \mathbf{B}_w are:

$$[\mathbf{B}_w] = \frac{1}{A} \begin{bmatrix} c_2s_2 - c_3s_3 & c_3s_3 - c_1s_1 & c_1s_1 - c_2s_2 \\ c_3s_3 - c_2s_2 & c_1s_1 - c_3s_3 & c_2s_2 - c_1s_1 \\ 2(c_3^2 - c_2^2) & 2(c_1^2 - c_3^2) & 2(c_2^2 - c_1^2) \end{bmatrix} \quad (3.15)$$

$$[\mathbf{B}_\theta] = \frac{1}{A} \begin{bmatrix} c_3^2L_3 & c_1^2L_1 & c_2^2L_2 \\ s_3^2L_3 & s_1^2L_1 & s_2^2L_2 \\ 2c_3s_3L_3 & 2c_1s_1L_1 & 2c_2s_2L_2 \end{bmatrix} \quad (3.16)$$

- *Linking the triangle to the prism*

In the local frame of the triangular finite element – which is also the frame of the associated prism –, the displacement of the six nodes of the prism projected on \mathbf{e}_z are denoted: $w_i, w_j, w_k, w_l, w_m, w_n$. A trivial method gives directly w_1, w_2, w_3 as a function of $w_i, w_j, w_k, w_l, w_m, w_n$:

$$w_1 = \frac{w_i + w_l}{2}; \quad w_2 = \frac{w_j + w_m}{2}; \quad w_3 = \frac{w_k + w_n}{2} \quad (3.17)$$

Using \mathbf{B}_w (B_{ij}^w : being the i^{th} row and the j^{th} column component) and performing a base change to make the nodal translations ($U_{Xi}, U_{Yi}, U_{Zi}, U_{Xj}, \dots, U_{Zn}$) be expressed in the global frame of the structure (X, Y, Z), a matrix $\bar{\mathbf{B}}_{w(3 \times 18)}^b$ detailed in the **Appendices** is obtained. This matrix connects the part of the curvatures due to the normal translations to the global displacements of the six nodes.

The direction cosines ($xX, xY, xZ, yX, yY, yZ, zX, zY$ and zZ) link the unit vectors of the local reference to the ones of the global reference:

$$\bar{\mathbf{e}}_x = xX \cdot \bar{\mathbf{X}} + xY \cdot \bar{\mathbf{Y}} + xZ \cdot \bar{\mathbf{Z}}; \quad \bar{\mathbf{e}}_y = yX \cdot \bar{\mathbf{X}} + yY \cdot \bar{\mathbf{Y}} + yZ \cdot \bar{\mathbf{Z}}; \quad \bar{\mathbf{e}}_z = zX \cdot \bar{\mathbf{X}} + zY \cdot \bar{\mathbf{Y}} + zZ \cdot \bar{\mathbf{Z}} \quad (3.18)$$

The last development for the expression of bending effects consists in linking $\theta_4, \theta_5, \theta_6$ to the 18 displacements ($U_{Xi}, U_{Yi}, U_{Zi}, U_{Xj}, \dots, U_{Zn}$) of the nodes I to n. For example, for the rotation θ_4 , we proceed as follows:

Two points ‘a’ and ‘b’ are located on the middle of the edges i-j and m-l (**Figure 3. 4**)

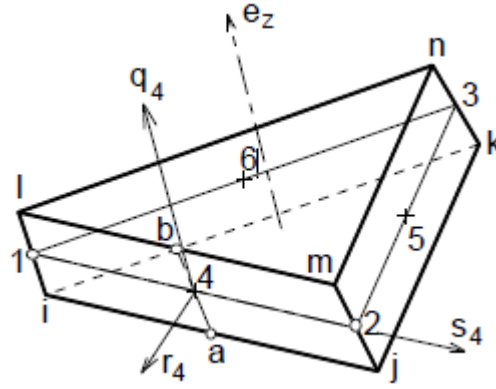


Figure 3. 4: Linking the triangle to the prism

A local basis at each mid-side node (4, 5 or 6) is expressed as follows:

$$\vec{r}_4 = \vec{12} \wedge \vec{ab} / \|\vec{12} \wedge \vec{ab}\| ; \vec{s}_4 = \vec{12} / \|\vec{12}\| ; \vec{q}_4 = \vec{r}_4 \wedge \vec{s}_4 ; \mathbf{R}_4 = \begin{bmatrix} s_{4x} & s_{4y} & s_{4z} \\ q_{4x} & q_{4y} & q_{4z} \\ r_{4x} & r_{4y} & r_{4z} \end{bmatrix} \quad (3.19)$$

$$\mathbf{R}_4 \text{ is used for the displacements } \begin{bmatrix} u_i^{(4)} \\ v_i^{(4)} \\ w_i^{(4)} \end{bmatrix} = [\mathbf{R}_4] \cdot \begin{Bmatrix} U_{Xi} \\ U_{Yi} \\ U_{Zi} \end{Bmatrix} \text{ and local coordinates: } \begin{bmatrix} s_i^{(4)} \\ q_i^{(4)} \\ r_i^{(4)} \end{bmatrix} = [\mathbf{R}_4] \cdot \begin{Bmatrix} X_i \\ Y_i \\ Z_i \end{Bmatrix}.$$

Expressions are similar for the nodes j, m, l.

The area A_4 of the "2D" surface i-j-m-l is given by:

$$A_4 = \left((s_m^{(4)} - s_i^{(4)})(q_l^{(4)} - q_j^{(4)}) + (q_m^{(4)} - q_i^{(4)})(s_j^{(4)} - s_l^{(4)}) \right) / 2 \quad (3.20)$$

Then

$$\theta_4 = w_{,q_4} \text{ with } \begin{Bmatrix} w_{,s_4} \\ w_{,q_4} \end{Bmatrix} = \frac{1}{2A_4} \begin{bmatrix} q_j^{(4)} - q_l^{(4)} & q_m^{(4)} - q_i^{(4)} & q_l^{(4)} - q_j^{(4)} & q_i^{(4)} - q_m^{(4)} \\ s_l^{(4)} - s_j^{(4)} & s_i^{(4)} - s_m^{(4)} & s_j^{(4)} - s_l^{(4)} & s_m^{(4)} - s_i^{(4)} \end{bmatrix} \begin{Bmatrix} w_i^{(4)} \\ w_j^{(4)} \\ w_m^{(4)} \\ w_l^{(4)} \end{Bmatrix} \quad (3.21)$$

Precisely, it is possible to find the latter relation by analogy with a conventional shape in the i-j-m-l quadrilateral: 's' takes the place of 'x' and 'q' of the 'y' while 'r' corresponds to 'z' and 'w' is the translation in the normal surface defined by the nodes i, j, m, l. We are therefore interested in derivatives $w_{,x}$ and $w_{,y}$, while the usual interpolation in the "parent" rectangular shape involves the parameters ξ and η ranging from -1 to 1:

$$w = \frac{1}{4}(1-\xi)(1-\eta)w_i^{(4)} + \frac{1}{4}(1+\xi)(1-\eta)w_j^{(4)} + \frac{1}{4}(1+\xi)(1+\eta)w_m^{(4)} + \frac{1}{4}(1-\xi)(1+\eta)w_l^{(4)} \quad (3.22)$$

The derivatives $w_{,\xi}$ and $w_{,\eta}$ at $\xi = 0$ and $\eta = 0$ (position of the node '4' in the middle of the face i-j-m-l) are expressed by the nodal displacements of the for nodes of the face.

$$\begin{Bmatrix} w_{,\xi} \\ w_{,\eta} \end{Bmatrix}_{(0,0)} = \frac{1}{4} \begin{bmatrix} -1 & 1 & 1 & -1 \\ -1 & -1 & 1 & 1 \end{bmatrix} \begin{Bmatrix} w_i^{(4)} \\ w_j^{(4)} \\ w_m^{(4)} \\ w_l^{(4)} \end{Bmatrix} ; \begin{Bmatrix} w_{,\xi} \\ w_{,\eta} \end{Bmatrix}_{(0,0)} = [\mathbf{J}_0] \begin{Bmatrix} w_{,s_4} \\ w_{,q_4} \end{Bmatrix}_{(0,0)} \quad (3.23)$$

Using these derivatives and the local coordinates of the nodes i, j, m, l , the 4 components of the matrix $\mathbf{J}_{0(2 \times 2)}$ - then these of \mathbf{J}_0^{-1} (involving A_4) - lead to the expression of θ_4 . To simplify

writing, let $P_4 = \frac{s_l^{(4)} - s_j^{(4)}}{2A_4}$ and $Q_4 = \frac{s_i^{(4)} - s_m^{(4)}}{2A_4}$

$$\theta_4 = P_4 \langle r_{4X} | r_{4Y} | r_{4Z} \rangle \cdot \begin{Bmatrix} U_{Xi} \\ U_{Yi} \\ U_{Zi} \end{Bmatrix} + Q_4 \langle r_{4X} | r_{4Y} | r_{4Z} \rangle \cdot \begin{Bmatrix} U_{Xj} \\ U_{Yj} \\ U_{Zj} \end{Bmatrix} - Q_4 \langle r_{4X} | r_{4Y} | r_{4Z} \rangle \cdot \begin{Bmatrix} U_{Xm} \\ U_{Ym} \\ U_{Zm} \end{Bmatrix} - P_4 \langle r_{4X} | r_{4Y} | r_{4Z} \rangle \cdot \begin{Bmatrix} U_{Xl} \\ U_{Yl} \\ U_{Zl} \end{Bmatrix} \quad (3.24)$$

The same expression for θ_5 and θ_6 with the index permutation.

Keeping in mind that r_{nX}, r_{nY}, r_{nZ} ($n = 4, 5, 6$) are the projections of the normal on the three faces, is finally got (in the global (X,Y,Z) frame) the matrix $\mathbf{T}_{(3,18)}$ (detailed in the **Appendices**):

$$\begin{Bmatrix} \theta_4 \\ \theta_5 \\ \theta_6 \end{Bmatrix} = [\mathbf{T}] \cdot \{\mathbf{U}_e\} \quad (3.25)$$

$$\{\mathbf{U}_e\}^T = \langle U_{Xi} | U_{Yi} | U_{Zi} | U_{Xj} | U_{Yj} | U_{Zj} | U_{Xk} | U_{Yk} | U_{Zk} | U_{Xl} | U_{Yl} | U_{Zl} | U_{Xm} | U_{Ym} | U_{Zm} | U_{Xn} | U_{Yn} | U_{Zn} \rangle$$

Again, a straightforward method simply gives u_1, u_2, u_3 (of the triangle 1-2-3) using $u_i, u_j, u_k, u_l, u_m, u_n$, and the same goes for v_1, v_2, v_3 by using $v_i, v_j, v_k, v_l, v_m, v_n$:

$$u_1 = \frac{(u_i + u_l)}{2}; u_2 = \frac{(u_j + u_m)}{2}; u_3 = \frac{(u_k + u_n)}{2}; v_1 = \frac{(v_i + v_l)}{2}; v_2 = \frac{(v_j + v_m)}{2}; v_3 = \frac{(v_k + v_n)}{2} \quad (3.26)$$

Thus with equation (3.18) and (3.26), the relation between u_1, u_2, u_3 and $U_{Xi}, U_{Yi}, U_{Zi}, U_{Xj}, \dots, U_{Zn}$ are given by:

$$\begin{aligned} u_1 &= 0.5(xX \cdot U_{Xi} + xY \cdot U_{Yi} + xZ \cdot U_{Zi} + xX \cdot U_{Xl} + xY \cdot U_{Yl} + xZ \cdot U_{Zl}) \\ u_2 &= 0.5(xX \cdot U_{Xj} + xY \cdot U_{Yj} + xZ \cdot U_{Zj} + xX \cdot U_{Xm} + xY \cdot U_{Ym} + xZ \cdot U_{Zm}) \\ u_3 &= 0.5(xX \cdot U_{Xk} + xY \cdot U_{Yk} + xZ \cdot U_{Zk} + xX \cdot U_{Xn} + xY \cdot U_{Yn} + xZ \cdot U_{Zn}) \end{aligned} \quad (3.27)$$

And in a similar way:

$$\begin{aligned} v_1 &= 0.5(yX \cdot U_{Xi} + yY \cdot U_{Yi} + yZ \cdot U_{Zi} + yX \cdot U_{Xl} + yY \cdot U_{Yl} + yZ \cdot U_{Zl}) \\ v_2 &= 0.5(yX \cdot U_{Xj} + yY \cdot U_{Yj} + yZ \cdot U_{Zj} + yX \cdot U_{Xm} + yY \cdot U_{Ym} + yZ \cdot U_{Zm}) \\ v_3 &= 0.5(yX \cdot U_{Xk} + yY \cdot U_{Yk} + yZ \cdot U_{Zk} + yX \cdot U_{Xn} + yY \cdot U_{Yn} + yZ \cdot U_{Zn}) \end{aligned} \quad (3.28)$$

According to equation (3.9), (3.27) and (3.28), the matrix $\bar{\mathbf{B}}^m$ - directly linking (in the local bases $\bar{e}_x, \bar{e}_y, \bar{e}_z$) to the translations of the six nodes of the prism ($\{\mathbf{U}_e\}$) expressed in the global frame -, corresponding to $\bar{\mathbf{B}}^m = \bar{\mathbf{B}}_u^m + \bar{\mathbf{B}}_v^m$ is given in the **Appendices**.

Finally, the membrane strain and the curvature are linked to the displacement DOFs as follows (for the detailed expression see the **Appendices**):

$$\{\boldsymbol{\varepsilon}^m\} = [\bar{\mathbf{B}}^m] \{\mathbf{U}_e\}; \bar{\mathbf{B}}^m = \bar{\mathbf{B}}_u^m + \bar{\mathbf{B}}_v^m; \{\boldsymbol{\kappa}\} = [\bar{\mathbf{B}}^b] \{\mathbf{U}_e\}; \bar{\mathbf{B}}^b = \bar{\mathbf{B}}_w^b + \bar{\mathbf{B}}_0^b; \bar{\mathbf{B}}_0^b = \mathbf{B}_0 \mathbf{T} \quad (3.29)$$

3.2.2 Pinching

In order to introduce the component, the standard 3D formulation of the prism is involved, except that the coordinates of the six nodes ($Z_i, Z_j, Z_k, Z_l, Z_m, Z_n$) are in the local frame (the frame of the triangle 1-2-3) as well as the nodal translations along e_z : $w_i, w_j, w_k, w_l, w_m, w_n$.

At $\xi = \eta = 1/3$ location, the shape functions are given by:

$$[\mathbf{N}] = \langle b\lambda | b\xi | b\eta | t\lambda | t\xi | t\eta \rangle \quad (3.30)$$

With $\lambda = 1 - \xi - \eta$; $b = (1 - \zeta) / 2$; $b = (1 + \zeta) / 2$; $z = \zeta \frac{h}{2}$; $u_{z,z} = \frac{2}{h} u_{z,\zeta}$

Finally,

$$\varepsilon_{zz} = \frac{2}{h} \frac{1}{6} \langle -1 | -1 | -1 | 1 | 1 | 1 \rangle \{ \mathbf{U}_z^e \} = [\mathbf{B}^p] \{ \mathbf{U}_z^e \}; \{ \mathbf{U}_z^e \}^T = \langle w_i | w_j | w_k | w_l | w_m | w_n \rangle \quad (3.31)$$

It can be also written in the global frame like $\varepsilon_{zz} = [\bar{\mathbf{B}}^p] \{ \mathbf{U}_e \}$, provided in **Appendices**.

- *Pinching proper stabilization*

Re-introducing the formulation, the deformation of direction zz can be easily decomposed in a constant component and a term of stabilization q_{zz} .

$$u_{z,z} = \langle \langle \mathbf{b}_z \rangle + \langle \gamma_1 \rangle h_1, z + \langle \gamma_2 \rangle h_2, z \rangle \cdot \{ \mathbf{U}_z^e \} = \varepsilon_{zz}^0 + q_{zz} \quad (3.32)$$

$$q_{zz} = \bar{J}_{33} \langle \langle \gamma_1 \rangle \eta + \langle \gamma_2 \rangle \xi \rangle \{ \mathbf{U}_z^e \} = \bar{J}_{33} (q_{1z} \eta + q_{2z} \xi) \quad (3.33)$$

In order to avoid the problems of locking in pinching, a small multiplier C_p has been taken for the out plane stiffness. Using to give the strain energy: $Q_{zz} = C_p E_z q_{zz}$

$$\iiint q_{zz} Q_{zz} dv = v \langle q_{1z} | q_{2z} \rangle \cdot [\mathbf{D}_{sz}^p] \cdot \langle q_{1z} | q_{2z} \rangle^T \quad (3.34)$$

$$[\mathbf{D}_{sz}^p] = \frac{1}{6} \bar{J}_{33}^2 E_z \begin{bmatrix} 1 & 1/2 \\ 1/2 & 1 \end{bmatrix}; E_z = C_p \frac{1}{2} \sum_{q=1}^{npih} D_{33}^{ep}(\zeta_q) \bar{w}_q \quad (3.35)$$

Where \bar{J}_{33} is the components of matrix $[\mathbf{J}_0^{-1}]$.

3.2.3 Transverse shear

To avoid shear locking problems, a special treatment was needed. The adopted methodology is extracted from Boisse [BOI 94]. It consists in interpolating the transverse shear computed at the apexes of the triangle (1 2 3) of **Figure 3. 5**. These transverse shear strains are obtained assuming that the transverse shear is constant in each side and is equal to the value taken at the center of each side. A similar solution was proposed in the paper of Bathe [LEE 04]

- *C0 shell element*

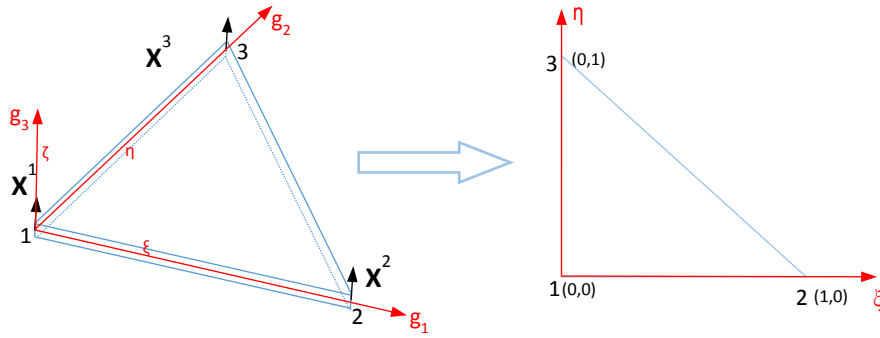


Figure 3. 5: Geometry of C^0 triangular element

C^0 shell element is based on the Mindlin kinematics. It is a triangle element with 3 apex nodes 1, 2, 3, For each node, it has three translational degrees of freedom two rotational dof. The position of an arbitrary point M is defined as:

$$\vec{x}(M) = \vec{x}(H) + \vec{y}(M) \quad (3.36)$$

Where $\vec{x}(H)$ is the position of the associated point of the mid-surface, and $\vec{y}(M)$ is defined based on the pseudonormal \mathbf{X} shown in **Figure 3. 5**.

$\vec{y}(M)$ and \mathbf{X} are interpolated as:

$$\begin{aligned} \vec{x}(H) &= \sum_{i=1}^3 N^i(\xi, \eta) \vec{x}^i \\ \vec{y}(M) &= \sum_{i=1}^3 N^i(\xi, \eta) \vec{y}^i(M) = \sum_{i=1}^3 N^i(\xi, \eta) \frac{h^i}{2} \zeta \vec{X}^i \end{aligned} \quad (3.37)$$

With $\langle N^i(\xi, \eta) \rangle = \langle 1 - \xi - \eta \quad \xi \quad \eta \rangle$

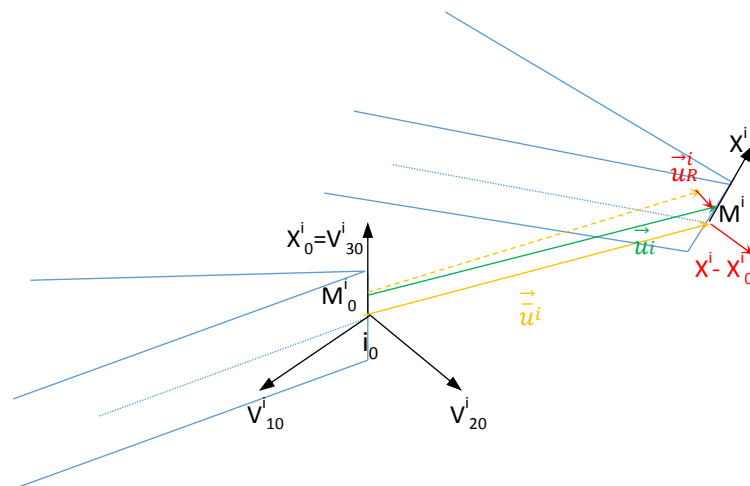


Figure 3. 6: Nodal kinematics

With the same way, the displacement of point M (**Figure 3. 6**) can be written as:

$$\vec{u}(M) = \vec{u}(H) + \vec{u}_R(M) \quad (3.38)$$

Where $\vec{u}(H)$ is the displacement at the associated point in the mid-surface and $\vec{u}_R(M)$ is the displacement given by the pseudonormal rotation.

With

$$\begin{aligned} \vec{u}(M) &= \sum_{i=1}^3 N^i(\xi, \eta) [\vec{u}^i + \vec{u}_R^i(\zeta)] \\ \vec{u}_R &= \frac{h^i}{2} \zeta (\vec{X}^i - \vec{X}_0) = \frac{h_i}{2} \zeta (\vec{R}^i - \vec{I}) \vec{X}_0 \end{aligned} \quad (3.39)$$

\vec{R}^i is the orthogonal tensor which transforms \vec{X}_0^i to \vec{X}^i , \vec{I} is the second-order identity tensor.

An orthogonal frame $(\vec{V}_{10}^i, \vec{V}_{20}^i, \vec{V}_{30}^i)$ is defined at each node with $\vec{V}_{30}^i = \vec{X}_0^i$. Assuming that the rotations in the loading step are small enough and denoting by $\vec{\theta}^i$ the rotation vector at node i ,

$$\begin{aligned} \vec{\theta}^i &= \theta_1^i \vec{V}_{10}^i + \theta_2^i \vec{V}_{20}^i \\ (\vec{R}^i - \vec{I}) \vec{X}_0^i &= \vec{\theta}^i \wedge \vec{X}_0^i \end{aligned} \quad (3.40)$$

The displacement interpolation is given:

$$\vec{u}(M) = \sum_{i=1}^3 N^i(\xi, \eta) \vec{u}^i + \zeta \sum_{i=1}^3 N^i(\xi, \eta) \frac{h^i}{2} (-\theta_1^i \vec{V}_{20}^i + \theta_2^i \vec{V}_{10}^i) \quad (3.41)$$

According to the interpolation of displacement, strain components can be obtained in different covariant frames. Here, the transverse shear is concerned, and is interpolated directly from the values of those components at nodes:

$$\{2\varepsilon_{\alpha 3}\} = \sum_{i=1}^3 N^i(\xi, \eta) \{2\varepsilon_{\alpha 3}^i\} ; \quad \alpha = 1, 2 \quad (3.42)$$

In order to calculate the values of nodal transverse shear strains $\{2\varepsilon_{\alpha 3}\}$, a covariant frame is built from the material co-ordinates along the element edges and the transverse shear strain $\{2\varepsilon_{\alpha 3}^{i*}\}$ in the associated contravariant frame is assumed to be constant along the sides connected to node i .

Firstly, the covariant basis $\vec{f}_1^i, \vec{f}_2^i, \vec{f}_3^i$ associated to contravariant coordinates (r_i^1, r_i^2, r_i^3) is computed at each apex using the natural basis of the prismatic element

$$\vec{g}_1 = \frac{\partial \vec{x}}{\partial \xi}, \vec{g}_2 = \frac{\partial \vec{x}}{\partial \eta}, \vec{g}_3 = \frac{\partial \vec{x}}{\partial \zeta} \quad (\text{see Table 3. 1})$$

$\vec{f}_1^1 = \vec{g}_1, \vec{f}_2^1 = \vec{g}_2$	$\vec{f}_1^2 = -\vec{g}_1 + \vec{g}_2, \vec{f}_2^2 = -\vec{g}_1$	$\vec{f}_1^3 = -\vec{g}_2, \vec{f}_2^3 = -\vec{g}_2 + \vec{g}_1$
$r_1^1 = \xi, r_2^1 = \eta$	$r_1^2 = \eta, r_2^2 = 1 - \xi - \eta$	$r_1^3 = 1 - \xi - \eta, r_2^3 = \xi$
$[D^1] = \begin{bmatrix} 1 & 0 \\ 0 & 1 \end{bmatrix}$	$[D^2] = \begin{bmatrix} 0 & -1 \\ 1 & -1 \end{bmatrix}$	$[D^3] = \begin{bmatrix} -1 & 1 \\ -1 & 0 \end{bmatrix}$

Table 3. 1: Definition of the two covariant basis

The transverse shear strain components $\varepsilon_{\alpha 3}^{i*}$ in $(\vec{f}_i^1, \vec{f}_i^2, \vec{f}_i^3)$ along the sides can be expressed as:

$$\varepsilon_{\alpha 3}^{i*} = \frac{1}{2} \left[\left(\frac{\partial \vec{u}}{\partial \zeta} \right)_m \cdot (\vec{f}_{i\alpha 0})_m + \left(\frac{\partial \vec{u}}{\partial r_{i\alpha}} \right)_m \cdot (\vec{g}_{30})_m \right]; \quad \alpha = 1, 2 \quad m = 4, 5, 6 \quad (3.43)$$

Where $\left(\frac{\partial \vec{u}}{\partial \zeta} \right)_m$ is related to the displacement of the point at the middle of the nodes (i, i+1)

$$\left(\frac{\partial \vec{u}}{\partial \zeta} \right)_m = \frac{1}{2} \left[\left(\frac{\partial \vec{u}}{\partial \zeta} \right)_i + \left(\frac{\partial \vec{u}}{\partial \zeta} \right)_{i+1} \right] = \frac{1}{4} \left[h^i (-\theta_1^i \vec{V}_{20}^i + \theta_2^i \vec{V}_{10}^i) + h^{i+1} (-\theta_1^{i+1} \vec{V}_{20}^{i+1} + \theta_2^{i+1} \vec{V}_{10}^{i+1}) \right] \quad (3.44)$$

And

$$\begin{aligned} \left(\frac{\partial \vec{u}}{\partial r_1^i} \right)_m &= \left(\sum_{i=1}^3 \frac{\partial N^i}{\partial \zeta} \vec{u}^i \frac{\partial \zeta}{\partial r_1^i} + \sum_{i=1}^3 \frac{\partial N^i}{\partial \eta} \vec{u}^i \frac{\partial \eta}{\partial r_1^i} \right)_m = \frac{\vec{u}^{i+1} - \vec{u}^i}{r_1^{i+1} - r_1^i} = \vec{u}^{i+1} - \vec{u}^i \\ \left(\frac{\partial \vec{u}}{\partial r_2^i} \right)_m &= \vec{u}^{i-1} - \vec{u}^i \end{aligned} \quad (3.45)$$

The nodal transverse shear strain in $(\vec{f}_i^1, \vec{f}_i^2, \vec{f}_i^3)$ is permitted to be transformed with the expressions detailed in [BOI 94] by the following form:

$$\{2\varepsilon_{\alpha 3}^{i*}\} = [C^i] \{\mathbf{u}_n^e\}; \quad \{2\varepsilon_{\alpha 3}^i\} = [D^i] \{2\varepsilon_{\alpha 3}^{i*}\} \quad (3.46)$$

$$\{2\varepsilon_{\alpha 3}\} = \sum_{i=1}^3 N^i(\xi, \eta) [D^i] [C^i] \{\mathbf{u}_n^e\} \quad (3.47)$$

Therefore, the transverse shear strain components at the barycenter of the triangle are interpolated and re-expressed in function of the DOFs of the triangle:

$$\begin{bmatrix} 2\varepsilon_{xz} \\ 2\varepsilon_{yz} \end{bmatrix} = \begin{bmatrix} \overline{J}_{11} & \overline{J}_{12} \\ \overline{J}_{21} & \overline{J}_{22} \end{bmatrix} \begin{bmatrix} 2\varepsilon_{13} \\ 2\varepsilon_{23} \end{bmatrix} = \begin{bmatrix} \overline{J}_{11} & \overline{J}_{12} \\ \overline{J}_{21} & \overline{J}_{22} \end{bmatrix} \sum_{i=1}^3 N^i(\xi, \eta) [D^i] [C^i] \{\mathbf{u}_n^e\} \quad (3.48)$$

Where \overline{J}_{ij} corresponds to the general term of the matrix $[J]^{-1}$ (inverse of the Jacobian matrix). $\{\mathbf{u}_n^e\}^T = \langle u^1, v^1, w^1, \theta_1^1, \theta_2^1, u^2, v^2, w^2, \theta_1^2, \theta_2^2, u^3, v^3, w^3, \theta_1^3, \theta_2^3 \rangle$

- **Linking the triangle to the prism**

Like in the in-plan shear part, the passage of this triangular element to the prismatic element can be expressed by the displacements of the nodes of the prism.

The displacement of M (arbitrary point in the edge i of prism) $\overline{u}_M^i, i = 1, 2, 3$ can be interpolated by the displacements of the two nodes (top and bottom) with relation:

$$\overline{u}_M^i = \frac{1+\xi}{2} \overline{u}_t + \frac{1-\xi}{2} \overline{u}_b = \frac{1}{2} (\overline{u}_t + \overline{u}_b) + \frac{1}{2} \xi (\overline{u}_t - \overline{u}_b) = \overline{\overline{u}}^i + \overline{u}_R^i \quad (3.49)$$

Where $\overline{\overline{u}}^i$ is the displacement of point i ($i=1,2,3$), \overline{u}_R^i is the displacement due to the relative rotation of the prismatic edge which can also be described:

$$\overline{u}_R^i = \frac{h^i}{2} \xi (\overline{\theta}^i \wedge \overline{\mathbf{X}}_0^i) \text{ with } \overline{\theta}^i = \theta_1^i \overline{\mathbf{V}}_{10}^i + \theta_2^i \overline{\mathbf{V}}_{20}^i \quad (3.50)$$

The rotations θ_1^i, θ_2^i of the points $i=1,2,3$ can be expressed in function of the nodal displacements of the prism with the equation:

$$\theta_1^i = -\frac{1}{2h^i} (\overline{u}_t - \overline{u}_b) \overline{\mathbf{V}}_{20}^i, \theta_2^i = \frac{1}{2h^i} (\overline{u}_t - \overline{u}_b) \overline{\mathbf{V}}_{10}^i \quad (3.51)$$

With the definition:

$$h^i = \left\| \overline{\mathbf{x}}^t - \overline{\mathbf{x}}^b \right\|, \overline{\mathbf{X}}_0^i = \frac{\overline{\mathbf{X}}_0^t - \overline{\mathbf{X}}_0^b}{\left\| \overline{\mathbf{X}}_0^t - \overline{\mathbf{X}}_0^b \right\|} \quad (3.52)$$

$$\overline{\mathbf{V}}_{30}^i = \frac{\overline{\mathbf{x}}^t - \overline{\mathbf{x}}^b}{h^i}, \overline{\mathbf{V}}_{20}^i = \frac{\overline{\mathbf{V}}_{30}^i \wedge (\overline{\mathbf{x}}^{i+1} - \overline{\mathbf{x}}^i)}{\left\| \overline{\mathbf{V}}_{30}^i \wedge (\overline{\mathbf{x}}^{i+1} - \overline{\mathbf{x}}^i) \right\|}, \overline{\mathbf{V}}_{10}^i = \overline{\mathbf{V}}_{20}^i \wedge \overline{\mathbf{V}}_{30}^i$$

Hence, the relation of the displacements of triangular element and the displacements of prism is linked with a transformation matrix $[\mathbf{T}_{ts}]$ detailed in the **Appendices**:

$$\{\mathbf{u}_n^e\} = [\mathbf{T}_{ts}] \{\mathbf{u}_e\} \quad (3.53)$$

$$\{\mathbf{u}_e\}^T = \langle u^i, v^i, w^i, u^j, v^j, w^j, u^k, v^k, w^k, u^l, v^l, w^l, u^m, v^m, w^m, u^n, v^n, w^n \rangle$$

Combining the equations (3.48) and (3.53), the transverse shear components of element SB6Y18 is obtained in the global frame:

$$\begin{bmatrix} 2\varepsilon_{xz} \\ 2\varepsilon_{yz} \end{bmatrix} = \begin{bmatrix} \overline{J}_{11} & \overline{J}_{12} \\ \overline{J}_{21} & \overline{J}_{22} \end{bmatrix} \sum_{i=1}^3 N^i(\xi, \eta) [\mathbf{D}^i] [\mathbf{C}^i] [\mathbf{T}_{ts}] [\mathbf{R}] \{\mathbf{U}_e\} \quad (3.54)$$

$$\text{or } \begin{bmatrix} 2\varepsilon_{xz} \\ 2\varepsilon_{yz} \end{bmatrix} = [[\mathbf{B}_{c0}] + \eta \cdot [\mathbf{B}_{c1}] + \xi \cdot [\mathbf{B}_{c2}]] \cdot \begin{Bmatrix} \{\mathbf{U}_x^e\} \\ \{\mathbf{U}_y^e\} \\ \{\mathbf{U}_z^e\} \end{Bmatrix} \quad (3.55)$$

$[\mathbf{B}_{c0}]$ represents the gradient matrix without stabilization. The other two matrixes $[\mathbf{B}_{c1}]$, $[\mathbf{B}_{c2}]$ permit to stabilize the stiffness matrix due to transverse shear if necessary. By introducing the Reissner's weight function, the distribution of the transverse shear along the thickness can be obtained:

$$\begin{bmatrix} 2\varepsilon_{xz} \\ 2\varepsilon_{yz} \end{bmatrix} = g(\zeta)[\mathbf{B}_{c0}] \cdot \begin{Bmatrix} \{\mathbf{U}_x^e\} \\ \{\mathbf{U}_y^e\} \\ \{\mathbf{U}_z^e\} \end{Bmatrix}; g(\zeta) = 5/4(1-\zeta^2) \quad (3.56)$$

3.2.4 Final assessment

Finally, the global gradient matrix \mathbf{B} is:

$$\begin{Bmatrix} \varepsilon_{xx} \\ \varepsilon_{yy} \\ \frac{2 \cdot \varepsilon_{xy}}{2} \\ \varepsilon_{zz} \\ \frac{2 \cdot \varepsilon_{xz}}{2} \\ \frac{2 \cdot \varepsilon_{yz}}{2} \end{Bmatrix} = [\mathbf{B}] \cdot \{\mathbf{U}_e\}; \mathbf{B} = \begin{bmatrix} \bar{\mathbf{B}}^m + z \cdot \bar{\mathbf{B}}^b \\ \langle \bar{\mathbf{B}}^p \rangle \\ \bar{\mathbf{B}}^{ts} \end{bmatrix} \cdot \{\mathbf{U}_e\} \quad (3.57)$$

While writing stresses and strains in the following order:

$\langle \varepsilon_{xx} \mid \varepsilon_{yy} \mid \varepsilon_{zz} \mid 2\varepsilon_{xy} \mid 2\varepsilon_{xz} \mid 2\varepsilon_{yz} \rangle$, $\langle \sigma_{xx} \mid \sigma_{yy} \mid \sigma_{zz} \mid \sigma_{xy} \mid \sigma_{xz} \mid \sigma_{yz} \rangle$, in the simplest case of an isotropic elastic case, and to ensure a plane stress state while keeping a non-zero stress σ_{zz} , the constitutive matrix \mathbf{D} is:

$$[\mathbf{D}] = \begin{bmatrix} \bar{\lambda} + 2\mu & \bar{\lambda} & 0 & & & \\ \bar{\lambda} & \bar{\lambda} + 2\mu & 0 & & & \\ 0 & 0 & E & & & \\ & & & \mu & & \\ & & & & \frac{5}{6}\mu & \\ & & & & & \frac{5}{6}\mu \end{bmatrix}; \quad \bar{\lambda} = \frac{\nu \cdot E}{(1-\nu^2)} \neq \lambda = \frac{\nu \cdot E}{(1-2\nu)(1+\nu)}$$

$$\mu = \frac{E}{2(1+\nu)} \quad (3.58)$$

A major drawback of this kind of behavior appears for elastoplasticity where, this time, there is coupling between normal effects and in plane phenomena. For instance, this can result on prohibitive contact forces due to an overestimated elastic prediction. Using the elements SC6R of the Abaqus software, any attempt to reduce the thickness by applying normal forces conduct to non-zero unexpected in plane stresses. In order to remedy this shortcoming a seventh node 'o' is added at the center ($\xi = \eta = 1/3$ and $\zeta = 0$) endowed with a single degree of freedom w_o : a

translation carried by \vec{e}_z , the normal to the plane 1-2-3. This adopted strategy is the same that was performed for a quadrilateral element in [BAS 12].

3.3 Solid-shell element SB7Y19: Supplementary degree of freedom

3.3.1 Full 3D behavior law

An extra degree of freedom is dedicated to ensure that the bending is correct while using a real three dimensional behavior law, that is with couplings between the x, y, and z directions. For this, it is imperative that the normal stress σ_{zz} is linear through the thickness and not constant. That is allowed, precisely, by the additional translation w_o normal to the mid-surface (shown in **Figure 3. 7**).

The added central node permits to describe a non-constant distribution of stress through the thickness with correct stress values on the top and bottom of the element in any case with the loading condition, which is necessary during the forming process.

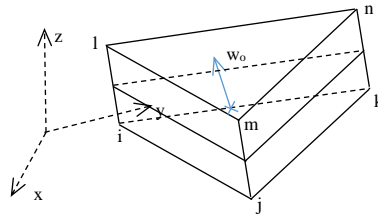


Figure 3. 7: Supplementary node and its dof. at the central of the element

The formulations of the membrane and bending effects as well as the formulations of the stabilizations are those of the 6 nodes prism. Only the component of normal strain ϵ_{zz} is changed. The evolution of the normal displacement (in the direction of the thickness h) is parabolic in z and it is assumed such that:

$$w(z) = w(0) + \left(\frac{2z^2}{h^2} - \frac{z}{h}\right)w^- - \frac{4z^2}{h^2}w_o + \left(\frac{2z^2}{h^2} + \frac{z}{h}\right)w^+ \quad (3.59)$$

$$\text{Where } w^+ = \frac{1}{3}(w_l + w_m + w_n); w^- = \frac{1}{3}(w_i + w_j + w_k)$$

After the derivation of the assumed displacement, the deformation can be expressed as:

$$\epsilon_{zz} = \frac{1}{h}(w^+ - w^-) + \frac{4z}{h^2}(w^+ + w^- - 2w_o) \quad (3.60)$$

Both for ease of interpretation, convenience to find nil forces at nodes on the opposite side (see 3.3.2) and because the value is generally very low (without significant influence on the kinetic energy for explicit dynamic time scheme), the “relative” translation w_o^* is used rather than the degree of freedom w_o :

$$w_o^* = w_o - \frac{1}{2}(w^+ + w^-) \quad (3.61)$$

The expression of ϵ_{zz} becomes therefore at $z = \zeta \frac{h}{2}$:

$$\varepsilon_{zz} = \frac{1}{h}(w^+ - w^-) - \frac{8z}{h^2}w_o^* = \frac{1}{h}(w^+ - w^- - 4\zeta \cdot w_o^*) \quad (3.62)$$

The matrix $\bar{\mathbf{B}}_{(1x19)}^p$ is obtained by adding one component to the matrix $\bar{\mathbf{B}}_{(1x18)}^p$ of the SB6γ18 finite element previously detailed in the **Appendices**.

Adding this additional degree of freedom – which makes the component of normal strain linear – is sufficient to allow the use of a fully 3D law while obtaining good results in bending. For linear isotropic elasticity, the constitutive matrix D is:

$$[\mathbf{D}] = \begin{bmatrix} \lambda + 2\mu & \lambda & \lambda & & & \\ \lambda & \lambda + 2\mu & \lambda & & & \\ \lambda & \lambda & \lambda + 2\mu & & & \\ & & & \mu & & \\ & & & & \frac{5}{6}\mu & \\ & & & & & \frac{5}{6}\mu \end{bmatrix} \quad (3.63)$$

3.3.2 Computing external nodal forces due to a normal pressure

Pressure acting on the face i-j-k is P^- ($P^- > 0$), and the pressure acting on the face l-m-n is P^+ ($P^+ < 0$). The objective is to express equivalent external nodal force $F_i, F_j, F_k, F_l, F_m, F_n$, and F_o^*

$$F_i \cdot \hat{w}_i + F_j \cdot \hat{w}_j + F_k \cdot \hat{w}_k + F_l \cdot \hat{w}_l + F_m \cdot \hat{w}_m + F_n \cdot \hat{w}_n + F_o^* \cdot \hat{w}_o^* = (p^+ + p^-) \cdot A \cdot \frac{1}{2}(\hat{w}^+ + \hat{w}^-) + \iiint \hat{\varepsilon}_{zz} \cdot \sigma_{zz} \cdot dv \quad (3.64)$$

It is known that:

$$\varepsilon_{zz} = \frac{1}{h}(\hat{w}^+ - \hat{w}^- - 4\zeta \cdot \hat{w}_o^*) ; z = \zeta \frac{h}{2} \quad (3.65)$$

With an elastic material (the nonlinear material case will be discussed in section 5.3.3), the waited stress component σ_{zz} is:

$$\sigma_{zz} = p^+ \cdot \frac{1}{2}(1 + \zeta) - p^- \cdot \frac{1}{2}(1 - \zeta) ; \begin{cases} \sigma_{zz} = p^+ & : \text{for } z = h/2 \\ \sigma_{zz} = -p^- & : \text{for } z = -h/2. \end{cases} \quad (3.66)$$

Then

$$\begin{aligned} \iiint \hat{\varepsilon}_{zz} \cdot \sigma_{zz} \cdot dx \cdot dy \cdot dz &= \iiint \hat{\varepsilon}_{zz} \cdot \sigma_{zz} \cdot \det \mathbf{J}_c \cdot d\xi \cdot d\eta \cdot d\zeta = \\ \frac{1}{h} \int_{-1}^1 (\hat{w}^+ - \hat{w}^- - 4\zeta \cdot \hat{w}_o^*) (p^+ \cdot \frac{1}{2}(1 + \zeta) - p^- \cdot \frac{1}{2}(1 - \zeta)) d\zeta \cdot \int_0^{1-\xi} \int_0^{1-\xi} d\eta \cdot d\xi &= \\ \frac{1}{2}(p^+ - p^-) A \cdot (\hat{w}^+ - \hat{w}^-) - \frac{2}{3}(p^+ + p^-) A \cdot \hat{w}_o^* \end{aligned} \quad (3.67)$$

Combining equation (3.64) and (3.67)

$$\Rightarrow F_i \cdot \hat{w}_i + F_j \cdot \hat{w}_j + F_k \cdot \hat{w}_k + F_l \cdot \hat{w}_l + F_m \cdot \hat{w}_m + F_n \cdot \hat{w}_n + F_o^* \cdot \hat{w}_o^* \quad (3.68)$$

$$= p^- . A . \hat{w}^- + p^+ . A . \hat{w}^+ - \frac{2}{3} (p^+ + p^-) . A . \hat{w}_o^*$$

Where, in the direction \vec{e}_z , normal to the plane 1-2-3:

$$F_i = F_j = F_k = \frac{1}{3} p^- . A, F_l = F_m = F_n = \frac{1}{3} p^+ . A, F_o^* = -\frac{2}{3} (p^+ + p^-) . A \quad (3.69)$$

In the case of a pressure acting on the face i-j-k, the equivalent nodal forces: F_l, F_m, F_n are zero. It remains to express F_i, F_j, F_k and F_o^* . Hence in the direction \vec{e}_z , but with $p < 0$:

$$F_i = F_j = F_k = \frac{1}{3} p^- . A, F_o^* = -\frac{2}{3} p^- . A \quad (3.70)$$

In the case of a pressure acting on the face l-m-n, the equivalent nodal forces: F_i, F_j, F_k are zero. It remains to express F_l, F_m, F_n and F_o^* . Hence in the direction \vec{e}_z , but with $p < 0$:

$$F_l = F_m = F_n = \frac{1}{3} p^+ . A, F_o^* = -\frac{2}{3} p^+ . A \quad (3.71)$$

NB: In the above expressions, the logic of a shell element has been met: the area is that of the 1-2-3 triangle, $p > 0$ indicates a pressure acting on the “bottom” side while $p < 0$ corresponds to a pressure acting on the “top” face. It may seem at a first look that the balance is not ensured, but it is because w_o^* is a “relative” translation. By taking w_o , the balance is correct but not nil forces appear at all nodes (i, j, k, l, m, n) even if the pressure acts on one side (lower or upper side).

3.4 Validation and numerical examples

In this section, in order to test the performance of the developed element, severe benchmark problems consisting of linear and non-linear tests that can be found in literatures are computed with a FEM implicit code developed in Matlab and an explicit code compiled by Fortran90. The results solved by other solid-shell elements and triangular shell elements in literatures are given for comparison.

3.4.1 Linear tests

- *Linear elementary bending tests*

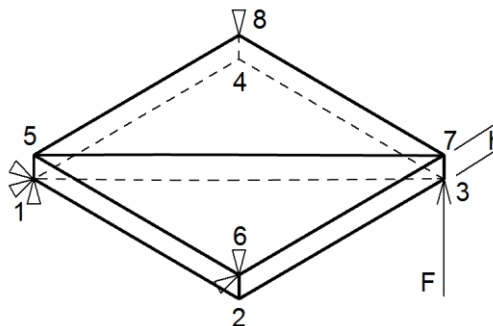


Figure 3. 8: Bending test

The first simple test has been done is the bending test (**Figure 3. 8**) of a square plate (length = 100, thickness $h = 1$) with its three corners (1, 6 and 8) simply supported. Material data are:

200000 MPa $\nu = 0.3$. A concentrated load ($F = 1$) is applied to the fourth one. Useful analytical results are: $\sigma_{xx} = \sigma_{yy} = 0$; and $\sigma_{xy} = -3$ (top), $\sigma_{xy} = 3$ (bottom) and normal deflection $U_{z3} = 0.39$ mm.

As is shown in **Table 3. 2**, all the proposed solid shell elements (SB6 γ 18, SB7 γ 19) give the exact theoretical results. While the hexahedral solid shell SC6R implemented in Abaqus code gives a normal deflection $U_{z3} = 0.3889$ (along 'z' axis) and the in-plane stresses (along 'x', 'y') are: $\sigma_{xx} = \sigma_{yy} = 2.10 \cdot 10^{-4}$ and $\sigma_{xy} = -2.993$ (top), $\sigma_{xy} = 2.986$ (bottom), while the usual solid finite element C3D8 gives $U_{z3} = 0.2230$ and wrong stresses.

	SB6 γ 18	SB7 γ 19	SC6R	C3D8	Ref
U_{z3}	0.39	0.39	0.3889	0.2230	0.39
$\sigma_{xx} = \sigma_{yy}$	0	0	2.10-4		0
$\sigma_{xy}(\text{top})$	-3	-3	-2.993	wrong	-3
$\sigma_{xy}(\text{bottom})$	3	3	2.986		3

Table 3. 2: Comparison of bending test with different elements

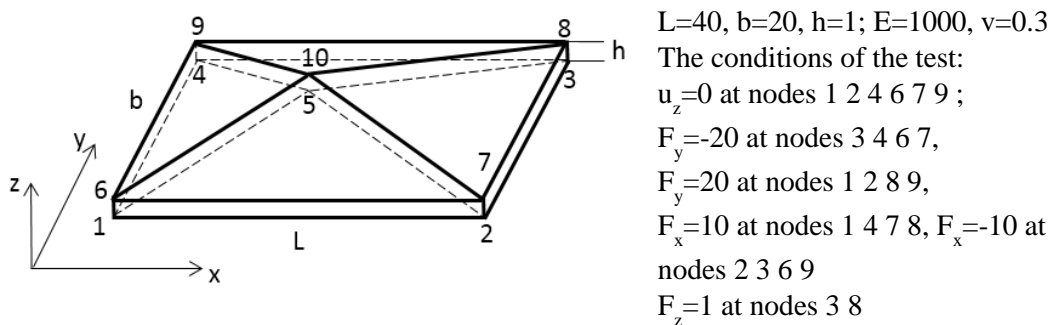


Figure 3. 9: Patch test

Another simple test is the patch test, with its definition in Reference [BAT 82], a theoretical constant state of bending moments all over the plate is given by its boundary conditions and concentrated loads (**Figure 3. 9**), the exact displacements at points 3, 5, 8 and 10 can be obtained with the proposed SB6 γ 18 and SB7 γ 19 elements, the **Table 3. 3** presents the comparison between the results of element SC6R in Abaqus and the proposed elements, from which, it can be seen that the proposed elements obtain the correct results.

	SB6 γ 18	SB7 γ 19	SC6R	Ref
$W3=W8$	-12,48	-12,48	-12,5334	-12,48
$W5=W10$	-1,62	-1,62	-1,62896	-1,62

Table 3. 3: Patch test: Displacements of the considering points

- Circular clamped plate

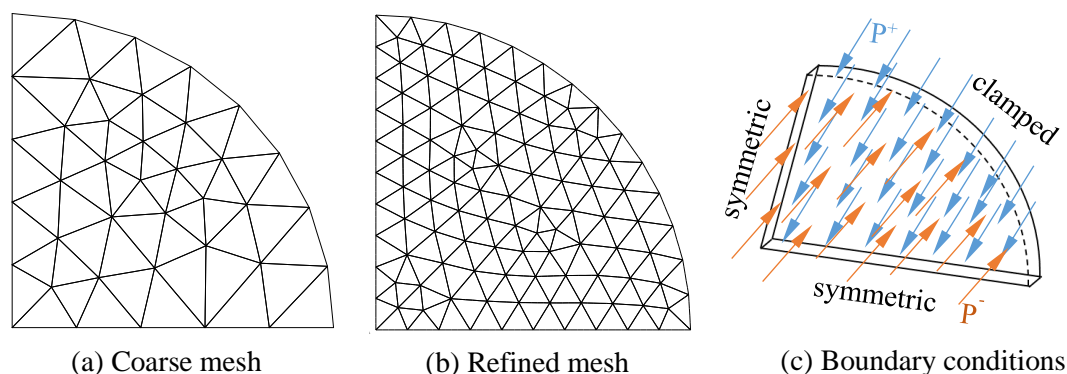


Figure 3. 10: Clamped circular plate (an only quarter due to symmetries)

A circular plate –the boundary of which is clamped– is subjected to a normal pressure. The useful data are: radius $R = 100$ mm; thickness = 1 mm; isotropic material: $E = 200000$ MPa, Poisson's ratio $\nu = 0.3$; uniform pressure normal to the plane $p = 0.01172$ N/mm². This value corresponds to a theoretical displacement of the plate center (C in **Figure 3. 10**) $U_C = 1$ mm according to Kirchhoff's theory and to Mindlin's theory (1.005) since this plate is a thin plate.

Coarse mesh	SB6 γ 18	SB7 γ 19	SC6R	DKT12	Ref
U_c	0,924083	0,924083	0,86347	1,1	1
σ_{zz} top	-0,00586058	0	0	0	0
σ_{zz} bottom	-0,00586058	-0,01172	0	0	-0,01172
Refined mesh					
U_c	1,0044	0,995576	0,99339	1.027	1
σ_{zz} top	-0,00586982	0	0	0	0
σ_{zz} bottom	-0,00586982	-0,01172	0	0	-0.01172

Table 3. 4: Center displacement and stress component normal to the mid-plane

Two different density of mesh have been done. From the **Table 3. 4** which contains the results of the proposal solid shell elements (SB6 γ 18, SB7 γ 19), solid shell element of Abaqus SC6R, and a classical Kirchhoff shell elements DKT12, with a supplementary node, the dof of which allows to employ 3D elasticity laws but not only, owing to this node, a part of the nodal forces equivalent to a normal pressure is prescribed on the extra node in order to get the proper normal stress repartition (section 3.3.2). In this case, the normal stress component (σ_{zz}) of SB7 γ 18 varies through the thickness from the value $\sigma_{zz} = -p = -0.01172$ ('p': pressure) to the value $\sigma_{zz} = 0$.

In order to verify the advantage of the developed solid-shell element with the normal stress component (σ_{zz}), two other clamped circular plate tests with different types of pressure have been employed.

Case 1: A pressure $P^+ = -0.01172$ is applied on the top surface, and a pressure $P^- = 0.01172$ is applied on the bottom surface (**Figure 3. 10**: Clamped circular plate (an only quarter due to symmetries) (c))

Coarse mesh	SB6 γ 18	SB7 γ 19	SC6R	Ref
σ_{zz} top	-0,01172	-0,01172	0	-0,01172
σ_{zz} bottom	-0,01172	-0,01172	0	-0,01172
Refined mesh				
σ_{zz} top	-0,01172	-0,01172	0	-0,01172
σ_{zz} bottom	-0,01172	-0,01172	0	-0,01172

Table 3. 5: Center displacement and stress component in case 1

Case 2: A pressure $P^+ = -0.5 * 0.01172$ is applied on the top surface, and a pressure $P^- = 1.5 * 0.01172$ is applied on the bottom surface

Coarse mesh	SB6 γ 18	SB7 γ 19	SC6R	Ref
Uc top	0.84288	0.92427	0.88854	1
Uc bottom	0.84288	0.92427	0.88854	1
σ_{zz} top	-0,01172	-0,01172*0.5	0	-0,01172*0.5
σ_{zz} bottom	-0,01172	-0,01172*1.5	0	-0,01172*0.5
Refined mesh				
Uc top	0.98818	0.99580	0.99339	1
Uc bottom	0.98818	0.99580	0.99339	1
σ_{zz} top	-0,01172	-0,01172*0.5	0	-0,01172*0.5
σ_{zz} bottom	-0,01172	-0,01172*1.5	0	-0,01172*0.5

Table 3. 6: Center displacement and stress component in case 2

According to these two supplementary clamped circular plate tests, it can be concluded that the proposed solid shell element with the added central node permits to describe a non-constant distribution of stress through the thickness with correct stress values on the top and bottom of the element in any case with the loading condition, which is necessary during the forming process.

- *Twisted beam*

The 90°-twisted beam is a linear problem intended to assess the effect of warping on the performance of any kind of shell element. The undeformed beam twisted by 90° with a 12 by 2 mesh is shown in **Figure 3. 11**. The length of the beam is 12.0 (along Z axis), width 1.1, thickness 0.32, elasticity modulus $2.9e7$, Poisson ratio 0.22. If an “in-plane” force P ($P=1$) is applied on the point C along Y direction (**Figure 3. 11** (a)), the analytical resulting displacement $U_Y(C) = 5.424 \times 10^{-3}$. If an “out-of-plane” force Q ($Q=1$) is prescribed along X, the theoretical displacement $U_X(C) = 1.754 \times 10^{-3}$.

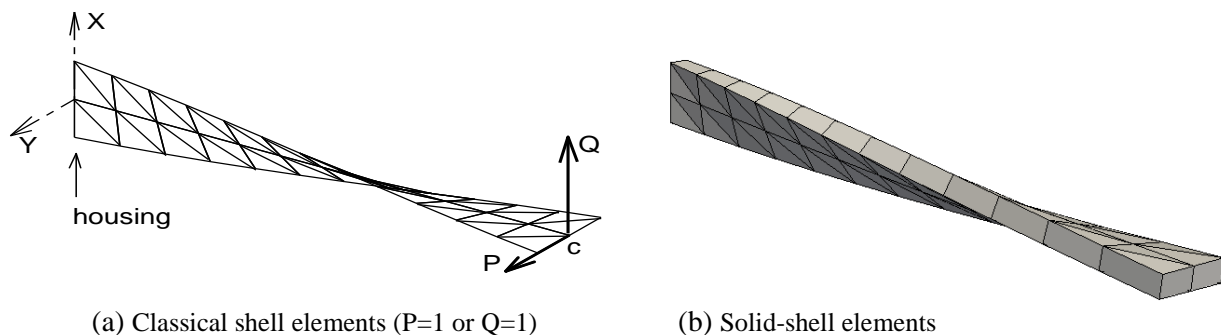


Figure 3. 11: Twisted beam

The results relating to a 12 by 2 mesh (**Figure 3. 11**) and a 48 by 8 mesh of different triangular shell elements and the solid shell elements are given in **Table 3. 7**. By comparing numerical values to analytical ones [SMO 99], it can be easily noted the solid shell elements are not prone to warping, nevertheless prismatic elements exhibit stiffer results. Like all the previous examples, this one shows tiny differences between the results respectively given by the elements under plane stress state and with a complete 3D constitutive law (with the additional DOF).

'In-plane "P"	SB6 γ 18	SB7 γ 19	SC6R	DKT18	Morley	S3	Ref
Mesh 12x2	0,99269912	0,99252581	0,99419248	0,9821	0,993	0,9749	1
Mesh 48x8	0,99529867	0,99524336	0,99693953	0,9935	0,995	0,988	1
Out-of-plane "Q"							
Mesh 12x2	0,8422691	0,84082098	1,05292474	0,8352	0,8449	0,8312	1
Mesh 48x8	0,97696693	0,97605473	0,99149943	0,9743	0,9755	0,9709	1

Table 3. 7: Twisted beam: Loading point displacement

- *Pinched hemisphere with a 18° hole*

As is shown in **Figure 3. 12** (a), a hemispherical and thin shell (radius $R = 10$, thickness $h = 0.04$), with an 18° circular cutout at its pole, is subjected to an inward force ($F_y = -2$) and to an outward force ($F_x = 2$). Young's modulus $E=6.825e7$ and Poisson's ratio $\nu=0.3$ are the useful characteristics of the isotropic elastic material. Owing to symmetry, one-quarter of the shell is modeled (**Figure 3. 12** (b)). The loading points displacements are compared to the reference result of Simo: $U_x = -U_y = 0.093$ [MAC 85]. It can be noted that other authors propose another reference value: 0.094 [CAR 09].

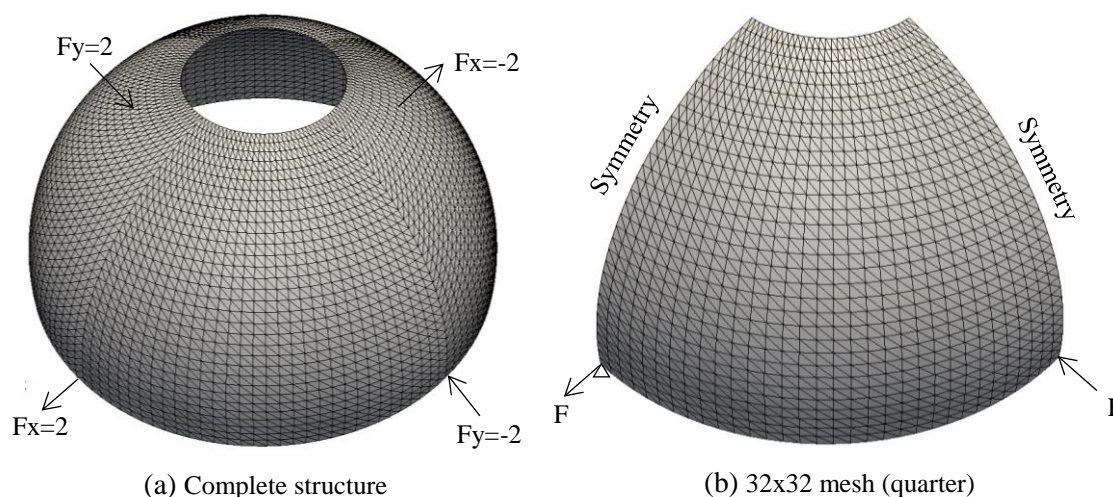


Figure 3. 12: Pinched hemispherical shell

For four meshes (4x4), (8x8), (16x16), (32x32), the displacements under the loads are compared with the reference result of Simo in **Figure 3. 13** (a), it can be seen that elements SB6 γ 18 and SB7 γ 19 are less stiff and slightly more precise than the Abaqus element SC6R.

	SB6r18	SB7r19	SC6R	DKT18	Morley	S3	Ref
Mesh 4x4	0,060870	0,059780	0,040690	0,09804	0,10961	0,08196	
Mesh 8x8	0,089640	0,089238	0,088650	0,09463	0,1	0,08367	0,093/0,094
Mesh 16x16	0,093820	0,093665	0,092260	0,09296	0,09522	0,08652	
Mesh 32x32	0,093430	0,093390	0,092820				

Table 3. 8: Pinched hemispherical: Loading point displacement for different type of elements

For this test, the sensitivity of coefficient for pinching has been studied. The curve in the **Figure 3. 13** (b) shows the displacement of loading points relative to the reference result as a function of the coefficient for pinching (C_p), for a fixed 16x16 mesh, the curve shows satisfactory convergence when $C_p \leq 10^{-2}$. This analysis was done in all of the tests presented in this thesis. With the exception of the hemisphere, none of them showed any sensitivity to the given value P_c . But all the calculations were also conducted with very low C_p values (10^{-4}) without showing the type of hourglass problem.

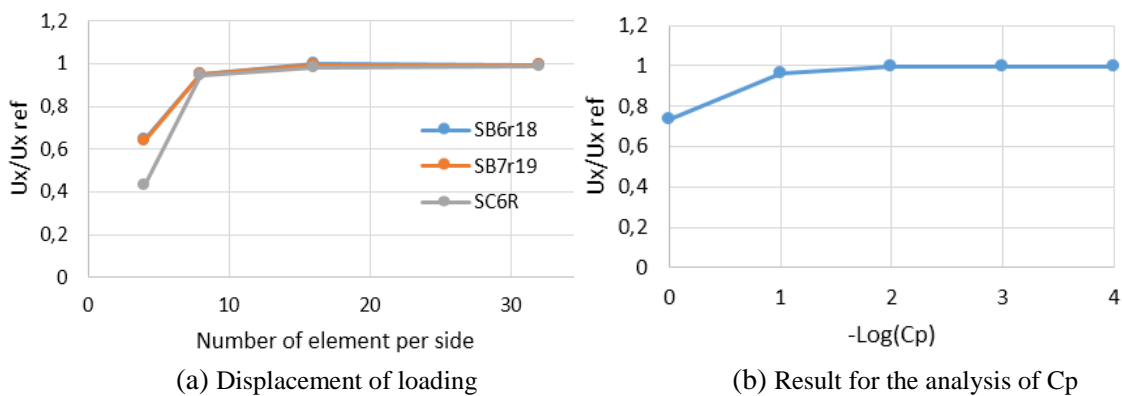


Figure 3. 13: Convergence of the displacement for the pinched hemisphere

- *The pinched cylinder with free end*

The pinched cylinder problem shown in **Figure 3. 14** was also frequently analyzed to test shell elements.

The useful data are:

- Cylinder: length $L = 10.35$, radius $R = 4.953$, thickness $h = 0.094$;
- Material: $E = 10.5E6$ and $\nu = 0.3125$;
- Load: Two equal and opposite forces $F = 100$.

Due to symmetries, only an eighth of a pinched cylinder (**Figure 3. 14** (b)) is meshed with different discretization. The vertical displacement of point C, which can be compared to the usually accepted solution: 0.1139, is shown in the **Table 3. 9**. It can be noted that, the accuracy of the proposed elements and the others are nearly equivalent in this test.

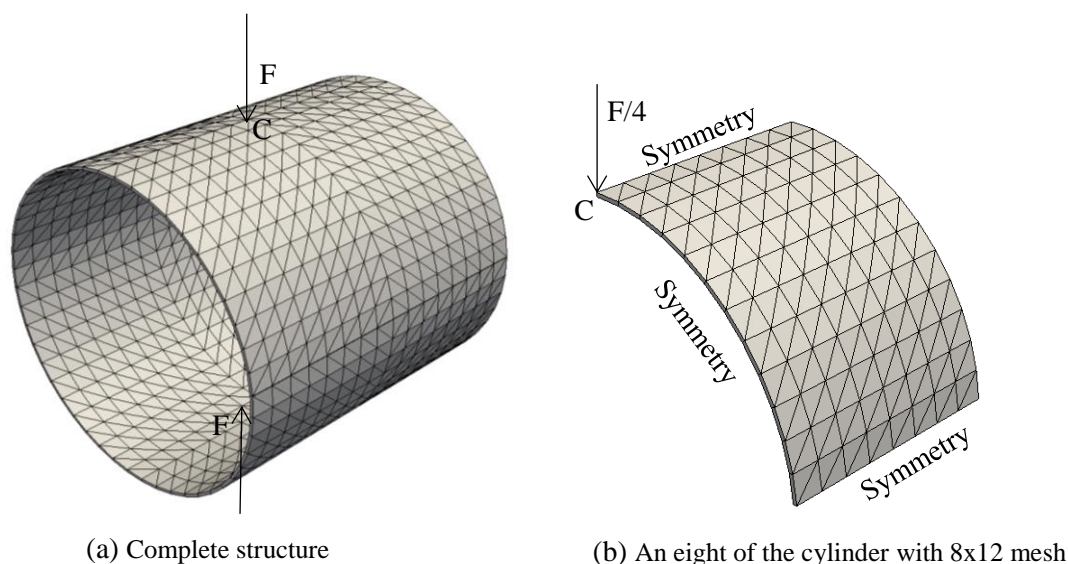


Figure 3. 14: Pinched cylinder with free ends.

	SB6r18	SB7r19	SC6R	DKT18	Morley	S3	C0	DKT12
Mesh 4x4	0,97827919	0,975505	0,897278	0,504	1,176	1,043	0,504	1,176
Mesh 4x6	1,01693591	1,048104	0,937902	0,756	1,13	1,015	0,756	1,13
Mesh 6x6	0,99736611	1,027752	0,945250	0,751	1,092	1,017	0,751	1,092
Mesh 6x8	1,04179104	1,041545	0,959482	0,877	1,076	1,009	0,877	1,076
Mesh 8x8	1,03338016	1,032792	0,965189	0,875	1,062	1,01	0,875	1,062
Mesh 8x12	1,03424056	1,034153	0,983406	0,975	1,047	1,002	0,975	1,047

Table 3. 9: Pinched cylinder: Loading point displacement for different type of elements

- The Scordelis-Lo roof

The geometry consists of a portion of a cylindrical shell as depicted in **Figure 3. 15:** Scordelis-Lo roof. (a), its two end sections are fixed using rigid diaphragms (boundary conditions $U_{Mx} = U_{Mz} = 0$) while its two lateral sides remain free. It is subjected to a distributed loading which simulates the effect of gravity. By the conditions of diaphragms, the element hourglass modes ‘mixed’ and ‘local Bbar’ do not develop, therefore their stabilization is inutile. Due to the problem’s symmetries, only one quarter of the structure needs to be modeled (**Figure 3. 15:** Scordelis-Lo roof. (b)).

The useful data are:

- Geometric: length $L = 50$, radius $R = 25$, thickness $t = 0.25$, $\Phi = 40^\circ$;
- Material: $E = 4.32E8$ and $\nu = 0.0$;
- Gravity Load: $g = 90$.

The test result most frequently displayed is the vertical displacement at the midpoint of the free edge. The theoretical value for this result is $u_{ref} = 0.3024$, but most element converge to a slightly lower value. For this problem, both of membrane and bending deformations contribute significantly to it, especially for a membrane-dominated behavior (a substantial part of the strain energy is membrane strain energy). Hence, it is subject lightly to locking, that the test numerical

could be easily solved. Nevertheless, it is an interesting problem to determine the ability of the proposed element to accurately solve complex states of membrane strain.

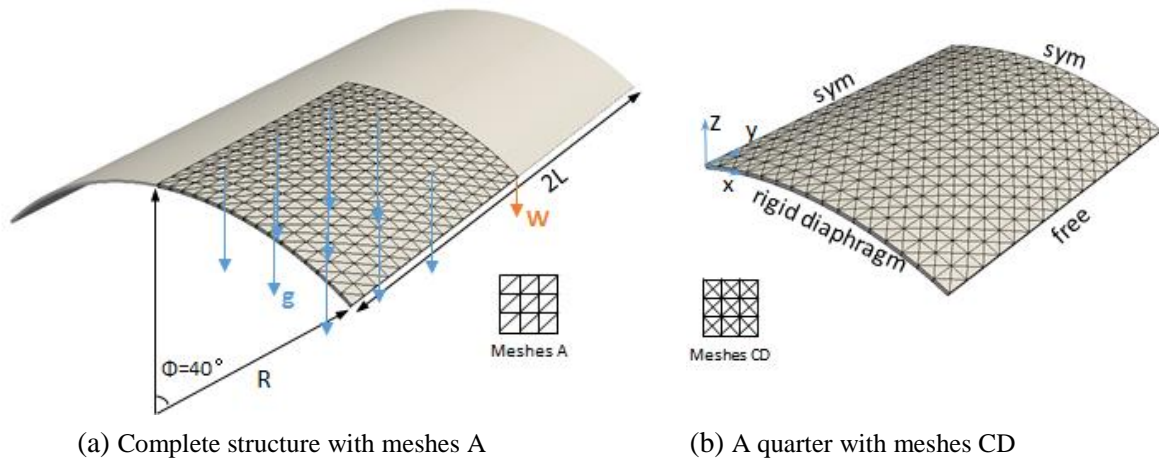


Figure 3.15: Scordelis-Lo roof.

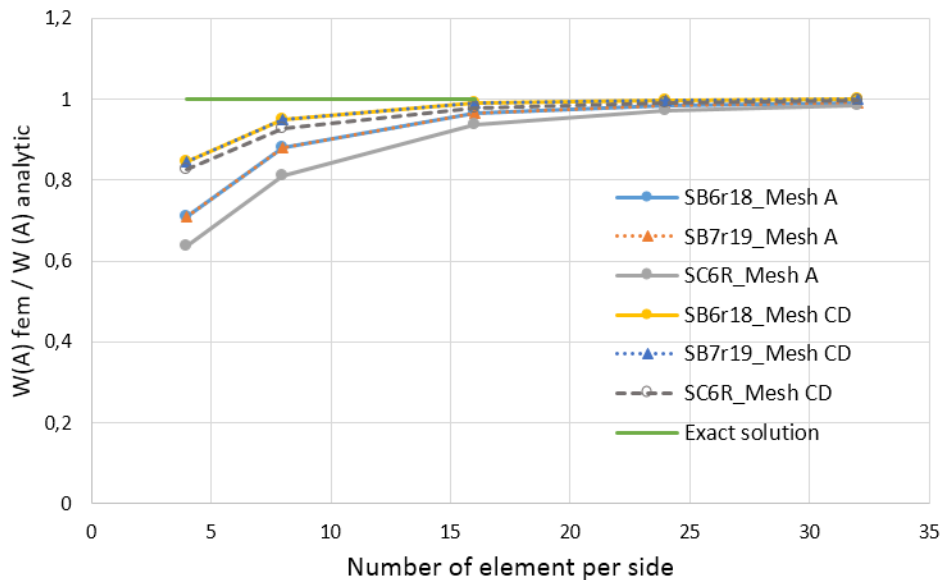


Figure 3.16: Convergence of normalized deflection at free edge's mid-point w

The **Figure 3.16** presents the curves of the values normalized by the reference solution with two different types of mesh: mesh A (seen **Figure 3.15**: Scordelis-Lo roof. (a)) and cross-diagonal (CD) mesh (seen **Figure 3.15**: Scordelis-Lo roof. (b)). It can be concluded that the results with mesh CD are more accuracy than that with mesh A, the proposed elements attain the reference solutions with a moderately refined mesh, and shows good mesh convergence properties.

- The partly clamped hyperbolic paraboloid problem

To better assess the ability of the proposed methods to deal with locking, we investigate here the partly clamped hyperbolic paraboloid problem (**Figure 3.17**). This interesting bending-dominated test was introduced in the work of Chapelle and Bathe [CHA 00] and further

developed in Bath et al. [BAT 00]. It consists of a shell whose mid-surface's equation is $Z = X^2 - Y^2$; $(X, Y) \in [(-L/2; L/2)]^2$, the surface is clamped along the side $X = -L/2$ and loaded by self-weight. By symmetry reasons, only one half of the geometry (**Figure 3. 17** (b)) is considered for the computation. The cases of thickness leading to slenderness $L/h=100$ and 1000 are employed. The convergences of the solution has been investigated in terms of displacements along the vertical direction at $(X, Y)=(L/2,0)$ and strain energy. Computed over the whole structure.

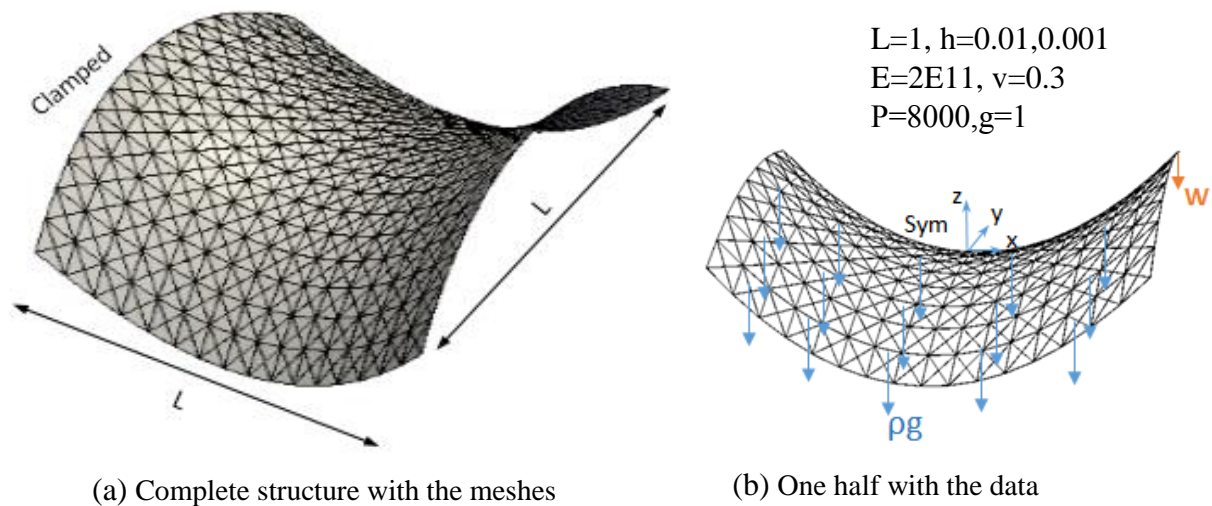


Figure 3. 17: The hyperbolic paraboloid problem.

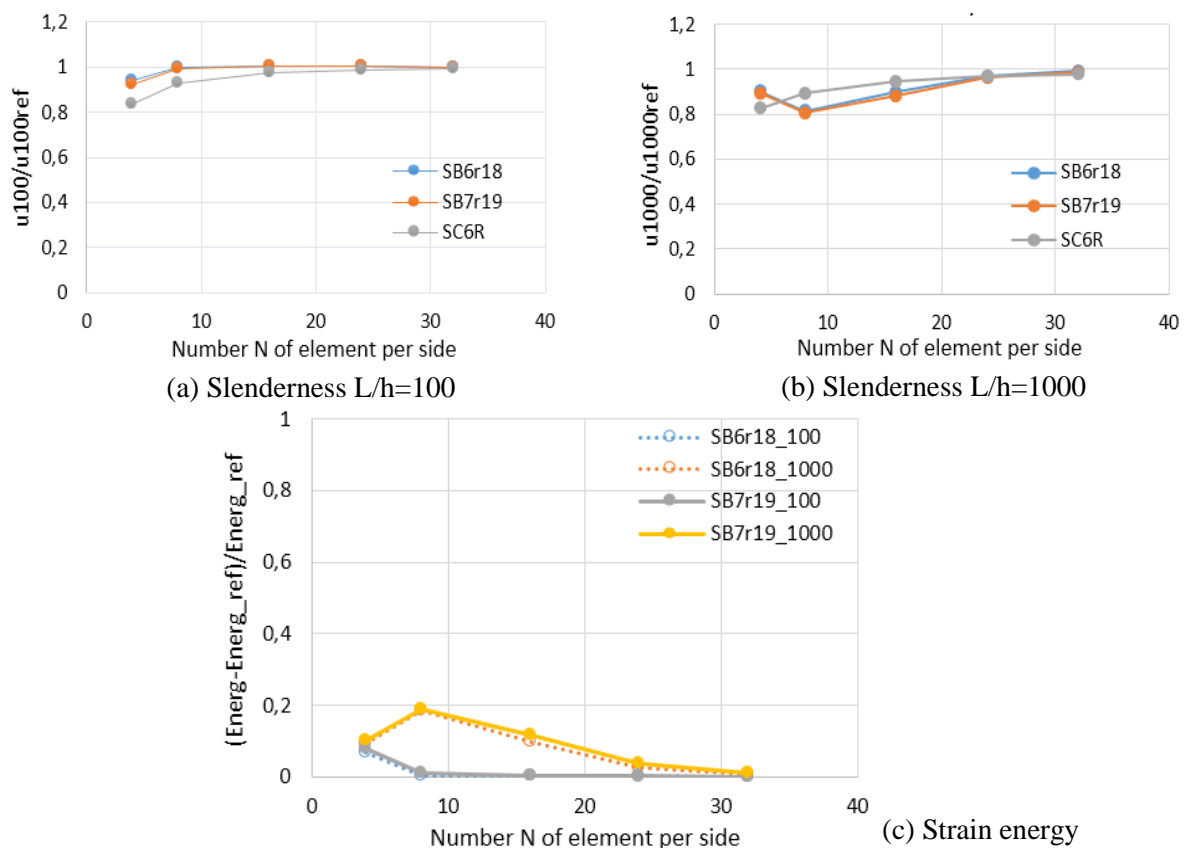


Figure 3. 18: Convergence of the displacement and in strain energy for the hyperbolic paraboloid problem

For modelling purposes, CD mesh sequences of $N \times N/2$ elements ($N=4, 8, 16, 24, 32$) were considered. The convergence of the displacement solution is shown in **Figure 3. 18** by the ratio u/u_{ref} to scale the different graphs ($L/h=100$ for **Figure 3. 18** (a) and $L/h=1000$ for **Figure 3. 18** (b)). Seen from the curves, the convergence gets slower when the slenderness increases, however, the locking would be better removed with a more refined mesh. In addition, the study of the solution in terms of global strain energy is figured in **Figure 3. 18** (c) with the plots in error ($(|Ener-Ener_{ref}|/Ener_{ref})$). It can be concluded that the proposed elements with a fine mesh show good convergence with little dependence on changes in the thickness of the shell structure. They own satisfying accuracy and good performance dealing with the locking problem even with very thin thickness.

3.4.2 Non-linear tests

To assess the performance of the solid-shell elements in geometric nonlinear analysis, several well-known shell benchmarks are carried out. The results are compared with reference values from [SZE 04] using Abaqus's S4R curved shell element model. Unless mentioned in opposite, the geometries are modelled with the presented solid-shell elements SB6r18 and SB7r19 implemented by the code PlasFib using a single layer and five integration points through the thickness direction.

- Cantilever subjected to end shear force

The cantilever shown in **Figure 3. 19** (a) is subjected to a shear force P ($P_{max}=4$) at the free end. The geometry with 16×1 mesh is $L=10$, $b=1$, $h=0.1$. The material data is: Young's modulus $E = 1.2 \times 10^6$, Poisson's ratio=0. **Figure 3. 19** (b) shows the calculated load-deflection curves from the solution with the solid-shell elements SB6r18, SB7r19 and the results from the work of Size [SZE 04]. The proposed elements show good performance in the solution of this problem.

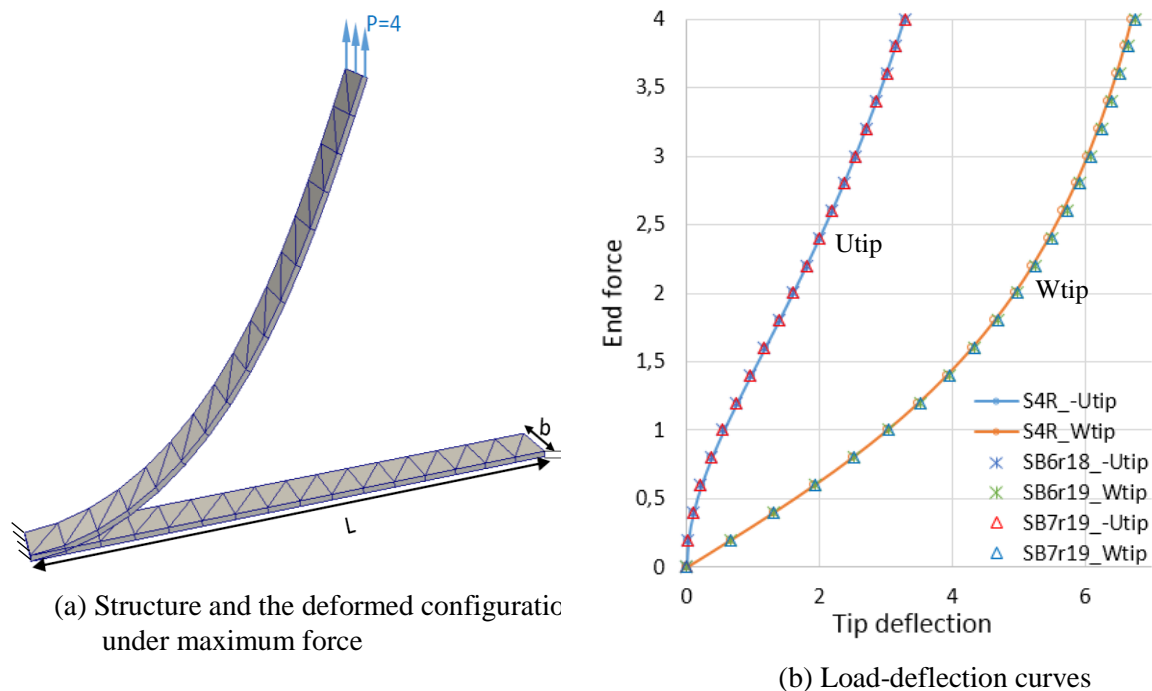


Figure 3. 19: Cantilever subjected to end shear force

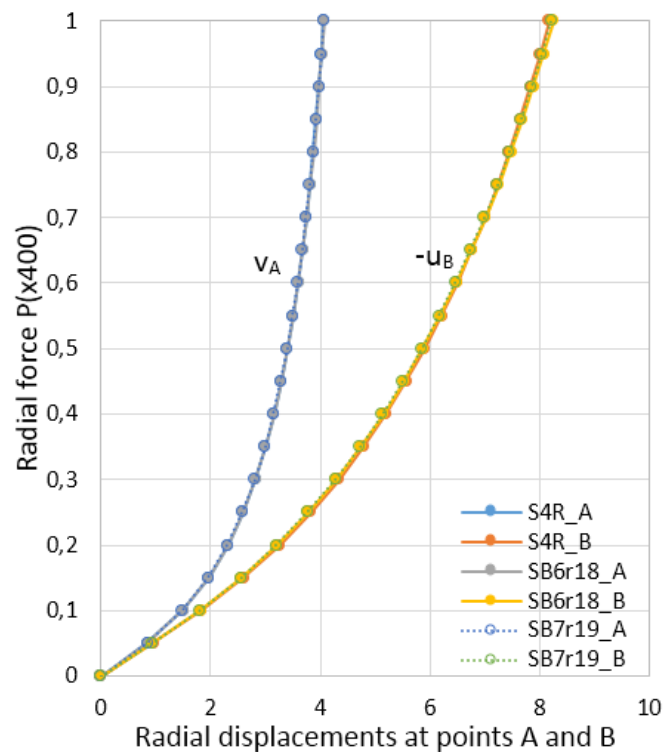
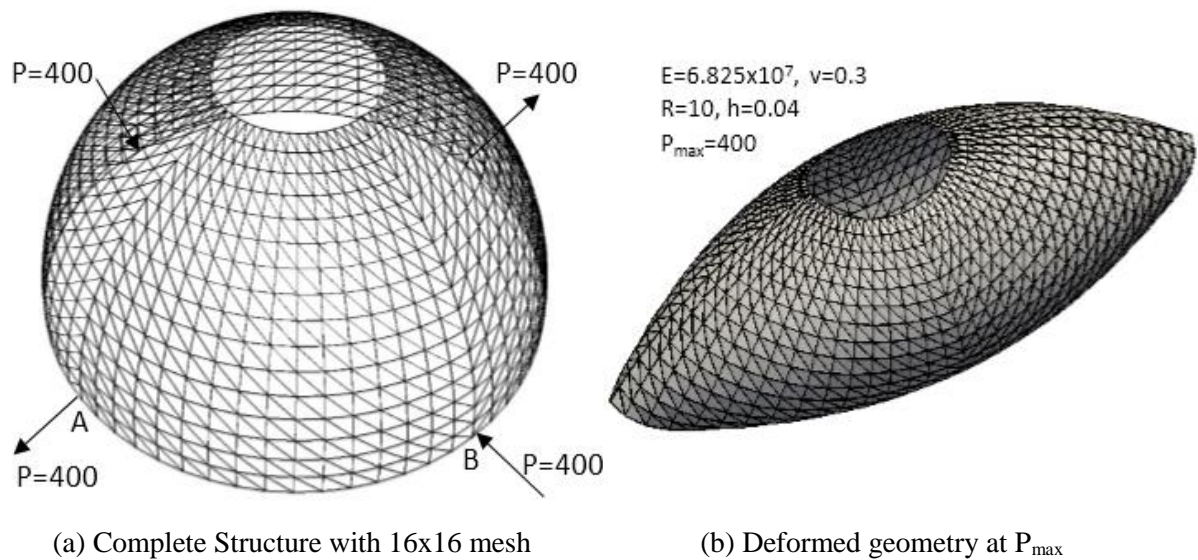
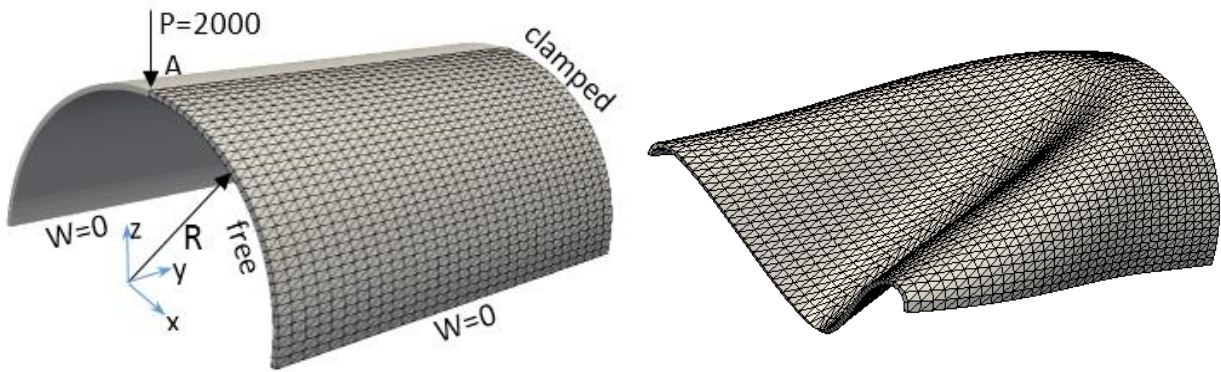
- *Hemispherical shell subjected to alternating radial forces*

Figure 3. 20: Hemispherical shell subjected to alternating radial forces

As depicted in **Figure 3. 20** (a), a hemisphere with an 18° circular cutout at its pole is under alternating radial point forces at 90° intervals. Due to symmetry, only one quarter of the hemisphere is modelled by a 16×16 mesh. The material and geometric properties are given in section 3.4.1 (Pinched hemisphere with a 18° hole). The point load is incrementally applied to a maximum value $P_{max}=400$, and **Figure 3. 20** (b) shows the deformed configuration obtained with the maximum load. The load-deflection curves at points A and B are plotted in **Figure 3.**

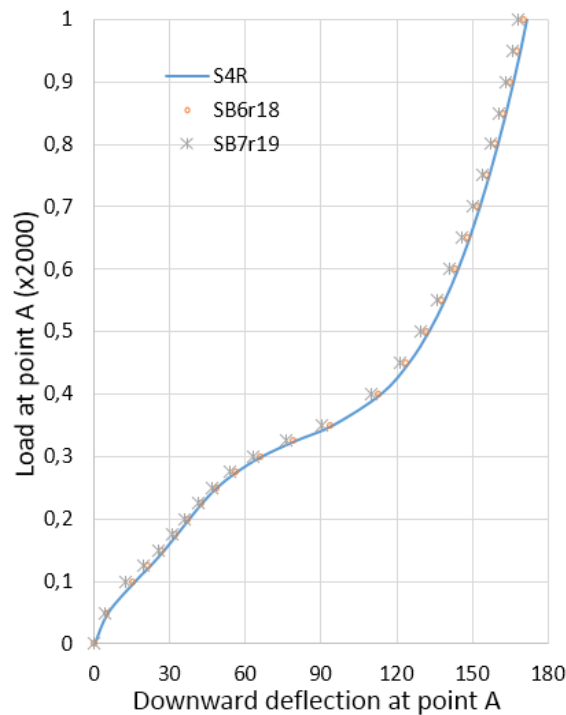
20 (c) where it can be seen that a very good agreement between the entire load-displacement path is noticeable.

- *Pinched semi-cylindrical isotropic shell*



(a) Complete Structure with 32x32 mesh

(b) Deformed geometry under maximum load



(c) Load-deflection curves

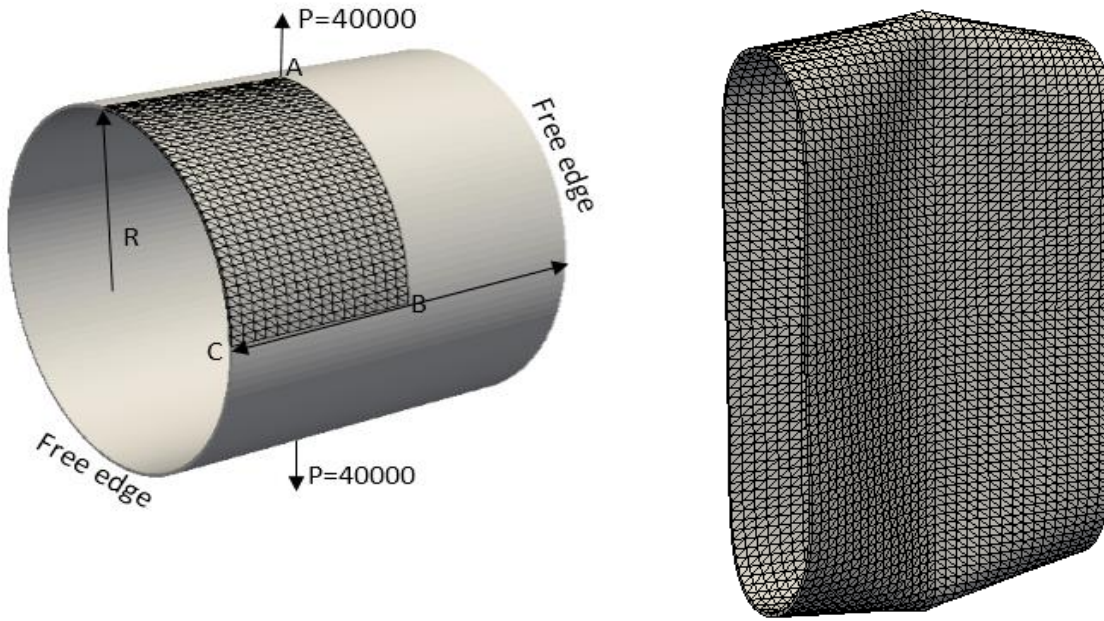
Figure 3. 21: Pinched semi-cylindrical isotropic shells subjected to an end pinching force.

A well-known benchmark problem for geometric nonlinear analysis of shells is the semi-cylindrical shell with a semi-circular edge clamped and the other free hanging (seen **Figure 3. 21** (a)). Along the two straight edges, all the nodal Z translations are restrained. The material constants are $E=2068.5$, $\nu=0.3$. The length and radius of the half cylinder are $L=3.048$ and $R=1.016$, respectively, and the thickness is $h=0.03$. The maximum load level at point A is set to $P_{max}=2000$. The structure is modeled using 32x32 element meshes of SB6 γ 18, SB7 γ 19 elements and the corresponding S4R shell element. **Figure 3. 21** (b) shows the deformed shape

for the maximum load level, and **Figure 3. 21** (c) gives the obtained load-displacement curves of point A. The results attest the accuracy and stability of the two elements comparing with the reference results.

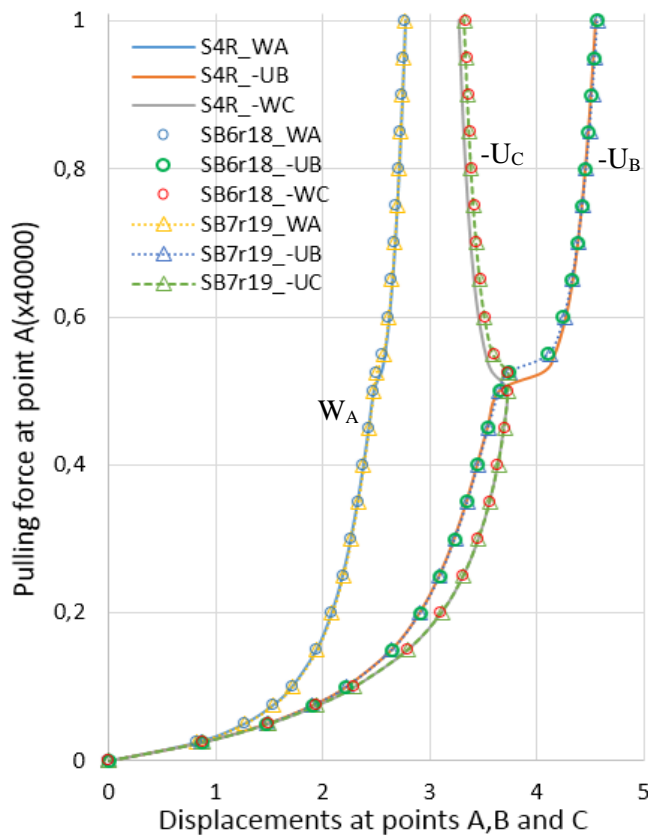
- *Pullout of an open-ended cylindrical shell*

As depicted in **Figure 3. 22** (a), an opened cylindrical shell is pulled by a pair of radial forces P . The parameters of the geometric are: the length $L=10.35$, the radius $R=4.953$, the thickness $h=0.094$. And for the material properties: $E=10.5e6$, $\nu=0.3125$. The maximum load is $P_{max}=4 \times 10^4$. Taking the advantage of the symmetry, only one octant of the cylinder is modelled and a 16×16 regular mesh is employed. **Figure 3. 22** (b) shows the deformed shell under the maximum load. In **Figure 3. 22** (c) the predicted displacements at points of loading are compared with the converged solution of S4R [SZE 04]. Close agreement can be noted especially for the beginning of the loading. When P is around 2×10^4 , a slight snap-through behavior caused by buckling was found, then the predictions of the elements have a little departure from the reference results. Nevertheless, the general trends of proposed elements and S4R are the same. This phenomena exists and can be explained in the work of Sze et al. [SZE 02b], the elements proposed in this manuscript are derived only in the updated Lagrangian (UL) framework, due to the finite strain nature of the test problem, predictions of the proposed elements derived in the total Lagrangian (TL) framework will be more consistent to that of the reference.



(a) Complete structure with 16x24 mesh

(b) Deformed geometry under maximum load



(c) Load-deflection curves

Figure 3. 22: Open-end cylindrical shell subjected to radial pulling forces.

3.5 Non-linear analysis of element SB7Y19 in large deformation

According to the previous section, the components of strain matrix are obtained by only concerning the linear part. In this section, the non-linear parts are taken into account and the total Lagrangian formulations are re-described, the import of the part non-linear allows to treat the problems with more complex behavior, and it offers the deformation gradient which will be used to model the behavior of our material in the next chapter.

3.5.1 Continuum mechanics in large deformation

- Deformation and motion

Figure 3. 23 shows the general motion of a deformable body. The domain of the body in the initial state is denoted by Ω_0 and called the initial configuration. The domain of the current configuration of the body is denoted by Ω_t . The motion of the body can be mathematically described by Φ a mapping between intimal and current particle positions as:

$$\mathbf{x} = \Phi(\mathbf{X}, t) \quad (3.72)$$

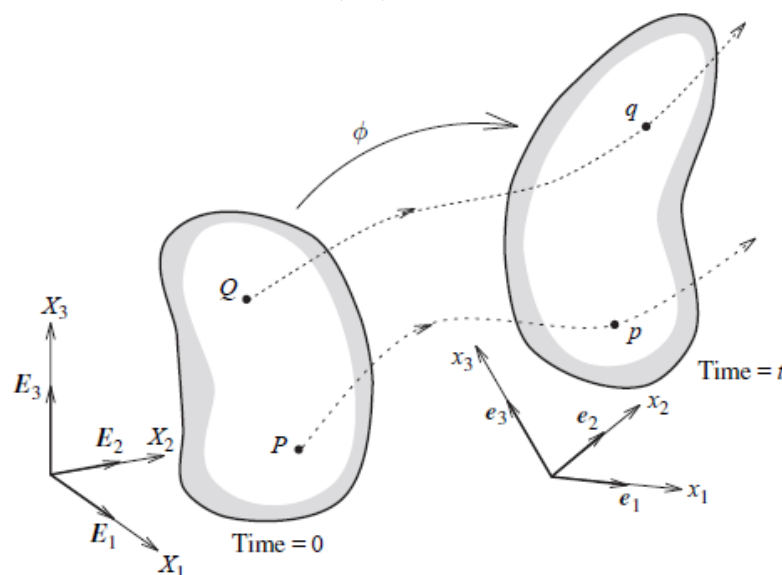


Figure 3. 23: Undeformed (initial) and deformed (current) configurations of a body

Where \mathbf{x} is the position of the point \mathbf{X} at time t .

The displacement of a material point is given by the difference between its current position and its original position, so

$$\mathbf{u}(\mathbf{X}, t) = \Phi(\mathbf{X}, t) - \Phi(\mathbf{X}, 0) = \mathbf{x} - \mathbf{X} \quad (3.73)$$

A key quantity in the characterization of deformation is the deformation gradient \mathbf{F} , which enables the relative spatial position of two neighboring particles after deformation to be described in terms of their relative material position before deformation. The deformation gradient is defined by:

$$\mathbf{F} = \frac{\partial \mathbf{x}}{\partial \mathbf{X}} \quad (3.74)$$

With the deformation gradient, an infinitesimal line segment $d\mathbf{x}$ in the current configuration can be given by the corresponding line segment $d\mathbf{X}$ in the reference configuration:

$$d\mathbf{x} = \mathbf{F} \cdot d\mathbf{X} \quad (3.75)$$

- *Strain measures*

In nonlinear continuum mechanics, many different measures of stain are used, only the Green-Lagrange strain \mathbf{E} is considered here.

$$\begin{aligned} d\mathbf{x} \cdot d\mathbf{x} - d\mathbf{X} \cdot d\mathbf{X} &= 2d\mathbf{X} \cdot \mathbf{E} \cdot d\mathbf{X} \\ d\mathbf{x} \cdot d\mathbf{x} &= (\mathbf{F} \cdot d\mathbf{X}) \cdot (\mathbf{F} \cdot d\mathbf{X}) = d\mathbf{X} \cdot (\mathbf{F}^T \cdot \mathbf{F}) \cdot d\mathbf{X} \end{aligned} \quad (3.76)$$

Using the above equation:

The Green-Lagrange strain can be expressed as follows:

$$\mathbf{E} = \frac{1}{2}(\mathbf{F}^T \cdot \mathbf{F} - \mathbf{I}) \quad (3.77)$$

- *Stress measures*

Normally, three stress measures are concerned in nonlinear problems, they are: Cauchy stress $\boldsymbol{\sigma}$, the first Piola-Kirchhoff stress \mathbf{P} , and the second Piola-Kirchhoff stress \mathbf{S} . Like in the **Figure 3. 24**, a deformable body is virtually cut into two domains before and after deformation.

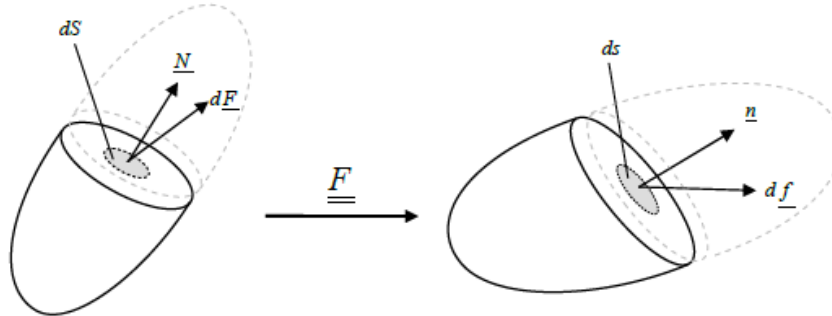


Figure 3. 24: Definition of the stress vector

The Cauchy stress is defined by:

$$\frac{df}{ds} = \boldsymbol{\sigma} \cdot \mathbf{n}, \text{ or } df = \boldsymbol{\sigma} \cdot \mathbf{n} \cdot ds \quad (3.78)$$

So the Cauchy stress represents the internal force expressed in the current configuration. With different descriptions of internal force, also the surface and the normal vector. The first Piola- Kirchhoff stress \mathbf{P} is defined as:

$$df = \mathbf{P} \cdot \mathbf{N} \cdot dS \quad (3.79)$$

While the second Piola- Kirchhoff stress \mathbf{S} is defined as:

$$d\mathbf{F} = \mathbf{S} \cdot \mathbf{N} \cdot dS \quad (3.80)$$

The relations between the three stresses can be denoted by the following equation

$$\mathbf{S} = \mathbf{F}^{-1} \mathbf{P} = \mathbf{J} \mathbf{F}^{-1} \boldsymbol{\sigma} \mathbf{F}^{-T} \quad (3.81)$$

Where \mathbf{J} is the determinant of the deformation gradient: $\mathbf{J} = \det(\mathbf{F})$

3.5.2 Tensor of deformation gradient

For the description of the motion in continuum mechanics, the finite element approximation to the motion and the displacement field are given by:

$$x_i(\mathbf{X}, t) = \sum_{l=1}^3 N^l x_{il}(t), \quad u_i(\mathbf{X}, t) = \sum_{l=1}^3 N^l u_{il}(t) \quad (3.82)$$

The deformation gradient is defined as:

$$F_{ij} = \frac{\partial x_i(\mathbf{X}, t)}{\partial X_j} = \sum_{l=1}^3 \frac{\partial N^l}{\partial X_j} x_{il}(t) = B_{jl}^0 x_{il} \quad (3.83)$$

Where $B_{jl}^0 = \frac{\partial N^l}{\partial X_j}$

For their variations are not function of time, so

$$\delta u_i(\mathbf{X}) = \sum_{l=1}^3 N^l \delta u_{il}, \quad \delta x_{il} = \delta(X_{il} + u_{il}) = \delta u_{il} \quad (3.84)$$

Then

$$\delta F_{ij} = \sum_{l=1}^3 \frac{\partial N^l}{\partial X_j} \cdot \delta x_{il} = B_{jl}^0 \delta u_{il}, \quad \text{so } \delta \mathbf{F} = \mathbf{B}_0 \delta \mathbf{u} \quad (3.85)$$

The incremental deformation gradient between configurations at time t and $t+\Delta t$ is defined in the form:

$$\begin{aligned} {}_{t+\Delta t} \mathbf{F} &= \frac{\partial \mathbf{x}(t + \Delta t)}{\partial \mathbf{x}(t)} = \Delta \mathbf{F}^t = \mathbf{I} + \frac{\partial \mathbf{u}(t)}{\partial \mathbf{x}(t)} \\ \Delta F_{ij}^t &= \delta_{ij} + \frac{\partial u_i(t)}{\partial x_j(t)} \end{aligned} \quad (3.86)$$

Where \mathbf{I} is a third-order identity tensor.

So the deformation gradient at time $t+\Delta t$ can be expressed by the incremental value and the value at time t :

$$\mathbf{F}_{t+\Delta t} = {}_0^{t+\Delta t} \mathbf{F} = {}_0^t \mathbf{F} \cdot {}_t^{t+\Delta t} \mathbf{F} = \mathbf{F}^t \cdot \Delta \mathbf{F}^t \quad (3.87)$$

According to the above equations, the objective is to calculate all the components of the incremental deformation gradient $\Delta \mathbf{F}^t$, in result, the actual deformation gradient could be updated.

- *In the cases of $i=j$*

$$\Delta F_{ii}^t = 1 + \frac{\partial u_i(t)}{\partial x_i(t)} = 1 + \varepsilon_{ii}, \quad i=1,2,3 \quad (3.88)$$

Where ε_{ii} are detailed in the previous section.

- $i=1, j=2$ and $i=2, j=1$

$$\Delta F_{12}^t = \frac{\partial u_1(t)}{\partial x_2(t)}, \Delta F_{21}^t = \frac{\partial u_2(t)}{\partial x_1(t)} \quad (3.89)$$

From the previous section, the kinematic description for element SB7Y19 in-plan strain problem which is based on the element DKT12 (DKT6 + CST), can be summarized in the manners of description for element C^0 . The geometric interpolation and the displacement field are given by:

$$\begin{aligned} \bar{x} &= \sum_{i=1}^3 N^i(x, y) \bar{x}^i + z \bar{X} \\ \vec{u} &= \sum_{i=1}^3 N^i(x, y) \vec{u}^i + z \sum_{i=1}^3 N^{*i}(x, y) (-\theta_n^i \vec{t}^i + \theta_t^i \vec{n}^i) \end{aligned} \quad (3.90)$$

Where $N^i(x, y)$ and $N^{*i}(x, y)$ are interpolation functions used in equation (3.1) and (3.11). \bar{X} is the same definition as in the C^0 element with all the three values are equal.

After the development of formulations, the components of deformation gradient are obtained:

$$\begin{aligned} \Delta F_{12}^t &= \frac{\partial u}{\partial y} = \left\langle \bar{\mathbf{B}}_{u3}^m \right\rangle + z \frac{1}{2} \left\langle \bar{\mathbf{B}}_3^b \right\rangle \{ \mathbf{U}_e \} \\ \Delta F_{21}^t &= \frac{\partial v}{\partial x} = \left\langle \bar{\mathbf{B}}_{v3}^m \right\rangle + z \frac{1}{2} \left\langle \bar{\mathbf{B}}_3^b \right\rangle \{ \mathbf{U}_e \} \end{aligned} \quad (3.91)$$

The vectors $\left\langle \bar{\mathbf{B}}_{u3}^m \right\rangle$ and $\left\langle \bar{\mathbf{B}}_{v3}^m \right\rangle$ are decomposed from the third row of matrix $\left[\bar{\mathbf{B}}^m \right]$ ($\bar{\mathbf{B}}^m(3,:) = \bar{\mathbf{B}}_{u3}^m + \bar{\mathbf{B}}_{v3}^m$), and $\left\langle \bar{\mathbf{B}}_3^b \right\rangle$ is the third row of matrix $\left[\bar{\mathbf{B}}^b \right]$. They are detailed in Appendices.

- $i=1, j=3; i=3, j=1$ and $i=2, j=3; i=3, j=2$

$$\begin{aligned} \Delta F_{13}^t &= \frac{\partial u_1(t)}{\partial x_3(t)}, \Delta F_{31}^t = \frac{\partial u_3(t)}{\partial x_1(t)} \\ \Delta F_{23}^t &= \frac{\partial u_2(t)}{\partial x_3(t)}, \Delta F_{32}^t = \frac{\partial u_3(t)}{\partial x_2(t)} \end{aligned} \quad (3.92)$$

Similar to the previous development, the displacement field is given in equation (3.41), the rest components are:

$$\begin{aligned} \Delta F_{13}^t &= \frac{\partial u}{\partial z} = \left\langle \mathbf{B}_{13}^c \right\rangle \{ \mathbf{U}_e \}; \Delta F_{31}^t = \frac{\partial w}{\partial x} = \left\langle \mathbf{B}_{31}^c \right\rangle \{ \mathbf{U}_e \} \\ \Delta F_{23}^t &= \frac{\partial v}{\partial z} = \left\langle \mathbf{B}_{23}^c \right\rangle \{ \mathbf{U}_e \}; \Delta F_{32}^t = \frac{\partial w}{\partial y} = \left\langle \mathbf{B}_{32}^c \right\rangle \{ \mathbf{U}_e \} \end{aligned} \quad (3.93)$$

The vectors $\langle \mathbf{B}_{13}^c \rangle, \langle \mathbf{B}_{31}^c \rangle, \langle \mathbf{B}_{23}^c \rangle, \langle \mathbf{B}_{32}^c \rangle$ are decomposed from the matrix $[\bar{\mathbf{B}}^{ts}]$ with the relation: $[\bar{\mathbf{B}}^{ts}] = \begin{bmatrix} \langle \mathbf{B}_{13}^c \rangle + \langle \mathbf{B}_{31}^c \rangle \\ \langle \mathbf{B}_{23}^c \rangle + \langle \mathbf{B}_{32}^c \rangle \end{bmatrix}$. More details are shown in **Appendices**.

3.5.3 Validation tests

Several validation tests are launched in this part with an explicit code compiled by Fortran90, the results are compared with the analytic results and the results from previous tests.

- Elementary tests for the verification of tensor of deformation gradient

Firstly, a series of elementary tests is applied in order to verify the tensor of deformation gradient. As figured in **Figure 3. 25**, the tests are based on a cube composed by two prismatic elements, the dimension is $L=1$. The results of tensor of deformation gradient are shown in **Table 3. 10** with different correspondent solicitations. Correct tensors of deformation gradient are obtained comparing with the analytic results. The above descriptions for the calculation this tensor are verified.

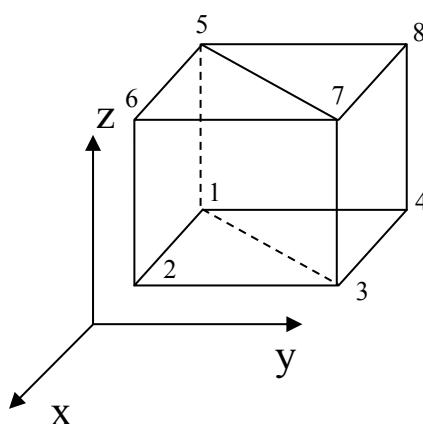
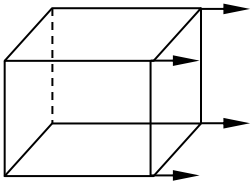
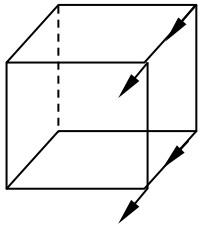


Figure 3. 25: Geometry of elementary test

	Boundary conditions	Tensor de deformation gradient
	Elongation in y direction: $U_{y3}=U_{y4}=U_{y7}=U_{y8}=1$	$F = \begin{Bmatrix} 1 & 0 & 0 \\ 0 & 2 & 0 \\ 0 & 0 & 1 \end{Bmatrix}$
	Shearing deformation: $U_{x3}=U_{x4}=U_{x7}=U_{x8}=1$	$F = \begin{Bmatrix} 1 & 1 & 0 \\ 0 & 1 & 0 \\ 0 & 0 & 1 \end{Bmatrix}$

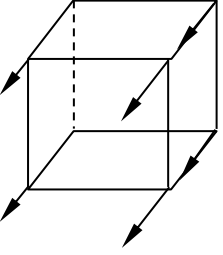
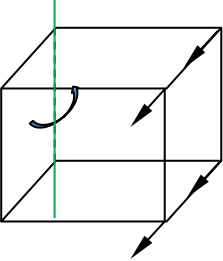
	Elongation in x direction + Shearing deformation: $U_{x3} = U_{x7} = 2$ $U_{x4} = U_{x8} = U_{x2} = U_{x6} = 1$	$F = \begin{Bmatrix} 2 & 1 & 0 \\ 0 & 1 & 0 \\ 0 & 0 & 1 \end{Bmatrix}$
	Shearing deformation + Rigid rotation: $U_{x3} = U_{x4} = U_{x7} = U_{x8} = 1$ $\theta = 90^\circ$	$F = \begin{Bmatrix} 0 & -1 & 0 \\ 1 & 1 & 0 \\ 0 & 0 & 1 \end{Bmatrix}$

Table 3. 10: Results of the elementary tests for validation of deformation gradient tensor

- ***Cantilever subjected to end shear force***

This test has been launched in previous part with an isotropic elasticity behavior. Here, for this test in large deformation case, the geometric data and its boundary conditions are the same. An isotropic hyper-elasticity behavior (Neo-Hookean material) is used, whose constitutive expression is based on the second Piola-Kichhoff stress tensor \mathbf{S} and the right Cauchy-Green deformation tensor $\mathbf{C} = \mathbf{F}^T \cdot \mathbf{F} : \mathbf{S} = \mu(\mathbf{I} - \mathbf{C}^{-1}) + \lambda(\ln \mathbf{J})\mathbf{C}^{-1}$. μ and λ are the Lamé's parameters in function of Young's modulus $E = 1.2 \times 10^6$, and Poisson's ratio $\nu = 0$.

	<i>SB7Y19</i>	<i>SB7Y19 with nonlinear part</i>	<i>S4R</i>
Wtip	6,737	6,69735	6,698
-Utip	3,245	3,2715	3,286

Table 3. 11: Loading point displacement of cantilever test

Table 3. 11 shows the deflection results for the loaded point with the maximum shear force $P=4$ at the free end. Comparing with the results of Abaqus solution S4R element and the developed element SB7Y19 in the small perturbation case. It attests that addition of the nonlinear part in grand deformation case can obtain a more precise.

- ***Hemispherical shell subjected to alternating radial forces***

The second test used to evaluate the element SB7Y19 in grand deformation case is also the hemispherical shell with an 18° circular hole. The details for its geometry and boundary conditions are shown previously. Neo-Hookean material is applied, the same Young's modulus and Poisson's ratio generate the equivalent Lamé's parameters. The point load is incrementally applied to a maximum value $P_{max}=400$. Radial displacements at points A and B are presented in **Table 3. 12**. Comparing to the results of element SB7Y19 in previous test and those of element S4R, the proposed solid-shell element shows an encouraging accuracy dealing with grand deformation problems.

	SB7 γ 19	SB7 γ 19 with nonlinear part	S4R
V _A	4.0518	4.0673	4.067
-U _B	8.2110	8.1754	8.178

Table 3. 12: Loading point displacement of hemispherical shell test

3.6 Conclusion of chapter 3

In this chapter, a new approach has been proposed extrapolating shell elements to develop a new solid-shell element. The prismatic element is a continuum-based element and with the technique of an assumed strain method, the shear locking has been avoided. This element has been presented with a shell-like theory formalism involving quantities that expresses curvatures, membrane and transverse shear deformations. Several integration points are distributed in the ‘thickness’ direction. A central node endowed with a local degree of freedom (translation) increases the order of the normal strain and allows the use of complete three-dimensional constitutive laws instead of taking into account a plane stress state hypothesis. Additionally, with this supplementary degree of freedom, the normal strain becomes linear through the thickness direction and an imposed pressure replaced by a force equivalent seems possible. A series of benchmark tests both for linear and nonlinear cases commonly employed for testing different kinds of lockings have been conducted. The proposed solid-shell element shows an excellent convergence behavior and encouraging accuracy, the little sign of locking phenomena seems negligible. In addition, compared to conventional shell elements, the convenience of three-dimensional finite elements is unaffected, it can be able to accommodate a 3D constitutive law, no rotational degrees of freedom are introduced, and the management of contact becomes easily. Above all, the predominance of this element is the feasibility to describe non constant distribution of transverse stress σ_{33} trough thickness with correct values on the two surfaces of element in any loading condition cases, which is necessary during the forming process. However, the solution may be sensitive to the mesh density but not more than with some other solid-shell elements (SC6R in Abaqus) or classical triangle shell elements.

Moreover, a nonlinear formulation for the grand deformation case has been developed, several tests with Neo- Hookean material has be conducted for dealing with the forming simulations.

Chapter 4

Viscoelastic characterization for consolidation behavior and a model for the prediction of the consolidation

4.1 Introduction

During the forming process, different modes of deformation mechanism are concerned at macroscopic scale, the elongation in the warp and weft directions, the in-plan shear strain, the bending deformation, and the transverse compaction strain during consolidation step. After the development of a new finite element approach for the modeling of complete three-dimensional constitutive laws, characterization of a consolidation model for the transverse compaction behavior of thermoplastic prepregs is another part of this work. According to the experimental observations in the second chapter, mechanical behaviors for thermoplastic pre-impregnated composites are summarized as follows: The tensile behavior is mainly related to fiber tensions and are not viscous [WAN 15]; For the bending behavior, it is perhaps viscous but this bending properties are not a very sensitive [GUZ 15] and the viscosity of the bending behavior will be ignored during forming. However, a thermo-dependence model proposed by Biao permits to characterize the bending deformation mode in function of temperature; Concerning the in-plan shear behavior, the viscosity behavior has been analyzed and modeled by Guzman, and a viscoelastic characterization model based on generalized relaxation model is proposed for in-plan shear deformation mode [GUZ 15]; When taking account of the compaction deformation, the resin flow presents a significant viscosity by the action of consolidation pressure. Hence, based on Guzman's model, a viscoelastic characterization completed with consolidation behavior will be presented in this chapter.

Firstly, within a hyperelastic framework, the strain potential energy formulation composed of different modes of deformation will be described. It involves Lagrangian tensors (second Piola-Kirchhoff and Right Cauchy-Green tensor) that are by definition objective. The major of deformation modes are represented by physical invariant, each of them are seemed independent. This approach has been already used for forming simulation of 2D woven fabric reinforcement [AIM 08] and 3D interlock [CHA 12].

Secondly, considering the influence of the resin and its flow during consolidation, viscoelasticity is introduced exclusively for the compaction mode not only for the in-plan shearing mode. The principle of this model is based on the generalization of classical rheological models such as the Maxwell model and its formulation in terms of the internal variables [SIM 98].

Thirdly, a model to predict the evolution of the consolidation is proposed. Accounting for resin flow through the fiber bed, this model involved in three processing parameters for consolidation is responsible for void resorption. Within this model, the level of consolidation can be predicted for the microstructure analysis of void presented within the prepreg.

Finally, within the proposed models in a hyperelastic framework developed Guzman [GUZ 15], the experimental results in chapter 2 are used to identify the associated parameters. A completed three-dimensional mechanical behavior with compaction effect for thermoplastic pre-impregnated composites allows to its forming simulation.

4.2 Hyper-elasticity law

4.2.1 Definition of hyper-elasticity

The definition of hyper-elasticity behavior laws starts from Clausius-Duhem inequality. Clausius-Duhem inequality equation can be given in the initial configuration as follows:

$$\Phi_0 = -\rho_0(\dot{\Psi} - \dot{\theta}\eta) - \frac{1}{\theta} \underline{Q} \cdot \frac{\partial \theta}{\partial \underline{x}} + \underline{S} : \underline{\dot{E}} \geq 0 \quad (4.1)$$

With Φ_0 the dissipation per volume unit in the initial configuration, Ψ free specific energy per mass unit, θ the temperature, η the specific entropy, and the heat flux vector \underline{Q} in the initial configuration. In the theory of purely mechanics, the temperature is considered homogeneous in an isothermal system. So the dissipation is written as:

$$\Phi_0 = -\rho_0 \dot{\Psi} + \underline{S} : \underline{\dot{E}} \quad (4.2)$$

A hyper-elastic material is a material whose initial strain energy per volume unite $w = \rho_0 \Psi$ is independent to its actual state and who is not dissipative ($\Phi_0 = 0$). Hence, two conditions relative to the bases of hyper-elasticity behavior laws are:

$$\begin{aligned} \dot{w}(\underline{F}) &= \underline{S} : \underline{\dot{E}} \\ w &= w(\underline{F}) = \rho_0 \Psi \end{aligned} \quad (4.3)$$

It was shown [CIA 88] that for the principle of material indifference, if and only if the strain energy is a function of the right Cauchy-Green deformation tensor $\underline{C} = \underline{F}^T \cdot \underline{F}$

$$\begin{aligned} w &= w(\underline{C}) = \rho_0 \Psi \\ \dot{w}(\underline{C}) &= \underline{S} : \underline{\dot{E}} = \frac{1}{2} \underline{S} : \underline{\dot{C}} \end{aligned} \quad (4.4)$$

Then

$$\dot{w}(\underline{C}) = \frac{\partial w}{\partial \underline{C}} : \frac{\partial \underline{C}}{\partial t} = \frac{1}{2} \underline{S} : \underline{\dot{C}} \Leftrightarrow \left(\frac{\partial w}{\partial \underline{C}} - \frac{1}{2} \underline{S} \right) = 0 \Leftrightarrow \underline{S} = 2 \frac{\partial w}{\partial \underline{C}} \quad (4.5)$$

Equation (4.5) constitutes the general expression of hyper-elasticity behavior laws. Hyper-elastic materials provide a natural framework for frame-invariant formulation of anisotropic material response by simply embodying the anisotropy in the potential w .

- *Isotropic hyper-elasticity*

The stored strain energy (potential) for an isotropic hyper-elastic material can be written as a function of the principal invariants (I_1, I_2, I_3) of the right Cauchy-Green deformation tensor.

$$w(\underline{\underline{C}}) \text{ is isotropic} \Leftrightarrow w(I_1, I_2, I_3) \quad (4.6)$$

Where the invariants are defined here as:

$$\begin{aligned} I_1 &= Tr(\underline{\underline{C}}) = \underline{\underline{C}} : \underline{\underline{I}} \\ I_2 &= \frac{1}{2} \left(Tr(\underline{\underline{C}})^2 - Tr(\underline{\underline{C}}^2) \right) = \underline{\underline{C}} : \underline{\underline{C}} \\ I_3 &= Det(\underline{\underline{C}}) = J^2 \end{aligned} \quad (4.7)$$

There exists other models with different expressions of potential. Such as the model of Rivlin [RIV 48] who describes the strain energy by a polynomial equation:

$$w = \sum_{i,j=0}^{\infty} C_{ij} (I_1 - 3)^i (I_2 - 3)^j \quad (4.8)$$

Three classical models ensue from the model of Rivlin:

- Neo-Hookeen model: $w = C_{10}(I_1 - 3)$
- Mooney-Rivlin model: $w = C_{10}(I_1 - 3) + C_{01}(I_2 - 3)$
- Yeoh model: $w = C_{10}(I_1 - 3) + C_{20}(I_1 - 3)^2 + C_{30}(I_1 - 3)^3$

The Neo-Hookeen material model is an extension of isotropic linear law (Hooke's law) to large deformation. The stored energy function for a compressible Neo-Hookeen material (isotropic with respect to the initial, unstressed configuration) is

$$w(\underline{\underline{C}}) = \frac{1}{2} \lambda_0 (\ln J)^2 - \mu_0 \ln J + \frac{1}{2} \mu_0 (tr(\underline{\underline{C}}) - 3) \quad (4.9)$$

And the stresses are given by

$$\underline{\underline{S}} = \lambda_0 \ln J \underline{\underline{C}}^{-1} + \mu_0 (\underline{\underline{I}} - \underline{\underline{C}}^{-1}) \quad (4.10)$$

With λ_0 and μ_0 are the Lamé constant of the linearized theory.

- *Orthotropic hyper-elasticity*

An orthotropic material is characterized by three privileged directions $\underline{\underline{L}}_1, \underline{\underline{L}}_2$ and $\underline{\underline{L}}_3$. These directions are used to define the structural tensors to characterize the physical symmetric group of the material, defined by:

$$\underline{\underline{L}}_{ij} = \underline{\underline{L}}_i \otimes \underline{\underline{L}}_j, \quad i, j = 1, 3 \quad (4.11)$$

The representation theorem permits to write the strain energy density expression as a function of invariants of transformation for an orthotropic behavior [QUA 94] [ITS 04]:

$$w^{orth} = w^{orth}(I_1, I_2, I_3, I_{41}, I_{42}, I_{43}, I_{412}, I_{413}, I_{423}, I_{51}, I_{52}, I_{53}) \quad (4.12)$$

Where I_1, I_2 and I_3 correspond to the classical invariants of Cauchy-Green (Equation (4.7)), and the mixt invariants I_{4i}, I_{4ij} and I_{5i} are defined as:

$$\begin{aligned} I_{4i} &= \underline{\underline{C}} : \underline{\underline{L}}_{ii} = \underline{\underline{L}}_i : \underline{\underline{C}} : \underline{\underline{L}}_i \\ I_{4ij} &= \underline{\underline{C}} : \underline{\underline{L}}_{ij} = \underline{\underline{L}}_i : \underline{\underline{C}} : \underline{\underline{L}}_j \\ I_{5i} &= \underline{\underline{C}}^2 : \underline{\underline{L}}_{ii} = \underline{\underline{L}}_i : \underline{\underline{C}}^2 : \underline{\underline{L}}_i \end{aligned} \quad (4.13)$$

4.2.2 Hyper-elasticity for woven reinforcement

A woven reinforcement can be considered as an orthotropic material, whose three main directions are respectively defined by the directions of warp, weft and the third direction perpendicular to the previous two directions.

Recent works have enabled the development of hyper-elastic laws adapted to 2D fabric [AIM 08] and 3D interlock [CHA 12] [MAT 15] formulated with the physically based invariants. This approach, inspired by the work of Criscione [CRI 01], is based on a multiplicative decomposition of the deformation gradient tensor $\underline{\underline{F}}$. Each terms of this decomposition is characterized by an invariant said "physical", linked to the classical invariants. The advantage of this type of formulation resides in decoupling the deformation modes, thereby highlight them and identify them separately.

The deformation modes and their respective invariants are in the following **Table 4. 1**:

Deformation modes	Invariant
Elongation of warp direction	$I_{elong1} = \ln(\sqrt{I_{41}})$
Elongation of weft direction	$I_{elong2} = \ln(\sqrt{I_{42}})$
In-plan shear	$I_{shear} = \frac{I_{412}}{\sqrt{I_{41}I_{42}}}$
Transverse shear in warp direction	$I_{ts1} = \frac{I_{413}}{\sqrt{I_{41}I_{43}}}$
Transverse shear in weft direction	$I_{ts2} = \frac{I_{423}}{\sqrt{I_{42}I_{43}}}$
Transverse compression	$I_{comp} = \frac{1}{2} \ln\left(\frac{I_3}{I_{41}I_{42}(1 - I_{shear}^2)}\right)$

Table 4. 1: Deformation modes and their respective invariants for a hyperelastic woven reinforcement

The volume stain energy can be then expressed as a function of these physical invariants with the hypothesis of decoupling.

$$w = w_{elong1}(I_{elong1}) + w_{elong2}(I_{elong2}) + w_{comp}(I_{comp}) + w_{shear}(I_{shear}) + w_{ts1}(I_{ts1}) + w_{ts2}(I_{ts2}) \quad (4.14)$$

The second Piola-Kirchhoff tensor can be obtained:

$$\underline{\underline{S}} = 2 \frac{\partial w}{\partial \underline{\underline{C}}} = 2 \frac{\partial w}{\partial I_k} \frac{\partial I_k}{\partial \underline{\underline{C}}} = \sum 2 \frac{\partial w_k}{\partial I_k} \frac{\partial I_k}{\partial \underline{\underline{C}}} \quad (4.15)$$

With I_k for all the physical invariants in table, and its correspondent stain energy w_k .

4.2.3 Visco-hyper-elasticity for thermoplastic preregs

For thermoplastic pre-impregnated composites, the material is usually considered as thin shell with Kirchhoff's theory. The internal potential energy per surface unit in the initial configuration is combined by the membrane energy and bending energy.

$$w = w_{mem} + w_{ben} \quad (4.16)$$

According to the previous section, three deformation modes constituting the membrane's strain energy are: elongation deformation mode in the warp and weft directions, and the in-plan shearing mode.

$$w_{mem}(\underline{\underline{C}}) = w_{elong1}(I_{elong1}(\underline{\underline{C}}, \underline{\underline{L}}_{11})) + w_{elong2}(I_{elong2}(\underline{\underline{C}}, \underline{\underline{L}}_{22})) + w_{shear}(I_{shear}(\underline{\underline{C}}, \underline{\underline{L}}_{12})) \quad (4.17)$$

where the invariants are given from **Table 4. 1** (λ_i is the elongation in the material direction $\underline{\underline{L}}_i$):

$$I_{elongi} = \ln(\sqrt{I_{4i}}) = \ln(\sqrt{\underline{\underline{L}}_i \cdot \underline{\underline{C}} \cdot \underline{\underline{L}}_i}) = \ln(\sqrt{C_{ii}}) = \ln(\sqrt{\lambda_i}) \quad (4.18)$$

I_{shear} is the in-plan shear invariant related to the angular variations between warp and weft directions ($\underline{\underline{L}}_1, \underline{\underline{L}}_2$). With γ shear angle between two yarns.

$$I_{shear} = \frac{I_{412}}{\sqrt{I_{41}I_{42}}} = \sin(\gamma) \quad (4.19)$$

Using Equation (4.15), the membrane stress results $\underline{\underline{S}}_{mem}$ are expressed as follows:

$$\underline{\underline{S}}_{mem} = 2 \left(\frac{\partial w_{elong1}}{\partial I_{elong1}} \frac{\partial I_{elong1}}{\partial \underline{\underline{C}}} + \frac{\partial w_{elong2}}{\partial I_{elong2}} \frac{\partial I_{elong2}}{\partial \underline{\underline{C}}} + \frac{\partial w_{shear}}{\partial I_{shear}} \frac{\partial I_{shear}}{\partial \underline{\underline{C}}} \right) \quad (4.20)$$

With:

$$\frac{\partial I_{elongi}}{\partial \underline{\underline{C}}} = \frac{1}{2I_{elongi}} \underline{\underline{L}}_{ii} \quad i = 1, 2 \quad (4.21)$$

$$\frac{\partial I_{shear}}{\partial \underline{\underline{C}}} = \frac{1}{\sqrt{I_{41}I_{42}}} (\underline{\underline{L}}_{12} + \underline{\underline{L}}_{21}) - \frac{1}{2} \frac{I_{shear}}{I_{41}} \underline{\underline{L}}_{11} - \frac{1}{2} \frac{I_{shear}}{I_{42}} \underline{\underline{L}}_{22} \quad (4.22)$$

The stain potential energy for elongation modes are defined as a second-order polynomial function:

$$w_{elongi} = T_i (I_{elongi})^2 \quad i = 1, 2 \quad (4.23)$$

T_i is the tensile stiffness in the direction of yarn i .

The in-plan shear energy is defined by a polynomial function:

$$w_{shear} = \sum_{k=2}^8 C_k (I_{shear})^k \quad (4.24)$$

For the bending part, its invariants are denoted by I_{χ_1} and I_{χ_2} in the warp and weft direction, they can be obtained from the curvature tensor in the current configuration $\underline{\underline{\chi}}$:

$$I_{\chi_i} = \underline{\underline{l}}_i \cdot \underline{\underline{\chi}} \cdot \underline{\underline{l}}_i = \chi_{ii} \quad i=1,2 \quad (4.25)$$

$\underline{\underline{l}}_i$ the direction of the yarn i in the current configuration.

Bending moments in the two directions are given by:

$$M_{ii} = \frac{1}{J} \frac{\partial w_{ben}}{\partial I_{\chi_i}} \quad i=1,2 \quad (4.26)$$

Where J is the surface ratio between the current and initial state. And the potential associated with the bending invariant is expressed with temperature dependence as follows:

$$w_{ben} = B_1(T)(I_{\chi_1})^2 + B_2(T)(I_{\chi_2})^2 \quad (4.27)$$

With the two thermo-dependent coefficients b_1 and b_2 obtained from experimental results in Chapter 2.

- *Viscoelastic model for in-plan shear deformation*

In the model of Guzman [GUZ 15], the viscoelastic behavior is primarily associated with the shear deformation mode in the plan. A free energy function is completed by the effect of viscoelastic internal variables:

$$\psi(\underline{\underline{C}}, \underline{\underline{Q}}_i) = w_{mem}(\underline{\underline{C}}) - \frac{1}{2} \sum_{i=1}^N (\underline{\underline{C}} : \underline{\underline{Q}}_i) + \Xi \left(\sum_{i=1}^N \underline{\underline{Q}}_i \right) \quad (4.28)$$

Where $\underline{\underline{Q}}_i$ represents a set of internal variables in the initial configuration not physical measurable and Ξ is a certain function of the internal variables. According to this free energy equation, the membrane stress tensor can be re-written:

$$\begin{aligned} \underline{\underline{S}}_{mem} &= 2 \frac{\partial \psi(\underline{\underline{C}}, \underline{\underline{Q}}_i)}{\partial \underline{\underline{C}}} = 2 \frac{\partial w_{mem}(\underline{\underline{C}})}{\partial \underline{\underline{C}}} - \sum_{i=1}^N \underline{\underline{Q}}_i = \underline{\underline{S}}_{elong1} + \underline{\underline{S}}_{elong2} + \underline{\underline{S}}_{shear} \\ \underline{\underline{S}}_{shear} &= 2 \frac{\partial w_{shear}(\underline{\underline{C}})}{\partial \underline{\underline{C}}} - \sum_{i=1}^N \underline{\underline{Q}}_i \end{aligned} \quad (4.29)$$

Just the in-plan shear deformation part has been completed by the viscoelastic internal variables, and the internal variables are solution of the following equations:

$$\begin{cases} \dot{\underline{\underline{Q}}}_i + \frac{1}{\tau_i} \underline{\underline{Q}}_i = \frac{\gamma_i}{\tau_i} \left[2 \frac{\partial w_{shear}(I_{hear})}{\partial \underline{\underline{C}}} \right] \\ \lim_{t \rightarrow \infty} \underline{\underline{Q}}_i(t) = 0 \end{cases} \quad (4.30)$$

Where $\tau_i > 0$ are the relaxation times and $\gamma_i \in [0,1]$, $\gamma_\infty = 1 - \sum_{i=1}^N \gamma_i$ are the dimensionless materials parameters. The solution of equation can be expressed as an integral convolution:

$$\underline{\underline{Q}}_i(t) = \frac{\gamma_i}{\tau_i} \int_{-\infty}^t \exp\left(-\frac{s-t}{\tau_i}\right) \frac{d}{ds} \left[2 \frac{\partial w_{shear}(I_{hear})}{\partial \underline{\underline{C}}} \right] ds \quad (4.31)$$

Consequently, the stress tensor associated to the in-plan shear part is:

$$\underline{\underline{S}}_{shear}(t) = \int_{-\infty}^t \left(\gamma_\infty + \sum_{i=1}^N \gamma_i \exp\left(-\frac{s-t}{\tau_i}\right) \right) \frac{d}{ds} \left[2 \frac{\partial w_{shear}(I_{hear})}{\partial \underline{\underline{C}}} \right] ds \quad (4.32)$$

All the parameters including C_k are temperature dependence, they can be identified from experimental results presented in Chapter 2, and these parameters for the worked material 2x2 twill in carbon/PA66 prepreg are shown as follows, and are used for the final forming simulation in the next chapter.

In-plan shear elastic properties

$$w_{shear}(I_{shear}, T) = \begin{cases} (\alpha_1^w T + \beta_1^w) \cdot \sum_{i=2}^8 C_i I_{shear}^i & 250^\circ\text{C} < T \leq 260^\circ\text{C} \\ (\alpha_2^w T + \beta_2^w) \cdot \sum_{i=2}^8 C_i I_{shear}^i & 260^\circ\text{C} < T < 300^\circ\text{C} \end{cases}$$

$$\alpha_1^w = -2.437E-03 \text{ K}^{-1}, \beta_1^w = 7.074$$

$$\alpha_2^w = -6.647E-03 \text{ K}^{-1}, \beta_2^w = 2.307$$

C_2	C_3	C_4	C_5	C_6	C_7	C_8	Unit
3.347	-1.963	-2.559	7.906	7.271	1.013	-6.543	[J mm ⁻²]

In-plan shear viscous properties

$$\gamma_1 = \alpha_1^\gamma T + \beta_1^\gamma, \quad \gamma_2 = \alpha_2^\gamma T + \beta_2^\gamma, \quad \tau_1 = \alpha_1^\tau T + \beta_1^\tau, \quad \tau_2 = \alpha_2^\tau T + \beta_2^\tau$$

α_1^γ	α_2^γ	α_1^τ	α_2^τ	Unit
-------------------	-------------------	-----------------	-----------------	------

-3.816E-04	6.716E-04	3.167E-03	2.210E+00	K ⁻¹
------------	-----------	-----------	-----------	-----------------

β_1^γ	β_2^γ	β_1^τ	β_2^τ	Unit
------------------	------------------	----------------	----------------	------

1.068E+00	-1.620E-01	1.872E-01	-4.084E+02	-
-----------	------------	-----------	------------	---

Table 4. 2: In-plan shear parameters with viscoelastic behavior

4.3 Viscoelastic characterization for consolidation behavior

4.3.1 Review of the relatives works

As final step of thermoplastic composites manufacturing process, consolidation appears to be the rate-determining step of the overall process. During this step, pressure is applied, plies are engaged in a full contact and inter- and intra-ply porosity is eliminated by means of compaction. Hence, modelling of consolidation step has received significant attention in order to predict the consolidation time and void content with the given process parameters like temperature, pressure, and compaction rate. Since there exists four primary resin flow

phenomena during the forming and consolidation steps: resin percolation, transverse squeeze flow, inter-ply slip, and intra-ply slip, the first two types are particularly important during consolidation step. Most of the current models focus on the two types of resin flow.

The squeeze flow is occurred between two impermeable surfaces and typically applied for thermoplastics such as PEEK, PS, and PP, where the laminate behaves as a highly viscous incompressible fluid. The first analytical model is proposed by Rogers for an ideal unidirectional fiber reinforced Newtonian fluid [ROG 89], two conditions (no-slip and zero-friction) have been investigated to obtain the relation between the applied pressure and the thickness. Based on this solution, many other authors have developed it taking account of more complex conditions. Like Kaprielian and O'Neil [KAP 89], for the purpose of description of the flow in a laminated composite which consists of an arbitrary number of plies, each layer is modelled as a Newtonian viscous fluid, and ply interaction condition is applied; Balasubramanyam et al. [BAL 89] have accounted partial slip; And dealing with the laps and gaps phenomena during processing, the transverse flow is described by the equations governing the flow of a power law fluid in the study of Wang [WAN 91]. Moreover, the transverse squeeze flow has been modelled for more complex forms of material behavior. For example, Shuler et al. [SHU 96] focuses on considering the flow behavior as Carreau fluid model (describing the viscosity as Newtonian behavior at low shear rates followed by shear thinning power-law behavior at higher shear rates), the effect of processing characteristics of thermoplastic composites has been investigated comparing with the experiences results.

The percolation (bleeding) flow is characterized by the motion of the resin relative to the fiber bed, is typically used for the description of low viscosity thermosetting resin systems. In percolation flow, the resin flow is described by Darcy's law. The model of Springer and Loos [SPR 82] [LOO 83] considers flow in both horizontal and vertical directions of the laminate, the vertical direction's flow is in terms of Darcy's Law for flow, and this model predicts the laminate mass loss and thickness variation during the cure cycle. Based on the soil consolidation theory, a three-dimensional resin flow model has been developed by Dave et al. [DAV 87]. In this model, the consolidation behavior of a composite laminate is explained by the spring and piston analogy (**Figure 4. 1**). The spring represents the compressible fiber bed, the liquid represents the epoxy in the void space of the fiber bed, and the stopcock opening represents the permeability. The fiber bed has an elastic behavior, while the resin flow is described by the rate of fluid bleeding out. The stress equilibrium equation is used to calculate only one resin pressure, other aspects related to resin flow like the consolidation profile of the laminate, the resin content profile, and void migration can also be predicted. In the study of Kelly [KEL 11], a viscoelastic model is proposed based on an empirical expression where a multiplicative decomposition of the compaction stress is in function of strain and strain-rate parts (elastic, viscous parts), and the viscosity of the fiber reinforced fluid represented by this multiplicative decomposition can considered to describe the percolation flow.

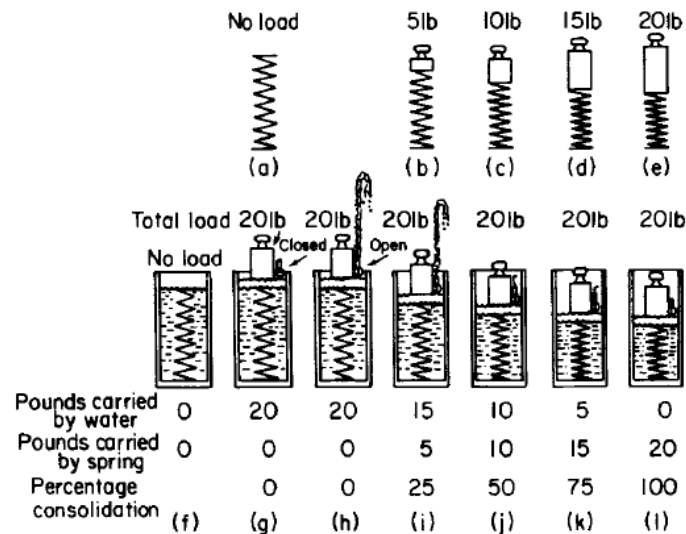


Figure 4. 1: Consolidation model by the piston and spring analogy [DAV 87]

Based on the two flow types, a recent investigation by Belnoue et al. [BEL 16] focuses on the resin flow in uncured toughened prepreg systems. A new phenomenological model considering both squeezing and percolation flows is proposed, a transition between the two flows is realized by a critical level ('locked' shear angle of fibers) (**Figure 4. 2**). In this model, the multiplicative decomposition of the apparent ply viscosity is with the terms of strain and strain rate dependents, which leads to a smooth transition from squeezing flow to percolation flow. Moreover, this model has been implemented in the form of a hyper-viscoelastic model with the viscous potential part of the matrix.

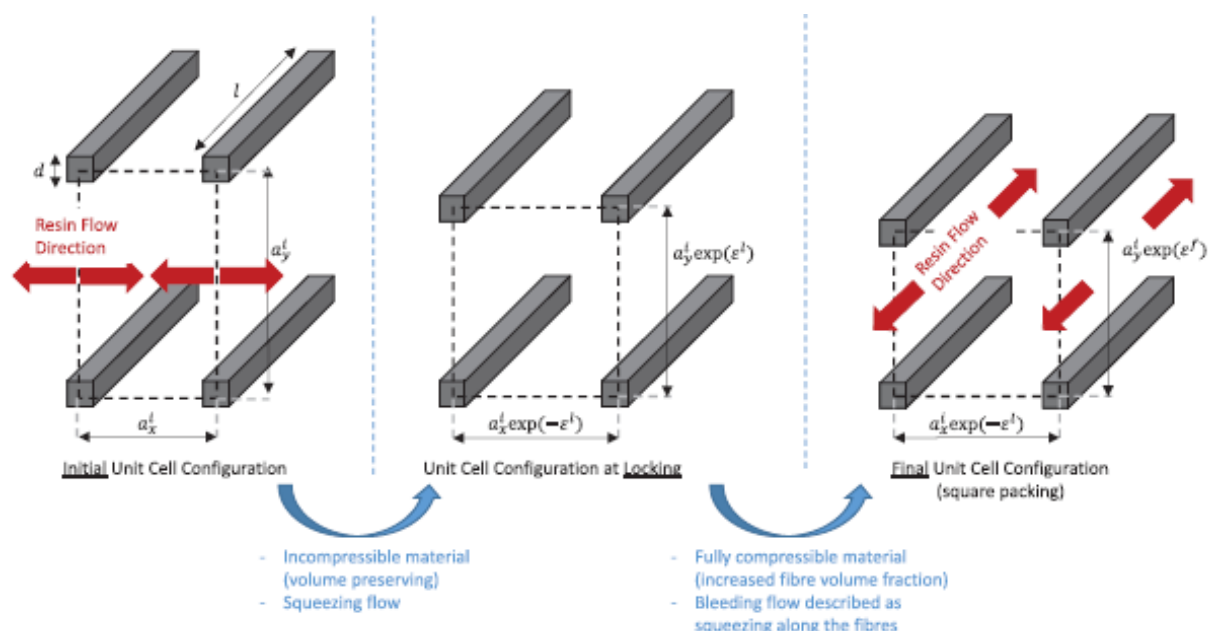


Figure 4. 2: Consolidation model containing squeezing and percolation flows [BEL 16]

Otherwise, there exists many models for the consolidation of commingled thermoplastic fabrics (the yarn containing both the reinforcement and the matrix in fiber form). Among them, one commonly mentioned model in literatures is the model of Van West [VAN 91a], which

contains three submodels. The physical processes is represented by a mechanical model shown in **Figure 4.3**. Firstly, the applied consolidation pressure is resisted only by the elastic behavior of inter-bundle of fibers, the compaction model is employed to express the relation between the applied pressure and the thickness. As the compaction continues (h_i), the matrix coalesces, the flow based on Darcy's law is forced to flow through the bundle permeability. At height h_b , the fiber bed elastic resistance is mainly from the intra-bundle, when the bundle chamber is full, the matrix will flow out and become in plan flow. Impregnation submodel is represented for the flow into the chamber. The Van West's model has detailedly presented the consolidation of commingled thermoplastic fabrics, and allows to predict the thickness, fiber volume fraction, and void content as a function of time. An experimental characterization of the consolidation of commingled composite is done by Long et al. [LON 01]. In this investigation, the evolution of the microstructure analysis is established, more clear consolidation phase is summarized, and the effects of compaction rate, temperature, and pressure on the consolidation have been identified.

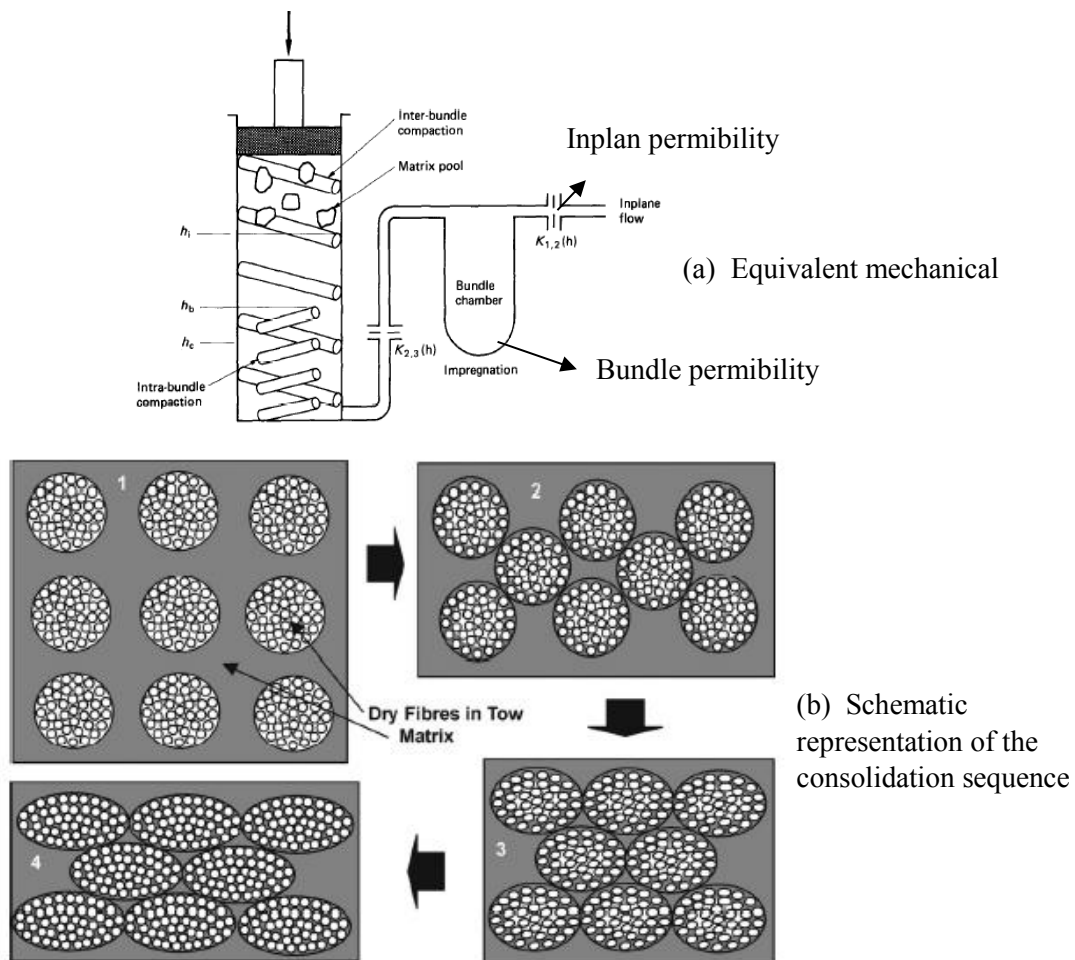


Figure 4.3: Consolidation and in-plane flow processes for the consolidation of commingled thermoplastic fabrics [VAN 91a]

Based on the aforementioned issues, considering the viscosity behavior of matrix flow and the elasticity of fiber-bed, a viscoelastic model for consolidation behavior as an extension of the model of Guzman is developed in the following study. The principle of this model is based on the generalization of classical rheological models such as the Maxwell model and its

formulation in terms of the internal variables [SIM 98]. Moreover, a model for the prediction of the evolution of the consolidation is also established, the applied pressure and temperature are taken into account in this model.

4.3.2 Viscoelastic model for consolidation behavior

Based on the visco-hyper-elasticity behavior for thermoplastic prepregs of Guzman, the transverse compression deformation mode is taken into account as the elasticity part from reinforcement. According to the section 4.2.2, the invariant of transverse compression mode is

$$I_{comp} = \frac{1}{2} \ln\left(\frac{I_3}{I_{41}I_{42}(1-I_{shear}^2)}\right) \quad (4.33)$$

Where I_3 , I_{41} and I_{42} are given in equation (4.7) and (4.13), I_{shear} is the sine of the in-plan shear angle given in equation (4.19). The invariant of the transverse compression mode I_{comp} is the Hencky strain in the thickness. Like the other deformation modes, the transverse compression deformation mode is assumed independent from the others. The strain energy per surface unit of equation (4.16) is added with the transverse compression deformation part:

$$W = W_{mem} + W_{ben} + W_{comp} \quad (4.34)$$

The transverse compression energy is defined by a sixth order polynomial function:

$$W_{comp} = \sum_{k=1}^3 D_k (I_{comp})^{2k} \quad (4.35)$$

The stress tensor resulting from the transverse compression component is:

$$\underline{\underline{S}}_{comp} = 2 \frac{\partial W_{comp}}{\partial I_{comp}} \frac{\partial I_{comp}}{\partial \underline{\underline{C}}} \quad (4.36)$$

With:

$$\begin{aligned} \frac{\partial I_{comp}}{\partial \underline{\underline{C}}} &= \frac{1}{2} \frac{\partial}{\partial \underline{\underline{C}}} \left(\ln(I_3) - \ln(I_{41}) - \ln(I_{42}) - \ln(1 - I_{shear}^2) \right) \\ &= \frac{1}{2} \left(\underline{\underline{C}}^{-1} - \frac{1}{I_{41}} \underline{\underline{L}}_{11} - \frac{1}{I_{42}} \underline{\underline{L}}_{22} + \frac{2I_{shear}}{1 - I_{shear}^2} \frac{\partial I_{shear}}{\partial \underline{\underline{C}}} \right) \end{aligned} \quad (4.37)$$

Taking account of the viscous matrix, the viscoelasticity behavior for the consolidation of thermoplastic prepreg can be characterized by generalized relaxation model [SIM 98] shown in the **Figure 4. 4**, $E_0 = E_\infty + \sum E_i$ is the elastic part from transverse compression mode of dry reinforcement, a series of Maxwell elements in parallel represents the viscous matrix's behavior.

In this model, the stress is defined by:

$$\sigma = E_0 \varepsilon - \sum_{i=1}^N E_i \alpha_i \quad (4.38)$$

The evolution equations to express the internal variables α_i are:

$$\begin{cases} \dot{\alpha}_i + \frac{\alpha_i}{\tau_i} = \frac{\varepsilon}{\tau_i} \\ \lim_{t \rightarrow -\infty} \alpha_i = 0 \end{cases} \quad (4.39)$$

With thermodynamic considerations, the free energy ψ^{comp} is defined as the elastic stored energy in the springs.

$$\psi^{comp}(\varepsilon, \alpha_i) = \frac{1}{2} E_\infty \varepsilon^2 + \frac{1}{2} \sum_{i=1}^N E_i (\varepsilon - \alpha_i)^2 \quad (4.40)$$

The expression of the stress can be rewritten by derivation of free energy:

$$\sigma = \frac{\partial w_0^{comp}(\varepsilon)}{\partial \varepsilon} - \sum_{i=1}^N q_i \quad (4.41)$$

Where the initial stored energy $w_0^{comp}(\varepsilon) = \frac{1}{2} E_0 \varepsilon^2$, τ_i is the relaxation time. $q_i = E_i \alpha_i$ is stress-like set of internal variables.

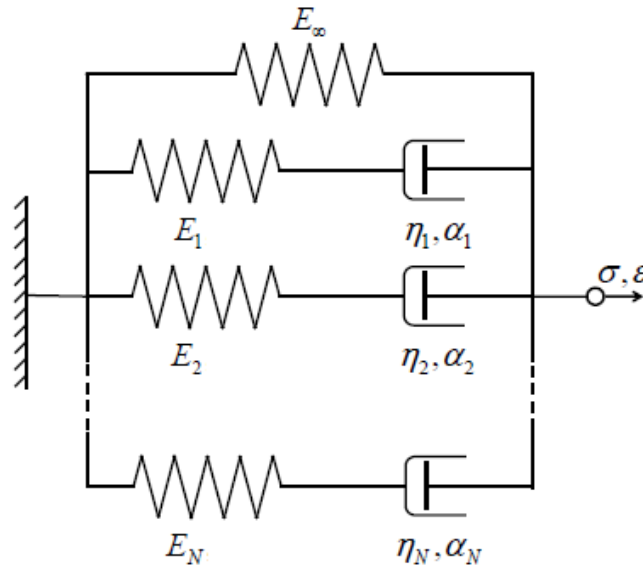


Figure 4. 4: Generalized relaxation model

For the nonlinear case in this study, the above equations are changed. The free energy equation is:

$$\psi^{comp}(\underline{\underline{C}}, \underline{\underline{Q}}_{\equiv i}^{comp}) = w_{comp}(\underline{\underline{C}}) - \frac{1}{2} \sum_{i=1}^N (\underline{\underline{C}} : \underline{\underline{Q}}_{\equiv i}^{comp}) + \Xi \left(\sum_{i=1}^N \underline{\underline{Q}}_{\equiv i}^{comp} \right) \quad (4.42)$$

The evolution equations related to internal variables $\underline{\underline{Q}}_{\equiv i}^{comp}$ are:

$$\begin{cases} \dot{\underline{\underline{Q}}}_{\equiv i}^{comp} + \frac{1}{\tau_i} \underline{\underline{Q}}_{\equiv i}^{comp} = \frac{\gamma_i}{\tau_i} \left[2 \frac{\partial w_{comp}(\underline{\underline{I}}_{comp})}{\partial \underline{\underline{C}}} \right] \\ \lim_{t \rightarrow -\infty} \underline{\underline{Q}}_{\equiv i}^{comp}(t) = 0 \end{cases} \quad (4.43)$$

Where $\gamma_i = E_i / E_0 \in [0,1]$, $\gamma_\infty = 1 - \sum_{i=1}^N \gamma_i$ are the dimensionless material parameters. The second Piola-Kirchhoff stress can be obtained from the derivation of energy:

$$\underline{\underline{S}}_{comp} = 2 \frac{\partial w_{comp}(\underline{\underline{C}})}{\partial \underline{\underline{C}}} - \sum_{i=1}^N \underline{\underline{Q}}_{comp}^i \quad (4.44)$$

The solution of equation (4.43) can be expressed as the convolution integral:

$$\underline{\underline{Q}}_{comp}^i(t) = \frac{\gamma_i}{\tau_i} \int_{-\infty}^t \exp\left(-\frac{s-t}{\tau_i}\right) \frac{d}{ds} \left[2 \frac{\partial w_{comp}(\underline{\underline{I}}_{comp})}{\partial \underline{\underline{C}}} \right] ds \quad (4.45)$$

Consequently, the stress tensor associated to the transverse compression part is:

$$\underline{\underline{S}}_{comp}(t) = \int_{-\infty}^t \left(\gamma_\infty + \sum_{i=1}^N \gamma_i \exp\left(-\frac{s-t}{\tau_i}\right) \right) \frac{d}{ds} \left[2 \frac{\partial w_{comp}(\underline{\underline{I}}_{comp})}{\partial \underline{\underline{C}}} \right] ds \quad (4.46)$$

According to [SIM 98], the internal (algorithmic) variables $\underline{\underline{H}}_i(t)$ are defined by expression:

$$\underline{\underline{H}}_i(t) = \int_{-\infty}^t \exp\left(-\frac{s-t}{\tau_i}\right) \frac{d}{ds} \left[2 \frac{\partial w_{comp}(\underline{\underline{I}}_{comp})}{\partial \underline{\underline{C}}} \right] ds \quad (4.47)$$

For time $t_{n+1} = t_n + \Delta t_n$, recurrence relationship can be obtained:

$$\underline{\underline{H}}_i(t_{n+1}) = \exp\left(-\frac{\Delta t_n}{\tau_i}\right) \underline{\underline{H}}_i(t_n) + \exp\left(-\frac{\Delta t_n}{2\tau_i}\right) (\underline{\underline{S}}_{n+1}^0 - \underline{\underline{S}}_n^0) \quad (4.48)$$

Where $\underline{\underline{S}}_n^0$ is stress tensor from the pure elastic part at time t_n . Combining equation (4.44) and (4.48), the stress tensor at time t_{n+1} is actualized as follows:

$$\underline{\underline{S}}_{comp}(t_{n+1}) = \gamma_\infty \underline{\underline{S}}_{n+1}^0 + \sum_{i=1}^N \gamma_i \underline{\underline{H}}_i(t_{n+1}) \quad (4.49)$$

The viscoelasticity to characterize the transverse compression behavior is established. The parameters for the model are: the coefficients D_k from equation, the relaxation time parameters τ_i , and the dimensionless material parameters γ_i . These parameters are identified by compaction test.

4.3.3 Identification of parameters

It's known that the consolidation behavior of thermoplastic prepreps is thermo-dependent due to the viscosity of matrix. All the material parameters are identified respectively. The method used for parameter identification is inverse method [SCH 92], the principle of this method is to match the measured experimental results to a finite element solution with proposed model by using a modified Levenberg-Marquardt method.

The Levenberg-Marquardt method [MAR 63] is developed to solve the unconstrained nonlinear least squares problem. It performs an optimum interpolation between the Taylor series method who leads the optimization process converge rapidly and the gradient method

who permits approach the solution more precisely. In Levenberg-Marquardt algorithm, the independent variables are defined in vector $\underline{p} = [x_1, x_2, \dots, x_k]^T$.

The result of fitted model is

$$\underline{y}_m(t; \underline{p}) = f(t; x_1, x_2, \dots, x_k) \quad (4.50)$$

The problem is to computer those estimates of the parameters which will minimize:

$$\phi = \sum_{i=1}^N \left[\underline{y}_e(t_i) - \hat{\underline{y}}_m(t_i; \underline{p}) \right]^2 \quad (4.51)$$

Where $\hat{\underline{y}}_m(t_i; \underline{p})$ is the value from the fitted model at time t_i , and $\underline{y}_e(t_i)$ is the correspondent experimental data.

The modified Levenberg-Marquardt method is taking account of a weighted penalty function for equation (4.51). And the focused error equation is re-expressed as:

$$\chi^2(\underline{p}) = \frac{1}{2} \sum_{i=1}^N \left[\frac{\underline{y}_e(t_i) - \hat{\underline{y}}_m(t_i; \underline{p})}{w_i} \right]^2 \quad (4.52)$$

And expression in the matrix form is:

$$\chi^2(\underline{p}) = \frac{1}{2} \underline{y}_e^T \underline{W} \underline{y}_e - \underline{y}_e^T \underline{W} \hat{\underline{y}}_m + \frac{1}{2} \hat{\underline{y}}_m^T \underline{W} \hat{\underline{y}}_m \quad (4.53)$$

With w_i being the non-negative weights. \underline{W} is a diagonal matrix composed with the terms $W_{ii} = 1/w_i^2$. The objective of the algorithm involves to search a vector \underline{h} adjusting the vector \underline{p} in order to minimize the equation (4.52).

The gradient method gives the \underline{h} in the form of:

$$\underline{h}_{grad} = \alpha \underline{J}^T \underline{W} (\underline{y}_e - \hat{\underline{y}}_m) \quad (4.54)$$

where α is a scalar positive coefficient, \underline{J} is the jacobian matrix representing the local sensibility of the result $\hat{\underline{y}}_m$ linking to \underline{p} .

While the vector \underline{h} in Taylor series method is given by:

$$\left[\underline{J}^T \underline{W} \underline{J} \right] \underline{h}_{ts} = \alpha \underline{J}^T \underline{W} (\underline{y}_e - \hat{\underline{y}}_m) \quad (4.55)$$

In Levenberg-Marquardt method who balances the two methods with a coefficient λ , the perturbation vector \underline{h} is interpolated as:

$$\left[\underline{J}^T \underline{W} \underline{J} - \lambda \text{diag}(\underline{J}^T \underline{W} \underline{J}) \right] \underline{h}_{lm} = \underline{J}^T \underline{W} (\underline{y}_e - \hat{\underline{y}}_m) \quad (4.56)$$

Hence, the next iteration for the vector \underline{p}_{i+1} is actualized by following equation:

$$\underline{p}_{i+1} = \underline{p}_i + h_{lm} \quad (4.57)$$

And the convergence of the calculation is reached when $\chi^2(\underline{p}_{i+1})$ is not superior to the given critical convergence value.

In this work, the vector of independent parameters is \underline{p} :

$$\underline{p} = [\tau_1, \dots, \tau_n, \gamma_1, \dots, \gamma_n, D_1, D_2, D_3]^T \quad (4.58)$$

The error is calculated from the experimental load $([t, u_{\text{exp}}(t)], F_{\text{exp}})$ and the load calculated from the viscoelastic model $([t, u_{\text{exp}}(t)], F_{\text{model}})$:

$$\chi^2(\underline{p}) = \frac{1}{2} \sum_{i=1}^N \left[F_{\text{exp}}(t_i, u_{\text{exp}}(t_i)) - F_{\text{model}}([t_i, u_{\text{exp}}(t_i)], \underline{p}) \right]^2 \quad (4.59)$$

During the optimization process, two relaxation time parameters τ_1 , τ_2 and two material parameters γ_1 , γ_2 are enough for correct description of the model. And the optimized parameters are obtained from the experimental results at each temperature (shown in **Table 4. 3**). **Figure 4. 5** plots the comparison of experimental load and optimal load at different temperature.

	260°C	270°C	280°C	300°C	Units
D ₁	2.274e-02	6.814e-02	2.177e-02	8.793e-02	[J mm ⁻²]
D ₂	4.113e-01	5.870e-01	3.607e-01	6.889e-01	[J mm ⁻²]
D ₃	2.478e+00	1.080e+00	1.279e+00	1.466e+00	[J mm ⁻²]
D ₄	5.386e+00	3.434e-01	1.974e+00	-3.411e-01	[J mm ⁻²]
D ₅	4.170e+00	1.383e+00	-9.312e-01	6.299e-01	[J mm ⁻²]
γ_1	7.293e+00	1.043e+00	5.236e-01	8.024e-01	-
γ_2	4.499e-01	5.754e-01	9.420e-02	4.443e-01	-
τ_1	3.587e+01	8.473e-01	5.787e-02	3.638e-01	[s]
τ_2	2.037e+01	6.724e-01	3.262e-01	3.881e-01	[s]

Table 4. 3: Optimized parameters related to consolidation deformation mode at different temperature

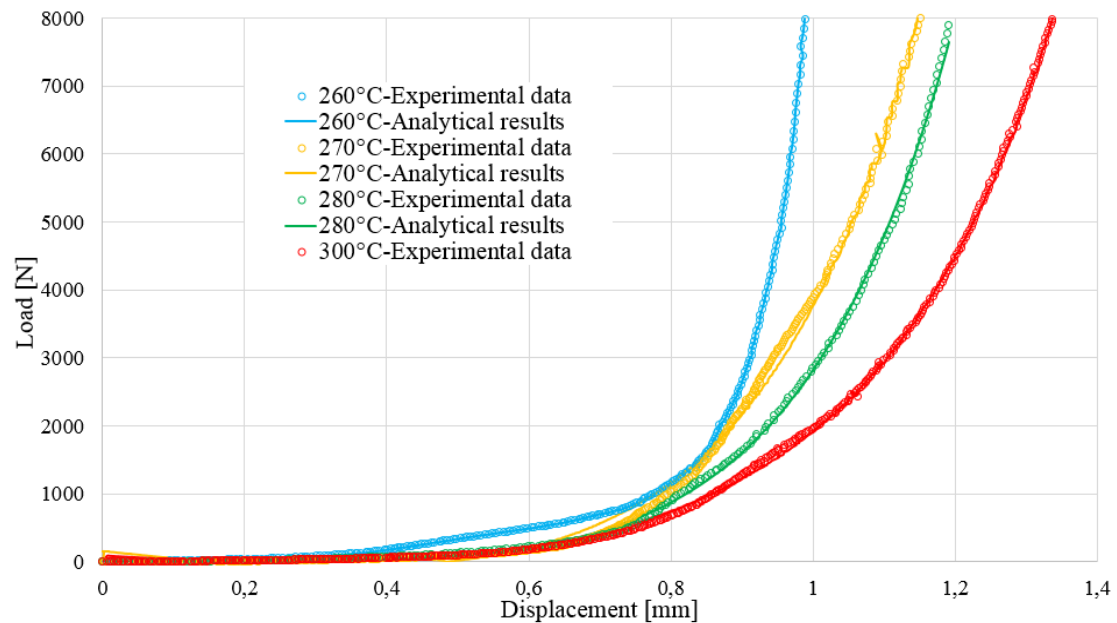


Figure 4. 5: Load vs. time curves of experimental data and optimal results

4.4 Intimate contact model for the prediction of consolidation

During the thermoforming process especially for the consolidation step, the ply surfaces are uneven, there exists spatial gaps between the plies and other porosities between and through the yarns. Not like thermoset matrix composites, the viscosity of thermoplastic is too high that the resin flow can't achieved at desired degree. However, it can be improved by controlling the manufacturing conditions. Hence, knowing the evolution of consolidation is important for the appearance of defects in final composite part. It depends on the processing parameters like pressure, temperature, and time. The intimate contact model will be used for the purpose of quantification and visualization of intimate contact between adjacent surfaces during forming simulation, which allows to appropriate processing condition for processing thermoplastic composites.

4.4.1 Intimate contact model

This model is proposed by Lee et al. [LEE 87] for the description of the coalescence of two adjacent ply surface for manufacturing thermoplastic composite plates, and it has been extended by Susan [MAN 92] even in the application of filament winding of cylinders. In the work of Phillips [PHI 98], the mechanism of intimate contact is employed to be responsible for the resorption, an associated model is proposed for the prediction of consolidation, and these predictions have shown good agreement with experimental results from optical microscopy and fracture tests.

Following the investigation of Lee and Springer, the initial irregular ply surface are represented as a series of identical rectangles (**Figure 4. 6**). At the initial state $t=0$, the mixture of reinforcement-matrix is represented by the rectangular elements of dimension $a_0 \times b_0$, while the other rectangular elements of dimension $w_0 \times b_0$ refer to the voids. With the action of applied force or pressure, the rectangular elements spread along the interface, the width of reinforcement-matrix mixture elements becomes b , while the width of void elements decrease

to $w (t > 0)$. The extent of this spread is defined as a function of temperature, force (pressure), and time, and it is called degree of intimate contact D in this model.

$$D = \frac{b}{w_0 + b_0} \quad (4.60)$$

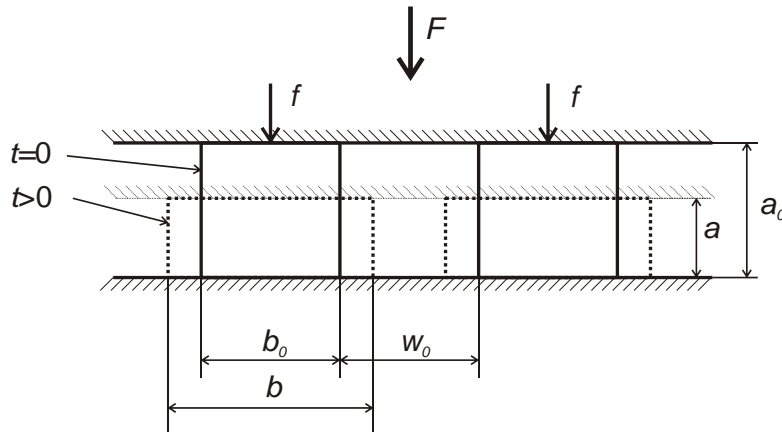


Figure 4. 6: Discretization by regular rectangular elements with intimate contact model

During processing, the sum of the widths of mixture element b and void element w remains constant, and the volume of each mixture element b remains constant too:

$$w_0 + b_0 = w + b, \quad a_0 b_0 = ab \quad (4.61)$$

According to equation (4.60), the ‘complete’ intimate contact is reached when $w=0$, $b=b_0+w_0$, $D=1$, the voids are completely eliminated.

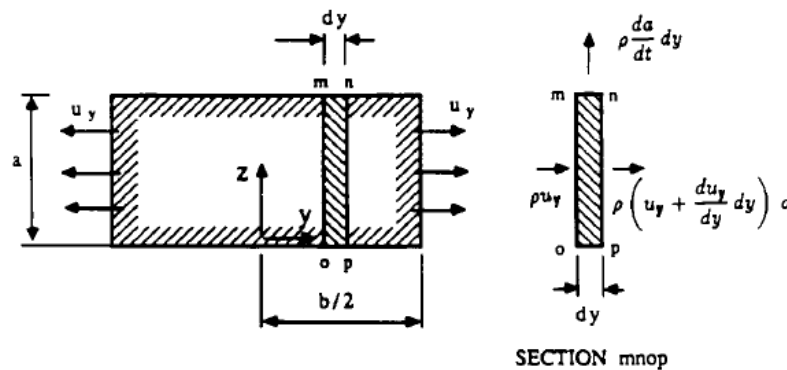


Figure 4. 7: Calculation of mass flows by volume control for one element at time t

In **Figure 4. 7** at time t , one mixture element is considered, a control volume of width dy is applied by the law of conservation of mass:

$$a \frac{dy_y}{dy} + \frac{da}{dt} = 0 \quad (4.62)$$

Assuming that the flow is laminar, Poiseuille’ law allows to describe the velocity field for this rectangular element:

$$v(z) = v_{\max} \left(\left| \frac{4z}{a} \right| - \frac{4z^2}{a^2} \right), \quad v_{\max} = -\frac{a^2}{8\eta} \frac{dp}{dy} \quad (4.63)$$

where the maximum velocity occurs in the middle of ply $z=a/2$, η is the viscosity (assuming that in isothermal case η is constant), dp/dy is the gradient of pressure.

The average velocity v_y can be obtained by integral of equation (4.63):

$$v_y = \frac{\int_0^a v(z) dz}{a} = -\frac{a^2}{12\eta} \frac{dp}{dy} \quad (4.64)$$

Combining equation (4.62) and (4.64):

$$-\frac{a^3}{12\eta} \frac{d^2 p}{dy^2} + \frac{da}{dt} = 0 \quad (4.65)$$

After integration of the equation, the pressure p is expressed as follows:

$$p = \frac{6\eta y^2}{a^3} \frac{da}{dt} + C_1 y + C_2 \quad (4.66)$$

With the boundary conditions:

$$p\left(y = \frac{b}{2}\right) = p\left(y = -\frac{b}{2}\right) = p_e \quad (4.67)$$

Two parameters C_1 C_2 are calculated, equation (4.66) can be rewritten:

$$p - p_e = \frac{6\eta}{a^3} \frac{da}{dt} \left(y^2 - \frac{b^2}{4} \right) \quad (4.68)$$

Where p_e is the pressure between two adjacent elements.

The force applied to the entire ply of length A and width B is F (**Figure 4. 6**). Correspondingly, the force applied per unit length to one mixture element is:

$$f = \frac{F}{A} \frac{1}{n} \quad (4.69)$$

n is the number of mixture elements in ply, $n=B/(b_0+w_0)$. Hence,

$$f = \frac{F}{AB} (b_0 + w_0) = p_{app} (b_0 + w_0) \quad (4.70)$$

where p_{app} is the applied pressure. The equilibrium of equation on one element is:

$$f = \int_{-b/2}^{b/2} (p - p_e) dy \quad (4.71)$$

From equation (4.68), (4.70) and (4.71), we obtain:

$$p_{app} (b_0 + w_0) = -\frac{\eta b^3}{a^3} \frac{da}{dt} \quad (4.72)$$

After integration with time, the equation (4.72) becomes:

$$\frac{1}{5a^5} = \frac{p_{app}(b_0 + w_0)}{a_0^3 b_0^3 \eta} t + C_3 \quad (4.73)$$

Since the applied pressure is not constant during processing, the focused equation will be discretized with very small increment of time Δt . After every increment, the time returns to 0, during the small increment of time, the applied pressure p_{appn} don't vary. And the width of mixture element is a_n , after Δt , we have the relations:

$$t = 0, a = a_n; \quad t = \Delta t, a = a_{n+1} \quad (4.74)$$

At time $t=0$, $C_3 = \frac{1}{5a_n^5}$. The width after the n^{th} time increment is

$$a_{n+1} = \left[\frac{5p_{appn}(b_0 + w_0)\Delta t}{a_0^3 b_0^3 \eta} + \frac{1}{a_n^5} \right]^{-1/5} \quad (4.75)$$

And the degree of intimate contact at $(n+1)^{\text{th}}$ time increment is:

$$D_{n+1} = \frac{a_0 / a_{n+1}}{1 + w_0 / b_0} \quad (4.76)$$

Two geometric ratios k_1, k_2 are introduced: $k_1 = \frac{a_0}{b_0}, k_2 = \frac{w_0}{b_0}$.

Equation and equation become to:

$$a_{n+1} = \left[\frac{5p_{appn}(1+k_2)k_1^2\Delta t}{a_0^5\eta} + \frac{1}{a_n^5} \right]^{-1/5} \quad (4.77)$$

$$D_{n+1} = \frac{a_0 / a_{n+1}}{1 + k_1}$$

Hence, the intimate contact model can be constituted by knowing the dimension of ply length A, width B, the applied force F or pressure P_{app} , temperature T, consolidation time t, matrix fiber viscosity η , and the geometric ratios, the last three parameters of material can be identified by compaction test.

4.4.2 Verification test

A series of numerical tests have been set up in order to verify the intimate contact model and investigate the influence of processing parameters. The tested thermoplastic prepreg is the T300/PEEK whose material properties are detailed in [LEE 87], the geometric coefficients of this material defined in the previous section are: $k_1=0.3$; $k_2=1$, and the viscosity is $\eta = 1.14 \times 10^{-12} \left[\exp \frac{26300}{T(^{\circ}\text{K})} \right]$. Based on this material, three levels of temperature and three levels of pressure are controlled for different numerical tests. The results of the degree of intimate contact D during the course of time are presented in the following figures (**Figure 4.8**), from which the influence of temperature and the influence of pressure are remarkable, the

higher temperature and the larger pressure are applied, completed intimate contact will be obtained more quickly.

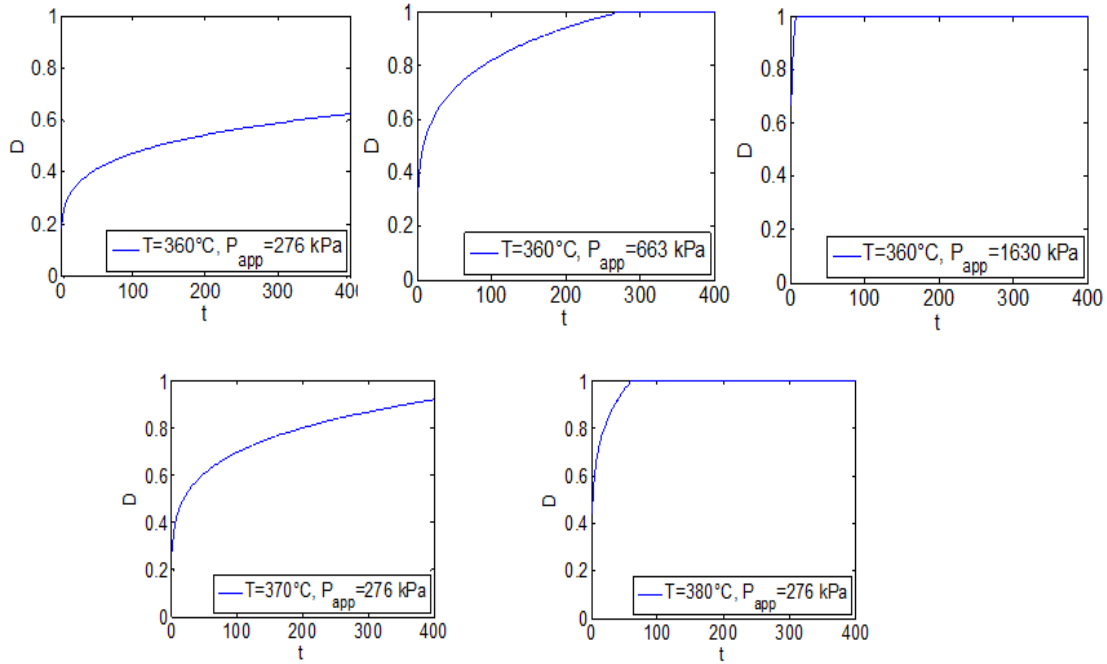


Figure 4. 8: Degree of intimate contact versus contact time as a function of applied pressure (three top) and temperature (two bottom)

4.4.3 Identification of parameters

As mentioned in previous section, the last three parameters of material matrix fiber viscosity η , and the geometric ratios k_1 , k_2 can be identified by compaction test with a given temperature. Similar to the identification method for the viscoelastic model, these three parameters are identified by inverse method by using the experimental results of compaction tests (detailed in chapter 2) as conference results.

The vector of independent parameters is \underline{p} :

$$\underline{p} = [k_1, k_2, \eta]^T \quad (4.78)$$

The error is calculated from the experimental displacement $([t, F_{\text{exp}}(t)], u_{\text{exp}})$ and the displacement calculated from the proposed model $([t, F_{\text{exp}}(t)], u_{\text{model}})$:

$$\chi^2(\underline{p}) = \frac{1}{2} \sum_{i=1}^N [u_{\text{exp}}(t_i, F_{\text{exp}}(t_i)) - u_{\text{model}}([t_i, F_{\text{exp}}(t_i)], \underline{p})]^2 \quad (4.79)$$

During the algorithm of optimization for the material's parameters, the simulated displacement of the model is calculated from a given experimental force. The transverse compaction stress obtained from this applied force represents the applied pressure on each mixture element. After the identification procedure, the parameters for the 2x2 Twill/PA66 thermoplastic pre-impregnated composites material at temperature 280° is $k_1=0.5$, $k_2=1.5$,

$\eta=110$ MPa·s. And the displacement vs. time curves of experimental results and simulation results are shown in **Figure 4. 9**. Some comments can explain the big difference between the curves. According to the hypotheses for the model, the dimension of the plate rests constant, and during each increment of time, the applied pressure remains constant too. While during experimental test, the significant emission of resin is not ignorable, hence it occurs to big change of the dimension. Otherwise, the investigation of the choice of incremental time is also important to conform to the hypotheses.

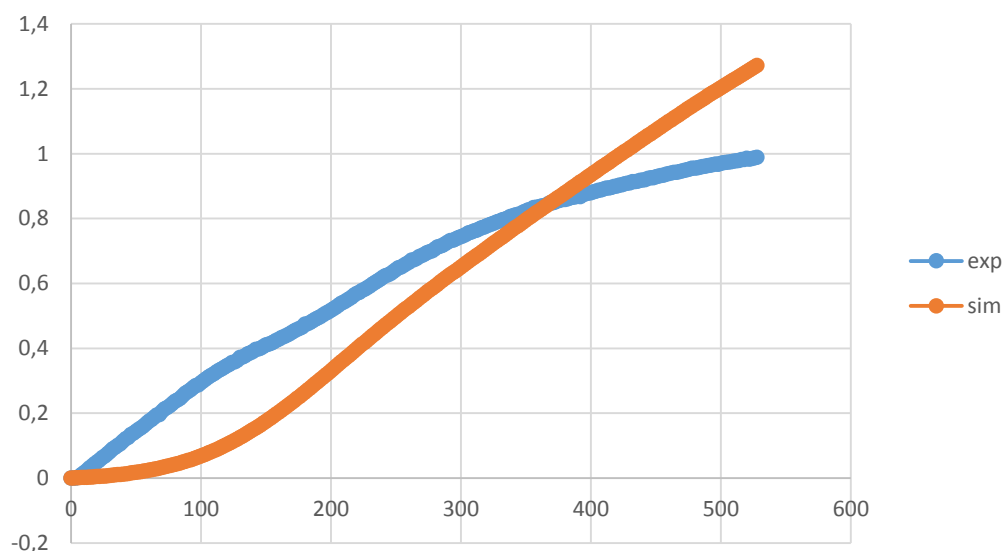


Figure 4. 9: Displacement vs. time curves of experimental data and the optimized results of intimate contact model

4.5 Conclusion of chapter 4

In this chapter, a viscoelastic model based on relaxation model is proposed for characterization of transverse consolidation deformation within a hyperelastic framework. A visco-hyper-elastic model is completed to describe mechanical behavior of thermoplastic prepreg composite forming. The potential energy is then composed of five deformation modes: elongation in the direction of warp yarn, elongation in the direction of weft yarn, in-plan shearing deformation, bending deformation, and transverse compression deformation. Among them, viscosity consideration is taken account for the in-plan shear part and also consolidation part. Each deformation mode is characterized by a physical invariant which permits the decoupling of internal energy, and each of them can be identified separately by simple tests (traction test, cantilever test, bias-extension test, and compaction test). Moreover, an intimate contact model is employed to predict the evolution of the consolidation which exhibits the microstructure prediction of void presented through the prepreg. The identification of material parameters associated to the models are launched by an inverse method. The two models will be implanted in a finite element software by using the developed solid-shell element to simulate the thermoforming processing particularly for the consolidation part. In which, the viscoelastic model is used to characterize the transverse consolidation deformation and get the transverse compaction stress through the thickness, while the intimate contact model acts in the post-treatment process of numerical simulation, to demonstrate the consolidation effect by using the transverse compaction stress.

Chapter 5

Numerical simulations

5.1 Introduction

After the developing of the new adapted finite element and the characterization of the transverse consolidation behavior for the thermoplastic prepreg composites, the final part of this work is to discretize the constitutive behavior of interested material and launch forming simulations in order to verify the efficiency of the proposed element and models. The simulations are carried out in a finite element explicit code Plasfib [PLA 11] developed by LaMCoS, focuses on the forming simulation of dry reinforcement composites [HAM 07]. There are several elements existing in the code: the rigid elements for the modeling of the forming tools; the shell elements and special membrane element for the modeling of 2D [BOI 05] [HAM 09] [BEL 11] and 3D fabrics [LUY 09]; the recently developed shell element for the simulation of thermoforming process of thermoplastic composites [GUZ 15]. In this work, a new solid-shell element is implanted, the rigidity of the thermoplastic composites composes of four principal rigidities: the tensile stiffness in the yarn's directions; the in-plan shear stiffness; the bending stiffness who calculates directly from the elementary DOF's displacements; the transverse consolidation stiffness.

The numerical simulations in this chapter are decomposed by two parts: the first part is the elementary simulations in order to validate different modes of deformation by using the developed element and consolidation model; after the elementary validations, the second part is the thermoforming simulation by taking account of the consolidation effect. Before them, nonlinear finite element discretization and the central difference method are firstly presented.

5.2 Central difference method of explicit schema

5.2.1 Principle of virtual work

The principle of virtual work at time t in the updated Lagrangian formulation can be written as:

$$\delta W_{\text{int}} - \delta W_{\text{ext}} + \delta W_{\text{kin}} = 0 \quad (5.1)$$

The virtual kinetic work is:

$$\delta W_{\text{kin}} = \int_{\Omega} \delta \mathbf{u} \cdot \rho \ddot{\mathbf{u}} d\Omega \quad (5.2)$$

The virtual internal work for the deformed continuum material contains four parts: membrane work, bending work, transverse compaction work, and transverse shear work.

$$\delta w_{\text{int}} = \delta w_{\text{memb}} + \delta w_{\text{bend}} + \delta w_{\text{comp}} + \delta w_{\text{ts}} = \int_{\Omega} \frac{\partial(\delta \mathbf{u})}{\partial \mathbf{x}} \boldsymbol{\sigma} d\Omega \quad (5.3)$$

The virtual external work results from the external loads (including body force, surface force, concentrated force etc.) is given as:

$$\delta w_{\text{ext}} = \int_{\Omega} \delta \mathbf{u} \cdot \rho \mathbf{b} d\Omega \quad (5.4)$$

5.2.2 Finite element discretization

The spatial discretization of the equilibrium equation of virtual works is realized by the finite element method. The current domain Ω is subdivided into solid prismatic elements Ω_e , the real and virtual displacement fields are interpolated by the real and virtual nodal displacements of proposed element SB7Y19 described in chapter 3. For each element, the internal nodal forces are defined from elementary virtual internal work:

$$\delta w_{\text{int}}^e = \int_{\Omega_e} \frac{\partial(\delta \mathbf{u})}{\partial \mathbf{x}} \boldsymbol{\sigma} d\Omega = \delta \mathbf{u}_e \int_{\Omega_e} \frac{\partial \mathbf{N}}{\partial \mathbf{x}} \boldsymbol{\sigma} d\Omega = \delta \mathbf{u}_e \mathbf{F}_{\text{int}}^e \quad (5.5)$$

The group of shape functions \mathbf{N} and their derivatives are defined in chapter 3. The internal nodal forces represent the stresses in the body, they also contain three part:

$$\mathbf{F}_{\text{int}}^e = \int_{\Omega_e} \frac{\partial \mathbf{N}}{\partial \mathbf{x}} \boldsymbol{\sigma}^t d\Omega = \underbrace{\int_{\Omega_e} \mathbf{B}_{m0} \boldsymbol{\sigma}_{\text{memb}}^T d\Omega}_{\text{membrane part}} + \underbrace{\int_{\Omega_e} \mathbf{B}_{b0} \mathbf{M}^T d\Omega}_{\text{bending part}} + \underbrace{\int_{\Omega_e} \mathbf{B}_{p0} \boldsymbol{\sigma}_{33} d\Omega}_{\text{compaction part}} + \underbrace{\int_{\Omega_e} \mathbf{B}_{c0} \boldsymbol{\sigma}_{i3}^T d\Omega}_{\text{transverse shear part}} \quad (5.6)$$

Similarly, the external nodal forces are defined in terms of the elementary virtual external work:

$$\delta w_{\text{ext}}^e = \int_{\Omega_e} \delta \mathbf{u} \cdot \rho \mathbf{b} d\Omega = \delta \mathbf{u}_e \int_{\Omega_e} \mathbf{N} \cdot \rho \mathbf{b} d\Omega = \delta \mathbf{u}_e \mathbf{F}_{\text{ext}}^e \quad (5.7)$$

Respectively, the kinetic nodal forces are defined by

$$\delta w_{\text{kin}}^e = \int_{\Omega_e} \delta \mathbf{u} \cdot \rho \ddot{\mathbf{u}} d\Omega = \delta \mathbf{u}_e \int_{\Omega_e} \mathbf{N} \cdot \rho \ddot{\mathbf{u}} d\Omega = \delta \mathbf{u}_e \mathbf{F}_{\text{kin}}^e \quad (5.8)$$

Combing equation (5.1), (5.5), (5.7) and (5.8), dynamic equilibrium equation can be written with the damping forces:

$$\mathbf{M} \ddot{\mathbf{u}} + \mathbf{C} \dot{\mathbf{u}} + \mathbf{F}_{\text{int}} - \mathbf{F}_{\text{ext}} = 0 \quad (5.9)$$

\mathbf{M} is the mass matrix of element $\mathbf{M} = \int_{\Omega_e} \rho \mathbf{N} \cdot \mathbf{N}^T d\Omega$, the simple method is to summation all terms of each line and obtain a diagonal matrix \mathbf{M}_{diag} [ZIE 05]:

$$M_{ij}^{\text{diag}} = \begin{cases} \sum_{k=1}^n M_{ik} & i=j \\ 0 & i \neq j \end{cases} \quad (5.10)$$

Each component for the three DOFs of six apex nodes in the diagonal matrix can be calculated from the work of Hughes [HUG 87]. For the seventh central node, the mass is equal to the sum of the masses at the apex nodes which is detailed in the thesis of Sansalone [SAN 11b].

\mathbf{C} is the damping matrix, calculated from the mass matrix with a damping coefficient α :

$$\mathbf{C} = \alpha \mathbf{M} \quad (5.11)$$

5.2.3 Temporal integration schema

Generally, two approaches widely used in the finite element are implicit approach and explicit approach. In a nonlinear dynamic problem which it is in the case of forming process, the explicit dynamic approach is more numerically efficient and used in present study. The dynamic motion equations can be solved step by step by using iterative temporal integration schema. The time is discretized by given time increments. The algorithms express the nodal accelerations, velocities, and displacements at each time increment from the values at its previous time increment. In Plasfib, the schema Newmark β -method [BEL 13] is used, especially the central difference method. The updated displacements, velocities, and accelerations are:

$$\begin{aligned} \mathbf{u}_{n+1} &= \mathbf{u}_n + \Delta t \cdot \dot{\mathbf{u}}_n + \frac{1}{2} \Delta t^2 \ddot{\mathbf{u}}_n \\ \dot{\mathbf{u}}_{n+1} &= \dot{\mathbf{u}}_n + \frac{1}{2} \Delta t \cdot (\ddot{\mathbf{u}}_n + \ddot{\mathbf{u}}_{n+1}) \\ \ddot{\mathbf{u}}_{n+1} &= \ddot{\mathbf{u}}_n + \Delta \ddot{\mathbf{u}}_n \end{aligned} \quad (5.12)$$

Where Δt is the time increment. The displacement increments at instant t_{n+1} is:

$$\Delta \mathbf{u}_{n+1} = \mathbf{u}_{n+2} - \mathbf{u}_{n+1} = \Delta t \cdot \dot{\mathbf{u}}_n + \frac{1}{2} \Delta t^2 \ddot{\mathbf{u}}_n + \frac{1}{4} \Delta t^2 \ddot{\mathbf{u}}_{n+1} \quad (5.13)$$

Combing equation (5.12) and (5.13), the updated velocities and accelerations are rewritten as:

$$\begin{aligned} \dot{\mathbf{u}}_{n+1} &= \frac{1}{2\Delta t} \Delta \mathbf{u}_{n+1} + \frac{1}{2} \dot{\mathbf{u}}_n + \frac{1}{4} \Delta t \cdot \ddot{\mathbf{u}}_n \\ \ddot{\mathbf{u}}_{n+1} &= \frac{1}{\Delta t^2} \Delta \mathbf{u}_{n+1} - \frac{1}{\Delta t} \dot{\mathbf{u}}_n - \frac{1}{2} \ddot{\mathbf{u}}_n \end{aligned} \quad (5.14)$$

The displacement increments at instant t_{n+1} can be obtained by taking equation (5.9) into dynamic motion equations:

$$\frac{\alpha/2 + 1/\Delta t}{\Delta t} \mathbf{M} \Delta \mathbf{u}_{n+1} = \mathbf{F}_{ext} - \mathbf{F}_{int} - \alpha \mathbf{M} \left(\frac{1}{2} \dot{\mathbf{u}}_n + \frac{1}{4} \Delta t \ddot{\mathbf{u}}_n \right) + \mathbf{M} \left(\frac{1}{\Delta t} \dot{\mathbf{u}}_n + \frac{1}{2} \ddot{\mathbf{u}}_n \right) \quad (5.15)$$

With the initial conditions $\mathbf{u}_0 = \mathbf{u}_{t=0}$, $\dot{\mathbf{u}}_0 = \dot{\mathbf{u}}_{t=0}$. The updated displacement increments permit computer the new internal nodal loads and new increment is used for the next calculation. The explicit schema is conditionally stable and restricts the allowable time increment Δt to less than the critical time increment Δt_{cri} . The critical time increment value depends on the smallest element size and material properties.

5.3 Elementary validation tests

5.3.1 Bias-extension test

The first test consisting in the validation of the in-plan shear deformation mode is bias-extension test. The fabric is initially rectangular with dimension 70mm x 210mm x 0.1mm, and

the mesh is shown in **Figure 5. 1** (a), the mechanical properties of the thermoplastic composites at temperature 270° are given in [GUZ 15]. The clamp is imposed with a displacement by increments of 10mm, the speed is 30min/min, and the total displacement is 50mm which corresponds a theoretical shear angle of 57° . The computed result using the finite element simulation with the proposed solid-shell element SB7Y19 is compared with the simulation of triangle shell element and the experimental data. In **Figure 5. 1** (b) and (c), the load versus time curves and shear angle versus displacement curves are presented. According to the results, the simulation of the proposed solid-shell element SB7Y19 have the same results with those from the shell element, and they show good agreement with the experimental data [GUZ 15].

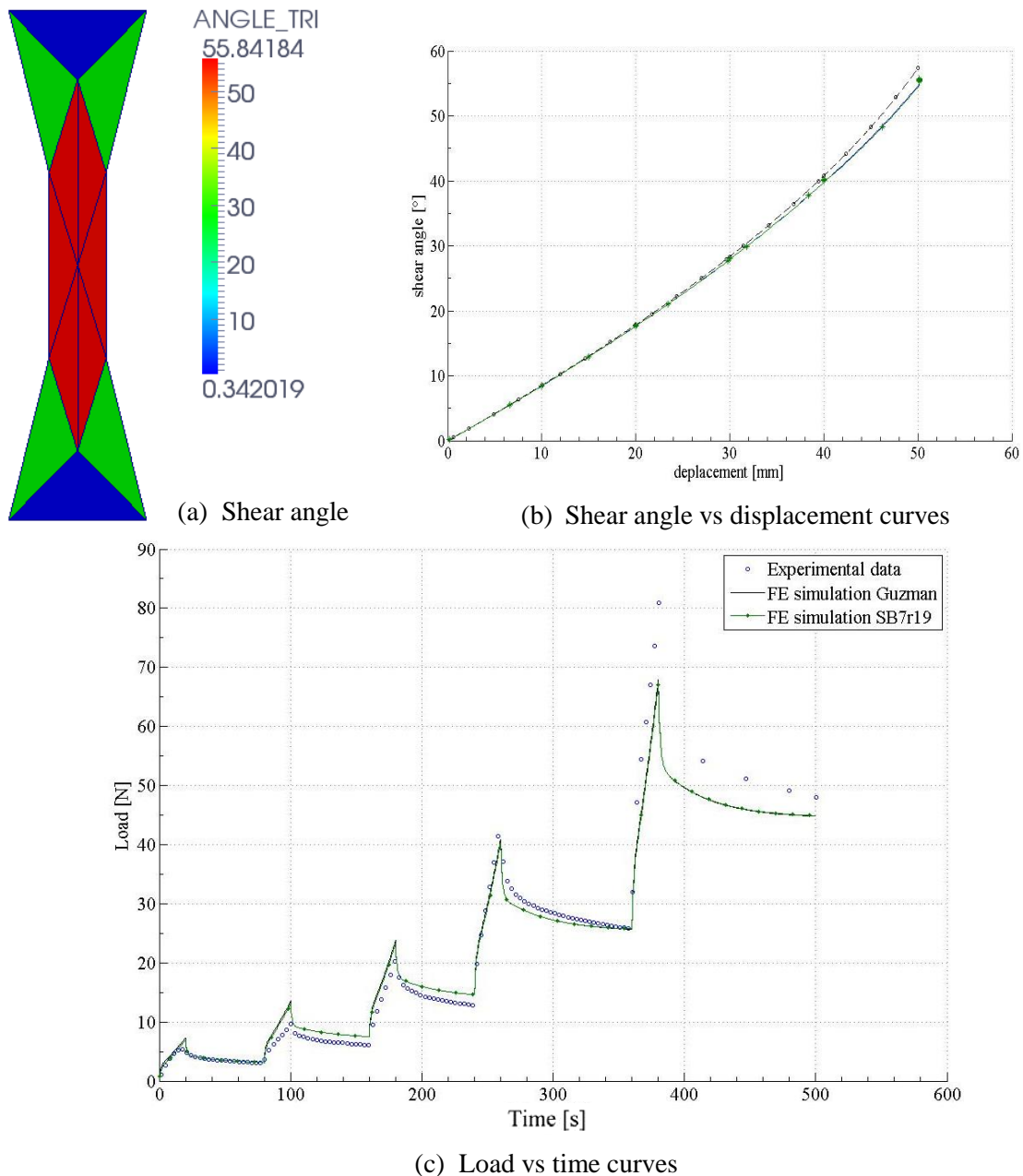


Figure 5. 1: Simulation of the Bias-extension test vs experimental data and simulation with shell element at $T = 270^{\circ}\text{C}$.

5.3.2 Bending test

The validation test for the bending deformation mode is about a clamped rectangular plate of fabric. Shown in **Figure 5. 2**, the geometry is $L \times b \times h=10 \times 1 \times 0.1$ and meshed with prismatic elements, the two directions of the yarn are \mathbf{e}_x and \mathbf{e}_y . In order to be concordant with an isotropic elasticity law: Young's modulus $E=100\,000$, Poisson's ratio $\nu=0$. The tensile stiffness of the fabric plate along the two yarns are the same and equal to E , and the bending stiffness is $k = Ebh^3 / 12 = 8.3333$. The free side is subjected to load F , the results of proposed solid-shell element is compared with the simulation of semi-discrete triangle element [HAM 07] and the analytic results from the Abaqus solution with the mesh of 10×100 S4R elements. The displacements along x and z directions of the loaded side are presented in **Table 5. 1** with two load values.

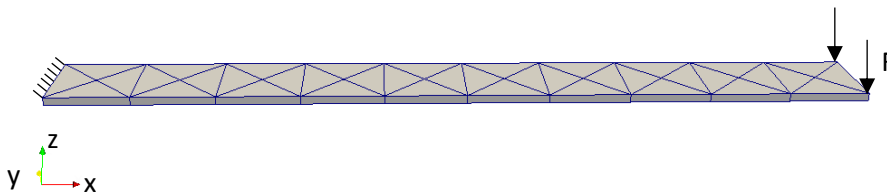


Figure 5. 2: Bending test of a clamped rectangular plate of fabric

F=0,1	Solid shell element	Semi-discrete shell element	Abaqus S4R element
U _z	-3,50490	-3,50617	-3,50512
U _x	-0,73485	-0,76812	-0,74654
F=0,2			
U _z	-5,47014	-5,46892	-5,47211
U _x	-1,95064	-2,01343	-1,96124

Table 5. 1: Results of bending test with three different finite element solutions

5.3.3 Compaction test

The first simple compaction test has been done is about a square thermoplastic composite plate (length = 10, thickness =2) meshed with 4 prismatic elements (**Figure 5. 3**). The boundary conditions are shown in the figure that all the top nodes are fixed at Z direction, and node 6 is also fixed at X and Y directions. The directions of yarns are \mathbf{e}_x and \mathbf{e}_y . The material properties at temperature 270° are obtained from experimental tests and given in chapter 4. A uniform pressure $P=0.6$ is normal to the bottom plane. The numerical test gives the uniform distribution of compression stresses $\sigma_{33}=-0.6$.

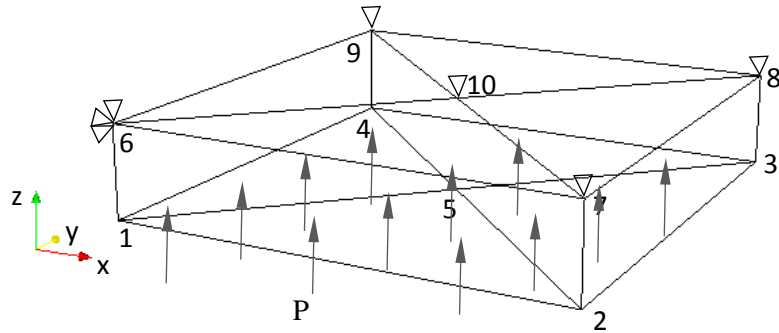


Figure 5. 3: Compaction test of a square thermoplastic composite plate with 4 element

The second test is the circular clamped plate of thermoplastic composite, the geometrical properties and its refined mesh have been presented in chapter 3. The directions of yarns are \mathbf{e}_x and \mathbf{e}_y . The material is presented in chapter 2, and its properties at temperature 270° are obtained from experimental tests and given in chapter 4. The uniform pressure $P=0.5\text{MPa}$ is applied normally to the bottom plane.

In the case with elastic behavior (section 3.3.2), the factor for the equivalent external force on the seventh central node is $-2/3$. For a nonlinear material behavior, which has been also explained in the work of Bassa [BAS 12], the factor is not exactly equal to $-2/3$. It is computed at each increment, depending on the aimed value obtained at the previous increment, to ensure (only) one over the following conditions: minus the pressure on the loaded surface, nil value on the free surface or a compromise solution. Extrapolated to one-sided contact force, the factor fluctuates to ensure an approximate nil value on the opposite side in contact with tooling. In a double-sided contact (like in previous test), nothing is imposed on the central node.

In the circular plate test with uniform pressure $P=0.5$, the factor is optimized as 0.2533. The correct distribution of stress σ_{33} is obtained as -0.4977 in the bottom plane, and almost nil ($-4.778\text{E}-003$) in the top plane.

Moreover, another test has been launched with a linear distribution of pressure along the radius of plate $P(r)=(1-r/R)*P_{\max}$, with $P_{\max}=0.5$, this pressure is also applied in the bottom plane. The factor is fixed as 0.2533 in this test. The distribution of stress σ_{33} in the bottom and top planes along the radius are shown in **Figure 5. 4**. It can be observed that good agreement is obtained comparing with analytical results.

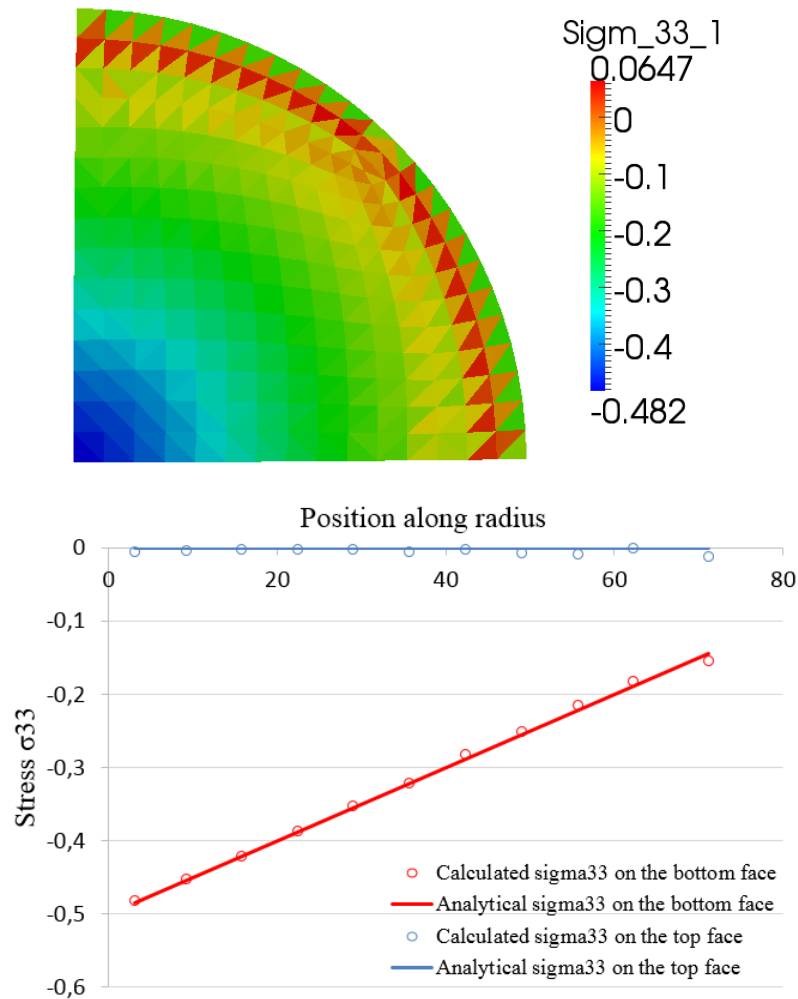
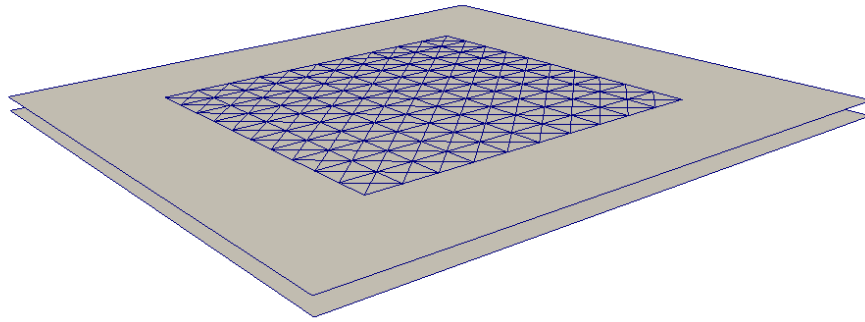
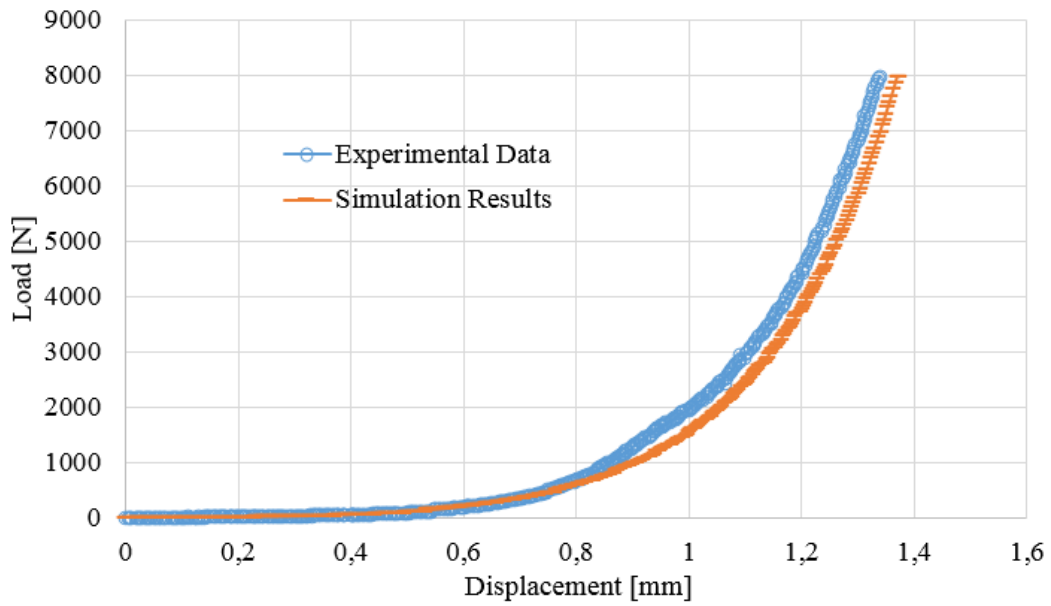


Figure 5. 4: Distribution of stress σ_{33} in the bottom face (top) and its stress distribution in bottom face along the radius comparing to analytical results

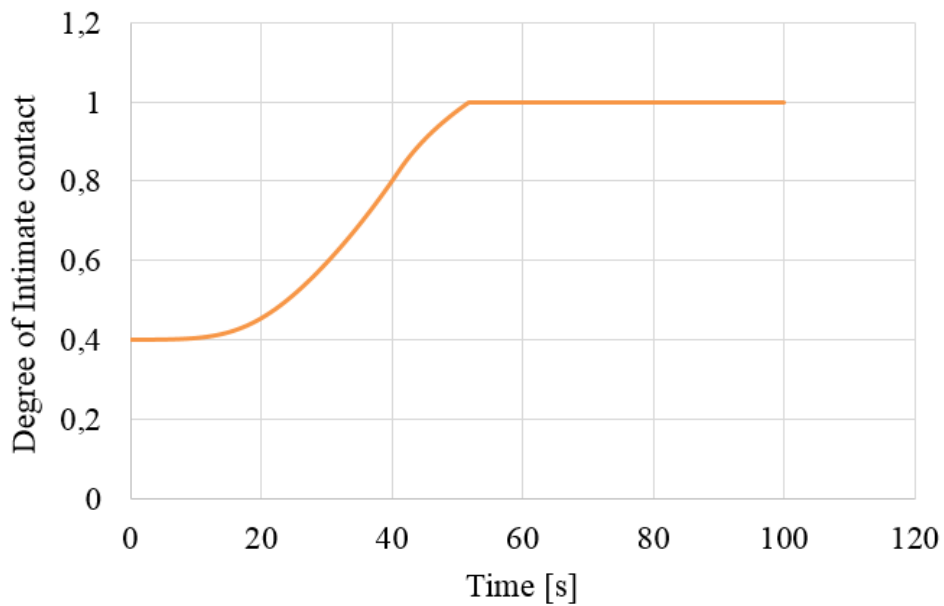
The third test is the simulation of the compaction test of thermoplastic composite. The experimental compaction test is presented in section 2.2.5. As figured in **Figure 5. 5** (a), the meshed thermoplastic plate with dimension of 60mm x 60mm x 2.5mm is placed between two rigid platens. The material is carbon-twill/PA66 thermoplastic composites. The identified mechanical properties at temperature 300°C are introduced for the simulation test. Similarly to the experimental load, a total displacement of 1.4mm with the speed of 2mm/min is applied on the top platen. The simulation load vs. displacement results are plotted in **Figure 5. 5** (b), comparing to the experimental results, it can be noted that the proposed consolidation model can describe the compaction behavior well, and the proposed solid-shell element reveals its feasibility and accuracy in the modelling of 3D constitutive law. Moreover, the model of intimate contact permits to know the thickness in function of load, time, and temperature. In **Figure 5. 5** (c) and (d), the results of degree of intimate contact in function of time and load (pressure) during the compaction test are shown that allows to predict the level of consolidation. It can be seen that the load reaches maximum value at about 40s, the degree of intimate contact is 0.8, and the complete consolidation reaches after about 10s by keeping this maximum value.



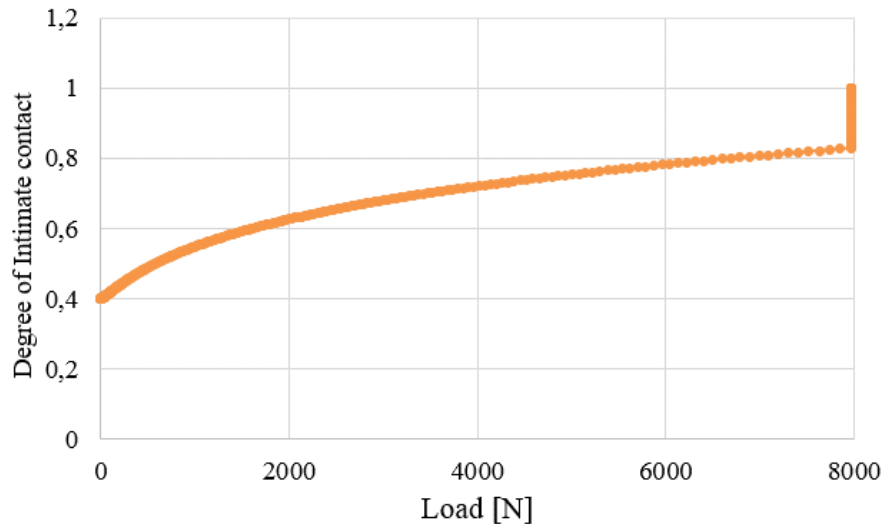
(a) Meshed geometry of compaction test (specimen is placed between rigid platens)



(b) Load versus displacement curve from simulation and experimental results



(c) Degree of intimate contact in function of time



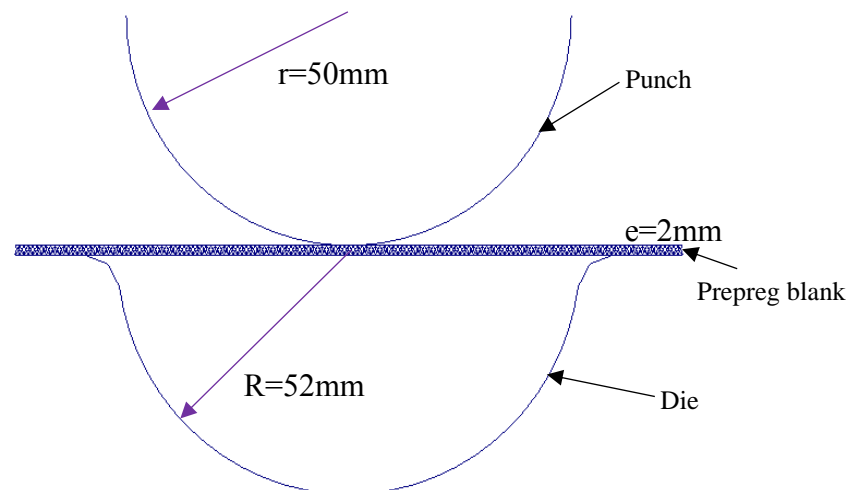
(d) Degree of intimate contact in function of load

Figure 5. 5: Compaction test of thermoplastic composite plate at 300°C

5.4 Simulation of thermoforming

5.4.1 Circular cylinder

The first simple thermoforming simulation test has been launched within a circular cylinder form shown in **Figure 5. 6**, the material of the prepreg blank is carbon-twill/PA66 thermoplastic composites with the material orientation of 0/90°. The identified mechanical properties at different temperature obtained in section 2.2.3 (bending), section 4.2.3 (in plan shear), and section 4.3.3, 4.4.3 (consolidation) are introduced for the simulation test. The temperature is assumed to be constant and homogeneous at 300°C.

**Figure 5. 6:** Geometry of circular cylinder test

After the first forming step with a total displacement of 52mm applied on the punch, the formed shape of prepreg, the distribution of transverse stress σ_{33} and degree of intimate contact D_n are given in **Figure 5. 7**, from which it can be seen that the transverse stress is small and the consolidation level is insufficient.

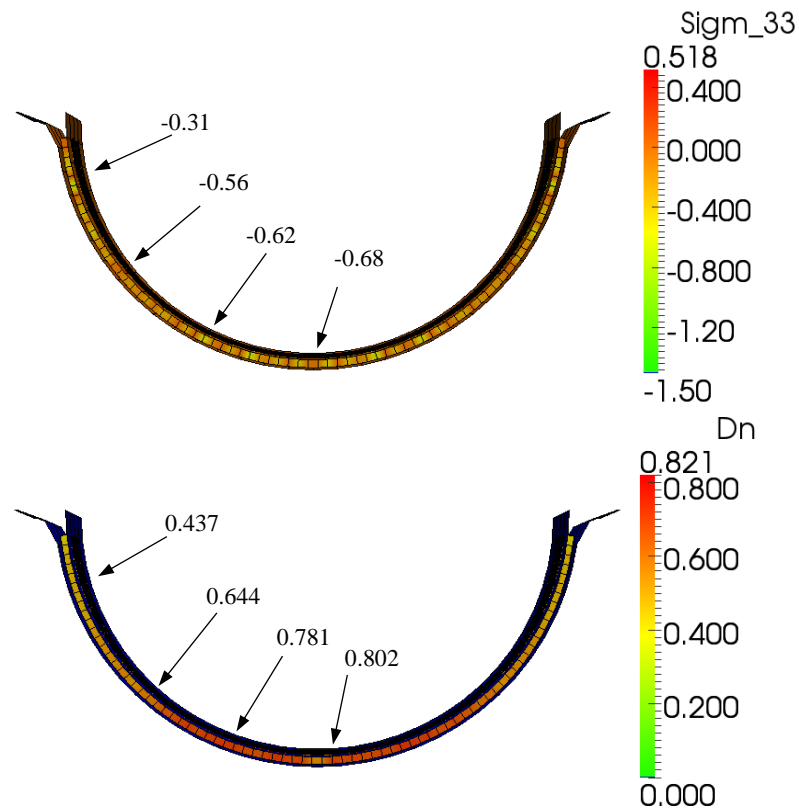


Figure 5. 7: Simulation results after forming process: distribution of transverse stress σ_{33} (MPa/top) and degree of intimate contact D_n (bottom)

During the consolidation process, the punch continues to be pressed by four different given displacement ($\Delta u=0.1\text{mm}$, 0.2mm , 0.3mm , 0.5mm), their correspondant pressed loads (F_n) on the punch can be integrated throught the internal forces of each element of prepreg. Follwing figures (**Figure 5. 8** and **Figure 5. 9**) demonstrate the distribution of transverse stress σ_{33} and thickness e_n for each imposed displacement simulation.

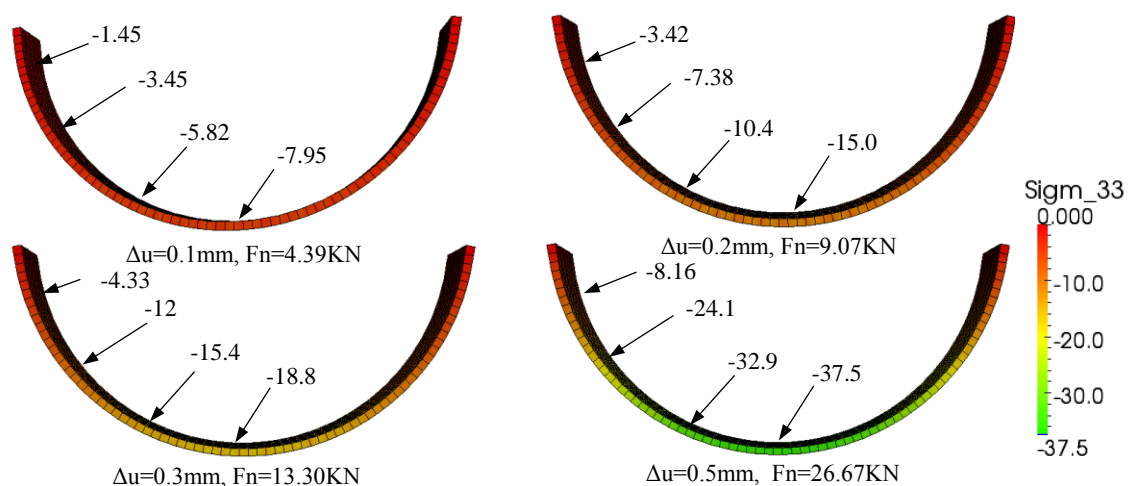


Figure 5. 8: Distribution of transverse stress σ_{33} (MPa) during consolidation process

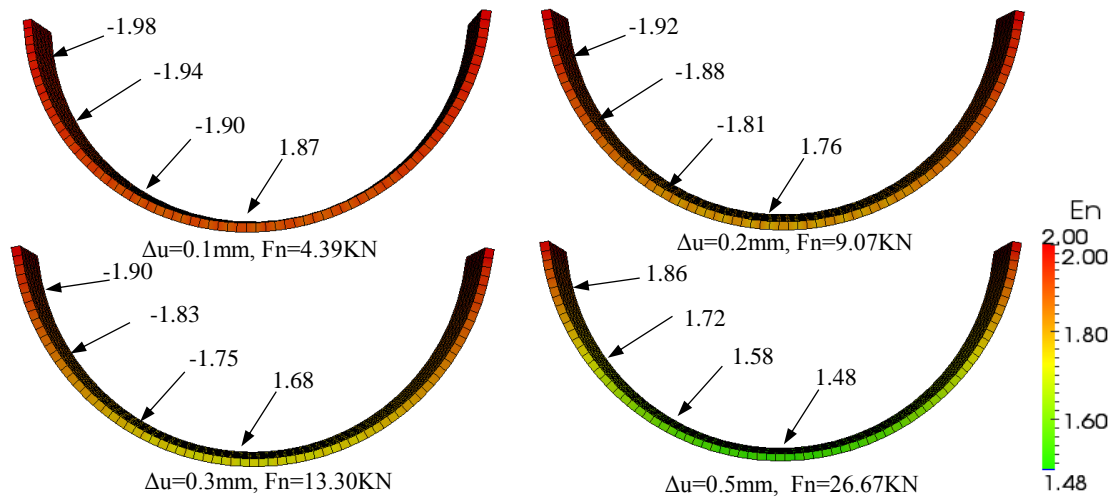


Figure 5. 9: Distribution of thickness E_n (mm) during consolidation process

After the consolidation process, the pressed load is maintained and let the consolidation's level evolve in function of time. **Figure 5. 10** depicts the evolution of consolidation after a consolidated displacement $\Delta u=0.1\text{mm}$. It can be seen that to obtain the completed consolidation level ($D_n=1$), it needs 60 seconds after a consolidated displacement $\Delta u=0.1\text{mm}$, while it costs only 4 seconds after a consolidated displacement $\Delta u=0.5\text{mm}$.

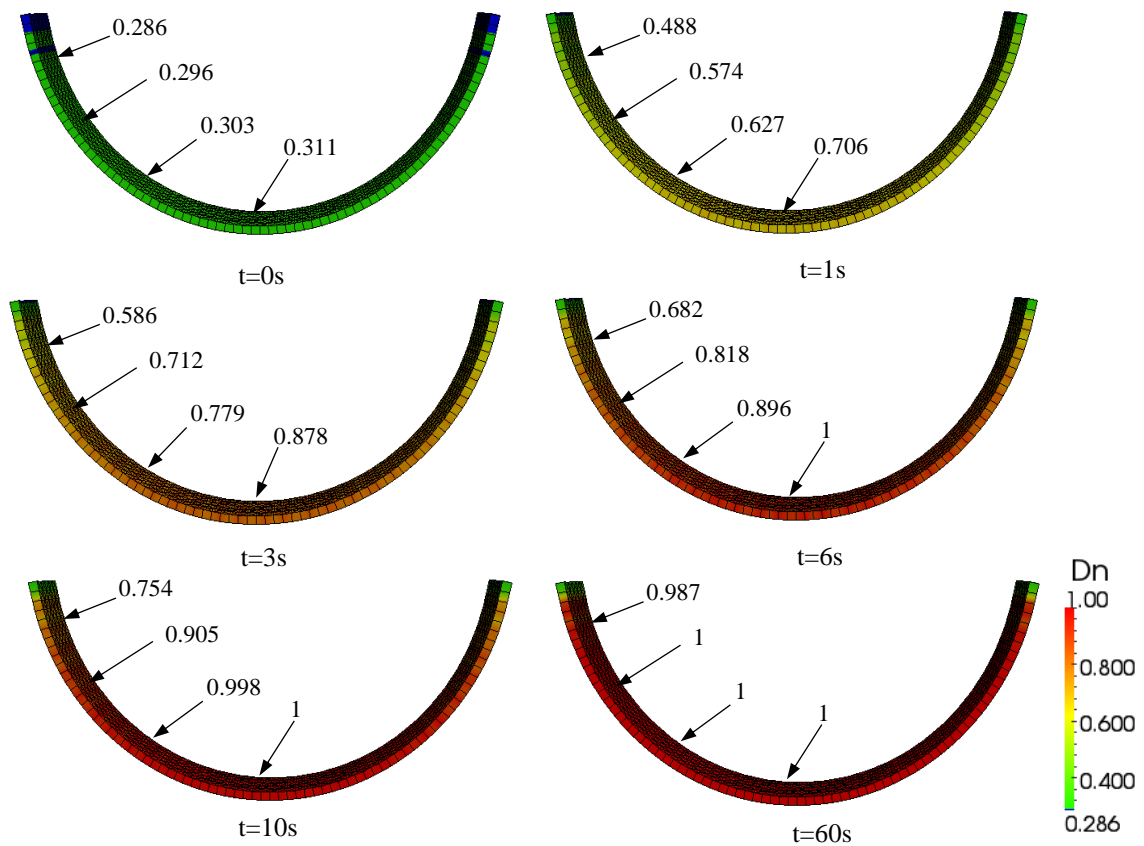


Figure 5. 10: Degree of contact intimate during the evolution of consolidation after a consolidated displacement $\Delta u=0.1\text{mm}$

5.4.2 Double dome at 0/90°

The benchmark example of Double Dome is a relatively complex double-curve geometry mainly used for comparative studies between existing models and approaches for the forming of continuous dry and pre-impregnated reinforcements [KHA 10] [SAR 10], but also to carry out the sensory analysis in relation to the boundary conditions and the process parameters [HAR 13].

Figure 5. 11 presents one quarter of the real geometry, which is composed by a punch, a die and a rectangular preimpregnated blank with dimensions 270mm x 190mm x 2mm maintained in contact with the die by six blank holders. The material used for the thermoforming simulation is carbon-twill/PA66 thermoplastic composites with the material orientation of 0/90°. The identified mechanical properties at different temperature are introduced for the simulation test. The temperature is assumed to be constant and homogeneous. The goal of this section is to investigate the evolution of consolidation during the thermoforming and consolidation steps.

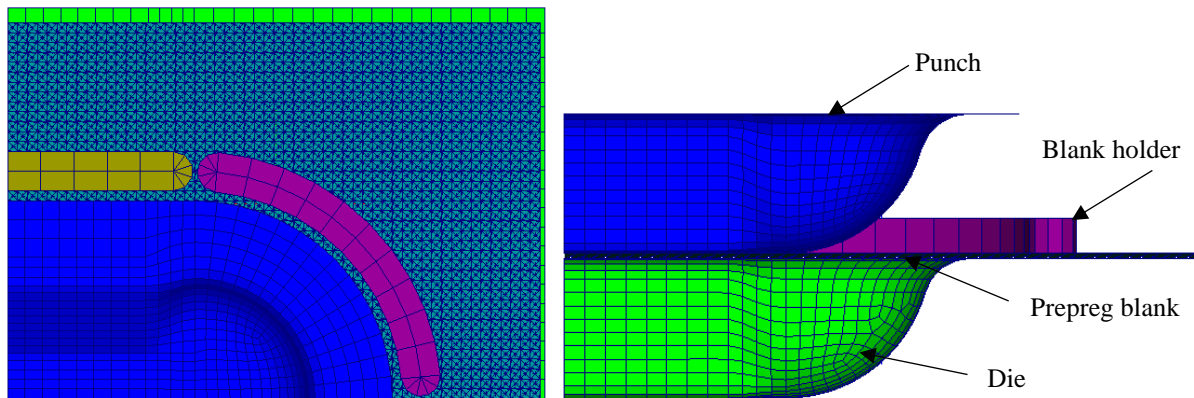
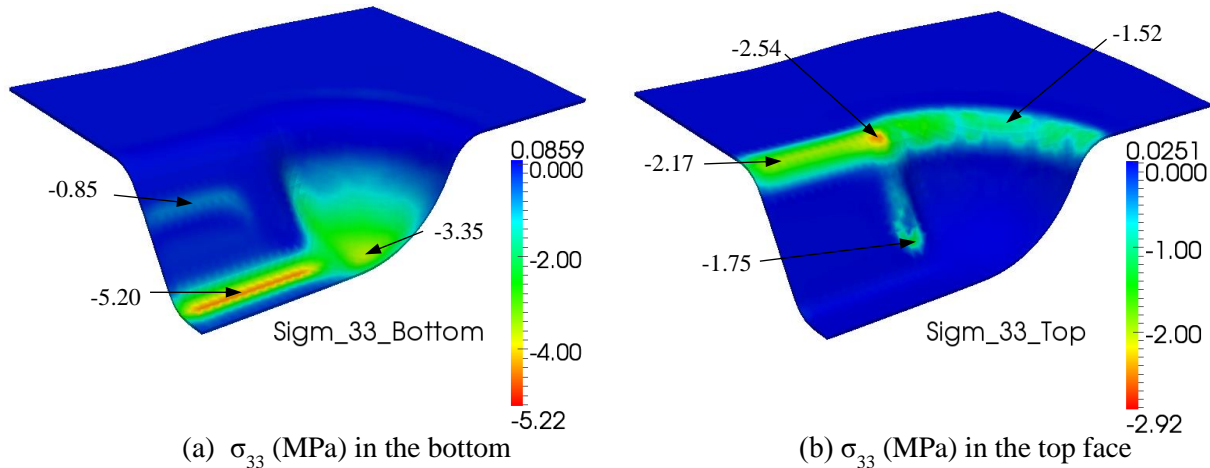


Figure 5. 11: Meshed geometry of double dome test

The simulation of forming stage at temperature 300°C is firstly applied, the velocity of the punch is 240mm/min with the total displacement of 60mm. The distributions of transverse stress σ_{33} in the bottom, top and middle faces are shown in **Figure 5. 12** (a), (b) and (c). Moreover, **Figure 5. 12** (d), (e) and (f) present the consolidation level by the degree of intimate contact D_n in the bottom, top and middle faces.



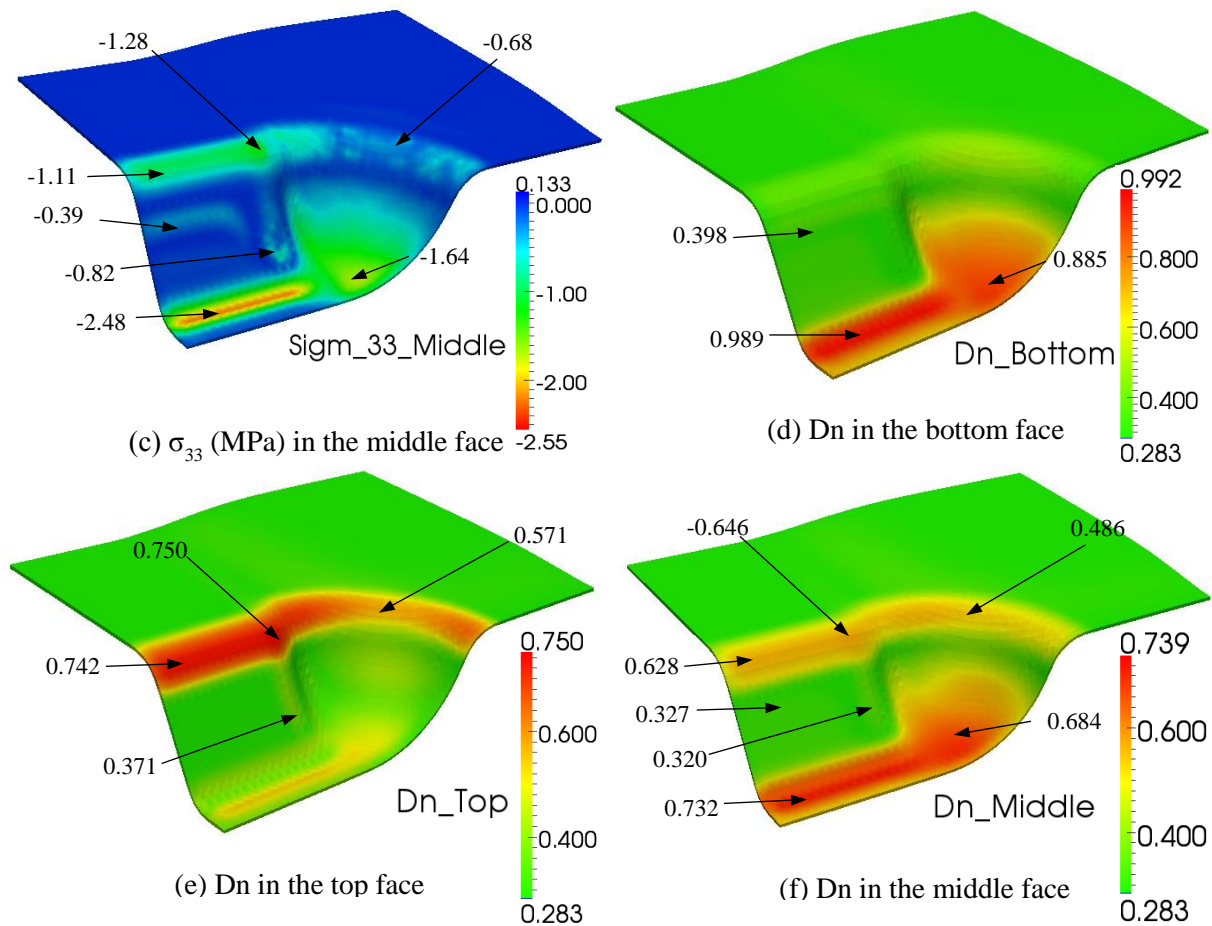


Figure 5. 12: Simulation results during foming step of Double dome test

After the forming step, it can be seen that most part of the deformed piece are not achieved the completed consolidation evaluated by the degree of contact intimate < 1 . The pressed load (Fn) applied on the punch is 2.85KN, which is integrated throught the internal forces of each element of prepreg. The consolidation step is then necessary by increasing this load, two levels of consolidation step have been launched by two given compressed displacements $\Delta u=0.2\text{mm}$ and 0.5mm , whose corresponding pressed loads are $F_n=4.95\text{KN}$ and 10.44KN . Their distribution of transverse stress σ_{33} in the middle face are presented in **Figure 5. 13**.

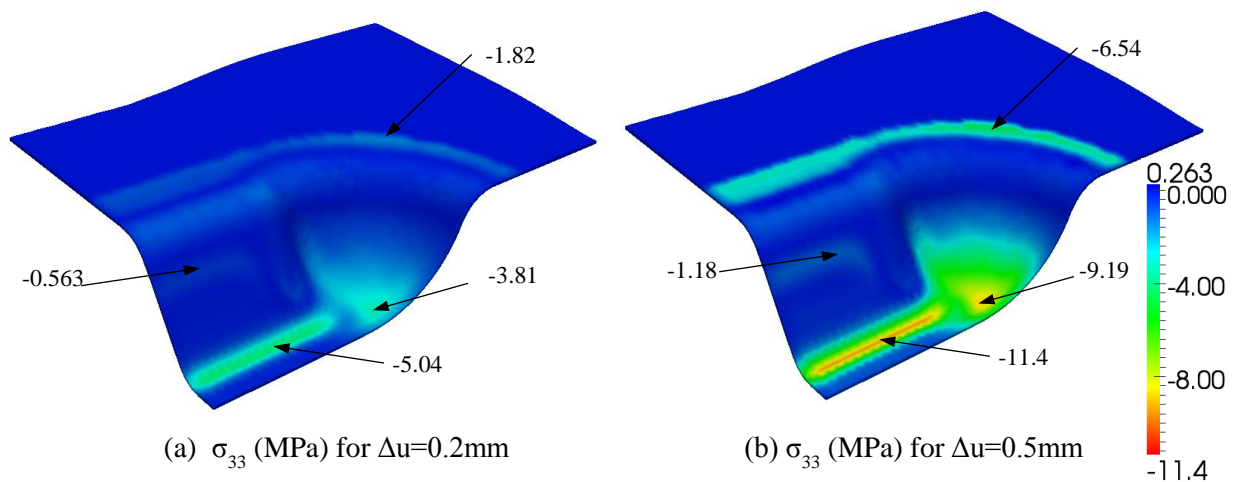
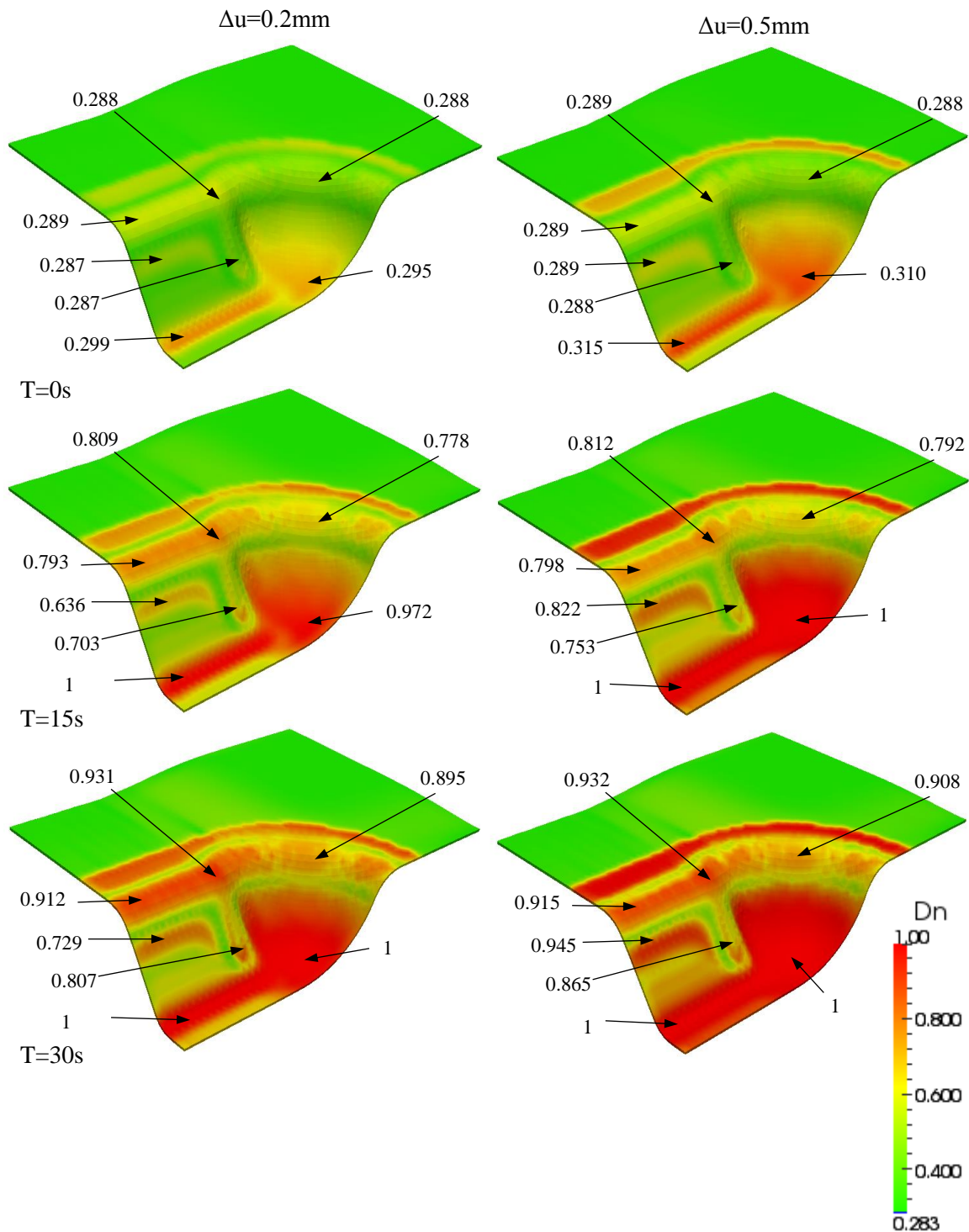


Figure 5. 13: Distribution of transverse stress σ_{33} (middle face) during consolidation process

Finally, by maintaining the final consolidated loads, the evolutions of consolidation in the middle face are displayed in **Figure 5. 14**. From which it shows that, a more complete consolidation level is appeared as time goes by. After about 3min of consolidation, this complete consolidation level is reached through all of the active region for the consolidated displacement 0.5mm, while it costs more than 5min for the consolidated displacement 0.2mm. What's more, the distribution of consolidation level through the prepreg geometry provides more guidance for industrial manufactory by controlling the processing parameters and the geometry design.



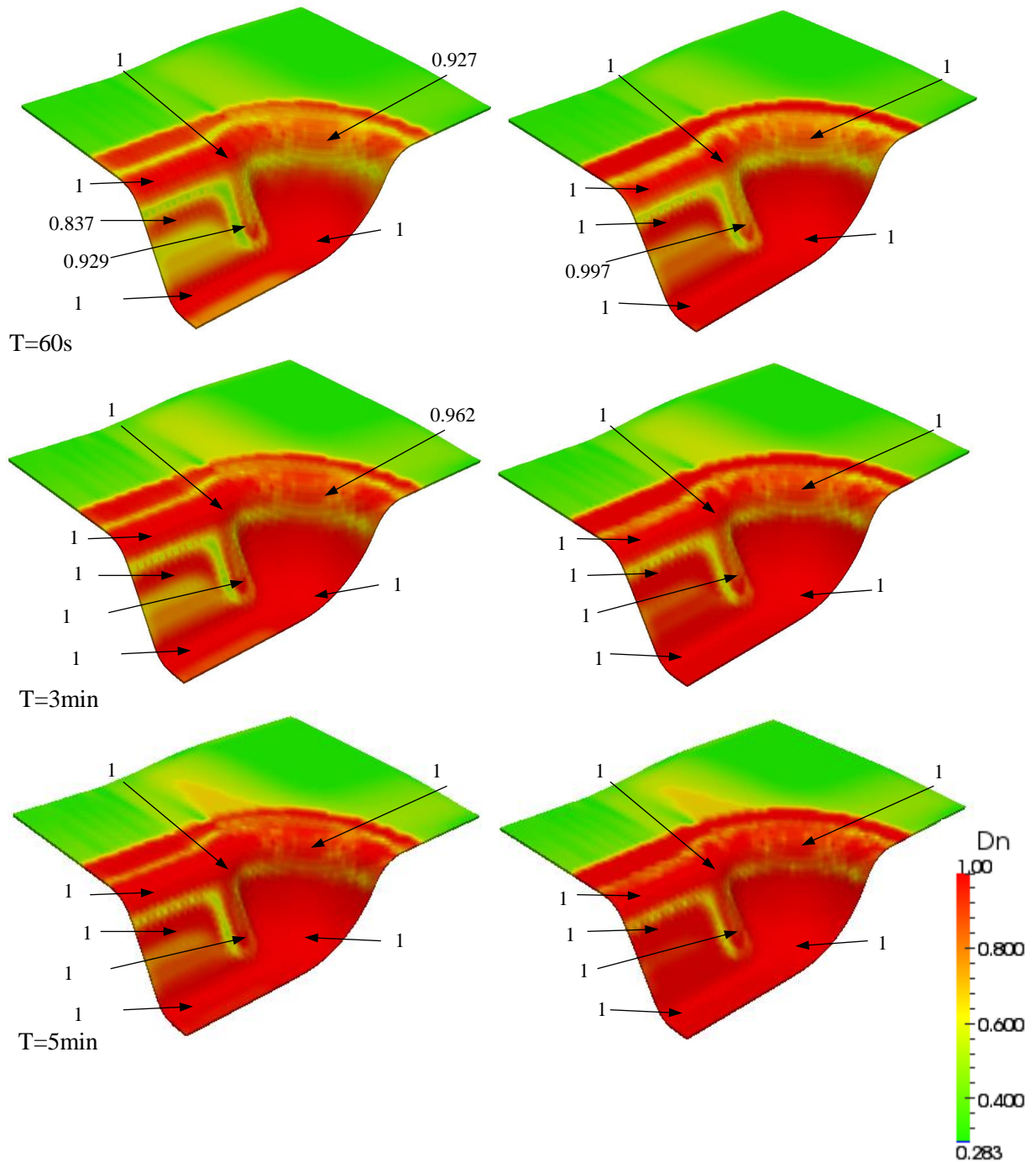


Figure 5. 14: Degree of contact intimate in the middle face during the evolution of consolidation after the consolidated displacement $\Delta u=0.2mm$ (left row) and $\Delta u=0.5mm$ (right row)

5.5 Conclusion of chapter 5

The last chapter has presented the implementation of the visco-hyperelastic law for the thermoforming of thermoplastic prepreg composites by finite element method in an explicit schema. Various elementary tests have been launched for the purpose of validation of the new proposed element and the reestablished three-dimensional constitutive law with the consolidation part. From which, it reveals that the proposed solid-shell element is able to model the bending and in-plan shear deformations without loss of accuracy. What's more, series of compaction tests demonstrate its capacity in modelling of the consolidation behavior with the correct transverse stress distributed through the thickness that the currently used shell element can't reach. In addition, with the intimate contact model, the degree of the intimate contact provides the level of the consolidation step in function of processing conditions (pressure, temperature and time). Finally, the thermoforming simulation of circular cylinder and double dome are done to present the ability of investigation of the consolidation step, during which the evolution of consolidation can be obtained, so that the complete consolidation level can be achieved though the final product by controlling with the processing parameters.

Conclusions and perspectives

As one member of the family of composite material, CFRTP has attracted more and more interests from various sectors in the automotive industry because of its exceptional properties and its high-speed manufacturing processes. And the application of this material is in full swing. Many different research topics have been motivated in the study of CFRTP material manufacturing. In the background of industrial manufacturing process of the material, this Ph.D. thesis work focus on the study of the numerical prediction of the deformation phenomenon during forming process, in particularly the consolidation behavior. It can be principally divided into two parts.

The first part is involved in development of a new solid shell finite element which permits to resolve the problem with three dimensional constitutive law. It is a seven-node prismatic solid-shell element: six are classically located at the apexes and are fitted with three translational DOFs whereas the seventh is sited at the center and is endowed with only one DOF (a local relative displacement along the ‘thickness’ direction). An intermediate material frame related to the element sides is introduced in order to fix nodal transverse shear strain components and that subdues transverse shear locking. Indeed, the enhanced assumed strain method and a reduced integration scheme are combined offering a linear varying strain field along the thickness direction to circumvent thickness locking, and the element’s rank deficiency for pinching is corrected by an hourglass stabilization procedure. The linear normal strain component, along with a full 3D constitutive strain-stress behavior, allows to achieve similar results in bending cases as those obtained with the usual plane stress state hypothesis. The predominance of this element is the ability of three dimensional analysis, especially for the transverse stress existence through the thickness of material, which is essential for the consolidation modelling. A series of benchmark tests both for linear and nonlinear cases commonly employed for testing different kinds of lockings reveals a good convergence behavior and encouraging accuracy for the proposed solid-shell element. In addition, compared to conventional shell elements, the convenience of three-dimensional finite elements is unaffected, it can be able to accommodate a 3D constitutive law, no rotational degrees of freedom are introduced, and the management of contact becomes easily. However, the solution may be sensitive to the mesh density but not more than with some other solid-shell elements (SC6R in Abaqus) or classical triangle shell elements.

The second part is the investigation of the consolidation behavior of thermoplastic prepregs at high temperature. A viscoelastic model for consolidation behavior is established taking account of the effect of resin flow. This model is seemed as the generalization of classical rheological models such as the Maxwell model and its formulation in terms of the internal variables. A completed three-dimensional mechanical behavior visco-hyper-elastic model to characterize the behavior of thermoplastic prepregs is constituted, which involves different independent modes of deformation: elongation mode, bending mode with thermo-dependent, viscoelastic in-plan shearing mode with thermo-dependent, and viscoelastic transverse consolidation mode with thermo-dependent. The associated parameters can be identified by

experimental benchmark tests at high temperature. Moreover, the intimate contact model in consideration of processing conditions (pressure, temperature, and time) is employed in order to predict the evolution of the consolidation which permits the microstructure prediction of void presented through the prepreg.

Finally, several tests including thermoforming test are launched by combining the new developed finite element and the completed behavior of thermoplastic preregs. Comparing with conventional shell element, the proposed solid-shell element not only preforms the equivalent accuracy dealing with the in-plan deformation and bending deformation problems, but also in analyzation of the consolidation behavior, correct distribution of transverse stress can be obtained, and the degree of intimate contact provides the level of consolidation by applied process conditions, which is essential for the appearance of defects in final composite part.

However, more additional studies can be completed in the future work. Firstly, the microstructure analysis can be launched to investigate the reinforcement, the resin, and its flow through the prepreg during consolidation step. More complex model containing different kind of resin flow (squeezing flow and percolation flow) can be completed for the consolidation behavior. Secondly, the experimental compaction test has to be improved to satisfy the hypothesis of consolidation model. As it is known that the temperature varies with big range during consolidation step, it's necessary to find the thermo-dependence relation. What's more, knowing the field of temperature distributed through prepreg material and modelling of the deformation field at this correspondent temperature approximate the true manufacturing process. Thirdly, concerning the thick material with several plies, the transverse shear deformation also becomes significant, and its behavior has to be investigated and its deformation mode can be completed in the hyperelastic potential. Finally, the proposed solid-shell element permits to model multi-ply with one element through thickness, and one ply with one element. The treatment of contact between the tool and the ply, ply and ply can be studied in the future work.

Appendices

Bending:

$$\bar{\mathbf{B}}_{w(3x18)} = \frac{1}{2} \begin{bmatrix} B_{11}^w \cdot zX & B_{11}^w \cdot zY & B_{11}^w \cdot zZ & B_{12}^w \cdot zX & B_{12}^w \cdot zY & B_{12}^w \cdot zZ & B_{13}^w \cdot zX & B_{13}^w \cdot zY & B_{13}^w \cdot zZ & B_{11}^w \cdot zX & B_{11}^w \cdot zY & B_{11}^w \cdot zZ & B_{12}^w \cdot zX & B_{12}^w \cdot zY & B_{12}^w \cdot zZ & B_{13}^w \cdot zX & B_{13}^w \cdot zY & B_{13}^w \cdot zZ \\ B_{21}^w \cdot zX & B_{21}^w \cdot zY & B_{21}^w \cdot zZ & B_{22}^w \cdot zX & B_{22}^w \cdot zY & B_{22}^w \cdot zZ & B_{23}^w \cdot zX & B_{23}^w \cdot zY & B_{23}^w \cdot zZ & B_{21}^w \cdot zX & B_{21}^w \cdot zY & B_{21}^w \cdot zZ & B_{22}^w \cdot zX & B_{22}^w \cdot zY & B_{22}^w \cdot zZ & B_{23}^w \cdot zX & B_{23}^w \cdot zY & B_{23}^w \cdot zZ \\ B_{31}^w \cdot zX & B_{31}^w \cdot zY & B_{31}^w \cdot zZ & B_{32}^w \cdot zX & B_{32}^w \cdot zY & B_{32}^w \cdot zZ & B_{33}^w \cdot zX & B_{33}^w \cdot zY & B_{33}^w \cdot zZ & B_{31}^w \cdot zX & B_{31}^w \cdot zY & B_{31}^w \cdot zZ & B_{32}^w \cdot zX & B_{32}^w \cdot zY & B_{32}^w \cdot zZ & B_{33}^w \cdot zX & B_{33}^w \cdot zY & B_{33}^w \cdot zZ \end{bmatrix}$$

$$\bar{\mathbf{T}}_{(3,18)} = \begin{bmatrix} P_4 \cdot r_{4X} & P_4 \cdot r_{4Y} & P_4 \cdot r_{4Z} & Q_4 \cdot r_{4X} & Q_4 \cdot r_{4Y} & Q_4 \cdot r_{4Z} & -P_4 \cdot r_{4X} & -P_4 \cdot r_{4Y} & -P_4 \cdot r_{4Z} & -Q_4 \cdot r_{4X} & -Q_4 \cdot r_{4Y} & -Q_4 \cdot r_{4Z} & -P_5 \cdot r_{5X} & -P_5 \cdot r_{5Y} & -P_5 \cdot r_{5Z} & -Q_5 \cdot r_{5X} & -Q_5 \cdot r_{5Y} & -Q_5 \cdot r_{5Z} \\ Q_6 \cdot r_{6X} & Q_6 \cdot r_{6Y} & Q_6 \cdot r_{6Z} & P_5 \cdot r_{5X} & P_5 \cdot r_{5Y} & P_5 \cdot r_{5Z} & P_6 \cdot r_{6X} & P_6 \cdot r_{6Y} & P_6 \cdot r_{6Z} & -Q_6 \cdot r_{6X} & -Q_6 \cdot r_{6Y} & -Q_6 \cdot r_{6Z} & -P_6 \cdot r_{6X} & -P_6 \cdot r_{6Y} & -P_6 \cdot r_{6Z} & -P_6 \cdot r_{6X} & -P_6 \cdot r_{6Y} & -P_6 \cdot r_{6Z} \end{bmatrix}$$

In the local frame of the four nodes: $A_4 = ((s_m - s_i)(q_l - q_j) + (q_m - q_i)(s_j - s_l))/2$; $P_4 = (s_l - s_j)/2 \cdot A_4$; $Q_4 = (s_i - s_m)/2 \cdot A_4$

Membrane:

$$\bar{\mathbf{B}}_u^m = \frac{1}{2} \begin{bmatrix} b_{x1} \cdot xX & b_{x1} \cdot xY & b_{x1} \cdot xZ & b_{x2} \cdot xX & b_{x2} \cdot xY & b_{x2} \cdot xZ & b_{x3} \cdot xX & b_{x3} \cdot xY & b_{x3} \cdot xZ & b_{x1} \cdot xX & b_{x1} \cdot xY & b_{x1} \cdot xZ & b_{x2} \cdot xX & b_{x2} \cdot xY & b_{x2} \cdot xZ & b_{x3} \cdot xX & b_{x3} \cdot xY & b_{x3} \cdot xZ \\ 0 & 0 & 0 & 0 & 0 & 0 & 0 & 0 & 0 & 0 & 0 & 0 & 0 & 0 & 0 & 0 & 0 & 0 \\ b_{y1} \cdot xX & b_{y1} \cdot xY & b_{y1} \cdot xZ & b_{y2} \cdot xX & b_{y2} \cdot xY & b_{y2} \cdot xZ & b_{y3} \cdot xX & b_{y3} \cdot xY & b_{y3} \cdot xZ & b_{y1} \cdot xX & b_{y1} \cdot xY & b_{y1} \cdot xZ & b_{y2} \cdot xX & b_{y2} \cdot xY & b_{y2} \cdot xZ & b_{y3} \cdot xX & b_{y3} \cdot xY & b_{y3} \cdot xZ \end{bmatrix}$$

$$\bar{\mathbf{B}}_v^m = \frac{1}{2} \begin{bmatrix} 0 & 0 & 0 & 0 & 0 & 0 & 0 & 0 & 0 & 0 & 0 & 0 & 0 & 0 & 0 & 0 & 0 & 0 \\ b_{y1} \cdot yX & b_{y1} \cdot yY & b_{y1} \cdot yZ & b_{y2} \cdot yX & b_{y2} \cdot yY & b_{y2} \cdot yZ & b_{y3} \cdot yX & b_{y3} \cdot yY & b_{y3} \cdot yZ & b_{y1} \cdot yX & b_{y1} \cdot yY & b_{y1} \cdot yZ & b_{y2} \cdot yX & b_{y2} \cdot yY & b_{y2} \cdot yZ & b_{y3} \cdot yX & b_{y3} \cdot yY & b_{y3} \cdot yZ \\ b_{x1} \cdot yX & b_{x1} \cdot yY & b_{x1} \cdot yZ & b_{x2} \cdot yX & b_{x2} \cdot yY & b_{x2} \cdot yZ & b_{x3} \cdot yX & b_{x3} \cdot yY & b_{x3} \cdot yZ & b_{x1} \cdot yX & b_{x1} \cdot yY & b_{x1} \cdot yZ & b_{x2} \cdot yX & b_{x2} \cdot yY & b_{x2} \cdot yZ & b_{x3} \cdot yX & b_{x3} \cdot yY & b_{x3} \cdot yZ \end{bmatrix}$$

Pinching:

$$\bar{\mathbf{B}}^p = \frac{1}{6} [-zX \ -zY \ -zZ \ -zX \ -zY \ -zZ \ -zX \ -zY \ -zZ \ zX \ zY \ zZ \ zX \ zY \ zZ \ zX \ zY \ zZ]$$

$$[\mathbf{C}^1] = \begin{bmatrix} C_{11}^1 & C_{12}^1 & C_{13}^1 \\ C_{21}^1 & C_{22}^1 & C_{23}^1 \end{bmatrix}; \quad [\mathbf{C}^2] = \begin{bmatrix} C_{11}^2 & C_{12}^2 & C_{13}^2 \\ C_{21}^2 & C_{22}^2 & C_{23}^2 \end{bmatrix}; \quad [\mathbf{C}^3] = \begin{bmatrix} C_{11}^3 & C_{12}^3 & C_{13}^3 \\ C_{21}^3 & C_{22}^3 & C_{23}^3 \end{bmatrix}$$

$$C_{11}^1 = \begin{pmatrix} -(g_{30}^4)_x & -(g_{30}^4)_y & -(g_{30}^4)_z & -\frac{1}{4}h_1\overrightarrow{V_{20}^1}g_{10} & \frac{1}{4}h_1\overrightarrow{V_{10}^1}g_{10} \end{pmatrix}; \quad C_{21}^1 = \begin{pmatrix} -(g_{30}^6)_x & -(g_{30}^6)_y & -(g_{30}^6)_z & -\frac{1}{4}h_1\overrightarrow{V_{20}^1}g_{20} & \frac{1}{4}h_1\overrightarrow{V_{10}^1}g_{20} \end{pmatrix};$$

$$C_{12}^1 = \begin{pmatrix} (g_{30}^4)_x & (g_{30}^4)_y & (g_{30}^4)_z & -\frac{1}{4}h_2\overrightarrow{V_{20}^2}g_{10} & \frac{1}{4}h_2\overrightarrow{V_{10}^2}g_{10} \end{pmatrix}; \quad C_{22}^1 = (0 \ 0 \ 0 \ 0 \ 0);$$

$$C_{13}^1 = (0 \ 0 \ 0 \ 0 \ 0); \quad C_{23}^1 = \begin{pmatrix} (g_{30}^6)_x & (g_{30}^6)_y & (g_{30}^6)_z & -\frac{1}{4}h_3\overrightarrow{V_{20}^3}g_{20} & \frac{1}{4}h_3\overrightarrow{V_{10}^3}g_{20} \end{pmatrix};$$

$$C_{11}^2 = (0 \ 0 \ 0 \ 0 \ 0); \quad C_{21}^2 = \begin{pmatrix} (g_{30}^4)_x & (g_{30}^4)_y & (g_{30}^4)_z & \frac{1}{4}h_1\overrightarrow{V_{20}^1}g_{10} & -\frac{1}{4}h_1\overrightarrow{V_{10}^1}g_{10} \end{pmatrix};$$

$$C_{12}^2 = \begin{pmatrix} -(g_{30}^5)_x & -(g_{30}^5)_y & -(g_{30}^5)_z & -\frac{1}{4}h_2\overrightarrow{V_{20}^2}(g_{20} - g_{10}) & \frac{1}{4}h_2\overrightarrow{V_{10}^2}(g_{20} - g_{10}) \end{pmatrix}; \quad C_{22}^2 = \begin{pmatrix} -(g_{30}^4)_x & -(g_{30}^4)_y & -(g_{30}^4)_z & \frac{1}{4}h_2\overrightarrow{V_{20}^2}g_{10} & -\frac{1}{4}h_2\overrightarrow{V_{10}^2}g_{10} \end{pmatrix};$$

$$C_{13}^2 = \begin{pmatrix} (g_{30}^5)_x & (g_{30}^5)_y & (g_{30}^5)_z & -\frac{1}{4}h_3\overrightarrow{V_{20}^3}(g_{20} - g_{10}) & \frac{1}{4}h_3\overrightarrow{V_{10}^3}(g_{20} - g_{10}) \end{pmatrix}; \quad C_{23}^2 = (0 \ 0 \ 0 \ 0 \ 0);$$

$$C_{11}^3 = \begin{pmatrix} (g_{30}^6)_x & (g_{30}^6)_y & (g_{30}^6)_z & \frac{1}{4}h_1\overrightarrow{V_{20}^1}g_{20} & -\frac{1}{4}h_1\overrightarrow{V_{10}^1}g_{20} \end{pmatrix}; \quad C_{21}^3 = (0 \ 0 \ 0 \ 0 \ 0);$$

$$C_{12}^3 = (0 \ 0 \ 0 \ 0 \ 0); \quad C_{22}^3 = \begin{pmatrix} (g_{30}^5)_x & (g_{30}^5)_y & (g_{30}^5)_z & \frac{1}{4}h_2\overrightarrow{V_{20}^2}(g_{20} - g_{10}) & -\frac{1}{4}h_2\overrightarrow{V_{10}^2}(g_{20} - g_{10}) \end{pmatrix};$$

$$C_{13}^3 = \begin{pmatrix} -(g_{30}^6)_x & -(g_{30}^6)_y & -(g_{30}^6)_z & \frac{1}{4}h_3\overrightarrow{V_{20}^3}g_{20} & -\frac{1}{4}h_3\overrightarrow{V_{10}^3}g_{20} \end{pmatrix}; \quad C_{23}^3 = \begin{pmatrix} -(g_{30}^5)_x & -(g_{30}^5)_y & -(g_{30}^5)_z & \frac{1}{4}h_3\overrightarrow{V_{20}^3}(g_{20} - g_{10}) & -\frac{1}{4}h_3\overrightarrow{V_{10}^3}(g_{20} - g_{10}) \end{pmatrix};$$

Bibliography

- [ABE 09] ABED-MERAIM F, COMBESURE A.
An improved assumed strain solid-shell element formulation with physical stabilization for geometric non-linear applications and elastic-plastic stability analysis. *International Journal for Numerical Methods in Engineering* 2009; 80:1640–1686.
- [AHM 70] AHMAD S, IRONS BM, ZIENKIEWICZ OC.
Analysis of thick and thin shell structures by curved shell elements. *International Journal for Numerical Methods in Engineering* 1970; 2: 419–451.
- [AIM 08] AIMENE Y., HAGEGE B., SIDOROFF F., VIDAL-SALLÉ E., BOISSE P., DRIDIS.
Hyperelastic approach for composite reinforcement forming simulations. *International Journal of Material Forming*, vol. 1, no 1, 2008, p. 811–814, Springer.
- [ALV 07] ALVES DE SOUSA R.J., YOON J.W., CARDOSO R.P.R., FONTES VALENTE R.A., GRÀCIO J.J.
On the use of a reduced enhanced solid-shell (RESS) element for sheet forming simulations *International Journal of plasticity* 2007, 23:490-515.
- [AUS 88] AUSSERER MF, LEE SW.
An eighteen-node solid element for thin shell analysis. *International Journal for Numerical Methods in Engineering* 1988; 26: 1345–1364.
- [AYA 09] AYAD, R., TALBI, N., & GHOMARI, T
Modified discrete Mindlin hypotheses for laminated composite structures. *Composites Science and Technology*, 69(1), 125 -128, 2009
- [BAL 89] BALASURBRAMANYAM, R., JONES, R.S., WHEELER, A.B.
Modelling trans-verse flows of reinforced thermoplastic materials. *Composites* 20, 33–37, 1989.
- [BAS 12] B. BASSA, F. SABOURIN, M. BRUNET.
A new nine-node solid-shell finite element using complete 3D constitutive laws. *Int. J. Numer. Meth. Engng* 2012; 92:589–636.
- [BAT 82] BATOZ J.-L.
An explicit formulation for an efficient triangular plate bending element', *Int. J. Numer. Methods Eng.*, 18, 1077-1089 (1982).
- [BAT 85] BATHE K.J., DVORKIN E.N.,
A four-node plate bending element based on Mindlin-Reissner plate theory and a mixed interpolation, *International Journal for Numerical Methods in Engineering* 1985; 21:367-383.
- [BAT 96] BATHE KJ.
Finite element procedures. New York: Prentice Hall; 1996.

- [BAT 00] BATHE KJ, IOSILEVICH A, CHAPELLE D.
An evaluation of the MITC shell elements. *Computers and Structures* 2000; 75:1–30.
- [BEL 84] BELYTSCSKO T, STOLARSKI H, CARPENTER N.
A C0 triangular plate element with one-point quadrature. *International Journal for Numerical Methods in Engineering* 1984;20:787–802.
- [BEL 94] BELYTSCSKO T., LEVIATHAN I.
Physical stabilisation of the 4-node shell element with one point quadrature, *Computer Methods in Applied Mechanics and Engineering*, 1994; 113:321-350.
- [BEL 11] BEL S.
Analyse et simulation de la mise en forme des renforts de composites NCF. Thèse de doctorat, INSA de Lyon, 2011.
- [BEL 13] BELYTSCSKO T., LIU W. K., MORAN B., ELKHODARY K.
Nonlinear finite elements for continua and structures. John Wiley & Sons, 2013.
- [BEL 16] J.P.-H. BELNOUE, O.J. NIXON-PEARSON, D. IVANOV, S.R. HALLET,
A novel hyper-viscoelastic model for consolidation of toughened prepregs under processing conditions, *Mechanics of Materials* 97 (2016) 118–134
- [BHA 06] BHATNAGAR A.
Lightweight ballistic composites: military and law-enforcement applications. Woodhead Publishing, 2006.
- [BIR 13] BIRCH S.
« BMW i3, the inside story: what it is made of, how it is made ». <http://articles.sae.org/12056/>, 2013.
- [BIS 00] BISCHOFF M., RAMM E.
On the physical significance of higher order kinematic and static variables in a three-dimensional shell formulation, *International Journal of Solids and Structures* 2000; 37:6933-6960.
- [BOE 13] BOEING
« Resource: 787 Aircraft Rescue & Firefighting Composite Structure », 2013.
- [BOI 94] BOISSE P, DANIEL JL, GELIN JC.
A C0 three-node shell element for non-linear structural analysis. *International Journal for Numerical Methods in Engineering* 1994; 37: 2339–64.
- [BOI 95] BOISSE P., CHEROUAT A., GELIN J., SABHI H.
Experimental study and finite element simulation of a glass fiber fabric shaping process.
Polymer composites, vol. 16, no 1, 1995, p. 83–95, Wiley Online Library.
- [BOI 04] BOISSE P.
Mise en forme des renforts fibreux de composites. *Techniques de l'ingénieur*, vol. TIB474DUO, no am3734, 2004.
- [BOI 05] BOISSE P., ZAOUARI B., GASSER A.
A mesoscopic approach for the simulation of woven fibre composite forming. *Composites Science and Technology*, vol. 65, no 3-4, 2005, p. 429-436.

- [BOI 06] BOISSE P.
Meso-macro approach for composites forming simulation. *Journal of Materials Science*, vol. 41, no 20, 2006, p. 6591-6598.
- [BOI 11] BOISSE P., HAMILA N., VIDAL-SALLE E., DUMONT F.
Simulation of wrinkling during textile composite reinforcement forming. Influence of tensile, in-plane shear and bending stiffnesses. *Composites Science and Technology*, vol. 71, no 5, 2011, p. 683–692, Elsevier Ltd.
- [BOR 02] BOROUCHE H., CHEROUAT A.
Une nouvelle approche géométrique pour le drapage des structures composites. *Revue des composites et des matériaux avancés*, vol. 12, 2002, p. 407-421.
- [BOR 03] BOROUCHE H., CHEROUAT A.
Drapage géométrique des composites. *Comptes Rendus Mécanique*, vol. 331, 2003, p. 437-442.
- [BOU 07] BOUBAKER B. B., HAUSSY B., GANGHOFFER J. F.
Discrete models of woven structures. Macroscopic approach. *Composites Part B: Engineering*, vol. 38, no 4, 2007, p. 498-505.
- [BRA 02] BRANK B., KORELC J., IBRAHIMBEGOVIC A.
Nonlinear shell problem formulation accounting for through-the-thickness stretching and its finite element implementation, *Computers and Structures* 2002, 80:699-717.
- [BRA 05] BRANK B.
Nonlinear shell models with seven parameters, *Computer Methods in Applied Mechanics and Engineering* 2005; 194:2336-2362.
- [BRØ 05] BRONSTED P., LILHOLT H., LYSTRUP A.
Composite materials for wind power turbine blades. *Annu. Rev. Mater. Res.*, vol. 35, 2005, p. 505–538, Annual Reviews.
- [BUE 01] BUET-GAUTIER K., BOISSE P.
Experimental analysis and modeling of biaxial mechanical behavior of woven composite reinforcements. *Experimental Mechanics*, vol. 41, no 3, 2001, p. 260-269.
p. 679-698.
- [CAM 10] CAMPBELL F. C.
Structural Composite Materials. ASM International, 2010.
- [CAO 08] CAO J., AKKERMAN R., BOISSE P., CHEN J., CHENG H., DE GRAAF E., GORCZYCA J., HARRISON P., HIVET G., LAUNAY J., LEEW., LIU L., LOMOV S., LONG A., DE LUYCKER E., MORESTIN F., PADVOISKIS J., PENG X., SHERWOOD J., STOILOVA T., TAO X., VERPOEST I., WILLEMS A., WIGGERS J., YU T., ZHU B.
Characterization of mechanical behavior of woven fabrics: Experimental methods and benchmark results. *Composites Part A: Applied Science and Manufacturing*, vol. 39, no 6, 2008, p. 1037–1053.

- [CAR 08] CARDOSO R.P.R., YOON J.W., MAHARDIKA M., CHOUDHRY S., ALVES DE SOUSA R.J., FONTES VALENTE R.A.
Enhanced assumed strain (EAS) and assumed natural strain (ANS) methods for one-point quadrature solid-shell elements, *International Journal for Numerical Methods in Engineering*, 2008; 75:156-187.
- [CAR 09] CARBONNIERE J., THUILLIER S., SABOURIN F., BRUNET M.
Comparison of the work hardening of metallic sheets in bending-unbending and simple shear, *International Journal of Mechanical Sciences* 2009; 51:122-130.
- [CEL 13] CELINO, A., FREOUR, S., JACQUEMIN, F., CASARI, P.
The hygroscopic behavior of plant fibers: A review. *Frontiers in chemistry*, 2013, 1:43
- [CHA 00] CHAPELLE D, BATHE KJ.
The mathematical shell model underlying general shell elements. *International Journal for Numerical Methods in Engineering* 2000; 48:289–313.
- [CHA 03] CHAPELLE D, BATHE KJ.
The finite element analysis of shells—fundamentals. Berlin: Springer-Verlag; 2003.
- [CHA 11] CHARMETANT A., VIDAL-SALLE E., BOISSE P.
Hyperelastic modelling for mesoscopic analyses of composite reinforcements. *Composites Science and Technology*, vol. 71, no 14, 2011, p. 1623–1631, Elsevier Ltd.
- [CHA 12] CHARMETANT A., ORLIAC J., VIDAL-SALLE E., BOISSE P.
Hyperelastic model for large deformation analyses of 3D interlock composite preforms. *Composites Science and Technology*, vol. 72, 2012, p. 1352-1360.
- [CHE 01] CHEROUAT A., BILLOET J. L.
Mechanical and numerical modelling of composite manufacturing processes deep drawing and laying-up of thin pre-impregnated woven fabrics. *Journal of Materials Processing Technology*, vol. 118, no 1-3, 2001, p. 460-471.
- [CHE 02] CHERUET A, SOULAT D, BOISSE P, SOCCARD E, MAISON-LE POEC S.
Analysis of the interply porosities in thermoplastic composites forming processes. *Int J Form Process* 2002;5 (2–4):247–58.
- [CIA 88] CIARLET P.
Mathematical Elasticity, Volume 1: Three dimensional elasticity. Elsevier, 1988.
- [CRE 06] CREECH G., PICKETT A. K.
Meso-modelling of Non-Crimp Fabric composites for coupled drape and failure analysis. *Journal of Materials Science*, vol. 41, no 20, 2006, p. 6725-6736.
- [CRI 01] CRISCIONE J., DOUGLAS A., HUNTER W.
Physically based strain invariant set for materials exhibiting transversely isotropic behavior. *Journal of the Mechanics and Physics of Solids*, vol. 49, 2001, p. 871-897.

- [DAV 87] R. DAVE, J. L. KARDOS, and M. P. DUDUKOVIC
A Model for Resin Flow During Composite Processing: Part 1 -General Mathematical Development, POLYMER COMPOSITES, FEBRUARY 1987, Vol. 8, No. 1
- [DEB 10] DE BILBAO E., SOULAT D., HIVET G., GASSER A.
Experimental study of bending behaviour of reinforcements. Experimental Mechanics, vol. 50, 2010, p. 333-351.
- [DEL 09] DE-LUYCKER E., MORESTIN F., BOISSE P., MARSAL D.
Simulation of 3D interlock composite preforming. Composite Structures, vol. 88, no 4, 2009, p. 615-623.
- [DUM 03] DUMONT F.
Contribution à l'expérimentation et à la modélisation du comportement mécanique de renforts de composites tissés. Thèse de doctorat, Université Paris 6, 2003.
- [DUR 10] DURVILLE D.
Simulation of the mechanical behavior of woven fabrics at the scale of fibers. International Journal of Material Forming, vol. 3, no S2, 2010, p. 1241-1251.
- [EAS 12] EASTERLING E.
Advanced materials for sports equipment: how advanced materials help optimize sporting performance and make sport safer. Springer Science & Business Media, 2012.
- [FLA 81] FLANAGAN D.P., BELYTSCSKO T.
A uniform strain hexahedron and quadrilateral with orthogonal hourglass control, International Journal for Numerical Methods in Engineering 1981; 17:679-706.
- [FLO 13a] FLORES F. G.
Development of a non-linear triangular prism solid-shell element using ANS and EAS techniques, Comput. Methods Appl. Mech. Engrg. 266 (2013) 81–97.
- [FLO 13b] FLORES F. G.
A “Prism” solid element for large strain shell analysis, Comput. Methods Appl. Mech. Engrg. 253 (2013) 274–286.
- [FON 04] FONTES VALENTE R.A., ALVES DE SOUSA R.J., NATAL JORGE R.M.
An enhanced strain 3D element for large deformation elastoplastic thin-shell applications, Computational Mechanics, 2004, 34:38-52.
- [FRA 51] FRAEIJIS DE VEUBEKE BM.
Diffusion des inconnues hyperstatiques dans les voilures à longeron couples. Bull. Serv. Technique de L'Aéronautique No. 24. Imprimerie Marcel Hayez: Bruxelles, 1951.
- [FRE 01] FREDERICK T. WALLENBERGER, JAMES C. WATSON, AND HONG LI.
Glass fibers. ASM Handbook, Vol. 21: Composites, 2001.

- [FUC 08] FUCHS E. R., FIELD F. R., ROTH R., KIRCHAIN R. E.
Strategic materials selection in the automobile body: Economic opportunities for polymer composite design. *Composites Science and Technology*, vol. 68, no 9, 2008, p. 1989 - 2002.
- [GAS 00] GASSER A., BOISSE P., HANKLAR S.
Mechanical behaviour of dry fabric reinforcements. 3D simulations versus biaxial tests. *Computational Materials Science*, vol. 17, no 1, 2000, p. 7-20.
- [GU 02] GU H., ZHILI Z.
Tensile behavior of 3D woven composites by using different fabric structures. *Materials & Design*, vol. 23, no 7, 2002, p. 671-674.
- [GUE 94] GUERIN B.
Polyamides PA. *Techniques de l'ingénieur*, vol. TIB147DUO, no a3360, 1994, Editions T.I.
- [GUZ 15] GUZMAN-MALDONADO E., HAMILA N., BOISSE P., BIKARD J.
Thermomechanical analysis, modelling and simulation of the forming of preimpregnated thermoplastics composites. *Composites Part A: Applied Science and Manufacturing*, vol. 78, 2015, p. 211–222, Elsevier.
- [HAA 14a] HAANAPPEL S., AKKERMAN R.
Shear characterisation of uni-directional fibre reinforced thermoplastic melts by means of torsion. *Composites Part A: Applied Science and Manufacturing*, vol. 56, 2014, p. 8–26, Elsevier.
- [HAA14b] HAANAPPEL SP, TEN THIJE RHW, SACHS U, RIETMAN B, AKKERMAN R.
Formability analyses of uni-directional and textile reinforced thermoplastics. *Composites Part A 2014*; 56: 80–92.
- [HAM 07] HAMILA N.
Simulation de la mise en forme des renforts composites mono et multi plis. Thèse de doctorat, INSA de Lyon, 2007.
- [HAM 09] HAMILA N., BOISSE P., SABOURIN F., BRUNET M.
A semi-discrete shell finite element for textile composite reinforcement forming simulation. *International Journal for Numerical Methods in Engineering*, vol. 79, 2009, p. 1443-1466.
- [HAR 02] HARRISON P., CLIFFORD M. J., LONG A. C., RUDD C. D.
Constitutive modelling of impregnated continuous fibre reinforced composites Micromechanical approach. *Plastics, Rubber and Composites*, vol. 31, no 2, 2002, p. 76-86.
- [HAR 05] HARRISON P., CLIFFORD M.
Design and manufacture of textile composites, chapter Rheological Behaviour of Preimpregnated Textile Composites. *WooWoodhead Publishing, Cambridge, UK, 2005.*
- [HAR 13] HARRISON P., GOMES R., CURADO-CORREIA N.
Press forming a 0/90 cross-ply advanced thermoplastic composite using the double dome benchmark geometry. *Composites Part A : Applied Science and Manufacturing*, vol. 54, 2013, p. 56–69, Elsevier Ltd.

- [HAU 98] HAUPTMANN R., SCHWEIZERHOF K.
A systematic development of 'solid-shell' element formulations for linear and non-linear analyses employing only displacement degrees of freedom, *International Journal for Numerical Methods in Engineering*, 1998; 42:49-69.
- [HAU 00] HAUPTMANN R., SCHWEIZERHOF K., DOLL S.
Extension of the 'solid-shell' concept for application to large elastic and large elastoplastic deformations. *International Journal for Numerical Methods in Engineering*, 2000; 49:1121-1141.
- [HIV 05] HIVET G., BOISSE P.
Consistent 3D geometrical model of fabric elementary cell. Application to a meshing preprocessor for 3D finite element analysis. *Finite Elements in Analysis and Design*, vol. 42, no 1, 2005, p. 25-49.
- [HOL 00] HOLZAPFEL G. A.
Nonlinear Solid Mechanics. Wiley, 2000.
- [HUG 87] HUGHES, T. J. R.
The finite element method, Prentice-Hall, 1987, 803 pages.
- [ITS 04] ITSKOV M., AKSEL N.
A class of orthotropic and transversely isotropic hyperelastic constitutive models based on a polyconvex strain energy function. *International Journal of Solids and Structures*, vol. 41, 2004, p. 3833-3848.
- [KAP 89] KAPRIELIAN, P.V., O'NEIL, J.M.
Shearing flow of highly anisotropic lam- inated composites. *Composites* 20 (1), 43-47, 1989.
- [KAW 73] KAWABATA S., NIWA M., KAWAI H.
The finite-deformation theory of plain-weave fabrics part I: the biaxial-deformation theory. *The Journal of The Textile Institute*, vol. 64, 1973, p. 21-46.
- [KAW 80] KAWABATA S.
The Standardization and Analysis of Hand Evaluation. Textile Machinery Society of Japan, 1980.
- [KEL 11] KELLY, P.A.
A viscoelastic model for the compaction of fibrous materials. *J. Textile Inst.* 102 (8), 689-699, 2011.
- [KHA 10] KHAN M., MABROUKI T., VIDAL-SALLE E., BOISSE P.
Numerical and experimental analyses of woven composite reinforcement forming using a hypoelastic behaviour-application to the double dome benchmark. *Journal of Materials Processing Technology*, vol. 210, 2010, p. 378-388.
- [KIM 88] KIM YH, LEE SW.
A solid element formulation for large deflection analysis of composite shell structures. *Computers and Structures* 1988: 30: 269-274.
- [KIM 05] KIM K.D., LIU G.Z., HAN S.C.
A resultant 8-node solid-shell element for geometrically non-linear analysis, *Computational Mechanics* 2005, 35:315-331.

- [LEB 03] LEBRUN G., BUREAU M. N., DENAULT J.
Evaluation of bias-extension and picture-frame test methods for the measurement of intraply shear properties of PP/glass commingled fabrics. *Composite Structures*, vol. 61, no 4, 2003, p. 341-352.
- [LEE 87] LEE, WI. AND SPRINGER G.S.
A model of the manufacturing process of thermoplastic matrix composites, *J. Comp. Mat.*, 1987, 21, 1017.
- [LEE 04] LEE PS, BATHE KJ.
Development of MITC isotropic triangular shell finite elements. *Comput Struct* 2004; 82: 945–62.
- [LEG 03] LEGAY A., COMBESURE A
Elastoplastic stability analysis of shells using the physically stabilized finite element SHB8PS, *International Journal for Numerical Methods in Engineering*, 2003; 57:1299-1322.
- [LIA 14] LIANG B., HAMILA N., PEILLON M., BOISSE P.
Analysis of thermoplastic prepreg bending stiffness during manufacturing and of its influence on wrinkling simulations. *Composites Part A*, vol. 67, 2014, p. 111-122.
- [LOM 00] LOMOV S. V., GUSAKOV A. V., HUYSMANS G., PRODROMOU A., VERPOEST I.
Textile geometry preprocessor for meso-mechanical models of woven composites. *Composites Science and Technology*, vol. 60, no 11, 2000, p. 2083-2095.
- [LOM 08] LOMOV S. V., IVANOV D. S., VERPOEST I., ZAKO M., KURASHIKI T., NAKAI H., MOLIMARD J., VAUTRIN A.
Full-field strain measurements for validation of meso-FE analysis of textile composites. *Composites Part A: Applied Science and Manufacturing*, vol. 39, no 8, 2008, p. 1218–1231, Elsevier.
- [LOM 11] LOMOV S. V.
Modelling the geometry of textile reinforcements for composites: *WiseTex*. Boisse P., Ed., *Composite reinforcements for optimum performance*, Chapter 7, p. 200-238 Elsevier, 2011.
- [LON 01] A.C. LONG, C.E. WILKS, C.D. RUDD
Experimental characterisation of the consolidation of a commingled glass/polypropylene composite, *Composites Science and Technology* 61 (2001) 1591–1603
- [LOO 83] LOOS, A.C. AND G.S. SPRINGER.
Curing of Epoxy Matrix Composites, *Journal of Composites Materials*, 17(2):135-169, 1983.
- [LUC 00] LUCAS D., PARNEIX P.
Les matériaux composites en construction navale militaire. Ed. Techniques Ingénieur, 2000.
- [LUS 02] LUSSIER D., CHEN J.
Material Characterization of Woven Fabrics for Thermoforming of Composites. *Journal of Thermoplastic Composite Materials*, vol. 15, no 6, 2002, p. 497-509.

- [LUY 09] DE LUYCKER E., MORESTIN F., BOISSE P., MARSAL D.
Simulation of 3D interlock composite preforming. *Composite Structures*, vol. 88, no 4, 2009, p. 615 - 623.
- [MAC 85] MACNEAL H., HARDER L.
A proposed standard set of problems to test finite element accuracy, *Finite elements in Analysis and Design* 1985; 1:3-20.
- [MAL 07] P.K. MALLICK
Fiber-reinforced composites: materials, manufacturing, and design. CRC Press Taylor & Francis Group, LLC, 2007.
- [MAN 92] SUSAN C. MANTELL, SPRINGER G.S.
Manufacturing process models for thermoplastic composites, *J. Comp. Mat.*, Vol.26, No. 16/1992
- [MAR 56] MARK C., TAYLOR H. M.
The fitting of woven cloth to surfaces. *Journal of the Textile Institute*, vol. 47, 1956, p. 477-488.
- [MAR 63] MARQUARDT D.
An algorithm for least squares estimation of nonlinear parameters. *Journal of the Society for Industrial and Applied Mathematics*, vol. 11, 1963, p. 431-441.
- [MAR 95] MARTIN T., BHATTACHARYYA D., COLLINS I.
Bending sheets of fiber-reinforced thermoplastic. *Composites Manufacturing*, vol. 6, no 3, 1995, p. 177-187.
- [MAR 15] MARGOSSIAN A., BEL S., HINTERHOELZL R.
Bending characterization of a molten unidirectional carbon fibre reinforced thermoplastic composite using a Dynamic Mechanical Analysis system. *Composites Part A: Applied Science and Manufacturing*, vol. 77, 2015, p. 154 - 163.
- [MAT 15] S MATHIEU, N HAMILA, F BOUILLON, P BOISSE
Enhanced modeling of 3D composite preform deformations taking into account local fiber bending stiffness, *Composites Science and Technology* 117, 322-333
- [MAZ 05] MAZUMDAR S.
Aerospace Market Forecast: What's in it for Composites? High-Performance Composites, vol. 13, no 2, 2005, page 9.
- [MCG 97] MCGUINNESS G., BRAIDAIGH C. O.
Development of rheological models for forming flows and picture-frame shear testing of fabric reinforced thermoplastic sheets. *J. Non-Newtonian Fluid Mech.*, vol. 73, 1997, p. 1-28.
- [MCG 98] MCGUINNESS G., BRAIDAIGH C.
Characterization of thermoplastic composite in rombus-shear: the picture frame experiment. *Composites Part A*, vol. 29A, 1998, p. 115-132.
- [MOR 71] MORLEY, L.S.D.
The constant plate-bending element. *Journal of Strain Analysis*, 1971; 4:20-24.
- [MOU 01] MOURITZ A., GELLERT E., BURCHILL P., CHALLIS K.
Review of advanced composite structures for naval ships and submarines. *Composite structures*, vol. 53, no 1, 2001, p. 21-42, Elsevier.

- [NAO 14] NAOUAR N., VIDAL-SALLE E., SCHNEIDER J., MAIRE E., BOISSE P.
Meso-scale FE analyses of textile composite reinforcement deformation based on X-Ray computed tomography. *Composite Structures*, vol. 116, no 0, 2014, p. 165 - 176.
- [NAO 15] NAOUAR N., VIDAL-SALLE E., SCHNEIDER J., MAIRE E., BOISSE P.
3D composite reinforcement meso FE analyses based on X-ray computed tomography.
Composite Structures, vol. 132, 2015, p. 1094–1104, Elsevier.
- [NGU 13] NGUYEN Q., VIDAL-SALLÉ E., BOISSE P., PARK C., SAOUAB A., BRÉARD J., HIVET G.
Mesoscopic scale analyses of textile composite reinforcement compaction. *Composites Part B: Engineering*, vol. 44, no 1, 2013, p. 231–241, Elsevier.
- [OKS 03] OKSMAN K., SKRIFVARIS M., SELIN J.-F.
Natural fibres as reinforcement in polylactic acid (PLA) composites. *Comp. Sci. Technol.* 63, 1317–1324 10.1016/S0266-3538(03)00103-9, 2003
- [PEI 30] PEIRCE F.
The "handle" of cloth as a measurable quantity. *The Journal of the Textile Institute*, vol. 21, 1930, p. 377-416.
- [PEN 05] PENG X. Q., CAO J.
A continuum mechanics-based non-orthogonal constitutive model for woven composite fabrics. *Composites Part A: Applied Science and Manufacturing*, vol. 36, no 6, 2005, p. 859-874.
- [PEN 13] PENG X., GUO Z., DU T., YU W.-R.
A simple anisotropic hyperelastic constitutive model for textile fabrics with application to forming simulation. *Composites Part B: Engineering*, vol. 52, 2013, p. 275-281, Elsevier.
- [PHI 98] PHILLIPS RICHARD, DEVRIM A. AKYUZ AND JAN-ANDERS E. MANSON,
Prediction of the consolidation of woven fibre-reinforced thermoplastic composites. Part I. Isothermal case.
Composites Part A 29A (1998) 395-402
- [PLA 11] PLASFIB
[Software] Paris, Inter Deposit certification, agence pour la protection des programmes. 2011.
- [QUA 94] QUANSHUI Z., BOEHLER J. P.
Tensor function representations as applied to formulating constitutive laws for clinotropic materials. *Acta Mech. Sin.*, vol. 10, 1994, p. 336-348.
- [RAM 01] RAMAKRISHNA S., MAYER J., WINTERMANTEL E., LEONG K. W.
Biomedical applications of polymer-composite materials : a review. *Composites science and technology*, vol. 61, no 9, 2001, p. 1189–1224, Elsevier.
- [REE 07] REESE S.
A large deformation solid-shell concept based on reduced integration with hourglass stabilization, *International Journal for Numerical Methods in Engineering*, 2007; 69:1671-1716.

- [RIV 48] RIVLIN R. S.
Large Elastic Deformations of Isotropic Materials. IV. Further Developments of the General Theory. Philosophical Transactions of the Royal Society of London A: Mathematical, Physical and Engineering Sciences, vol. 241, no 835, 1948, p. 379–397, The Royal Society.
- [ROE 92] J. M. ROELANDT, J. L. BATOZ
Shell Finite Element for Deep Drawing Problems: Computational Aspects and Results, Finite Inelastic Deformations — Theory and Applications, International Union of Theoretical and Applied Mechanics 1992, pp 423-430.
- [ROG 89] ROGERS, T.G.
Squeezing flow of fibre-reinforced viscous fluids. J. Eng. Math. 23, 81–89, 1989.
- [SAB 06] SABOURIN F., BRUNET M.
Detailed formulation of the rotation-free triangular element “S3” for general purpose shell analysis, Engineering Computations 2006; 23:469-502.
- [SAN 11a] SANSALONE M., SABOURIN F., BRUNET M.
A new shell formulation using complete 3D constitutive laws. International Journal for Numerical Methods in Engineering 2011; 86:688–716.
- [SAN 11b] SANSALONE M.
A new shell formulation using complete 3D constitutive laws. Application to sheet metal forming simulations. Thèse de doctorat – INSA de Lyon – Ecole doctorale MEGA – 2011
- [SAR 10] SARGENT J., CHEN J., SHERWOOD J., CAO J., BOISSE P., WILLEM A., VANCLOOSTER K., LOMOV S., KHAN M., MABROUKI T., FETFATSIDIS K., JAUFFRES D.
Benchmark Study of Finite Element Models for Simulating the Thermoforming of Woven-Fabric Reinforced Composites. International Journal of Material Forming, vol. 3, no 1, 2010, p. 683-686, Springer-Verlag.
- [SCH 92] SCHNUR D. S., ZABARAS N.
An inverse method for determining elastic material properties and a material interface. International Journal for Numerical Methods in Engineering, vol. 33, no 10, 1992, p. 2039–2057, John Wiley & Sons, Ltd.
- [SCH 09a] SCHWARZE M., VLADIMIROV I.N., REESE S.
On the implementation of the EAS and ANS concept into a reduced integration continuum shell element and applications to sheet forming, International Journal Material Forming, 2009; Vol. 2 Suppl. 1:919-922.
- [SCH 09b] SCHWARZE M., REESE S.
A reduced integration solid-shell finite element based on the EAS and the ANS concept – Geometrically linear problems, International Journal for Numerical Methods in Engineering, 2009; 80:1322-1355.
- [SCH 11] SCHWARZE M., REESE S.
A reduced integration solid-shell finite element based on the EAS and ANS concept – Large deformation problems, International Journal for Numerical Methods in Engineering, 2011; 85:289-329.

- [SHA 04] SHARMA S. B., SUTCLIFFE M. P. F.
A simplified finite element model for draping of woven material. *Composites Part A: Applied Science and Manufacturing*, vol. 35, no 6, 2004, p. 637–643.
- [SHE 07] SHERBURN M.
Geometric and mechanical modelling of textiles. Thèse de doctorat, Université de Nottingham, 2007.
- [SHU 96] S.F. SHULER, S.G. ADVANI,
Transverse squeeze flow of concentrated aligned fibers in viscous fluids, *J. Non-Newtonian Fluid Mech.*, 65 (1996) 47–74
- [SIM 87] J.C. SIMO,
On a fully three-dimensional finite-strain viscoelastic damage model: formulation and computational aspects, *Comput. Methods Appl. Mech. Eng.* 60 (2) (1987) 153–173.
- [SIM 90] SIMO J.C., FOX D.D., RIFAI M.S.
On a stress resultant geometrically exact shell model Part 3: computational aspects of the non-linear theory, *Computer Methods in Applied Mechanics and Engineering* 1990; 79:91-126.
- [SIM 98] SIMO J., HUGES T.
Computational Inelasticity. Springer, New York, 1998.
- [SKO 07] SKORDOS A. A., MONROY ACEVES C., SUTCLIFFE M. P. F.
A simplified rate dependent model of forming and wrinkling of pre-impregnated woven composites. *Composites Part A: Applied Science and Manufacturing*, vol. 38, no 5, 2007, p. 1318–1330.
- [SMI 90] SMITH C.
Design of marine structures in composite materials. Barking, Essex, England : Elsevier Science Publishers, 1990.
- [SMO 99] SMOLENSKI W.M.
Statically and kinematically exact nonlinear theory of rods and its numerical verification, *Computer Methods in Applied Mechanics and Engineering*, 1999; 178:89-113.
- [SPR 82] G.S. SPRINGER.
Resin Flow during the Cure of Fiber Reinforced Composites, *Journal of Composites Materials*, 16(5):400-410, 1982.
- [SUD 05] SUDDLELL B. C., EVANS W. J.
Natural fiber composites in automotive applications in *Natural Fibers in Biopolymers and Their BioComposites*, eds Mohanty A. K., Misra M., Drzal L. T., editors. (CRC Press;), 2005, 231–259
- [SZE 00] SZE K. Y., YAO L. Q.
A hybrid stress ANS solid-shell element and its generalization for smart structure modeling, Part 1-solid-shell element formulation. *International Journal for Numerical Methods in Engineering*, 2000; 48:545-564.
- [SZE 01] SZE K. Y., CHAN W. K.
A six-node pentagonal assumed natural strain solid-shell element. *Finite elements in analysis and design* 37 (8), 639-655, 2001

- [SZE 02a] SZE K. Y.
Three-dimensional continuum finite element models for plate/shell analysis. *Progress in Structural Engineering and Materials*. 2002; 4 (4), 400-407
- [SZE 02b] SZE K. Y., CHAN W. K., PIAN T. H.
A eight-node hybrid-stress solid-shell element for geometric non-linear analysis of elastic shells, *International Journal for Numerical Methods in Engineering*, 2002; 55:853-878.
- [SZE 02c] SZE K. Y., LIU X. H., LO S. H.
Hybrid-stress six-node prismatic elements. *International Journal for Numerical Methods in Engineering*, 2002; 55:853-878.
- [SZE 04] K.Y. SZE, X.H. LIU, S.H. LO.
Popular benchmark problems for geometric nonlinear analysis of shells. *Finite Elements in Analysis and Design* 40 (2004) 1551–1569.
- [SZE 05] SZE K. Y., LIU X. H.
A new skeletal model for fabric drapes. *International Journal of Mechanics and Materials in Design*, vol. 2, no 3-4, 2005, p. 225-243.
- [VAN 91a] B. P. VAN WEST, R. BYRON PIPES, and S. G. ADVANI
The consolidation of commingled chermoplastic fabrics, *POLYMER COMPOSITES*, DECEMBER 1991, Yo/. 72, No. 6
- [VAN 91b] VAN DER WEEEN F.
Algorithms for draping fabrics on doubly-curved surfaces. *International journal for numerical methods in engineering*, vol. 31, no 7, 1991, p. 1415–1426, Wiley Online Library.
- [VER 06] VERREY J., WAKEMAN M., MICHAUD V., MANSON J.A.
Manufacturing cost comparison of thermoplastic and thermoset RTM for an automotive floor pan. *Composites Part A: Applied Science and Manufacturing*, vol. 37, no 1, 2006, p. 9–22, Elsevier.
- [VU 03] VU-QUOC L., TAN X.G.
Optimal solid shells for non-linear analyses of multilayer composites. 1 *Satics, Computer Methods in Applied Mechanics and Engineering* 2003; 192:975-1016.
- [WAN 91] WANG, E.J., GUTOWSKI, T.G.
Laps and gaps in thermoplastic composites processing. *Compos. Manuf.* 2 (2), 69–78, 1991.
- [WAN 99] WANG J., PATON R., PAGE J. R.
The draping of woven fabric preforms and prepregs for production of polymer composite components. *Composites Part A: Applied Science and Manufacturing*, vol. 30, no 6, 1999, p. 757-765.
- [WAN 08] WANG J.
Predictive modelling and experimental measurement of composite forming behaviour. PhD thesis, University of Nottingham, 2008.
- [WAN 14] WANG P., HAMILA N., PINEAU P., BOISSE P.
Thermomechanical analysis of thermoplastic composite prepregs using bias-extension test. *Journal of Thermoplastic Composite Materials*, vol. 27, 2014, p. 679-698, SAGE Publications.

- [WAN 15] WANG P., HAMILA N., BOISSE P., CHAUDET P., LESUEUR D.
Thermo-mechanical behavior of stretch-broken carbon fiber and thermoplastic resin composites during manufacturing. *Polymer Composites*, vol. 36, no 4, 2015, p. 694–703.
- [WIL 08] WILLEMS A., LOMOV S. V., VERPOEST I., VANDEPITTE D.
Optical strain fields in shear and tensile testing of textile reinforcements. *Composites Science and Technology*, vol. 68, no 3-4, 2008, p. 807-819.
- [YU 02] YU W. R., POURBOGHRAT F., CHUNG K., ZAMPALONI M., KANG T. J.
Non-orthogonal constitutive equation for woven fabric reinforced thermoplastic composites. *Composites Part A: Applied Science and Manufacturing*, vol. 33, no 8, 2002, p. 1095-1105.
- [ZIE 05] O.C. ZIENKIEWICZ, R.L. TAYLOR.
The finite element method for solid and structural mechanics. Butterworth-heinemann, 2005.
- [ZOU 06] ZOUARI B., DANIEL J.-L., BOISSE P.
A woven reinforcement forming simulation method. Influence of the shear stiffness. *Computers & structures*, vol. 84, no 5, 2006, p. 351–363, Elsevier.